SINGLE MOLECULE ELECTRONICS IN IONIC LIQUID MEDIA

Thesis submitted in accordance with the requirements of the University Of Liverpool for the degree of Doctor in Philosophy

by

Nicola Julie Kay

June 2012

Abstract

The field of single molecule electronics, where the charge transport properties of a variety of single molecular systems are investigated, has vastly increased in popularity over the last decade. This thesis in particular explores the single molecule conductance and electron transfer over a range of molecules in a room temperature ionic liquid medium. Prior to the work contained in this thesis, no conductance measurements of a single molecule had been recorded in a room temperature ionic liquid medium, to the best of our knowledge. Due to the novelty of room temperature ionic liquids in this field, it was decided that alkanedithiols would be an ideal starting point, largely due to their simplicity and reputation as a model system in single molecule electronics. Ionic liquids have several notable advantages as a medium in such measurements and the aim of the research contained in this thesis is first to show that ionic liquids are indeed a viable medium and secondly, to demonstrate their advantages over more widely used, conventional aqueous or organic media. The redox active molecular wire pyrrolo-tetrathiafulvalene is a particular molecule which would highlight the benefits of an ionic liquid medium, as it has a redox transition which is outside of the potential window available to aqueous electrolytes. Single molecule conductance measurements were obtained using a scanning tunnelling microscope (STM), in particular, the current-distance $I(s)$ technique, and for alkanedithiols also the STM break junction technique. The electrochemistry of pyrrolo-tetrathiafulvalene was investigated using cyclic voltammetry and a monolayer of pyrrolo-tetrathiafulvalene was characterised using polarisation modulation infrared reflection absorption spectroscopy (PM-IRRAS).

Acknowledgements

I would first of all like to offer my greatest appreciation and thanks to my supervisor Professor Richard Nichols for his patience, support and advice throughout my research. I would also like to thank my secondary supervisor Professor Simon Higgins and Professor Don Bethell for useful discussion and advice, especially during group meetings.

Much appreciation must go to the rest of the Nichols/Higgins group, both past and present, with special mention going to Dr. Wolfgang Haiss and Dr. Edmund Leary for the inspiration for this research and useful discussion. Finally, Dr. Gita Sedghi, whose help and support I could not have done without.

I would like to offer my gratitude to our collaborators in this project, Professor Walther Schwarzacher of Bristol University, Professor Bing-Wei Mao of Xiamen University, China, and Professor Jens Ulstrup of the Danish Technical University, Denmark. Special thanks to the Ulstrup group in the DTU for being so welcoming and helpful during my visit in September 2010.

On a personal note, I would like to thank all my friends and family, including those who are no longer with us, for their support during my PhD. A special mention must go to my Grandad George for always being so supportive and enthusiastic during my studies.

Finally, I would like to thank my husband for his support and patience over the past four years.

Contents

List Of Figures

List Of Tables

Chapter 1

Introduction

1 Introduction

1.1 A History Of Single Molecule Electronics

Over the last sixty years, technology has evolved beyond recognition. The invention of the transistor in 1948[1, 2] was a pivotal moment in the history of electrical devices. Moore's Law, developed in 1965 by Intel's co-founder Gordon Moore, describes how the number of components on an integrated circuit is expected to double approximately every eighteen months.[3, 4] As traditional "top-down" methods of manufacturing integrated circuits, such as photolithography[5-7] will start to reach their limit in the near future, new methods of creating extremely small components will need to be realised in order to continue this exponential growth of components per chip. Single molecule electronics (SME), in which single molecules could be used as such components, shows ethereal promise due to a single molecule's small size and functionality.

The concept of nanotechnology, which SME is a branch of, was first conceived in 1959 by the renowned physicist Richard Feynman in his lecture to the American Physical Society in Caltech entitled "There's Plenty Of Room At The Bottom".[8] Feynman envisaged a future where the miniaturisation of technology progresses to the atomic scale, and described the field which we know today as nanotechnology. However, technology at that time did not allow for Feynman's dream of the manipulation of single atoms to become reality. Fifteen years later, Arieh Aviram and Mark Ratner of IBM and New York University respectively, laid the foundations of the field of SME.[9] They proposed a single molecular diode, an organic molecule which in theory would have rectifying properties and could one day have potential uses in electrical devices. The technology to allow them to practically study such systems was still seven years away from its invention, but Aviram and Ratner's vision of single molecular wires laid the foundations of what would prove to be a fruitful field of research. Aviram and Ratner's rectifying molecule contained a donor tetrathiafulvalene (TTF) and acceptor tetracyanoquinodimethane (TCNQ) group.

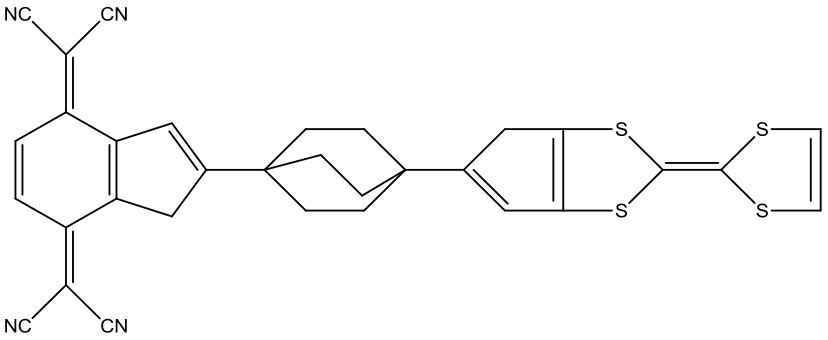

Figure 1: A theoretical molecular rectifier TTF-TCNQ designed by Aviram and Ratner.[9]

In 1988, Aviram *et al.* used a scanning tunnelling microscope (STM) to observe the *I-V* characteristics of an asymmetrical hemiquinone molecule.[10] This was the first measurement of its kind, addressing a monolayer between two metallic electrodes. A monolayer was assembled on a Au(111) on mica surface by immersion in a solution containing the hemiquinone molecule, which binds to the Au via the sulfur on the thioether. Measurements were taken using a Pt tip and *I-V* scans were obtained at several positions on the surface. On flat areas where it is assumed that there are no molecules present, the *I-V* characteristics were reminiscent of bare Au. However, when a hemiquinone molecule was positioned between the Pt tip and Au substrate, the current peaked at approximately -200 mV when the potential was swept in a negative direction. This abrupt increase in current was however, not observed when the potential was swept in a positive direction. This result in itself is not spectacular, as two different metals were used for the electrodes, which may in itself result in rectification, but the fact that the experiment was performed was a huge leap forward in the field.[10, 11]

1.1.1 Benzenedithiol

Benzenedithiol (BDT) is widely recognised as the first molecule to have its conductance measured quantitatively. Since Reed *et al.*'s pioneering measurements in 1997[12], several groups have undertaken their own conductance measurements of BDT, with varying, and sometimes apparently contradictory results.[13-19]

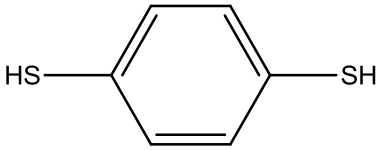

Figure 2: Benzenedithiol, the first molecule to have its conductance quantitatively measured. It is also the subject of several conflicting results.

Reed *et al*. used a mechanically controlled break junction (MCBJ) at room temperature to perform their measurements.[12] This was fabricated by adsorbing a monolayer of BDT onto a length of gold wire. This wire was then stretched until finally, breakage occurred, resulting in the formation of two tips of atomic sharpness. These tips were then brought closer together so that a single molecule of BDT bridges the gap. *I-V* measurements were performed and the conductance of a single molecule was measured to be 45 nS.[12] Xiao *et al.* obtained a conductance of 851 nS for a single molecule of BDT[14], which is approximately 20 times larger than Reed *et al*.'s value. They used their STM controlled break junction (BJ) technique[14, 20] which is described in detail in a later section of this thesis. Lörtscher *et al*. and Martin *et al*. both used MCBJ in UHV conditions and both obtained different conductance values for BDT, at 3.85 nS and 77 nS respectively.[15-17] Lörtscher *et al*. however found that the conductance of BDT does exhibit a temperature dependence.[17] Haiss *et al*. used the STM *I(t)* technique to study the effect of molecular tilting on the conductance.[18] This involved holding the STM tip at a set distance above the surface and measuring current jumps as molecules spontaneously bridged the gap between tip and substrate. Haiss *et al.* found that the conductance of BDT increased as the tilt angle increased. An untilted BDT molecule was found to have a conductance of 8.6 nS. This increased significantly when the tilt angle was greater than about 50°.[18] Discrepancies between the different research groups could be partly explained by this occurrence. It was also found more recently that different conductance groups exist depending on the nature of the adsorption site.[21] This could also help to provide an explanation for the many different conductance values measured for this molecule.

1.1.2 Model System: Alkanedithiols

Alkanedithiols are simple hydrocarbon chains where the carbons are joined by single bonds and are terminated on either end by a thiol group. They are the most studied

system in single molecule electronics, partly due to their stability and large HOMO-LUMO gap.[19, 22]

Xu and Tao used their celebrated STM BJ technique to measure the conductance of hexanedithiol (HDT), octanedithiol (ODT) and decanedithiol (DDT), and measured conductance values of about 93 nS, 20 nS and 1.5 nS respectively.[20] These measurements demonstrated the exponential dependence of conductance on length for these alkanedithiols. Another important parameter which quantifies the exponential length dependence, specifically how much the current decays per unit length, is the decay factor β, calculated using the equation $I = I_0\exp(-\beta N)$ where N is unit length. Throughout the majority of the literature, long chain alkanedithiols have been found to have a decay factor $\beta \approx 1$ Å^{-1}.[20, 22-25] Xu and Tao's conductance values for N-alkanedithiols[20] are quantitatively different to those of Cui *et al*. who used a conducting atomic force microscope (c-AFM) to measure the conductance of various alkanedithiols.[26-28] This technique used a mixed monolayer of alkanethiols and alkanedithiols, which was treated with Au nanoparticles. The Au nanoparticles attach to the terminating sulfur of the alkanedithiol, which could then be contacted by the Au-coated AFM tip. The conductance values obtained by Cui *et al*. were about one order of magnitude smaller than Xu and Tao's values. They also obtained a smaller decay factor of $\beta \approx 0.5$ Å^{-1}.[26] Haiss *et al*. have measured alkanedithiols using both their *I*(*s*) and *I*(*t*) techniques and found the conductance of HDT and ODT to be very similar to Cui *et al*.'s values, at approximately 0.5 nS and 1 nS respectively, with a decay factor of $\beta \approx 1$ Å^{-1}.[23, 29] The discrepancies in the conductances obtained by Xu and Tao, Cui *et al*. and Haiss *et al*. can be described by the different conductance groups which exist due to the nature of the adsorbance site.[21] Break junctions are known to create a rough junction where a molecule is much more likely to be adsorbed on a step site. The *I*(*s*) technique on the other hand is capable of picking up molecules which are adsorbed on a terraced surface. Haiss *et al*. confirmed this by using both the STM *I*(*s*) and BJ techniques to investigate the conductance of various alkanedithiols. They confirmed both Cui *et al*.'s lower conductance values, and also Xu and Tao's higher conductances.[23] They also found that the conductance of shorter alkanedithiols has an anomalous length dependence in contrast to an exponential length dependence for longer alkanedithiols.

1.1.3 Redox-Active Systems: Molecular Switches

Redox-active molecular wires are of considerable interest in the field of SME. They exhibit a switching behaviour when the potential is swept, which changes their redox state, resulting in a jump in conductance. The first reversible redox-active switch studied was a (2)catenane-based system, consisting of two interlocked molecules, one being a crown ether containing a tetrathiafulvalene (TTF) moiety and a 1,5-dioxynaphthalene unit on opposing sides of the molecule, and the other being a cyclophane containing two bypyridinium moieties.[30] A Langmuir-Blodgett (LB) film of the catenane was sandwiched between a Ti/Al electrode and a polycrystalline n-Si electrode.

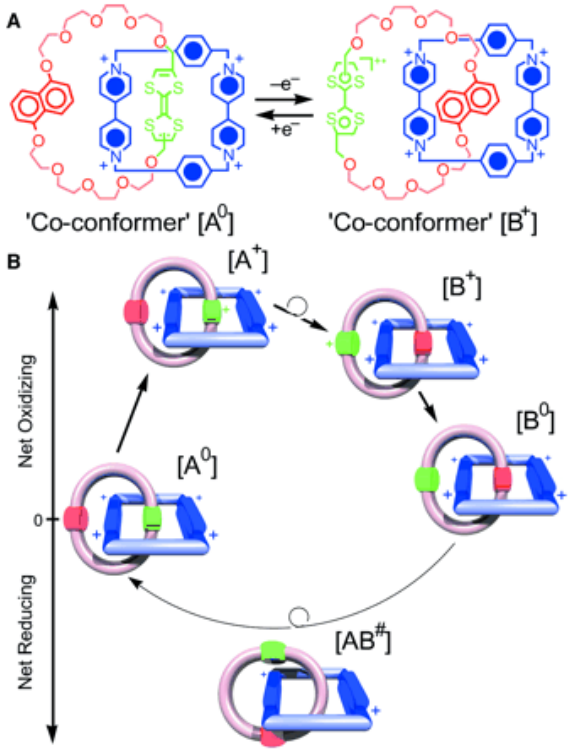

Figure 3: **(A)** the electron transfer between (A^0) and (B^+) and **(B)** the mechanism proposed describing the operation of the system. First of all, the TTF moiety in (A^0) where the switch is in the "off" position, is oxidised, creating (A^+). Due to electrostatic repulsion, the crown ether rotates leading to the creation of (B^+) where the TTF^+ is located outside the cyclophane. (B^0) where the switch is in the "on" position, is formed when the bias voltage is returned to 0 V. In order to regenerate (A^0) thus opening the switch, a bias of +2 V must be applied. "Off" refers to a lower

conductance state for the molecular film, while "on" refers to a higher conductance state. Figure taken from reference 30.

In the ground state (A^0), the TTF unit is located inside the cyclophane, having a bipyridinium unit on either side. When a bias of -2 V is applied, the TTF is oxidised and a new conformer (B^+) is formed as the TTF^+ moves outside the cyclophane ring. As the bias is reduced to 0 V, the TTF^+ is reduced, forming compound (B^0). The conformer will revert back to its ground state when a bias of +2 V is applied. It was determined that the HOMO-LUMO gap for conformer (B^0) is smaller than for (A^0), which means that the electrical conductance is greater for (B^0) than for (A^0), meaning that (A^0) represents the "switch open" state and (B^0) represents the "switch closed" state. This is shown in *Figure 3*.[30] Both oxidation and reduction are essential for device switching, as illustrated by the fact that the compound can only be cycled reproducibly if the opening voltage is greater than 2 V and the closing voltage less than -1.5 V.

Another class of molecular switches are inorganic transition metal complexes, with Os and Co complexes being studied by the Ulstrup group.[31-34] They are particularly attractive due to their ease of synthesis, versatility of the ligands, and stability as well as the reproducibility of their switching behaviour. Albrecht *et al*. have extensively studied three of these compounds.[31-34]

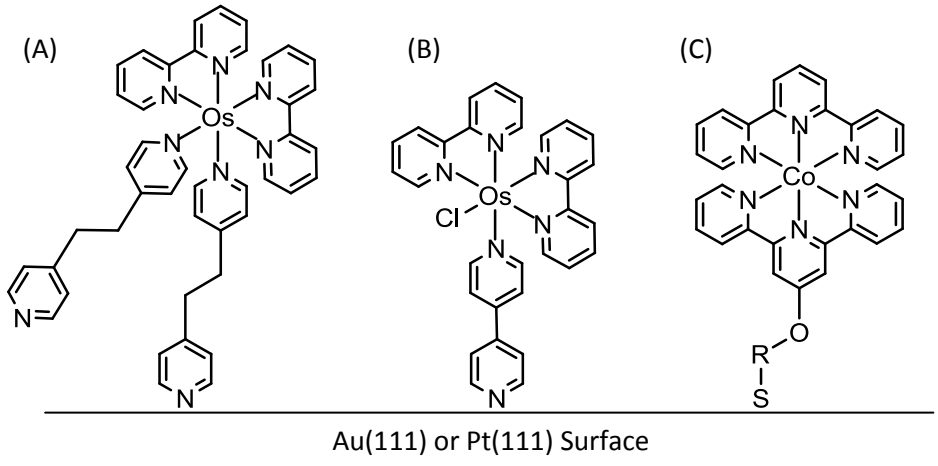

Figure 4: The three inorganic transition metal complexes studied by Albrecht *et al*. They were adsorbed on either a Au(111) or a Pt(111) substrate.[31-34]

The electrochemistry of these compounds was investigated using cyclic voltammetry. Self assembled monolayers (SAMs) were assembled on either Au(111) or Pt(111) substrates.

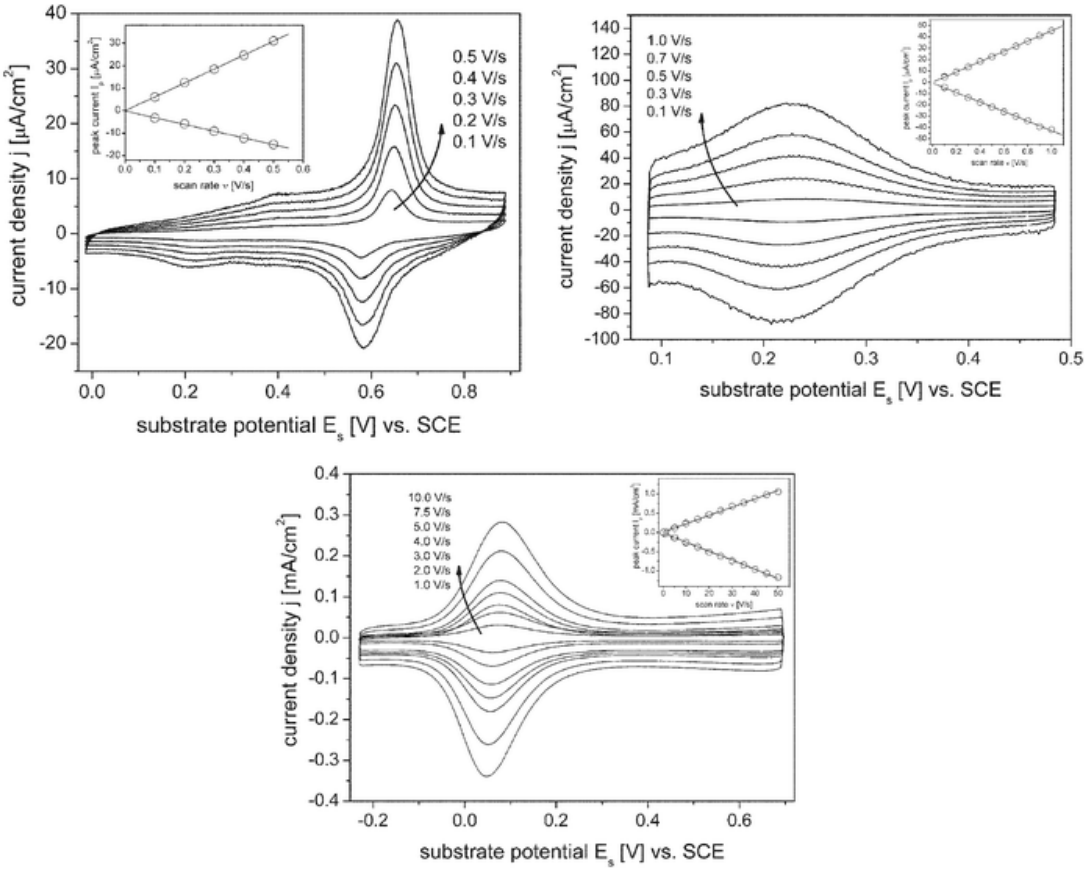

Figure 5: Cyclic voltammetry for compounds **(A)**, **(B)** and **(C)**, referred to in *Figure 4*, at various scan rates. Figure adapted from reference 32.

In all three voltammograms in *Figure 5*, the redox properties are clearly visible. The peak height I_p increases linearly with scan rate υ which confirms that the compound is adsorbed onto the electrode surface. The interfacial electron transfer (ET) kinetics of compounds **(A)** and **(B)** are much faster than for compound **(C)**.[32, 35, 36] In situ scanning tunnelling spectroscopy (STS) was then performed on the compounds. $I_t(E_s)$ spectroscopy with constant bias, where the tunnelling current (I_t) was measured as potential (E_s) was swept with the feedback loop switched off, showed an increase in tunnelling current for all three compounds, as expected for redox-active compounds. This increase in tunnelling current is much stronger for **(A)** and **(B)** which is possibly due to the interfacial ET kinetics described previously.[32-34] The

mechanism of electron tunnelling through these compounds is a two-step process involving vibrational relaxation. This is known as the Kuznetsov-Ulstrup (KU) model and is described in further detail later in this thesis.[32-34]

Viologens contain a 4,4'-bipyridinium (bipy) functional group and are one of the most widely studied redox-active molecular wires, undergoing a reversible redox reaction at about -0.4 V vs. SCE.[37-47]

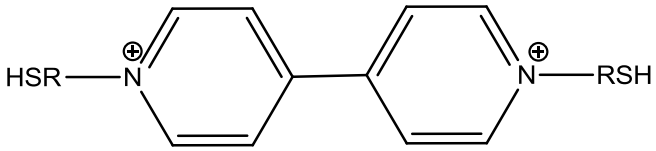

Figure 6: A viologen molecule, containing the bipy moiety. Carbon chains of varying lengths can be attached to either end of the moiety and are thiol-terminated, allowing for the molecule to be adsorbed onto a Au substrate. R = $(CH_2)_n$

Theoretically, ET through viologen should proceed via the KU model.[38, 39, 41, 42, 44, 46, 47] However, this is now known not to be the case. Haiss *et al.* developed the STM *I*(*s*) technique for measuring single molecule conductance on a viologen molecule, specifically 6-(1'-(6-mercapto-hexyl)-(4,4')bipyridinium)-hexane-1-thiol, using EC in situ STM. They observed a conductance change from about 0.5 nS to 2.8 nS, as the molecule was swept through its equilibrium redox potential and switched from its oxidised state to its reduced state. However, a maximum in the tunnelling current was not observed, indicating that the KU ET model is not applicable in this instance.[40]

Li *et al*. studied the differences between symmetric and asymmetric junctions in viologen molecular wires.[46] Symmetric junctions were formed by a method similar to the *I*(*s*) method, using a dithiolated viologen.[40] The Au STM tip was positioned at a distance from the surface by applying a very low setpoint current. The feedback loop was then disabled and the tip was moved closer to the surface by about 1 nm. The tip was then kept very close to the surface, with care taken to avoid mechanical contact with the surface and was kept at this distance for 100 ms, to allow for molecular junctions to form. The tip was then retracted from the surface by 2 nm. This process was repeated many times and resulted in current plateaux representing the formation

of viologen junctions. It was found that by using this same technique for the monothiolated viologen monolayer, these current plateaux were not observed, since this molecule lacks a second thiol group to bind to the Au STM tip. The conductance of the dithiolated viologen was measured using the method described above and varying the sample potential (E_s) between -0.25 V and -0.75 V, which is where the first reduction of the viologen moiety takes place, from the dication form to the radical cation form. Similarly to Haiss *et al*., a plot of tunnelling current vs. sample potential was created and a similar shape was observed, although beyond approximately -0.7 V, the curve acquired by Li *et al*. levels off. They attribute this minor difference to the difference in electrolyte used and the absence of oxygen, as the experiment by Haiss *et al*. was performed in ambient conditions whereas the experiment performed by Li *et al*. was under an argon atmosphere.[40, 46] Li *et al*. then went on to study asymmetric viologen junctions using a monothiolated viologen, which was assembled on the Au STM tip. A setpoint current of 100 pA was applied and with a constant bias of +0.1 V, the tip potential was swept and *I-V* curves were recorded between -0.15 V and -0.65 V with a scan rate of 2.0 Vs^{-1}. An average of twenty scans were plotted and the resulting curve is reminiscent of the KU model, with a maximum tunnelling current close to the equilibrium redox potential of the first reduction. Only a small number of viologen molecules situated on the apex of the STM tip are believed to contribute to this tunnelling current, as the tunnelling current decreases exponentially with distance. As the tip potential approaches the equilibrium redox potential, the LUMO of the viologen approaches the Fermi energy of the substrate, initiating the first step of the two-step ET, hence the maximum in the tunnelling current.[46]

Pobelov *et al*. expanded this research into asymmetric molecular junctions, again using the monothiolated viologen molecule.[42] However, differing from the study by Li *et al*., a monolayer of the monothiolated viologen is assembled on the Au(111) substrate and not the Au tip. Two different methods of STS were used; constant bias, where the sample and tip potentials were swept, and variable bias where the sample potential was kept constant and the tip potential was swept. In the resulting *I-V* plots, a clear maximum can be observed at the equilibrium redox potential. This is evidence that ET proceeds by the KU model. However, this model assumes a strong adsorbate interaction with both electrodes whereas in an asymmetric junction, the

adsorbed molecules are not attached to the STM tip and are instead separated from it by the electrolyte solution. Nevertheless, the data obtained suggests that this model of ET prevails.[42]

Pyrrolo-tetrathiafulvalenes (PTTF) are particularly interesting, as they are stable in three redox states, $PTTF^0$, $PTTF^+$ and $PTTF^{2+}$. The first of these redox reactions has an equilibrium redox potential within the range where the Au-thiol bond is stable in aqueous electrolyte.[47-51]

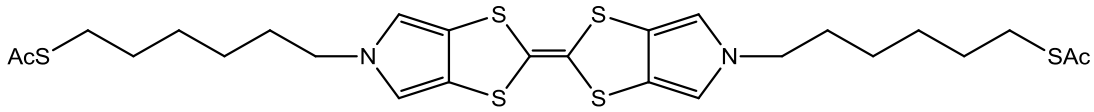

Figure 7: Structure of the redox-active molecule pyrrolo-tetrathiafulvalene (PTTF).

A comparison of the electrochemical and conductance properties of viologen and PTTF was carried out by Leary *et al*.[47] As described earlier, viologen exhibits a broad off-on transition instead of the sharp off-on-off switching predicted by the KU model.[40, 42, 46, 47] $I(s)$ measurements of PTTF were taken under electrochemical potential control, and the conductance vs. electrode potential plots exhibit a maximum in the tunnelling current, reminiscent of the KU model.[47]

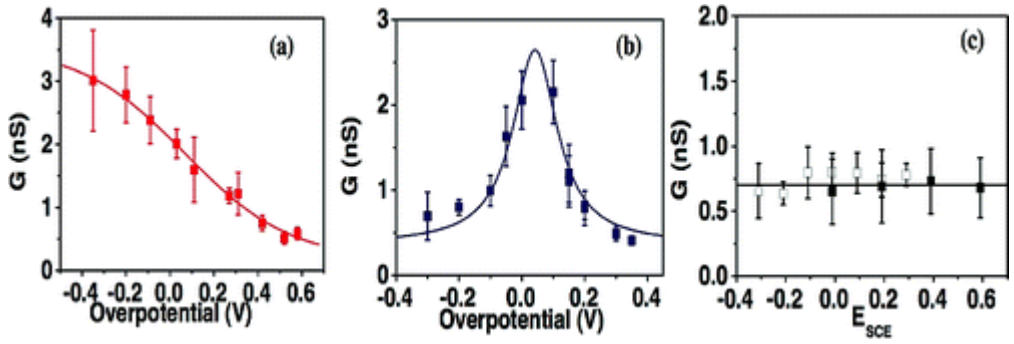

Figure 8: Conductance vs. overpotential plots of (a) viologen, (b) PTTF and (c) 6Ph6, where Ph refers to a phenylene group. Viologen exhibits a broad on-off transition as the potential is swept through the equilibrium potential of the molecule. PTTF has a sharp off-on-off switching behaviour at the redox potential, which is predicted by the KU model. 6Ph6 is redox-inactive so as expected, the conductance isn't affected by changes in potential. Figure taken from reference 47.

A possible explanation as to why the viologen and PTTF behave differently is that PTTF is planar in both the $PTTF^0$ and $PTTF^+$ redox states, whereas V^{2+} can be twisted and possibly becomes more coplanar upon reduction, which may have an impact on the ET mechanism.[47]

1.1.4 Single Molecule Devices

One of the main objectives of the extensive research undertaken in the field of SME is the fabrication of devices containing a single molecule, or arrays of single molecules. This has also turned out to be a major stumbling block in the field. One issue is how to connect each individual molecule in a device to the metal electrodes; it has proven difficult to reduce the width of a metal wire to the molecular scale, meaning that the advantages of the small size of molecules have not yet been fully realised.[52] Current semiconductor technologies have changed the way we live, although they are not without their disadvantages. Presently, as the components in a device get smaller, they suffer from current leakage, which increases power consumption.[53] We will also one day in the not too distant future, reach the limit of what the widely used lithography techniques can achieve. Utilising single molecules in such devices could drastically reduce power consumption as well as greatly increase their capacity. However, it has to be said that such ideas are futuristic and it is unclear if they can ever be practically realised. Nevertheless, an integration of molecules within a more conventional semiconductor microelectronics platform is conceivable and may find future application. These may be niche applications, for example array sensing devices.

Okawa *et al*. managed to connect a conductive polymer nanowire to a nanocluster of metal-free phthalocyanine molecules, using a 10,12-nonacosadiynoic acid SAM, in a technique they described as "chemical soldering".[52] An STM tip was used to stimulate the diacetylene functional group of a 10,12-nonacosadiynoic acid molecule by applying a pulsed bias voltage, which then initiates a chain polymerisation of the diacetylene, forming a polydiacetylene (PDA) chain. This PDA chain grows until it makes contact with the phthalocyanine molecules. This chemical soldering is a promising development in the field and could be developed for practical applications in molecular devices in the future.[52]

One application in particular which molecular electronics may possibly benefit is information storage or memory. Lindsay and Bocian discussed how porphyrin molecules show potential to be incorporated into data storage devices in the future.[54] Porphyrins in particular are relatively simple to synthesise, are customisable, stable and are capable of storing charge, without an applied potential, for several minutes. They typically have two stable redox states, which can be cycled reproducibly for extended periods of time with no degradation, and porphyrin monolayers can survive at high temperatures in an inert atmosphere, which is particularly important during the manufacture of such devices.[54] Porphyrin molecules could possibly be incorporated into dynamic random access memory (DRAM), thus creating a hybrid device which utilises existing semiconductor technology with single molecules acting as components. The traditional lithography techniques used to produce DRAM currently suffer the disadvantage that due to the small dimensions of the transistor gate of the widely used "trench/stack" design, the transistor has a leakage current which depletes the charge stored on the capacitor in the storage cell. If single porphyrin molecules could be used as a storage cell, then the amount of data able to be stored per unit area would massively increase, as well as being more energy efficient.[54] A hybrid data storage prototype was produced in 2004 by Kuhr *et al*. which used a porphyrin molecule in conjunction with the existing metal oxide semiconductor technology.[54, 55] This prototype was a 1 Mb DRAM chip, consisting of four 256 kbit arrays of the molecular capacitors. One major advantage of these hybrid devices was realised as the charge-storage density was found to be greater or equal to the charge storage density of existing semiconductor devices. This development is not yet viable for practical use as of yet, but it shows a glimpse of the potential of single molecular devices in the future.[54, 55] Porphyrins have also shown potential for use in flash memory devices. Shaw *et al*. integrated a monolayer of a Co porphyrin in a flash memory structure successfully.[56] The Co porphyrin demonstrated three reversible redox states which would be particularly useful in flash memory devices.[56]

1.1.5 Room Temperature Ionic Liquids In Electrochemistry

Room temperature ionic liquids (RTIL) are salts which are molten at room temperature and show great promise in the field of electrochemistry and SME as they

have several advantages over conventional aqueous electrolytes. These include a wider potential window, low volatility and high conductivity.[57-61] The wider potential window is of particular interest, as aqueous electrolytes are hindered by hydrogen evolution and surface oxidation at low and high potentials respectively, which may obscure some redox processes. The high conductivity of RTILs means that a carrier electrolyte is not required, which reduces the likelihood of contamination being present in the electrolyte solution.

The wider potential window enjoyed by ionic liquids has been demonstrated by Albrecht *et al*. using an Os bisterpyridine complex (Ossac). Cyclic voltammetry was performed on Ossac in both aqueous electrolyte and the RTIL 1-butyl-3-methylimidazolium hexafluorophosphate ($BMIPF_6$).[57]

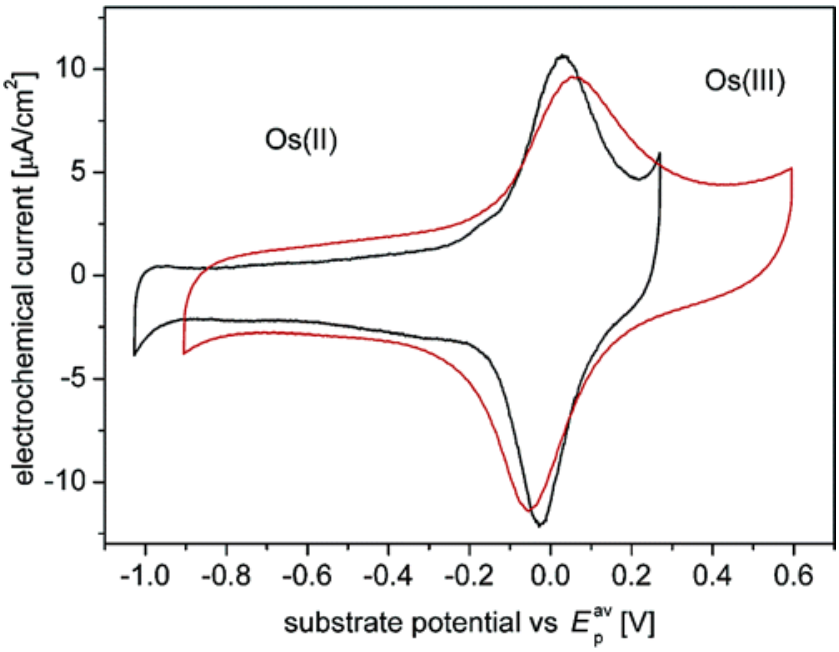

Figure 9: Cyclic voltammetry of the Os bisterpyridine complex (Ossac) assembled on Au(111) in the aqueous electrolyte $HClO_4$ (black) and in the RTIL $BMIPF_6$ (red). The wider potential window accessible using the RTIL is clear at potentials greater than approximately +0.3 V. Figure taken from reference 57.

Albrecht *et al*. also studied the Ossac system under $BMIPF_6$ using STM. They measured the change in tunnelling current as the bias potential and the sample potential were swept. As expected, when the sample potential was varied, a peak in the tunnelling current was observed at the redox potential of Ossac. When the bias

potential was swept, a larger tunnelling current was observed at positive potentials. The tunnelling current dropped to approximately 0 nA below the cathodic peak potential, which is a demonstration of rectification behaviour. The bias range studied was wider than would have been possible using an aqueous electrolyte, highlighting once more one of the advantages of using RTILs in SME.[57]

There have in RTILs, been a range of defined electrochemical surface studies of single crystal electrodes, which have addressed issues such as surface etching and reconstruction. Lin *et al.* monitored the change in the Au(111) surface structure in the RTIL 1-butyl-3-methylimidazolium tetrafluoroborate ($BMIBF_4$) at a range of potentials using STM.[62] It was found that the Au(111) surface undergoes surface restructuring at larger negative potentials greater than approximately -0.9 V. Between -0.9 and -1.2 V, on the terraces, tiny pits of atomic height started to emerge. These pits remained up to approximately – 2.4 V, which is when the bulk RTIL is reduced. When the potential is kept between -1.2 and -2.4 V for an extended period of time, the pits enlarge to form a "worm-like" structure. It is suggested that the BMI^+ cation interacts with the substrate, causing the metal-metal bonds to weaken, leading to defects in the electrode surface.[62] The effect of the RTIL on the substrate may have consequences if RTILs were to be used in SME measurements at negative potential excursions. It was found more recently by Su *et al*. that the BMI^+ cation in imidazolium based RTILs also has a destructive effect on a Au(100) surface.[59]

RTILs have been used as an electrolyte in cyclic voltammetric experiments studying the electrochemical properties of the Fe based porphyrin Hemin.[63] Compton and Laszlo found that the redox potential of Hemin could be modified by varying the RTIL. $BMIPF_6$ was found to produce a reduction potential about 30 mV more negative than the less polar RTIL 1-octyl-3-methylimidazolium hexafluorophosphate ($OMIPF_6$).[63] RTILs show great potential for exploring the electrochemical properties of molecules which may have a redox reaction in a potential inaccessible with conventional aqueous electrolytes.

1.2 Cyclic Voltammetry

In cyclic voltammetry, the potential is swept in a specified range and then the direction reversed and swept once more and the current is measured and plotted onto a voltammogram, which is a plot of current versus electrode potential.

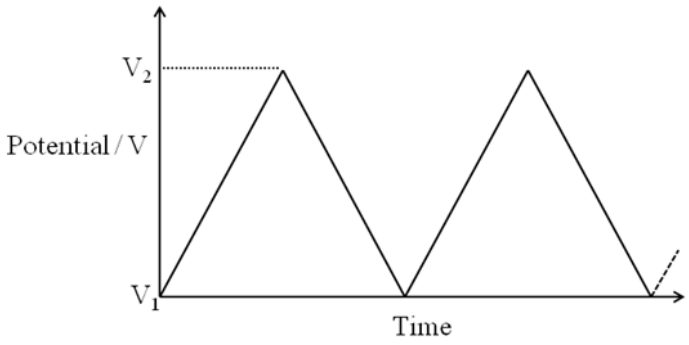

Figure 10: Potential waveform of a cyclic voltammogram. Potential is swept linearly between V_1 and V_2 over time.

Cyclic voltammetry uses a 3-electrode set up in a liquid electrolyte. The working electrode is where the reaction in question takes place, with a counter electrode completing the circuit and counterbalancing the charge flow at the working electrode. It should be of a large surface area in order to easily counterbalance the charge flowing from the working electrode, otherwise it may impede the electrochemical reaction being studied, adversely affecting any results. The counter electrode completes the cell and for example, an anodic reaction taking place at the working electrode must be balanced by a cathodic reaction at the counter electrode. A platinum wire mesh is often used. The reference electrode is used to measure the potential of the system, and must have a known and stable potential. There are many different reference electrodes available and each has its own potential which is referenced back to the standard hydrogen electrode (SHE).

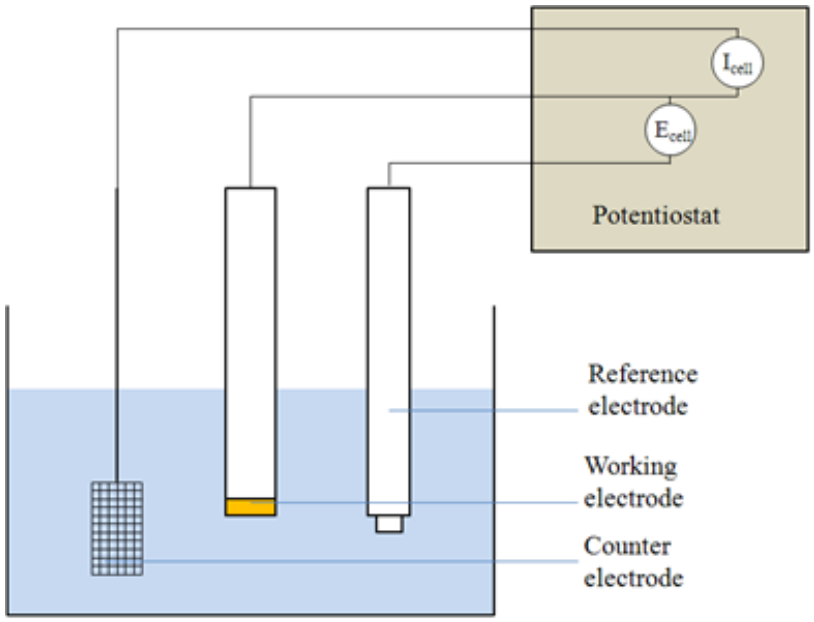

Figure 11: A simple 3-electrode electrochemical cell connected to a potentiostat.

In aqueous electrochemistry, the saturated calomel electrode (SCE) is often employed as it is relatively stable and easy to use. The equilibrium reaction of the SCE is:[64]

$$\tfrac{1}{2}Hg_2Cl_2(s) + e^- \rightleftharpoons Hg(l) + Cl^-(aq)$$

The SCE has a potential of +0.242 V when referenced to the SHE at room temperature (25°C).[64]

Cyclic voltammetry is very useful for preliminary investigations of reaction mechanisms, as the reversibility, potential and kinetics of a reaction can be determined. An example of a cyclic voltammogram of a species in solution is shown in *Figure 12*.

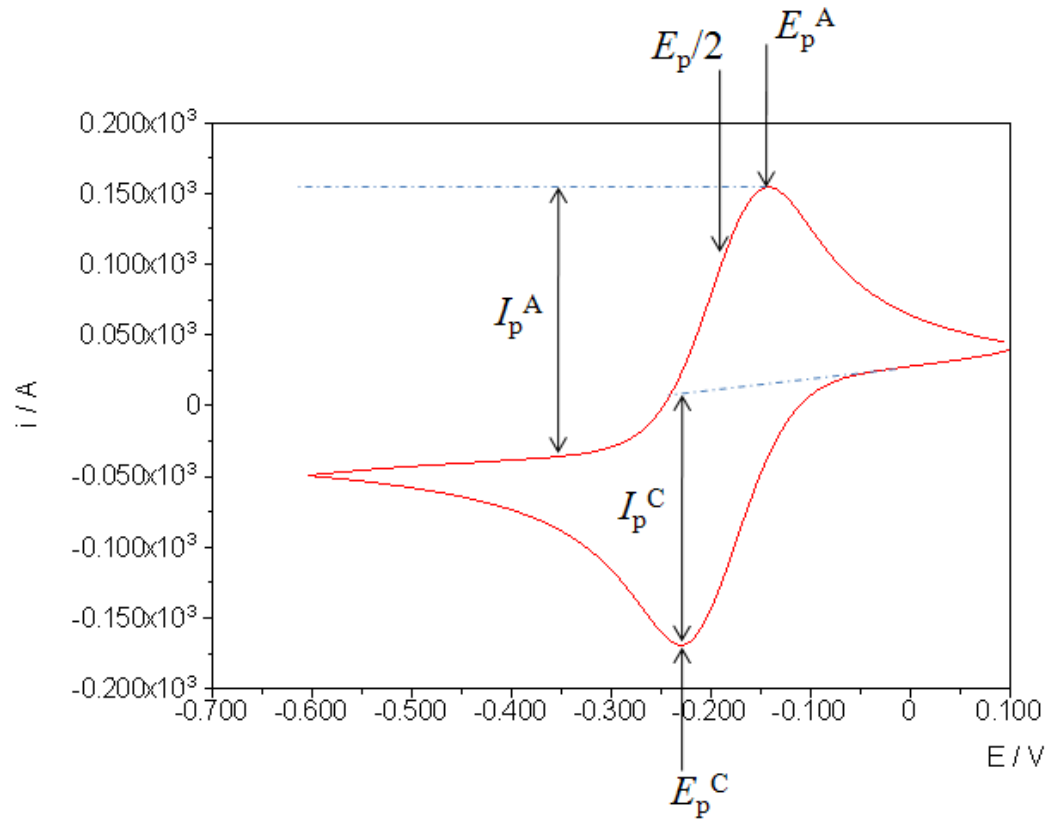

Figure 12: Example cyclic voltammogram showing the anodic peak potential (E_p^A), anodic peak current (I_p^A), cathodic peak potential (E_p^C), cathodic peak current (I_p^C) and the half peak potential ($E_p/2$).

The peak current for a reversible electrochemical reaction follows the Randles-Sevčik equation.[65, 66]

$$I_p = (2.69 \times 10^5)\, n^{3/2}\, A\, D^{1/2}\, C_\infty\, \upsilon^{1/2} \qquad \textit{Equation 1.1}$$

Where n is the number of electrons transferred in the reaction, A is the surface area of the electrode (cm^2), D is the mean diffusion coefficient of the solution redox species (cm^2s^{-1}), C_∞ is the bulk concentration ($molcm^{-3}$) and υ is the sweep rate (Vs^{-1}). *Table 1* illustrates the diagnostic tests used to confirm a reversible reaction.[65, 67]

Table 1: Diagnostic tests for cyclic voltammograms of reversible processes.

1	$\Delta E_p = E_p^A - E_p^C = {}^{59}/_{n}\ mV$
2	$\left\| I_p^A / I_p^C \right\| = 1$
3	I_p is proportional to $\upsilon^{1/2}$
4	E_p is independent of υ
5	At potentials beyond E_p, I is proportional to $t^{-1/2}$

1.2.1 Cyclic Voltammetry And Surface Reactions

As well as being useful for quantitatively investigating solution properties, cyclic voltammetry can be used to investigate species adsorbed on an electrode surface. A fully reversible redox-active species adsorbed on an electrode surface would ideally possess a symmetrical voltammogram. This is due to there being a fixed amount of the reactant species present and the reaction taking place at the electrode is not subject to diffusion as is the case with solution voltammetry.[65, 68] However, quasi reversible surface reactions have asymmetric redox peaks.

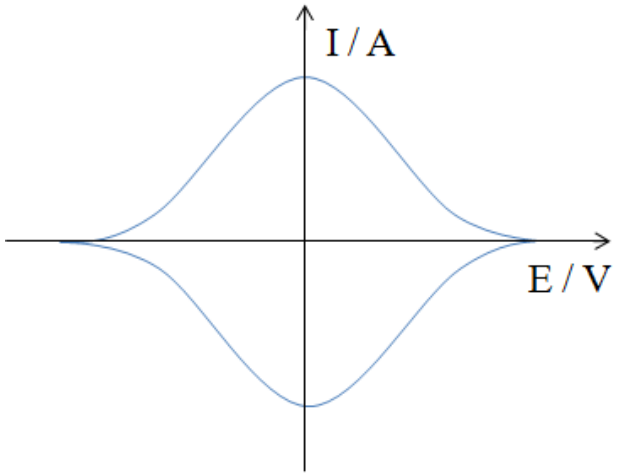

Figure 13: Example of a cyclic voltammogram of the redox reaction of an ideal species adsorbed on the working electrode.

Cyclic voltammetry may also be used to monitor the condition of the working electode surface. Hamelin demonstrated how cyclic voltammetry is a useful tool for checking the quality of Au single crystals.[69-72] The voltammetry of Au(111) in a

H_2SO_4 electrolyte contains a defined pattern, known as the "butterfly" peak in the double layer region. This occurs due to sulfate adsorption on the electrode surface, and the quality of this butterfly peak can be used to check the quality of a Au(111) surface.

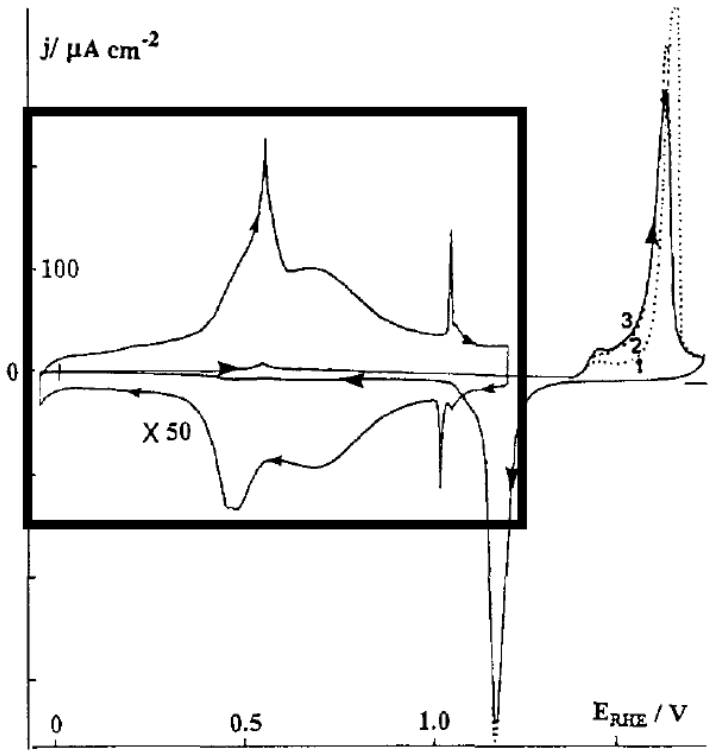

Figure 14: Cyclic voltammograms of a Au(111) surface in a H_2SO_4 electrolyte. The butterfly peak is contained in the black box and has been enlarged. This occurs due to the adsorption of sulfate anions. Figure adapted from reference 69.

Cyclic voltammetry is an important technique in the field of SME, as it can be used in conjunction with an STM to monitor the electron transfer of redox-active molecules. It is usually performed as a preliminary experiment prior to SMC measurements being performed, so that the redox potential of the molecule in question is known. Zhou *et al*. used ultrafast cyclic voltammetry in conjunction with Tao's STM-BJ technique,[20] described later, to investigate the relationship between molecular conductance and the rate of electron transfer, using three different redox active molecular systems.[73] It was observed that high conductances relate to fast electron transfer rate constants.[73]

1.3 The History Of STM

The scanning tunnelling microscope (STM) was invented in 1981 by Gerd Binnig, Heinrich Rohrer and colleagues of the IBM Zurich Research Laboratory.[74-78] To this day, STM remains one of the most important surface characterisation techniques and can be used to image and manipulate individual atoms on a substrate surface in several different environments, including under UHV, ambient conditions (in air), under a liquid medium and also at extreme temperatures. Two years after its invention, atomic resolution was achieved using STM.[77] Since then, atomic resolution of a great number of conducting substrates has been achieved, including for example Au(111), both bare and with an organothiol monolayer, Highly Ordered Pyrolytic Graphite (HOPG), and iodine adsorption on Pt(111), to name a few examples.[79-81]

A schematic diagram of an STM set up is shown in *Figure 15*. The tip is first moved under visual observation as close to the substrate as possible. A stepper motor then approaches the tip to the substrate up to a specified current. The precision control which allows the STM to work over such small areas is attained by the use of piezo crystals, which expand/contract when a voltage is applied. The piezo crystals then move the tip to the tunnelling current specified. This is known as the setpoint current (I_{set}). A bias voltage between the tip and sample must be applied to obtain a tunnelling current (V_{BIAS}).

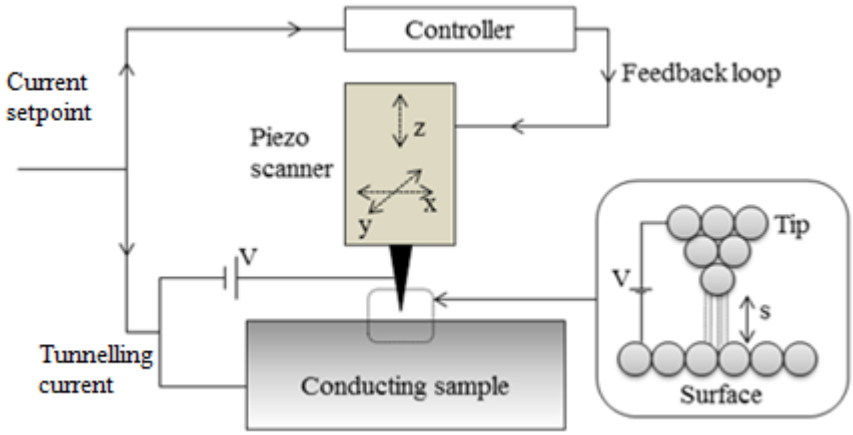

Figure 15: Schematic of a Scanning Tunnelling Microscope. The STM tip is a fine needle which is scanned across a substrate surface. A bias voltage is applied between the tip and substrate which results in electrons traversing the gap. Piezo crystals

contained in the scanner expand and contract with application of voltage and these are used to provide the fine precision control of the tip.

There are two methods of imaging a surface. The first is constant current mode. A feedback loop maintains the current and the output is a plot of the height of the tip. The second method for STM imaging is constant height mode. The feedback loop maintains the height and the output is a plot of current. This method is only suitable for very flat surfaces otherwise the tip would be susceptible to crashing.

1.3.1 Quantum Tunnelling

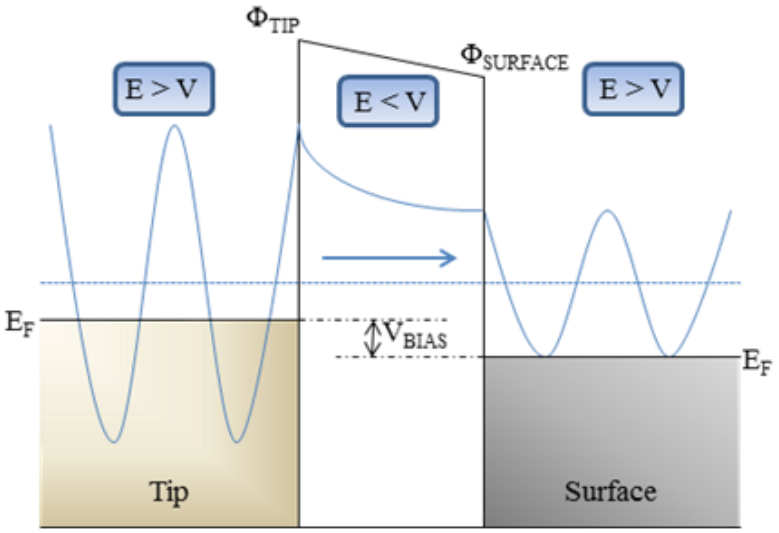

Figure 16: Quantum tunnelling through a potential barrier. In the tip and surface, the energy of the electron (E) is greater than the potential (V). However, in the gap between the electrodes, the potential is larger than the energy of the electron so the electron is forbidden to be located in this region according to classical mechanics. However, quantum mechanics allows the electron to "tunnel" through the gap, as the probability of the electronic wavefunction being present across the gap is > 0.

STM is dependent on the phenomenon of quantum tunnelling. Classically, an electron is forbidden to exist in a region where the potential (V) is greater than the energy of the electron (E). However, when the barrier is sufficiently thin, the electron can traverse the barrier and present itself on the other side. The Schrödinger equation can be used to evaluate this process.[82-84]

$$0 = \frac{-\hbar^2}{2m}\frac{d^2}{dx^2}\varphi + [V - E]\varphi \qquad \textit{Equation 1.2}$$

When the electron resides in the region where E > V, which describes the metallic contacts, then the solution to the Schrödinger equation is:

$$\varphi = Ae^{ikx} + Be^{-ikx} \qquad \textit{Equation 1.3}$$

Where A and B are constants, φ describes the wavefunction, i is an imaginary number which explains the oscillation of φ, and k is the wave vector:

$$k = \frac{\sqrt{2m(E - V)}}{\hbar} \qquad \textit{Equation 1.4}$$

In the classically forbidden region where E < V, the current has an exponential decay, hence the Schrödinger equation has a solution of the form:

$$\varphi = Ce^{\kappa x} + De^{-\kappa x} \qquad \textit{Equation 1.5}$$

Where κ is a decay constant. The further into the barrier, the lower the probability of the electron being present, hence the decay.

$$\kappa = \frac{\sqrt{2m(V - E)}}{\hbar} \qquad \textit{Equation 1.6}$$

In the case of STM, the tip and substrate are the regions where E>V and the electronic wavefunction oscillates. The barrier, where the electron is classically forbidden to exist and where V>E is the gap between the tip and substrate. Provided this barrier is thin enough, then electrons will tunnel between the STM tip and substrate and a current will flow.

It has been shown that at low temperature and voltage, the tunnelling current is proportional to the distance of the tip from the surface.[85]

$$I \propto e^{-2\kappa s} \qquad \textit{Equation 1.7}$$

Where I is the tunnelling current, s is the distance between the tip and surface (width of the barrier) and κ is the decay constant:

$$\kappa = \frac{\sqrt{2m\phi}}{\hbar}$$ *Equation 1.8*

Where ϕ is the workfunction.

This means that the further away the tip is from the surface, the lower the tunnelling current will be. The exponential dependence on tip-sample separation is shown in *Figure 17*, from exponential data recorded during retraction of an STM tip.

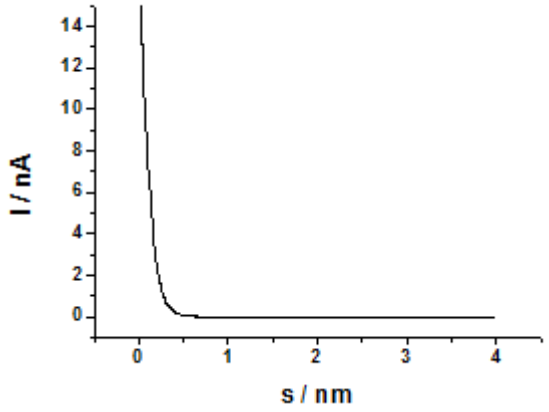

Figure 17: Current-distance plot demonstrating the current exponential decay as the STM tip is withdrawn from the substrate surface. This plot was taken in a BMIOTf medium, the STM tip was Au wire and the substrate was a gold-on-glass substrate. The decay constant for this plot is -11.69 nm^{-1}.

1.4 STM In Single Molecule Electronics

1.4.1 Electron Transport

The previous section describes the simplest model of vacuum tunnelling between two metals along a one dimensional barrier. Electron transport across a molecule positioned between two metallic contacts is rarely adequately described by such a simple model. Much depends on the type of molecular wire used. The length of the molecule[23, 86, 87], the terminating group[88, 89] and redox properties[30, 32, 33, 40-43, 45-47, 90-103] all impact the electron transport mechanism.

1.4.2 Coherent Transport

Coherent transport occurs when the electron resides on the molecule for a short enough period of time that it does not inelastically interact with any particles within the molecule.

Table 2: Table of possible coherent electron transfer mechanisms (adapted from references 19, 82, and 104)

Conduction mechanism	Schematic representation of tunnelling mechanism	Characteristic behaviour
Direct tunnelling	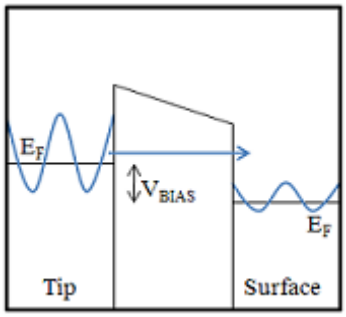	$J \approx V_{BIAS}\, exp\left(-\frac{2s}{\hbar}\sqrt{2m\phi}\right)$
Fowler-Nordheim tunnelling	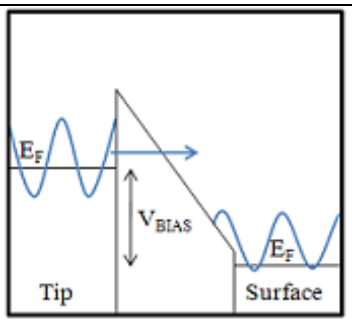	$J \approx {V_{BIAS}}^2\, exp\left(-\frac{4s\sqrt{2m}\phi^{3/2}}{3e\hbar V_{BIAS}}\right)$
Thermionic emission	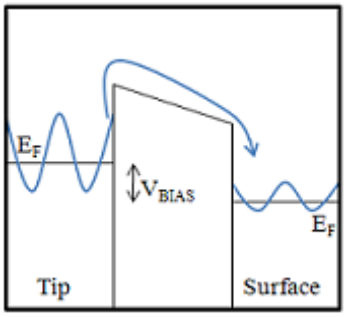	$J \approx T^2\, exp\left(-\frac{\phi - e\sqrt{eV_{BIAS}/4\pi\varepsilon s}}{k_B T}\right)$

Fowler-Nordheim tunnelling differs from direct tunnelling, as the bias voltage applied is larger than the barrier height. This means that the electron tunnels through

a barrier of reduced effective width, as illustrated in *Table 2*. In general, coherent transport is temperature independent, with the exception of thermionic emission, which has an exponential temperature dependence.[105] Thermionic emission differs from both direct and Fowler-Nordheim tunnelling, as the electron is excited over the potential barrier as opposed to tunnelling through it. As can be predicted, thermionic emission depends strongly on the temperature of the system as well as the width of the potential barrier.[19, 82, 88, 104]

1.4.3 Superexchange

Superexchange is a coherent regime which occurs when the molecular orbitals aid ET despite being far away from the Fermi level of the metallic contacts. This is also described as "off-resonant" ET. Superexchange is particularly significant in the natural world as it is believed that electron transfer in photosynthesis occurs through this mechanism.[106]

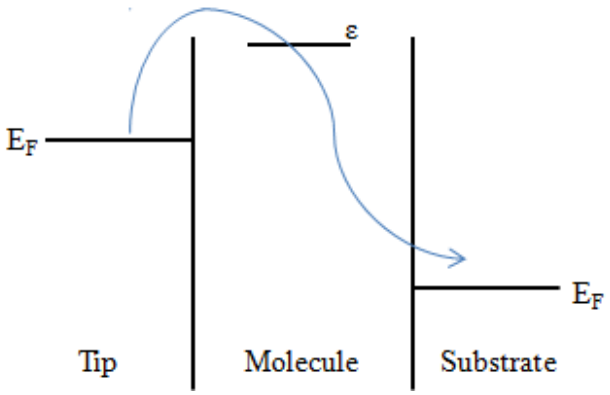

Figure 18: Non-resonant coherent superexchange tunnelling through a molecular bridge. In the superexchange tunnelling mechanism, the electron transfer is aided by the molecular orbital despite its large distance from the Fermi levels of the metallic contacts.

1.4.4 Simmons Model

The Simmons model (*Equation 1.9*) developed by John G. Simmons in 1963, is a coherent regime which describes direct tunnelling between two electrodes separated by a thin insulating film which presents a rectangular barrier.[88, 107] Direct tunnelling occurs when the Fermi Energies (E_F) of the metal electrodes are between the HOMO

and LUMO of the molecular bridge in question. When the electrons tunnel via a molecular orbital, then a different tunnelling regime dominates, which is explained later.

$$J = \frac{e}{2\pi h(\beta s)^2}\left\{\left(\phi - \frac{V_{BIAS}}{2}\right)exp\left[-\frac{4\pi\beta s}{h}(2m)^{1/2}\alpha\left(\phi - \frac{V_{BIAS}}{2}\right)^{\frac{1}{2}}\right] - \left(\phi + \frac{V_{BIAS}}{2}\right)exp\left[-\frac{4\pi\beta s}{h}(2m)^{1/2}\alpha\left(\phi + \frac{V_{BIAS}}{2}\right)^{\frac{1}{2}}\right]\right\} \quad \textit{Equation 1.9}$$

There is a typing error in reference 107 for equation (26). This mistake has been rectified in this thesis for *Equation 1.9*.

J is the tunnel current density, V_{BIAS} is the bias voltage applied and β is a correction factor which can be taken to be 1 when $V_{BIAS} < \phi/e$.[107, 108] The addition of the constant α is used for fitting. The exact physical meaning of α is unclear, although it has been suggested that it takes into account the effective mass of the tunnelling electron m_{eff}, or the barrier being non-rectangular.[19, 23, 104, 108]

With modification, the Simmons model can take into account the image charge, which in turn would affect the transmission probability by rounding the potential barrier and reducing the effective width. This is represented in *Figure 19*. The Simmons model only considers a rectangular barrier and not a rounded barrier, so ϕ is replaced with the effective rectangular barrier height:

$$\phi_{eff} = \phi - \frac{2\phi c}{\Delta s}\, ln\left(\frac{s + \Delta s}{s - \Delta s}\right) \quad \textit{Equation 1.10}$$

Where c is approximately equal to $0.288/\phi\varepsilon_r$, ε_r is the relative permittivity of the barrier. Δs is the change in barrier width and is given by:[23, 108]

$$\Delta s = s\left(1 - \frac{4c}{s}\right)^{1/2} \quad \textit{Equation 1.11}$$

The Simmons model can be used to understand the *I-V* characteristics of a system and provides a good fit to the *I-V* data obtained for alkanedithiols.[19, 23, 107-109]

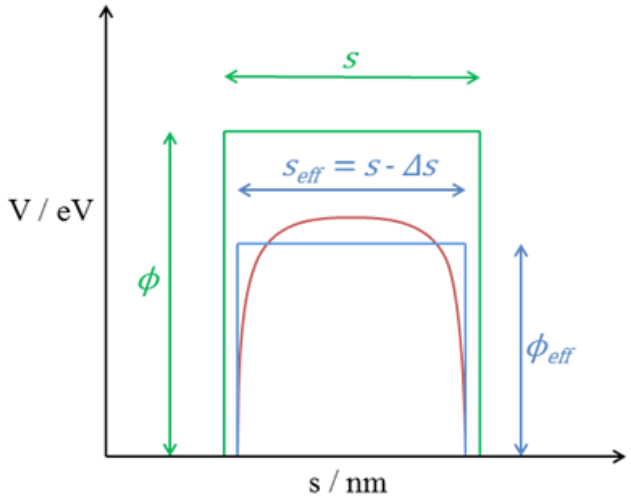

Figure 19: Representation of the Simmons model, describing direct tunnelling. The original Simmons model rectangular barrier is shown in green. When image charge is taken into account, the potential barrier is reduced in height and rounded (red). Since the Simmons model employs rectangular barriers, the effective height and width of the potential barrier are used (blue). This representation is not to scale.

1.4.5 Double Barrier Tunnelling

The conductance of a molecular wire can be increased by sandwiching a barrier indentation between two tunnelling barriers.[90, 110, 111] The presence of this barrier indentation facilitates electron transfer as it is easier for an electron to tunnel through two shorter barriers than one long barrier. This is demonstrated by a comparison of dodecanedithiol and the redox-active viologen moiety, which are both very similar in length. Electron transport through dodecanedithiol proceeds via direct tunnelling resulting in a conductance of (0.122 ± 0.014) nS,[26] whereas Haiss *et al*. find that the presence of a barrier indentation endows the viologen with a significantly greater conductance of (0.44 ± 0.04) nS at 0 V vs SCE.[40] Double barrier tunnelling is a well-known phenomenon in semiconductor devices and was first observed by Chang *et al*. in 1974.[110] The semiconductor used was *n*-type GaAs, containing layers of $Ga_{0.3}Al_{0.7}As$ layers, which act as tunnelling barriers. Semiconductor devices which make use of double barrier tunnelling are useful in components such as transistors, and memory.[82]

1.4.6 Resonant Tunnelling

Coherent resonant electron tunnelling is a two-step ET mechanism which involves the molecular orbitals of the molecular bridge. When the LUMO or HOMO lie close to the E_F of the electrodes, then electron (hole) transport is dominated by the orbital lying close to the Fermi level.[19, 42, 95, 102, 112, 113] Resonant tunnelling is one of the dominant electron transfer regimes through a redox-active molecule.[34, 95] The redox state of the molecular wire is altered by varying the sample potential. Around the redox potential of the molecule, there is a large increase in conductance, as more electrons can more favourably traverse the molecule at the redox potential.

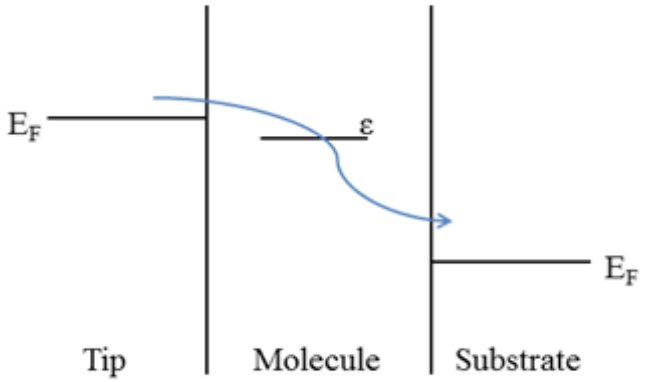

***Figure 20*:** Resonant tunnelling through a molecular bridge. The electron tunnels via a molecular orbital which results in an increase in conductance compared to direct tunnelling where the molecular orbitals do not aid tunnelling to such an extent.

Resonant tunnelling tends to result in a higher conductance than direct tunnelling or superexchange. When the electrode potential is swept through the redox potential, the conductance of the viologen molecule increases from approximately 0.5 nS to 2.8 nS.[38, 40] Again, this can be compared to the conductance of dodecanedithiol, which at (0.122 ± 0.014) nS is significantly lower than the viologen in both the on and off state. Viologen exhibits a broad sigmoidal on-off transition as opposed to the classical "bell-shaped" model predicted for resonant tunnelling, where the conductance has a sharp off-on-off transition with the on state being at the redox potential.[40, 47, 111] The overpotential at which the peak current occurs and the peak width are dependent on the inner and outer sphere reorganisation energies λ_{intra} and

λ_{solv} respectively, which are combined to give the total reorganisation energy λ_{reorg}, as described by Schmickler and Tao.[97, 113] Changes in λ_{intra} and λ_{solv} may also change the shape of the peak, resulting in the appearance of a shoulder. This can be compared to the Kuznetsov-Ulstrup model of ET, described below, where the λ_{reorg} affects the height of the current peak.

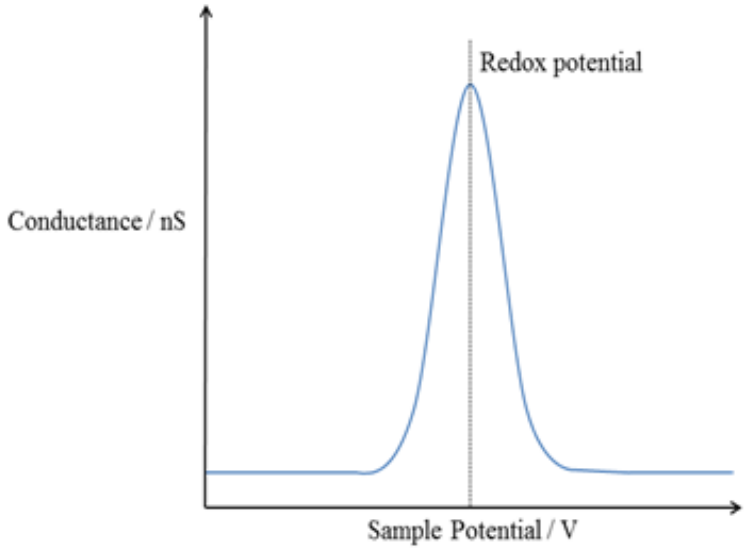

Figure 21: A plot of conductance vs. sample potential, showing the conductance increase at the redox potential of the molecular wire, a feature of resonant tunnelling.

1.4.7 Kuznetsov-Ulstrup Electron Transfer Model

Resonant tunnelling may also involve a vibrational relaxation of the orbital which aids the electron tunnelling.[34, 42, 99, 114-116] The first step involves the electron tunnelling from the tip (assuming a positive sample bias) to the unoccupied molecular orbital. Due to solvent fluctuations, the LUMO may move closer to the Fermi level of the tip, which initiates the first ET.[42] How the second step proceeds depends on the strength of the electronic coupling between the redox centre and the electrodes (tip and substrate). For strong electronic coupling, once the electron is present on the LUMO of the redox centre, this orbital then undergoes a partial vibrational relaxation, as the Kuznetsov-Ulstrup (KU) model suggests.[41, 42, 93, 94, 99, 102, 114-116] In this scenario, the electron tunnels via the LUMO of the molecular wire. The presence of the electron on the LUMO causes it to undergo a partial vibrational relaxation. The electron is then transferred to the second electrode before the

vibrational relaxation is complete; before the LUMO relaxes below the Fermi level of the second electrode. This process may be repeated, as once the LUMO is vacated, it then relaxes towards higher energies, towards the Fermi level of the first electrode, resulting in a "boost" of the current. This is known as the adiabatic regime.[42, 93, 102] The equation describing the adiabatic KU model of ET is shown below in *Equation 1.12*.[31, 42, 116]

$$I_e = e\kappa\rho(eV_{BIAS})\frac{\omega}{2\pi}\left\{exp\left[\frac{e}{4\lambda_{reorg}k_BT}(\lambda_{reorg} + \xi\eta + \gamma V_{BIAS})^2\right]\right. \quad \textit{Equation 1.12}$$
$$\left. + exp\left[\frac{e}{4\lambda_{reorg}k_BT}(\lambda_{reorg} + V_{BIAS} - \xi\eta - \gamma V_{BIAS})^2\right]\right\}^{-1}$$

Where I_e is the enhanced current, κ is the electronic transmission coefficient, which is assumed to be 1 in the adiabatic regime, ρ is the density of electronic states in the electrodes near the Fermi level, ω is the characteristic nuclear vibration frequency, V_{BIAS} is the bias potential, λ_{reorg} is the reorganisation energy, η is the overpotential applied to the substrate, and ξ and γ are modelling parameters relating to the proportion of electrochemical potential and the bias potential respectively, that affect the redox moiety.[42] *Equation 1.12* can be simplified when the same values of κ and ρ are assumed for both ET steps and using the approximation $\kappa\rho\omega e^2/4\pi = 9.1\text{x}10^{-7}$ $C^2eV^{-1}s^{-1}$.[31, 42]

$$I_e = 1820 \cdot V_{BIAS}\left\{exp\left[\frac{9.73}{\lambda_{reorg}}(\lambda_{reorg} + \xi\eta + \gamma V_{BIAS})^2\right]\right. \quad \textit{Equation 1.13}$$
$$\left. + exp\left[\frac{9.73}{\lambda_{reorg}}(\lambda_{reorg} + V_{BIAS} - \xi\eta - \gamma V_{BIAS})^2\right]\right\}^{-1}$$

Assuming η and V_{BIAS} are lower than λ_{reorg}, the above equation can be simplified to[42]:

$$I_e = \frac{910 \cdot V_{BIAS} \cdot exp[-9.73(\lambda_{reorg} + V_{BIAS})]}{\cosh[19.4(\xi\eta + (\gamma - 0.5)V_{BIAS})]} \quad \textit{Equation 1.14}$$

For weak electronic coupling, the reduced molecular orbital fully relaxes so its energy is below that of the Fermi level of the second electrode. This means the electron has to overcome an energy barrier to reach the second electrode. This is known as the diabatic regime and results in a smaller "boost" to the current than the adiabatic regime.[42, 93, 102]

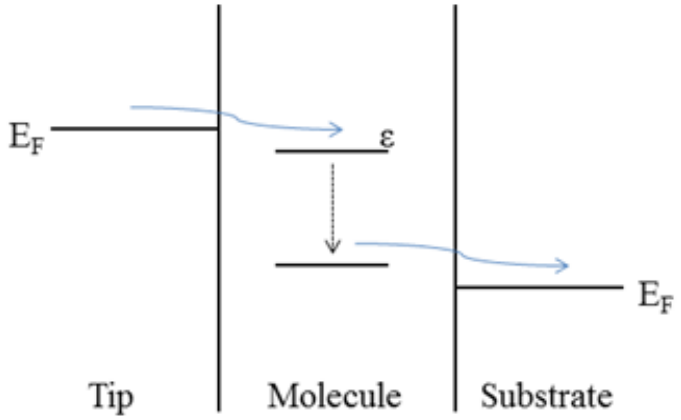

***Figure 22*:** Adiabatic two-step electron transfer with partial vibrational relaxation. The electron tunnels to the LUMO, which then relaxes in energy after being reduced. The electron vacates the LUMO it reaches the E_F of the second electrode. The re-oxidised LUMO can then relax back up to higher energies, where this process repeats itself. This results in a "boost" of current.

1.4.8 Marcus Theory

The Nobel Prize winning Marcus Theory of electron transfer explains the reorganisation energy λ_{reorg}, which is an important component of the above KU model. Marcus Theory describes ET in a solution between two spherical species.[84, 117-121] How fast the ET proceeds is dependent on the activation energy $\Delta G^{\ddagger}$.

$$\Delta G^{\ddagger} = \frac{\left(E - \lambda_{reorg}\right)^2}{4\lambda_{reorg}} \qquad \textit{Equation 1.15}$$

The Marcus Theory can be described using potential energy diagrams, where the energy is plotted against the reaction coordinate, as shown in *Figure 23*. (A) is known as the "normal" region and $\Delta G^{\ddagger} = 0.25(\lambda_{reorg})$. As E, the difference in energy between the two redox states gets larger, the reaction rate increases. (B) is the "activationless" region and $\Delta G^{\ddagger} = 0$. In this region, the ET proceeds very quickly and λ_{reorg} = E. As E gets larger, one enters the "inverted" region, where the reaction rate decreases as E gets larger.

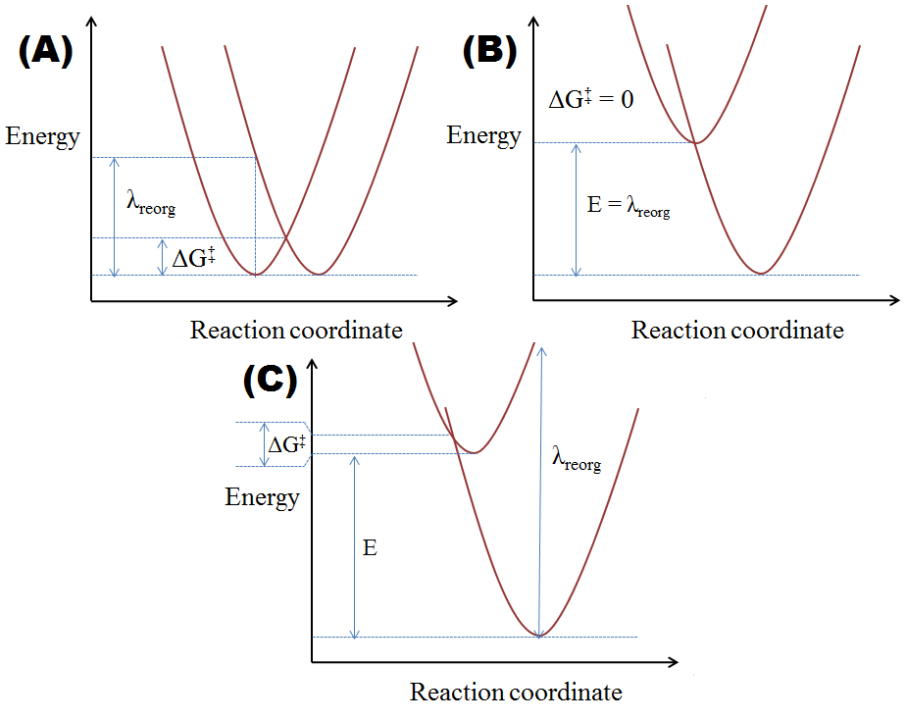

Figure 23: Energy curves depicting the Marcus Theory of ET. (A) shows the ET in the "normal" region, (B) is "activationless" and (C) is the "inverted" region.[121]

The Marcus Theory explains that the reorganisation energy λ_{reorg} consists of two components added together, the "inner-sphere" λ_{intra} which is the reorganisation energy of intramolecular interactions as the ET occurs, such as orbitals, and the "outer-sphere" λ_{solv} which describes how the solvent reorganises around the species at the ET. λ_{solv} can be calculated with relative ease in a solution.[117, 118, 122]

$$\lambda_{solv} = \left(\frac{e^2}{4\pi\varepsilon_0}\right)\left(\frac{1}{2(R_A)} + \frac{1}{2(R_B)} - \frac{1}{r}\right)\left(\frac{1}{n^2} - \frac{1}{\varepsilon_r}\right) \qquad \textit{Equation 1.16}$$

ε_0 is the relative permittivity of free space, R_A and R_B are the ionic radii, r is the distance between the centre of the ions, which is taken to be $R_A + R_B$. n is the refractive index of the solvent and ε_r is the relative permittivity of the solvent.[118, 122] A simple example of the Marcus Theory in practice is a self-exchange reaction, a well-known example being:[121]

$$(Fe(OH_2)_6)^{3+} + (Fe(OH_2)_6)^{2+} \rightarrow (Fe(OH_2)_6)^{2+} + (Fe(OH_2)_6)^{3+}$$

It is assumed that the Fe^{2+} and Fe^{3+} form a weak "outer-sphere complex" and the electron tunnels between the two. Marcus Theory can be used to calculate the rate of

ET between the two Fe complexes and the λ_{solv} plays a major role in the reaction rate.[121]

1.4.9 Non-Coherent Transport: Hopping

When the time it takes for the electron to travel through the molecular wire is longer than the time it takes for inelastic interactions to occur, then the electron transfer is said to be non-coherent. In the case of fairly long molecules where the transversal time of the electron is considerably longer than the time taken for inelastic scattering events to occur, then ET occurs by the electrons "hopping" from one fragment of the molecule to another.[19, 87, 88]

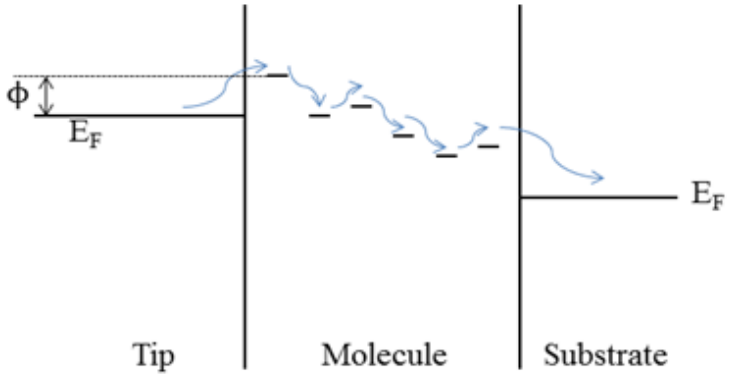

Figure 24: Non-coherent electron hopping through a long molecular wire. Due to the long length of the molecule, it is preferable for the electron to hop from one fragment of the molecule to another, rather than tunnel. Hopping requires thermal activation for the electron to overcome ϕ, the difference in energy between the E_F of the tip and the energy of the receiving molecular fragment.

In contrast to coherent tunnelling, non-coherent hopping is thermally activated and often has a linear length dependence as opposed to an exponential length dependence, as is the case with coherent tunnelling. The nature of the contact groups present on a molecule have less influence when ET proceeds via a hopping mechanism than when ET is coherent.[87] Hopping has an exponential thermal dependence, shown in *Equation 1.17*.[19, 104]

$$J \approx V_{BIAS}\, exp\left(\frac{-\phi}{k_B T}\right) \qquad \textit{Equation 1.17}$$

Choi *et al*. demonstrated the change in ET regime from tunnelling to hopping using conjugated oligophenyleneimine (OPI) molecules of lengths varying between 1.5 nm and 7.3 nm by use of a conducting Atomic Force Microscope (c-AFM).[86, 87] They found that ET proceeds via a hopping mechanism in the OPI molecular wires at lengths ≳ 4 nm (>OPI5). A semilog plot of the resistance vs. the molecular length confirmed this as the length dependence showed a clear change from an exponential dependence to a linear dependence, shown in *Figure 25*.

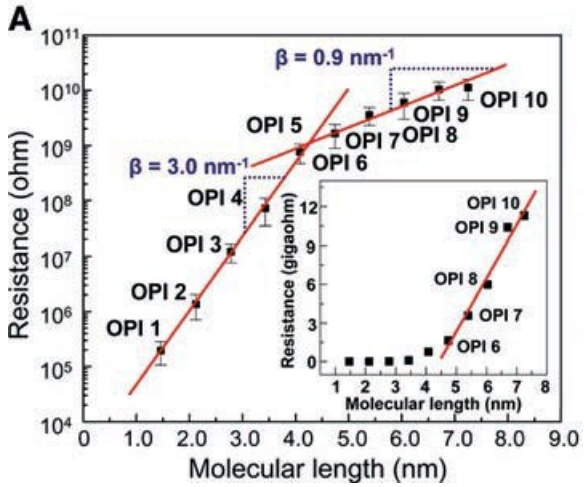

Figure 25: Semilog plot of resistance vs. molecular length of conjugated OPI molecular wires. A very distinct change in the length dependence behaviour is observed between OPI 4 and OPI 6 at approximately 4 nm length. This is the change in ET mechanism from coherent tunnelling to non-coherent hopping. Figure taken from references 86, 87.

As further confirmation of this change in ET behaviour, Choi *et al*. also determined the temperature dependence of the OPI molecular wires.[86, 87] As expected, there is an obvious difference between OPI 4 and OPI 6, with OPI 4 showing no defined temperature dependence, and OPI 6 exhibiting an exponential temperature dependence, as shown in *Figure 26*.

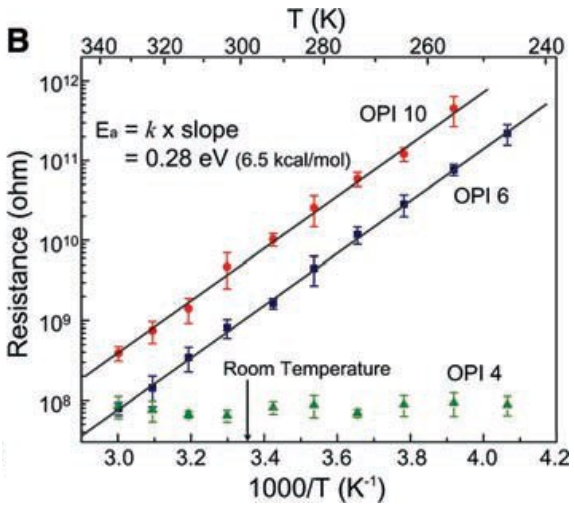

Figure 26: Arrhenius plot conjugated OPI 4, OPI 6 and OPI 10 conjugated molecular wires. The temperature dependence shows an obvious change from OPI 4 to OPI 6 from no dependence to an Arrhenius dependence. This acts as further confirmation of a ET regime change from coherent tunnelling to non-coherent hopping. Figure taken from reference 86.

1.4.10 Metal-Molecule Contacts

Gold is the most widely used material for the metallic contacts in single molecule junctions. This is due to its stability and its affinity for several functional groups enabling strong metal-molecule contacts, which in turn facilitates electron transport. The most widely studied contact used between metal and molecule is the Au-S bond, which is a relatively strong chemical bond with relatively low contact resistance. Thiols are stable, easy to synthesise and have a high affinity for Au, making them a popular choice for a contact group. There are many other possible contact groups including carboxylate/carboxylic acid[88, 89, 123, 124], pyridine[32, 125], amine[88, 89, 126-128], π-π-stacked benzene rings[129] and fullerene[16, 88, 98] end groups.

The Landauer formula, shown in *Equation 1.18* can be used to calculate the conductance of a molecular junction, by taking into account the transmission probabilities (T_n) of the metal-molecule contacts.[88, 130, 131]

$$G = G_0 \sum T_n \qquad \textit{Equation 1.18}$$

The quantised conductance is the conductance of a 1-D wire of metal atoms and is given by:[131-135]

$$G_0 = \frac{2e^2}{h} \approx 77\ \mu S \qquad \textit{Equation 1.19}$$

G_0 can be viewed as the maximum single channel conductance possible of a molecular wire. Very few molecular wires measured to date exhibit a conductance close to G_0.

The higher conductance demonstrated by molecules with a Au-S contact group than Au-N for example, is because the transmission probability of Au-S is higher than the transmission probability of Au-N. The computed transmission probabilities of various contact groups are given in *Table 3* below.[88, 89]

Table 3: The transmission probabilities of various contact groups. Table adapted from references 88, 89.

Contact group	**Transmission Probability (T_n)**
Au-S	0.81
Au-N	0.19
Au-OOC	0.08
Au-HOOC	0.06

1.4.11 Conductance Groups

As well as the nature of the contact groups, the conductance can also be affected by the adsorption site on the substrate and tip.[21, 23] In general, three conductance groups are observed for a molecular wire, showing a low, medium and high conductance. These are also referred to as the **A**, **B** and **C** groups respectively. It has been suggested that the **A** group is observed when the molecule is adsorbed on a flat, terraced surface. When the molecule is adsorbed at a step-edge at one, or both ends, then the **B** and **C** groups respectively are observed.

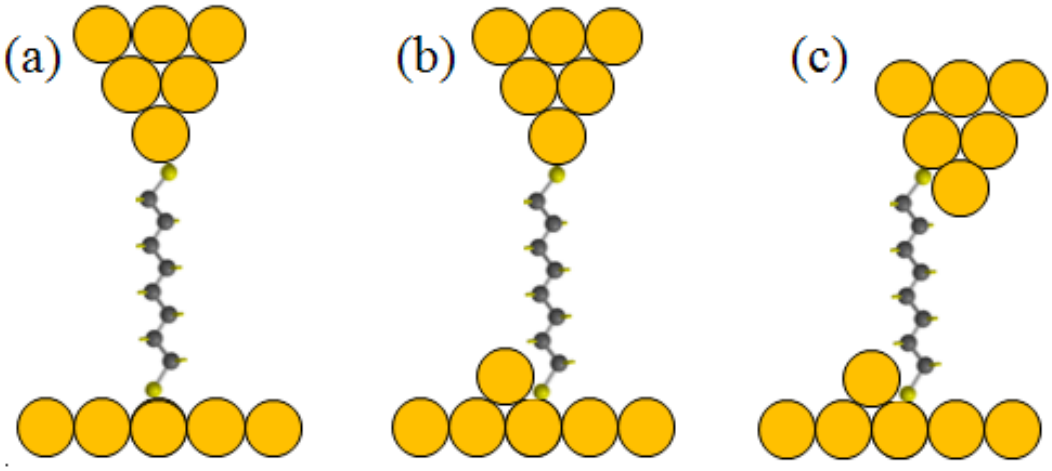

Figure 27: The three different conductance groups **A** (a), **B** (b) and **C** (c). The molecule exhibiting a group **A** conductance is adsorbed on a flat, terraced surface, or connected to a single gold adatom. For a group **B** conductance, one of the terminal groups is adsorbed at a step edge site whereas both the terminal groups are adsorbed at a step edge when the **C** group conductance is observed.

For the model molecular wire 1,8-octanedithiol (ODT), the conductances of the **A**, **B** and **C** group are ~1 nS, ~4 nS and ~18 nS respectively.[21]

1.5 STM Techniques

Two STM techniques were used to measure the single molecule conductance, the break-junction and *I*(s), and a combination is best to observe the 3 conductance groups.

1.5.1 STM-*I*(s)

The *I*(s) technique measures the current as a function of distance.[21, 23, 29, 38, 40, 136] A low-coverage self-assembled monolayer (SAM) is attached to the substrate surface. The STM tip is brought to a specified distance above the substrate, by selecting the setpoint current as described. The tip is then retracted from the surface in the z-direction only at a set rate and to a given distance. As shown in *Equation 1.7* and *Figure 17*, when no molecule is present in the junction, the current decays exponentially with distance. However, when a molecule bridges the gap between the electrodes, a current plateau is observed. This plateau occurs as a result of the current flowing through the molecule. The plateau abruptly ends when the molecule snaps off one of the electrode contacts. This "break-off" distance can be used to estimate the length of the molecular wire in the junction. This estimated break-off distance can then be compared to the actual molecular length and this acts as confirmation together with the histogram analysis, that the conductance measurements do indeed correspond to a single molecule. The experimental break-off distance is expected to be longer than the actual molecular length by multiples of the height of a gold atomic step. This is because alkylthiol SAMs cause the Au surface to be altered and adatoms to be formed, leading to an increase in the tip-substrate separation.[137]

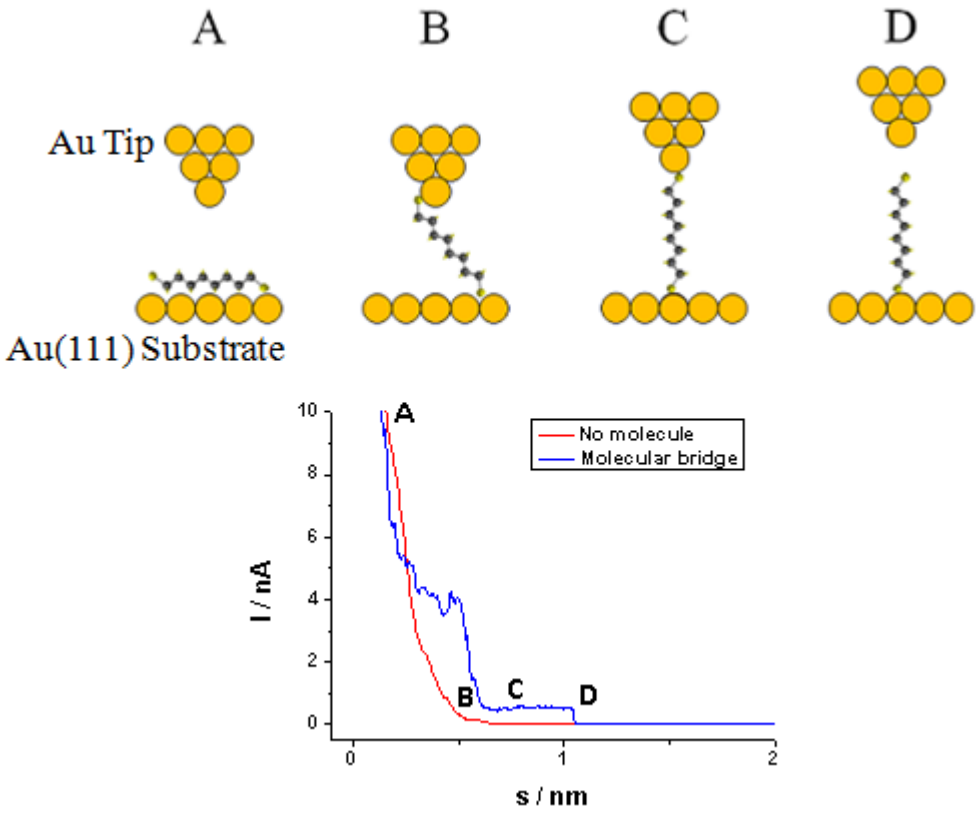

Figure 28: The STM-*I*(s) technique, which is used to measure the conductance of single molecules. The tip is held above the substrate at a distance dictated by the current setpoint I_{set} (A). Occasionally, a molecule will spontaneously bridge the gap between tip and substrate (B). The tip is then retracted from the surface in the z-direction (C). When the molecule is held between the two electrodes, a current plateau is observed on the *I*(s) scan (blue). As the tip continues to retract, the molecule breaks off from one of the electrodes (D) and the plateau abruptly comes to an end.

To determine the conductance, a large number of *I*(s) scans are plotted into a histogram. The resulting peaks correspond to the conductance of the molecular wire in question. The conductance of two and even three molecules can also often be seen on these conductance histograms.

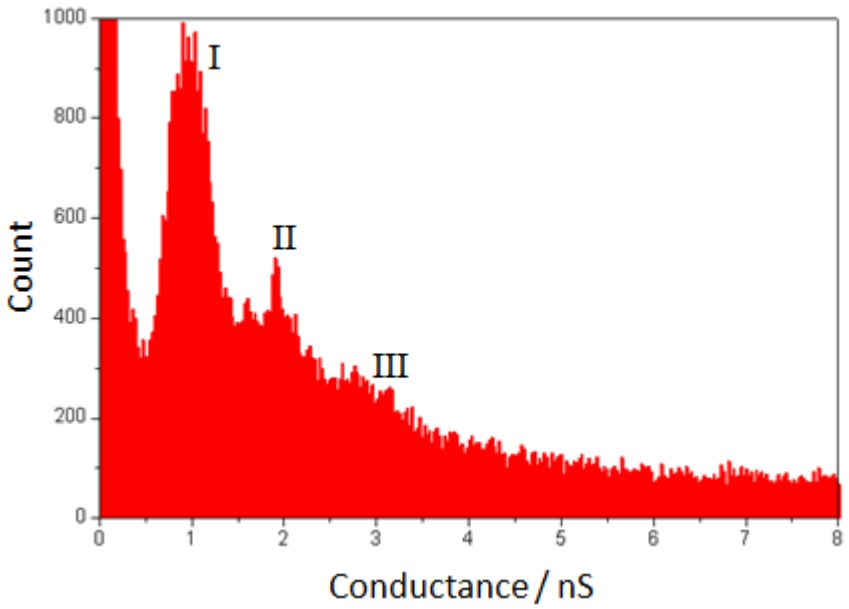

Figure 29: A conductance histogram of ODT in ambient conditions, showing one (I), two (II) and three (III) molecules in the junction at ~1 nS, ~2 nS and ~3 nS respectively. 505 *I*(s) scans were used to create this histogram.

The *I*(s) technique is especially useful for observing the lower conductance groups **A** and **B**. The **C** group is difficult to observe using this method so it is desirable to use a different method which creates rougher junctions to see the higher conductance groups.

1.5.2 STM Controlled Break-Junction

The STM controlled break-junction (BJ) technique was developed by Xu *et al*. in 2003.[138] The STM tip is crashed into the surface and then retracted. This results in a chain of gold atoms which exhibits a conductance of integer values of G_0. As the tip is retracted further, this bridge of atoms snaps, resulting in a drop of current. A molecular wire can then attach itself to the tip and substrate. As with the *I(*s) technique, molecular junctions give rise to plateaux in the current-distance scans. Xu used this BJ technique to measure the conductance of 4,4' bipyridine which was given as 0.01 G_0.[138] Due to the nature of the junction formation, the break-off distance cannot be readily calculated when using the standard BJ technique.

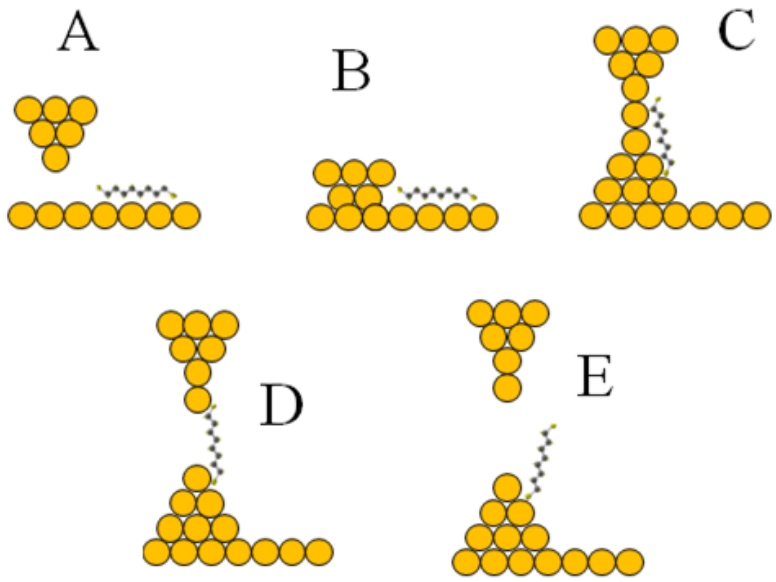

Figure 30: The STM-BJ technique used to measure the single molecule conductance of molecular wires. The STM tip is crashed into the substrate surface (B). The tip is then retracted (C) until the bridge of atoms joining the tip and substrate snaps (D). If a molecule bridges the gap, then as with the *I*(s) technique, a plateau is seen in the current-distance scan. As the tip is retracted further, the molecule breaks off from one of the electrodes, which results in the current dropping sharply.

The BJ technique is especially useful for observing the higher conductance groups **B** and **C**. This is because this method of junction formation results in a rougher electrode surface.

1.5.3 Electrochemical In-situ STM

Redox-active molecular wires as previously stated are of particular interest due to their switching behaviour when the electrode potential is altered.[32, 34, 40-42, 45, 47, 94, 96, 98, 100, 101, 103, 139] This can be achieved by use of a bipotentiostat interfaced with the STM controller. This allows the sample or the tip potential to be changed, while maintaining a constant bias, or the electrochemical potential of the tip can be maintained at a constant value with respect to the reference electrode, as the sample bias is changed. Cyclic voltammetry in the STM cell can also be performed using a bipotentiostat. Similarly to cyclic voltammetric experiments, an electrochemical cell is used with a working, reference and counter electrode. The tip is a 4th electrode and

a bias voltage is applied between the tip and the sample, which is also the working electrode. The counter and reference electrodes in an in-situ STM experiment are typically metal wires, platinum or gold for example. An electrolyte must be present in order to carry charge between the electrodes.[140] The tip must have a protective coating in order to prevent faradaic currents flowing between the tip and substrate. Apiezon® wax is a common coating used.[141]

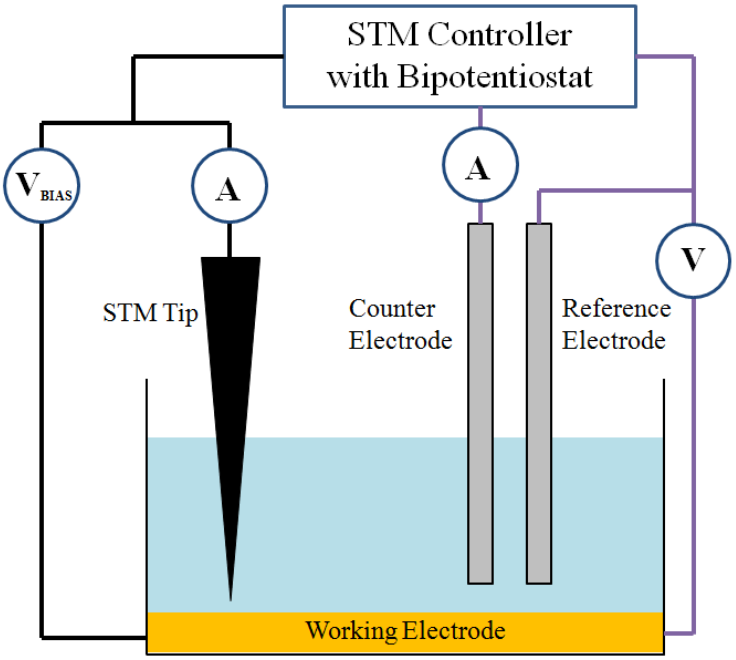

Figure 31: A schematic of an in-situ electrochemical STM cell. The STM controller contains a bipotentiostat which allows measurements to be performed under electrochemical potential control. Four electrodes are contained in the cell; the substrate acts as the working electrode, metal wires are used as the counter and reference electrodes and the STM tip acts as the 4th electrode. The tip must have a protective coating to reduce faradaic currents flowing between the tip and electrolyte. This is known as the leakage current.

1.6 References

1. J. Bardeen and W. H. Brattain, Physical Review, 1948, 74, 230-231.

2. W. Shockley, J. Bardeen and W. H. Brattain, Science, 1948, 108, 678-679.

3. G. E. Moore, Proceedings of the Ieee, 1998, 86, 82-85.

4. G. E. Moore and Ieee, No exponential is forever: But "forever" can be delayed!, San Francisco, Ca, 2003.

5. F. H. Blecher, Bell System Technical Journal, 1970, 49, 1995-1996.

6. W. B. Glendinning, T. F. Brooks, A. Mark and S. Marshall, Ieee Transactions on Component Parts, 1964, CP11, 19-22.

7. J. Spanos, Journal of the Electrochemical Society, 1961, 108, C176-C176.

8. R. P. Feynman, in Caltech Engineering And Science, California Institute of Technology, California Institute of Technology, 1960, vol. 23:5, ch. 22, pp. 22-36.

9. A. Aviram and M. A. Ratner, Chemical Physics Letters, 1974, 29, 277-283.

10. A. Aviram, C. Joachim and M. Pomerantz, Chemical Physics Letters, 1988, 146, 490-495.

11. J. Jortner, M. A. Ratner and International Union of Pure and Applied Chemistry, Molecular electronics, Blackwell Science, 1997.

12. M. A. Reed, C. Zhou, C. J. Muller, T. P. Burgin and J. M. Tour, Science, 1997, 278, 252-254.

13. X. L. Li, B. Q. Xu, X. Y. Xiao, X. M. Yang, L. Zang and N. J. Tao, Faraday Discussions, 2006, 131, 111-120.

14. X. Y. Xiao, B. Q. Xu and N. J. Tao, Nano Letters, 2004, 4, 267-271.

15. C. A. Martin, D. Ding, H. S. J. van der Zant and J. M. van Ruitenbeek, New Journal of Physics, 2008, 10, 065008.

16. C. A. Martin, D. Ding, J. K. Sorensen, T. Bjornholm, J. M. van Ruitenbeek and H. S. J. van der Zant, Journal of the American Chemical Society, 2008, 130, 13198-13199.

17. E. Löertscher, H. B. Weber and H. Riel, Physical Review Letters, 2007, 98, 176807.

18. W. Haiss, C. Wang, R. Jitchati, I. Grace, S. Martin, A. Batsanov, S. Higgins, M. Bryce, C. Lambert, P. Jensen and R. Nichols, Journal of Physics-Condensed Matter, 2008, 20, 374119.

19. J. C. Cuevas and E. Scheer, Molecular electronics : an introduction to theory and experiment, World Scientific, Singapore ; Hackensack, NJ, 2010.

20. B. Q. Xu and N. J. J. Tao, Science, 2003, 301, 1221-1223.

21. W. Haiss, S. Martin, E. Leary, H. van Zalinge, S. Higgins, L. Bouffier and R. Nichols, Journal of Physical Chemistry C, 2009, 113, 5823-5833.

22. N. J. Kay, R. J. Nichols, S. J. Higgins, W. Haiss, G. Sedghi, W. Schwarzacher and B.-W. Mao, Journal of Physical Chemistry C, 2011, 115, 21402-21408.

23. W. Haiss, S. Martin, L. E. Scullion, L. Bouffier, S. J. Higgins and R. J. Nichols, Physical Chemistry Chemical Physics, 2009, 11, 10831-10838.

24. V. B. Engelkes, J. M. Beebe and C. D. Frisbie, Journal of the American Chemical Society, 2004, 126, 14287-14296.

25. M. Paulsson, C. Krag, T. Frederiksen and M. Brandbyge, Nano Letters, 2009, 9, 117-121.

26. X. D. Cui, A. Primak, X. Zarate, J. Tomfohr, O. F. Sankey, A. L. Moore, T. A. Moore, D. Gust, L. A. Nagahara and S. M. Lindsay, Journal of Physical Chemistry B, 2002, 106, 8609-8614.

27. X. D. Cui, A. Primak, X. Zarate, J. Tomfohr, O. F. Sankey, A. L. Moore, T. A. Moore, D. Gust, G. Harris and S. M. Lindsay, Science, 2001, 294, 571-574.

28. X. D. Cui, X. Zarate, J. Tomfohr, O. F. Sankey, A. Primak, A. L. Moore, T. A. Moore, D. Gust, G. Harris and S. M. Lindsay, Nanotechnology, 2002, 13, 5-14.

29. W. Haiss, R. Nichols, H. van Zalinge, S. Higgins, D. Bethell and D. Schiffrin, Physical Chemistry Chemical Physics, 2004, 6, 4330-4337.

30. C. P. Collier, G. Mattersteig, E. W. Wong, Y. Luo, K. Beverly, J. Sampaio, F. M. Raymo, J. F. Stoddart and J. R. Heath, Science, 2000, 289, 1172-1175.

31. T. Albrecht, A. Guckian, J. Ulstrup and J. G. Vos, Ieee Transactions on Nanotechnology, 2005, 4, 430-434.

32. T. Albrecht, K. Moth-Poulsen, J. B. Christensen, A. Guckian, T. Bjornholm, J. G. Vos and J. Ulstrup, Faraday Discussions, 2006, 131, 265-279.

33. T. Albrecht, A. Guckian, A. M. Kuznetsov, J. G. Vos and J. Ulstrup, Journal of the American Chemical Society, 2006, 128, 17132-17138.

34. J. D. Zhang, A. M. Kuznetsov, I. G. Medvedev, Q. J. Chi, T. Albrecht, P. S. Jensen and J. Ulstrup, Chemical Reviews, 2008, 108, 2737-2791.

35. E. Laviron, Journal of Electroanalytical Chemistry, 1979, 101, 19-28.

36. R. J. Forster and L. R. Faulkner, Analytical Chemistry, 1995, 67, 1232-1239.

37. W. Haiss, R. J. Nichols, S. J. Higgins, D. Bethell, H. Hobenreich and D. J. Schiffrin, Faraday Discussions, 2004, 125, 179-194.

38. R. J. Nichols, W. Haiss, S. J. Higgins, E. Leary, S. Martin and D. Bethell, Physical Chemistry Chemical Physics, 2010, 12, 2801-2815.

39. W. Haiss, H. van Zalinge, H. Hobenreich, D. Bethell, D. J. Schiffrin, S. J. Higgins and R. J. Nichols, Langmuir, 2004, 20, 7694-7702.

40. W. Haiss, H. van Zalinge, S. Higgins, D. Bethell, H. Hobenreich, D. Schiffrin and R. Nichols, Journal of The American Chemical Society, 2003, 125, 15294-15295.

41. W. Haiss, T. Albrecht, H. van Zalinge, S. Higgins, D. Bethell, H. Hobenreich, D. Schiffrin, R. Nichols, A. Kuznetsov, J. Zhang, Q. Chi and J. Ulstrup, Journal of Physical Chemistry B, 2007, 111, 6703-6712.

42. I. V. Pobelov, Z. H. Li and T. Wandlowski, Journal of the American Chemical Society, 2008, 130, 16045-16054.

43. N. S. Lee, W. S. Choi, H. K. Shin, D. J. Qian and Y. S. Kwon, Japanese Journal of Applied Physics, 2008, 47, 2, 1173-1177.

44. A. Bagrets, A. Arnold and F. Evers, Journal of the American Chemical Society, 2008, 130, 9013-9018.

45. Z. H. Li, I. Pobelov, B. Han, T. Wandlowski, A. Blaszczyk and M. Mayor, Nanotechnology, 2007, 18, 044018.

46. Z. Li, B. Han, G. Meszaros, I. Pobelov, T. Wandlowski, A. Blaszczyk and M. Mayor, Faraday Discussions, 2006, 131, 121-143.

47. E. Leary, S. Higgins, H. van Zalinge, W. Haiss, R. Nichols, S. Nygaard, J. Jeppesen and J. Ulstrup, Journal of The American Chemical Society, 2008, 130, 12204-12205.

48. F. Giacalone, M. A. Herranz, L. Gruter, M. T. Gonzalez, M. Calame, C. Schonenberger, C. R. Arroyo, G. Rubio-Bollinger, M. Velez, N. Agrait and N. Martin, Chemical Communications, 2007, 4854-4856.

49. A. L. Kanibolotsky, J. C. Forgie, S. Gordeyev, F. Vilela, P. J. Skabara, J. E. Lohr, B. M. Petersen and J. O. Jeppesen, Macromolecular Rapid Communications, 2008, 29, 1226-1230.

50. J. O. Jeppesen, C. P. Collier, J. R. Heath, Y. Luo, K. A. Nielsen, J. Perkins, J. F. Stoddart and E. Wong, Journal de Physique IV, 2004, 114, 511-513.

51. J. O. Jeppesen and J. Becher, European Journal of Organic Chemistry, 2003, 3245-3266.

52. Y. Okawa, S. K. Mandal, C. Hu, Y. Tateyama, S. Goedecker, S. Tsukamoto, T. Hasegawa, J. K. Gimzewski and M. Aono, Journal of the American Chemical Society, 2011, 133, 8227-8233.

53. A. M. Ionescu and H. Riel, Nature, 2011, 479, 329-337.

54. J. S. Lindsey and D. F. Bocian, Accounts of Chemical Research, 2011, 44, 638-650.

55. W. G. Kuhr, A. R. Gallo, R. W. Manning and C. W. Rhodine, Mrs Bulletin, 2004, 29, 838-842.

56. J. Shaw, Y.-W. Zhong, K. J. Hughes, T.-H. Hou, H. Raza, S. Rajwade, J. Bellfy, J. R. Engstrom, H. D. Abruna and E. C. Kan, Ieee Transactions on Electron Devices, 2011, 58, 826-834.

57. T. Albrecht, K. Moth-Poulsen, J. B. Christensen, J. Hjelm, T. Bjornholm and J. Ulstrup, Journal of the American Chemical Society, 2006, 128, 6574-6575.

58. Y. C. Fu, Y. Z. Su, D. Y. Wu, J. W. Yan, Z. X. Xie and B. W. Mao, Journal of the American Chemical Society, 2009, 131, 14728-14737.

59. Y. Z. Su, Y. C. Fu, J. W. Yan, Z. B. Chen and B. W. Mao, Angewandte Chemie-International Edition, 2009, 48, 5148-5151.

60. Y. M. Wei, X. S. Zhou, J. G. Wang, J. Tang, B. W. Mao and D. M. Kolb, Small, 2008, 4, 1355-1358.

61. X. B. Ji, D. S. Silvester, L. Aldous, C. Hardacre and R. G. Compton, Journal of Physical Chemistry C, 2007, 111, 9562-9572.

62. L. G. Lin, Y. Wang, J. W. Yan, Y. Z. Yuan, J. Xiang and B. W. Mao, Electrochemistry Communications, 2003, 5, 995-999.

63. D. L. Compton and J. A. Laszlo, Journal of Electroanalytical Chemistry, 2002, 520, 71-78.

64. R. Compton and G. H. W. Sanders, Electrode potentials, Oxford University Press, 1998.

65. D. Pletcher and S. E. Group, Instrumental methods in electrochemistry, Ellis Horwood, 2001.

66. A. J. Bard and L. R. Faulkner, Electrochemical methods: fundamentals and applications, Wiley, 2001.

67. D. H. Evans, K. M. O'Connell, R. A. Petersen and M. J. Kelly, Journal of Chemical Education, 1983, 60, 290-293.

68. A. C. Fisher, Electrode dynamics, Oxford University Press, 1996.

69. A. Hamelin, Journal of Electroanalytical Chemistry, 1996, 407, 1-11.

70. A. Hamelin and A. M. Martins, Journal of Electroanalytical Chemistry, 1996, 407, 13-21.

71. H. Angersteinkozlowska, B. E. Conway, A. Hamelin and L. Stoicoviciu, Journal of Electroanalytical Chemistry, 1987, 228, 429-453.

72. A. Hamelin, Journal of Electroanalytical Chemistry, 1982, 142, 299-316.

73. X.-S. Zhou, L. Liu, P. Fortgang, A.-S. Lefevre, A. Serra-Muns, N. Raouafi, C. Amatore, B.-W. Mao, E. Maisonhaute and B. Schoellhorn, Journal of the American Chemical Society, 2011, 133, 7509-7516.

74. G. Binning, H. Rohrer, C. Gerber and E. Weibel, Physical Review Letters, 1982, 49, 57-61.

75. G. Binnig and H. Rohrer, Helvetica Physica Acta, 1982, 55, 726-735.

76. G. Binnig, H. Rohrer, C. Gerber and E. Weibel, Applied Physics Letters, 1982, 40, 178-180.

77. G. Binnig, H. Rohrer, C. Gerber and E. Weibel, Physical Review Letters, 1983, 50, 120-123.

78. G. Binnig and H. Rohrer, Ibm Journal of Research and Development, 1986, 30, 355-369.

79. Y. T. Kim, R. L. McCarley and A. J. Bard, Journal of Physical Chemistry, 1992, 96, 7416-7421.

80. B. C. Schardt, S. L. Yau and F. Rinaldi, Science, 1989, 243, 1050-1053.

81. L. M. Eng and H. Fuchs, Materials Science and Engineering a-Structural Materials Properties Microstructure and Processing, 1991, 139, 230-238.

82. S. M. Sze and K. K. Ng, Physics of semiconductor devices, Wiley-Interscience, Hoboken, N.J., 2007.

83. P. Atkins and J. de Paula, Elements Of Physical Chemistry, Oxford University Press, 2005.

84. P. Atkins and J. de Paula, Physical Chemistry, Oxford University Press, 2010.

85. P. K. Hansma and J. Tersoff, Journal of Applied Physics, 1987, 61, R1-R23.

86. S. H. Choi, B. Kim and C. D. Frisbie, Science, 2008, 320, 1482-1486.

87. L. Luo, S. Choi and C. Frisbie, Chemistry of Materials, 2011, 23, 631-645.

88. S. Karthauser, Journal of Physics-Condensed Matter, 2011, 23, 013001.

89. F. Chen, X. L. Li, J. Hihath, Z. F. Huang and N. J. Tao, Journal of the American Chemical Society, 2006, 128, 15874-15881.

90. E. Leary, S. Higgins, H. van Zalinge, W. Haiss and R. Nichols, Chemical Communications, 2007, 3939-3941.

91. D. I. Gittins, D. Bethell, R. J. Nichols and D. J. Schiffrin, Journal of Materials Chemistry, 2000, 10, 79-83.

92. A. M. Kuznetsov, I. G. Medvedev and J. Ulstrup, Journal of Chemical Physics, 2007, 127, 104708.

93. E. P. Friis, Y. I. Kharkats, A. M. Kuznetsov and J. Ulstrup, The Journal of Physical Chemistry A, 1998, 102, 7851-7859.

94. J. D. Zhang, A. M. Kuznetsov and J. Ulstrup, Journal of Electroanalytical Chemistry, 2003, 541, 133-146.

95. W. Schmickler and C. Widrig, Journal of Electroanalytical Chemistry, 1992, 336, 213-221.

96. N. J. Tao, B. Q. Xu and X. Y. Xiao, Abstracts of Papers of the American Chemical Society, 2005, 229, U726-U726.

97. N. J. Tao, Physical Review Letters, 1996, 76, 4066-4069.

98. T. Morita and S. Lindsay, Journal of Physical Chemistry B, 2008, 112, 10563-10572.

99. A. M. Kuznetsov and J. Ulstrup, Journal of Electroanalytical Chemistry, 2004, 564, 209-222.

100. W. Haiss, D. Bethell, R. Nichols and D. Schiffrin, Abstracts of Papers of the American Chemical Society, 2003, 225, U507-U507.

101. T. Albrecht, A. Guckian, J. Ulstrup, H. Vos, 4th IEEE Conference on Nanotechnology, 2004, 134-136.

102. A. Alessandrini, S. Corni and P. Facci, Physical Chemistry Chemical Physics, 2006, 8, 4383-4397.

103. W. Haiss, R. Nichols, S. Higgins, D. Bethell, H. Hobenreich and D. Schiffrin, Faraday Discussions, 2004, 125, 179-194.

104. T. Lee, W. Wang and M. A. Reed, Annals of the New York Academy of Sciences, 2003, 1006, 21-35.

105. D. R. Stewart, D. A. A. Ohlberg, P. A. Beck, C. N. Lau and R. S. Williams, Applied Physics A: Materials Science and Processing, 2005, 80, 1379-1383.

106. E. A. Weiss, J. K. Kriebel, M.-A. Rampi and G. M. Whitesides, Philosophical Transactions of the Royal Society a-Mathematical Physical and Engineering Sciences, 2007, 365, 1509-1537.

107. J. G. Simmons, Journal of Applied Physics, 1963, 34, 1793-1803.

108. H. B. Akkerman, R. C. G. Naber, B. Jongbloed, P. A. van Hal, P. W. M. Blom, D. M. de Leeuw and B. de Boer, Proceedings of the National Academy of Sciences of the United States of America, 2007, 104, 11161-11166.

109. J. H. Coombs, M. E. Welland and J. B. Pethica, Surface Science, 1988, 198, L353-L358.

110. L. L. Chang, L. Esaki and R. Tsu, Applied Physics Letters, 1974, 24, 593-595.

111. W. Haiss, H. van Zalinge, H. Hobenreich, D. Bethell, D. Schiffrin, S. Higgins and R. Nichols, Langmuir, 2004, 20, 7694-7702.

112. W. Schmickler, Surface Science, 1993, 295, 43-56.

113. W. Schmickler and N. J. Tao, Electrochimica Acta, 1997, 42, 2809-2815.

114. A. M. Kuznetsov and J. Ulstrup, Journal of Chemical Physics, 2002, 116, 2149-2165.

115. A. M. Kuznetsov and J. Ulstrup, Russian Journal of Electrochemistry, 2006, 42, 760-766.

116. J. Zhang, Q. Chi, A. M. Kuznetsov, A. G. Hansen, H. Wackerbarth, H. E. M. Christensen, J. E. T. Andersen and J. Ulstrup, Journal of Physical Chemistry B, 2002, 106, 1131-1152.

117. J. R. Bolton and M. D. Archer, Electron Transfer in Inorganic, Organic, and Biological Systems, 1991, 228, 7-23.

118. R. A. Marcus, Angewandte Chemie-International Edition in English, 1993, 32, 1111-1121.

119. A. Nitzan, Chemical dynamics in condensed phases: relaxation, transfer and reactions in condensed molecular systems, Oxford University Press, 2006.

120. G. L. Closs, L. T. Calcaterra, N. J. Green, K. W. Penfield and J. R. Miller, Journal of Physical Chemistry, 1986, 90, 3673-3683.

121. D. Shriver, P. Atkins, T. Overton and J. Rourke, Inorganic Chemistry, W. H. Freeman, 2009.

122. M. Liang, A. Kaintz, G. A. Baker and M. Maroncelli, Journal of Physical Chemistry. B, 2012, 116, 1370-1384.

123. S. Martin, W. Haiss, S. Higgins, P. Cea, M. C. Lopez and R. J. Nichols, Journal of Physical Chemistry C, 2008, 112, 3941-3948.

124. S. Martin, D. Manrique, V. Garcia-Suarez, W. Haiss, S. Higgins, C. Lambert and R. Nichols, Nanotechnology, 2009, 20, 125203.

125. M. Kamenetska, S. Y. Quek, A. C. Whalley, M. L. Steigerwald, H. J. Choi, S. G. Louie, C. Nuckolls, M. S. Hybertsen, J. B. Neaton and L. Venkataraman, Journal of the American Chemical Society, 2010, 132, 6817-6821.

126. L. Venkataraman, J. E. Klare, C. Nuckolls, M. S. Hybertsen and M. L. Steigerwald, Nature, 2006, 442, 904-907.

127. L. Venkataraman, Y. S. Park, A. C. Whalley, C. Nuckolls, M. S. Hybertsen and M. L. Steigerwald, Nano Letters, 2007, 7, 502-506.

128. I. Kristensen, D. Mowbray, K. Thygesen and K. Jacobsen, Journal of Physics-Condensed Matter, 2008, 20, 374101.

129. S. T. Schneebeli, M. Kamenetska, Z. L. Cheng, R. Skouta, R. A. Friesner, L. Venkataraman and R. Breslow, Journal of the American Chemical Society, 2011, 133, 2136-2139.

130. Y. Imry and R. Landauer, Reviews of Modern Physics, 1999, 71, S306.

131. E. H. Huisman, M. L. Trouwborst, F. L. Bakker, B. de Boer, B. J. van Wees and S. J. van der Molen, Nano Letters, 2008, 8, 3381-3385.

132. Z. F. Huang, F. Chen, P. A. Bennett and N. J. Tao, Journal of the American Chemical Society, 2007, 129, 13225-13231.

133. X. L. Li, J. He, J. Hihath, B. Q. Xu, S. M. Lindsay and N. J. Tao, Journal of the American Chemical Society, 2006, 128, 2135-2141.

134. N. J. Tao, Journal of Materials Chemistry, 2005, 15, 3260-3263.

135. J. L. Xia, I. Diez-Perez and N. J. Tao, Nano Letters, 2008, 8, 1960-1964.

136. W. Haiss, C. Wang, I. Grace, A. Batsanov, D. Schiffrin, S. Higgins, M. Bryce, C. Lambert and R. Nichols, Nature Materials, 2006, 5, 995-1002.

137. N. A. Kautz and S. A. Kandel, Journal of the American Chemical Society, 2008, 130, 6908-6909.

138. B. Xu and N. J. Tao, Science, 2003, 301, 1221-1223.

139. B. Han, Z. H. Li, C. Li, I. Pobelov, G. J. Su, R. Aguilar-Sanchez and T. Wandlowski, in Templates in Chemistry Iii, 2009, vol. 287, pp. 181-255.

140. D. M. Kolb, Angewandte Chemie-International Edition, 2001, 40, 1162-1181.

141. R. J. Nichols, O. M. Magnussen, J. Hotlos, T. Twomey, R. J. Behm and D. M. Kolb, Journal of Electroanalytical Chemistry, 1990, 290, 21-31.

Chapter 2

Conductance Measurements Of Alkanedithiols In A Room Temperature Ionic Liquid

2 Conductance Measurements Of Alkanedithiols In A Room Temperature Ionic Liquid

2.1 Introduction

Alkanedithiols are simple molecules consisting of a polymethylene chain terminated at either end by a thiol group, with the general formula $HS(CH_2)_nSH$. This thiol termination enables them to form a strong chemical bond to a Au substrate, which is one feature which makes them especially suitable for SMC measurements. Their simplicity and stability also makes them an ideal model system as they behave in a predictable manner. They benefit from a wide HOMO/LUMO gap, which in conjunction with the Fermi level of the Au electrodes used, means that direct tunnelling is the dominant ET mechanism.[1, 2] They are the most studied molecular systems in the field of SME,[1, 3-10] meaning that they are the ideal system to use when testing a novel approach, such as a new medium or measurement technique.

There has been extensive research on the conductance of alkanedithiol chains under ambient conditions.[4, 5, 10-13] It has been found that the conductance is dependent on the length of the carbon chain; the longer the chain, the lower the conductance. Haiss *et al*. showed that the conductance of alkanedithiols decays exponentially as the length of the chain increases when N>8, as seen in *Figure 32* below.[4] At shorter chain lengths, there is an anomalous chain length dependence.

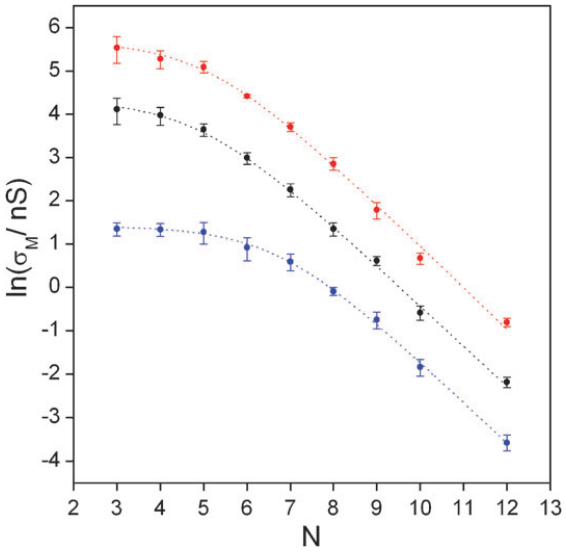

Figure 32: Logarithm of the low conductance group **A** (blue), medium conductance group **B** (black) and high conductance group **C** (red) measured for alkanedithiols in ambient conditions, as a function of the number of CH_2 groups (N) at a bias voltage V_{bias} = +0.6 V. Figure taken from reference 4.

ET through alkanedithiols proceeds by direct tunnelling. The Simmons model, which is described in the previous chapter, provides a good representation of ET through these molecules. To confirm this, the bias voltage dependence was measured and the Simmons model was fitted to the resulting *I-V* curves. Haiss *et al*. demonstrated this in *Figure 33* for octanedithiol (ODT).[4]

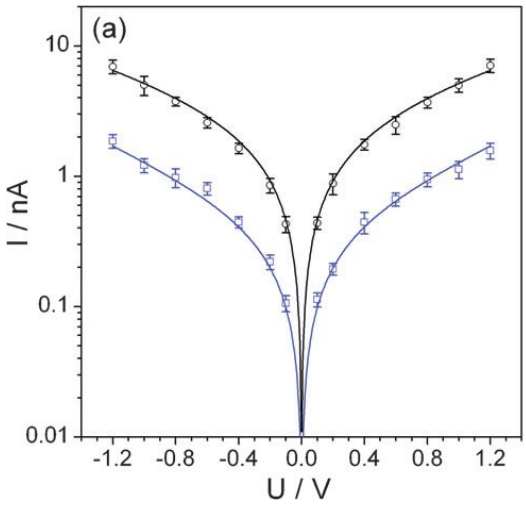

Figure 33: Current through ODT as a function of the bias voltage for both the low conductance group **A** (blue) and the medium conductance group **B** (black). The solid lines are fits to the Simmons model. Figure taken from reference 4.

Room temperature ionic liquids (RTILs) are salts, which are in a liquid state at room temperature.[14] They could provide exciting new avenues in electrochemistry and SME, due to their unique properties, including a wider potential window than conventional aqueous electrolytes, high conductivity and low volatility.[14-20] The wider potential window made possible by RTILs is particularly interesting, as redox processes which are obscured in aqueous electrolytes at low and high potentials by hydrogen evolution and surface oxidation respectively, can be investigated. This widening of the potential window has been demonstrated by Albrecht *et al.,* using a redox-active osmium bisterpyridine complex (Ossac).[15] They also used scanning tunnelling spectroscopy (STS) to observe how the tunnelling current behaves when

either the sample potential, or the tip-substrate bias voltage are swept. As expected for the redox-active Ossac molecule, an enhancement in tunnelling current was observed around the redox potential of the molecule.[15]

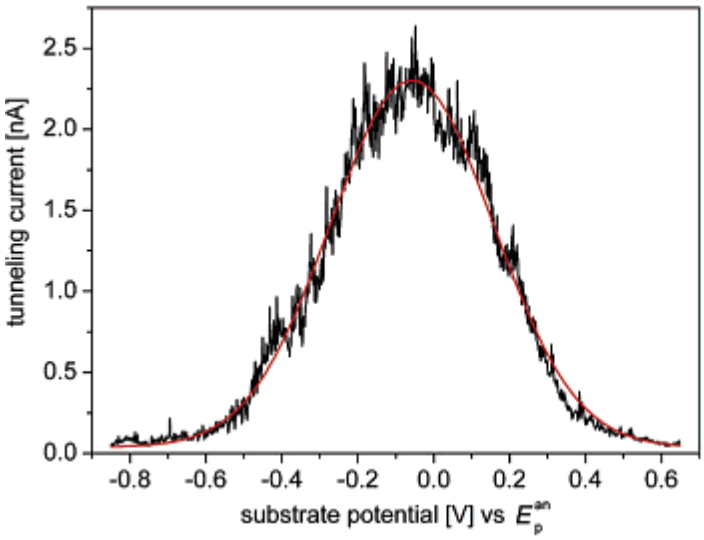

Figure 34: Tunnelling current enhancement when the sample potential is swept as the bias potential is kept constant at +0.7 V. Figure taken from reference 15.

2.2 Aim

Conductance measurements of single molecular wires have not been performed previously in a RTIL medium. The utilisation of RTILs in SME will be of great interest with regards to redox-active systems due to the wider potential window described previously. However, since a method for these measurements has not been established, a simpler system such as alkanedithiols would be desirable for these primary measurements. The aim of this study is to demonstrate that the conductance of a single molecule, namely alkanedithiols, can be measured using an STM in a RTIL. The *I-V* characteristics of alkanedithiols will also be observed and plotted against the Simmons model. It is accepted that ET occurs through alkanedithiols by direct tunnelling and since specific chemical interactions between the RTIL and the polymethylene backbone are not expected, alkanedithiols are the ideal system to test this novel medium in SME.[1] This data will then be compared to the previous measurements recorded by Haiss *et al.*,[4] in order to determine whether single molecule conductance measurements are indeed viable in a RTIL medium.

2.3 Experimental Methods

All of the experiments were performed using an Agilent 2500 STM controller in conjunction with the Agilent Picoscan 5.3.3 software. RTILs tend to be sensitive to air/water so care must be taken to ensure the system remains as dry as possible. Therefore, an environmental chamber was fitted to the STM head which maintained an inert dry N_2 atmosphere. This also contained a small amount of silica dessicant. Au STM tips were prepared using 0.25 mm Au wire (99.99%, Goodfellows), which were electrochemically etched in a 1:1 solution of HCl and ethanol at a potential of approximately +7.0 V. The Au tips were then coated with a layer of apiezon® wax, ensuring that only the very end of the tip was exposed. Commercial gold-on-glass substrates (Arrandee®) were flame annealed prior to use. The alkanedithiols were used as received; 1,3-propanedithiol (PrDT) and 1,8-octanedithiol (ODT) from Alfa Aesar and 1,5-pentanedithiol (PDT), 1,6-hexanedithiol (HDT), 1,9-nonanedithiol (NDT) and 1,11-undecanedithiol (UDT) from Sigma Aldrich. 5 x 10^{-5} M methanolic solutions of these alkanedithiols were produced and the flame annealed gold-on-glass substrate was immersed for 2 minutes to allow the alkanedithiol molecules to adsorb onto the surface. The substrate was then rinsed thoroughly with ethanol to remove excess alkanedithiol molecules and blown dry using N_2. The resulting alkanedithiol SAMs are stable for several days. The RTIL used in these measurements was 1-butyl-3-methylimidazolium trifluoromethanesulfonate (BMIOTf) and was purchased from Iolitec. This was heated to 110-120 °C with dry N_2 flow for a minimum of 1 hour prior to use. This was handled in a glove box environment and treated with 3 Å molecular sieves (Sigma Aldrich) to aid the removal of trace water. After the STM cell was set up, the environmental chamber was purged with dry N_2 for approximately 16 hours prior to measurements being taken.[1] BMIOTf is a hydrophobic RTIL so water content was not expected to be an issue.[21]

Both the STM $I(s)$ and BJ techniques were used in these measurements. The $I(s)$ measurements were made by performing scans from 0 to +4 nm relative to the current setpoint, with a scan duration of 0.0946 seconds. A bias voltage (V_{BIAS}) of +0.6 V and a setpoint current (I_0) of 20 nA were used for the length dependence measurements. The BJ measurements were made by performing scans from -4 to +4 nm with a scan duration of 1 second. The resulting current-distance scans were then

plotted into a histogram in order to determine the molecular conductance. The bias voltage dependence measurements were made using bias voltage values of ±0.1, ±0.2, ±0.4, ±0.6, ±0.8, ±1.0, ±1.2, and ±1.5 V and histograms were plotted to determine the molecular conductance.[1]

The initial tip-to-sample distance s_0 was tentatively calculated using *Equation 2.1*.[22] A number of exponential decay scans, where no evidence of molecular bridging is evident, were used. For each scan, ln(*I*) versus distance (*s*) was plotted and extrapolated back to the point of contact where the y-intercept would be G_0. The gradient of this plot was then used in *Equation 2.1* to estimate the initial tip-sample separation.

$$s_0 = \frac{ln\left(G_0 \, {V_{BIAS}}/{I_0}\right)}{{dlnI}/{ds}} \qquad \textit{Equation 2.1}$$

This is then added to the distance from I_0 at which the molecule breaks away from one of the Au electrodes (Δs), which then gives the break-off distance of the molecule. This is compared to the molecular length calculated using Spartan '08® molecular modelling software in order to confirm that there is indeed a single molecule bridging the gap between the substrate and tip.[1]

2.4 Results And Discussion

The *I*(*s*) technique was used to determine the single molecule conductance of the alkanedithiols PrDT, PDT, HDT, ODT, NDT and UDT in the RTIL BMIOTf. Care was taken to avoid contact with air and water so all of the *I*(*s*) measurements were performed under a dry N_2 atmosphere in an environmental chamber. *I*(*s*) scans were recorded by setting the current setpoint and bias voltage, and then rapidly retracting the tip by temporarily disabling the feedback loop, at a rate of 42.3 nm s^{-1}. Approximately 5% of all the *I*(*s*) scans obtained contained a current plateau that is characteristic of molecules bridging the gap between the Au substrate and STM tip.

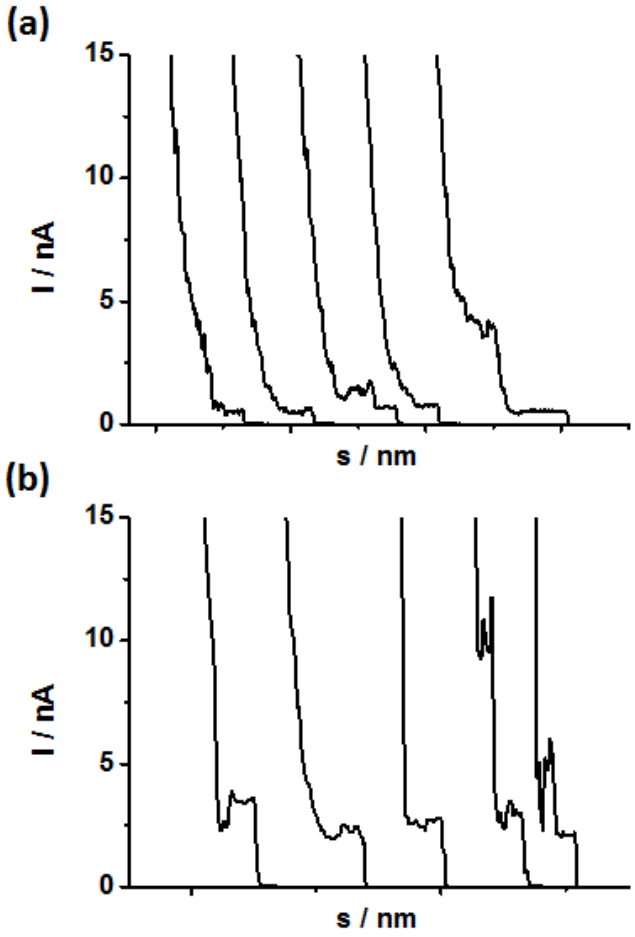

Figure 35: Examples of *I*(*s*) scans for the low conductance **A** group (a) and BJ scans for the medium conductance **B** group (b) for ODT in BMIOTf.

All of these *I*(*s*) scans containing a plateau were used in the histogram analysis and each histogram consisted of at least 500 *I*(*s*) scans. In all of these histograms, a clear peak is observed and from this peak, the conductance of the molecule can be calculated. The conductance was found to decrease with molecular length.

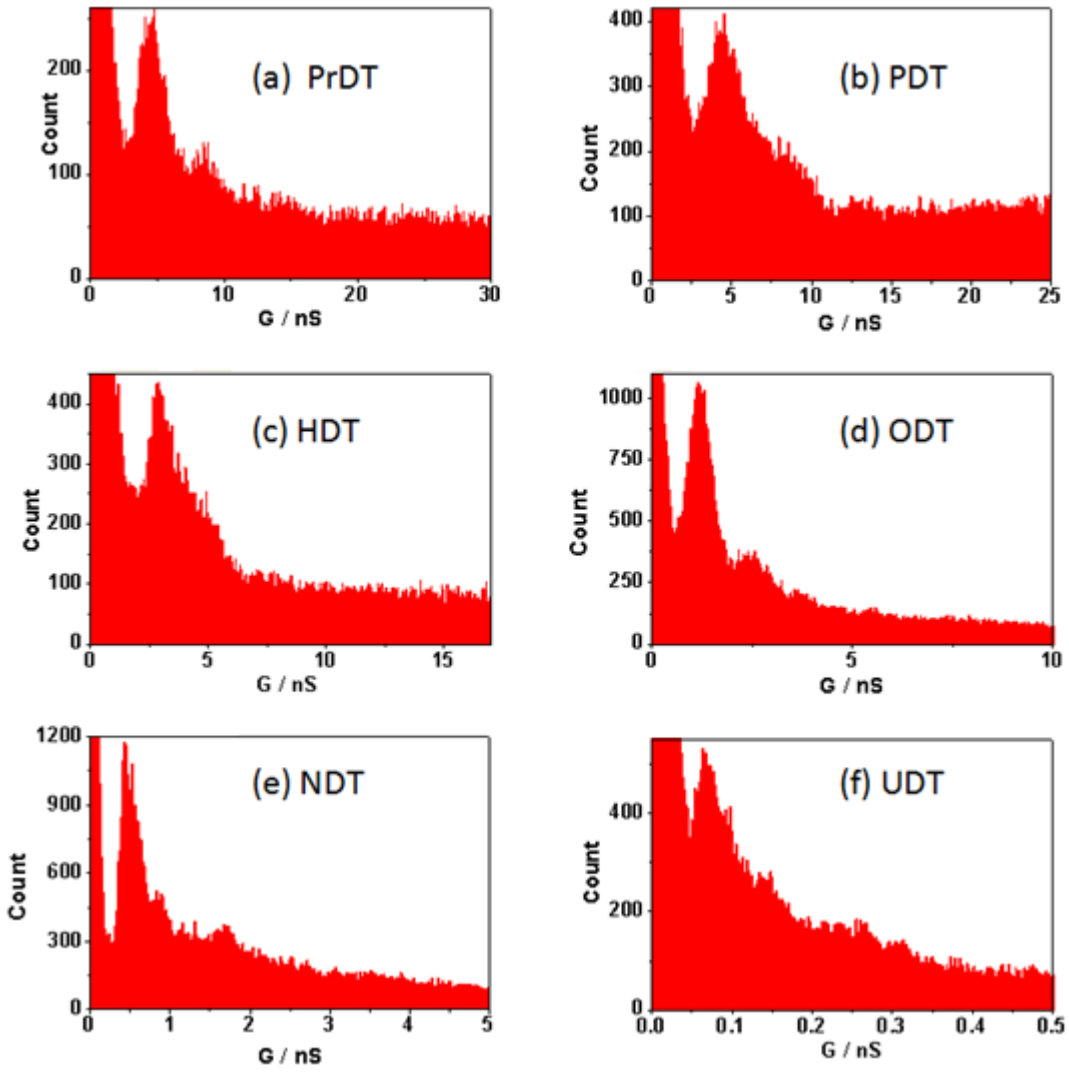

Figure 36: Conductance histograms of (a) PrDT, (b) PDT, (c) HDT, (d) ODT, (e) NDT, and (f) UDT on Au(111) obtained using the *I*(*s*) method; V_{BIAS} = +0.6 V ; I_0 = 20 nA ; 500, 501, 500, 538, 578, and 503 scans were analysed respectively.

It is known that several different conductance groups exist, and these have been observed for alkanedithiols.[4, 13, 23-25] These are commonly referred to as the low (**A**), medium (**B**) and high (**C**) conductance groups. Haiss *et al*. suggest that this is caused by the molecule binding to the Au leads in different ways.[4, 25] For the **A** group, the molecule is adsorbed on a terrace site on the substrate and to a single Au atom on the tip. The **B** and **C** groups are attributed to the sulfur attaching to multiple Au atoms at one or both of the electrodes.[25] The *I*(*s*) technique is especially useful for observing the **A** group at relatively low setpoint currents, or possibly the **B** group at higher setpoint currents. To see the higher conductance groups **B** and **C** however, the BJ

technique can be used. This is due to the tip crashing into the surface resulting in a rougher surface.[25] Therefore, the *I*(*s*) technique was used to observe the **A** group, and also the **B** group for NDT. To observe the higher conductance groups, the STM BJ technique pioneered by Tao and Xu was used.[3] Histograms were plotted in a similar manner to the *I*(*s*) method and these show considerably higher conductance values than were witnessed using the *I*(*s*) technique, as seen in *Figure 37*. The BJ technique was not used for NDT as a conductance peak for the **B** group was seen in the *I*(*s*) measurements.

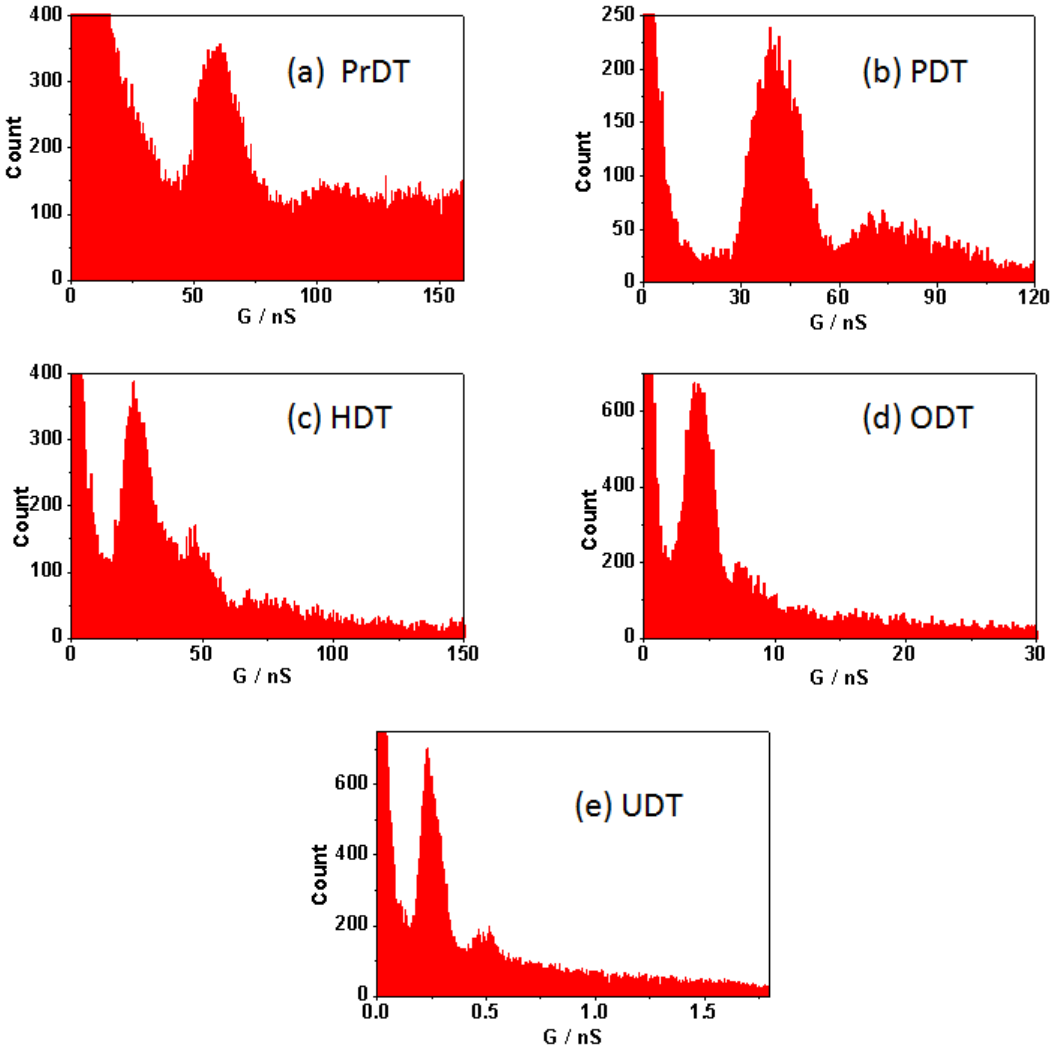

Figure 37: Conductance histograms of (a) PrDT, (b) PDT, (c) HDT, (d) ODT, and (e) UDT on Au(111) obtained using the BJ method; V_{BIAS} = +0.6 V ; I_0 = 20 nA ; 501, 500, 507, 504, and 505 scans were analysed respectively.

The conductance values obtained using the BJ technique are not multiples of the corresponding **A** group values, therefore they can be attributed to the higher **B** conductance group. It is interesting to note at this point that no **C** group was observed for any of the alkanedithiols measured in BMIOTf. This observation is discussed later.[1] The conductance values obtained for both the **A** and **B** groups are shown in *Table 4*.

Table 4: Conductance values for the **A** and **B** conductance groups for the alkanedithiols measured

Alkanedithiol (N)	**A** group conductance / nS	**B** group conductance / nS
PrDT (3)	4.70 ± 0.78	60.8 ± 6.3
PDT (5)	4.68 ± 0.67	40.5 ± 5.5
HDT (6)	3.07 ± 0.42	25.7 ± 3.9
ODT (8)	1.21 ± 0.19	4.17 ± 0.75
NDT (9)	0.51 ± 0.09	1.68 ± 0.08
UDT (11)	0.07 ± 0.01	0.25 ± 0.04

The break-off distance of the molecule is a good way of confirming that the conductance of the molecule in question has been reliably determined. The break-off distance is expected to be close to the length of the molecule in question. Alkanethiol monolayers however, are known to cause the Au surface to undergo a degree of restructuring, creating Au adatoms and islands on even, supposedly flat single crystal surface. This is one possible explanation as to why the break-off distances estimated in these measurements are often slightly larger than the length of the molecule.[26] It should also be noted that the molecule does not necessarily adsorb to the terminal gold atom of the tip (or substrate), meaning that a range (distribution) of break-off distances are possible.

Table 5: Estimate of the break-off distance for all alkanedithiols measured compared to the calculated molecular length.

Alkanedithiol (N)	Length of molecule / nm	Break-off distance / nm
PrDT (3)	0.8	1.3 ± 0.2
PDT (5)	1.0	1.4 ± 0.2
HDT (6)	1.2	1.5 ± 0.2
ODT (8)	1.4	1.6 ± 0.2
NDT (9)	1.5	1.6 ± 0.2
UDT (11)	1.8	1.9 ± 0.2

The conductance histograms are an excellent way of presenting the molecular conductance values. However, they do lack information about the break-off distances. A 2-D histogram however, retains this information, allowing both the conductance and the break-off distance to be shown on the same data plot. The conductance is shown on the *y* axis and the total tip-to-substrate separation is shown on the *x* axis. The density of data points is shown by the colour scaling, ranging from low (darker blue) to high (red). The example 2-D histogram shown in *Figure 38* represents the data obtained from 538 $I(s)$ scans of ODT, and uses a bin size of 0.012 nS for the conductance values and a bin size of 0.015 nm for the break-off distance values. The distance values shown on the *x*-axis are the total tip-to-substrate distances (s) calculated by adding the initial tip-to-substrate distance s_0 to the change in this distance as the tip is withdrawn Δs. This procedure is described in more detail in the Experimental Methods section of this chapter.

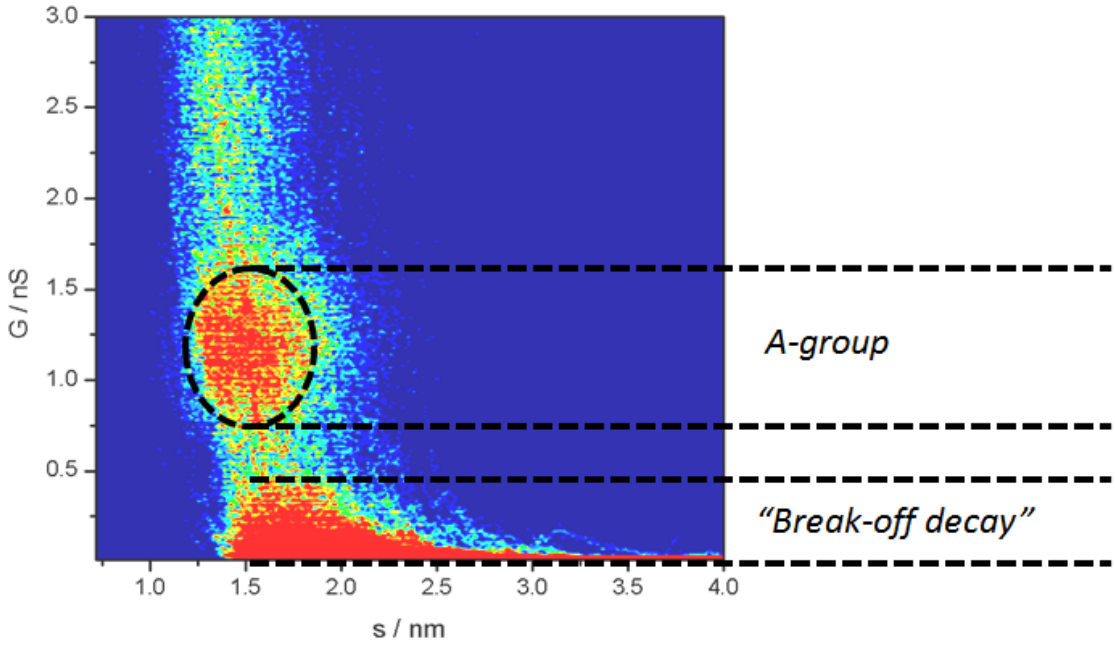

Figure 38: Example of a 2-D histogram for ODT which shows both the break-off distance and the conductance, obtained using the *I*(*s*) method including 538 scans. Both the **A** conductance group and the "break-off tail" have been labelled.

The **A** group in this histogram is clearly visible, and has been labelled by the dashed ellipse. At low current conductance values, another area of high density data points (red) can be observed, which occurs due to the decay of current as the molecular bridge is broken. For ODT, the high density red area which illustrates the **A** group shows both the conductance value of (1.21 ± 0.19) nS and the break-off distance obtained, estimated to be (1.6 ± 0.2) nm, which corresponds to the calculated molecular length of 1.4 nm. The 2-D histograms plotted for the *I*(*s*) measurements of the alkanedithiols are shown in *Figure 39* and clearly show the **A** group in each case. The distance range for each of these histograms corresponds to the expected break-off distances for the lengths of each molecule. The 2-D histogram for NDT also contains the **B** group. However, this is not clear as the number of data points for this conductance group are significantly fewer than for the **A** group, although there are a higher density of data points around the conductance of **B**.

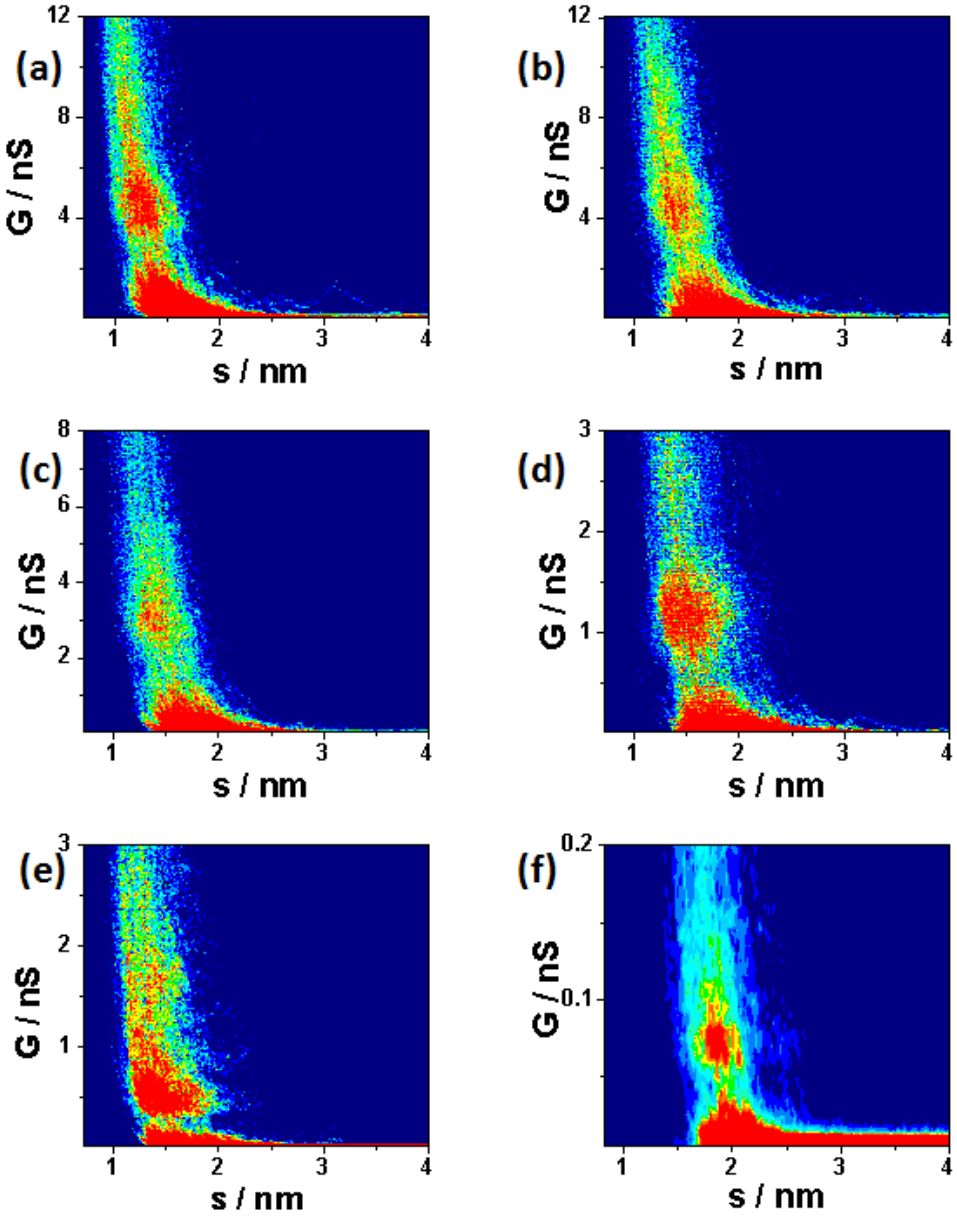

Figure 39: 2-D histogram representations of (a) PrDT, (b) PDT, (c) HDT, (d) ODT, (e) NDT, and (f) UDT, obtained using the *I*(*s*) method. The **A** group and break-off decay regions are clearly visible on each plot. The streaking seen on the 2-D histogram of UDT is due to the large bin sizes required for the very low conductance values.

2-D histograms were also plotted for the data obtained from using the BJ method and the **B** group is clearly visible in each plot. Due to the nature of these measurements however, the break-off distance cannot be quantitatively measured. These plots instead contain a distance scale bar.

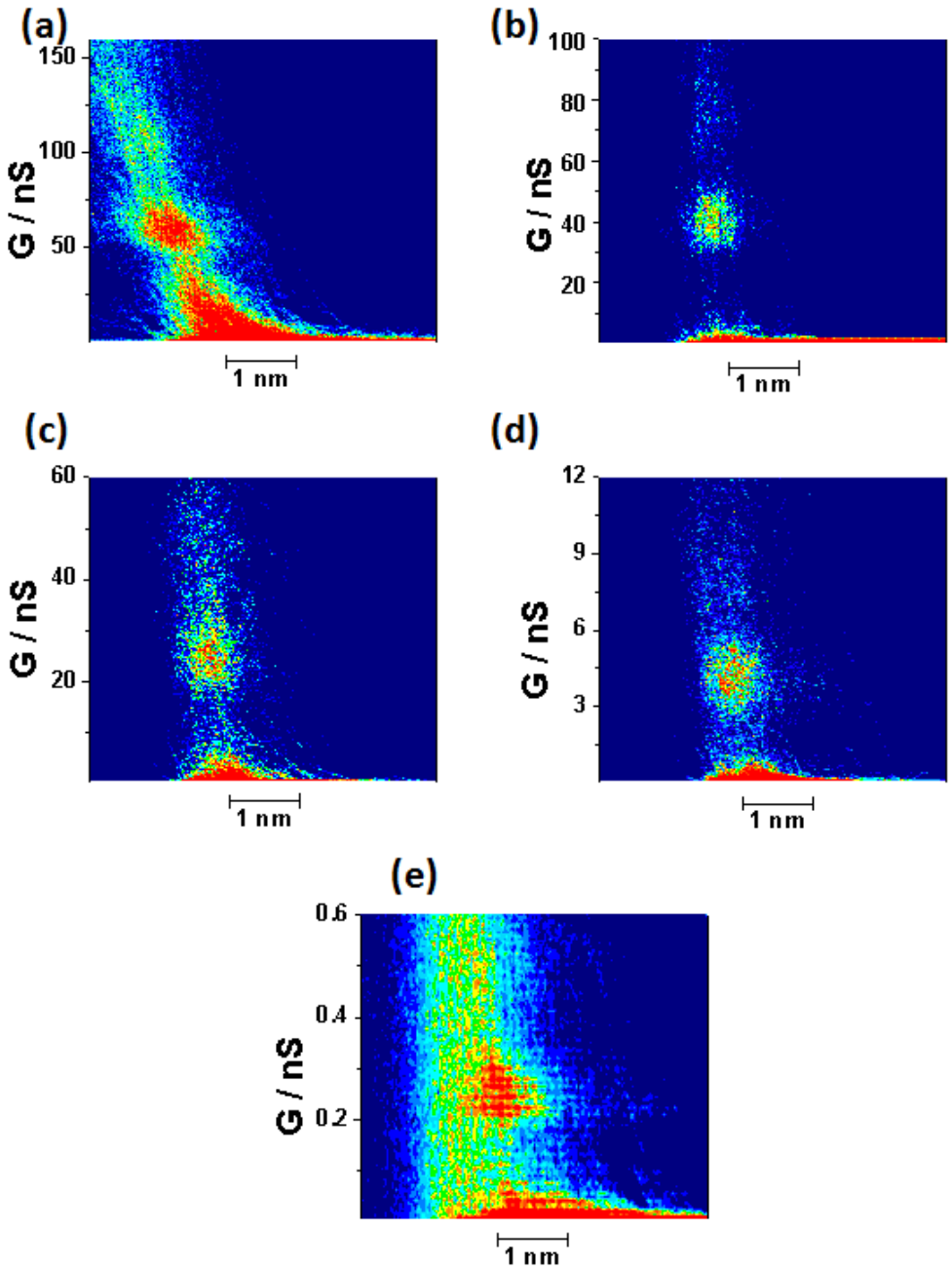

Figure 40: 2-D histograms of (a) PrDT, (b) PDT, (c) HDT, (d) ODT, and (e) UDT, obtained using the STM BJ method. The medium conductance group **B** is clearly visible on all plots. As the total tip-to-substrate distance *s* cannot be quantitatively measured, a distance scale bar is instead given for the *x*-axis showing a distance of 1 nm.

All of the conductance data collected is plotted in *Figure 41*, which shows the logarithm of the conductance versus the number of CH_2 units in the polymethylene chain.

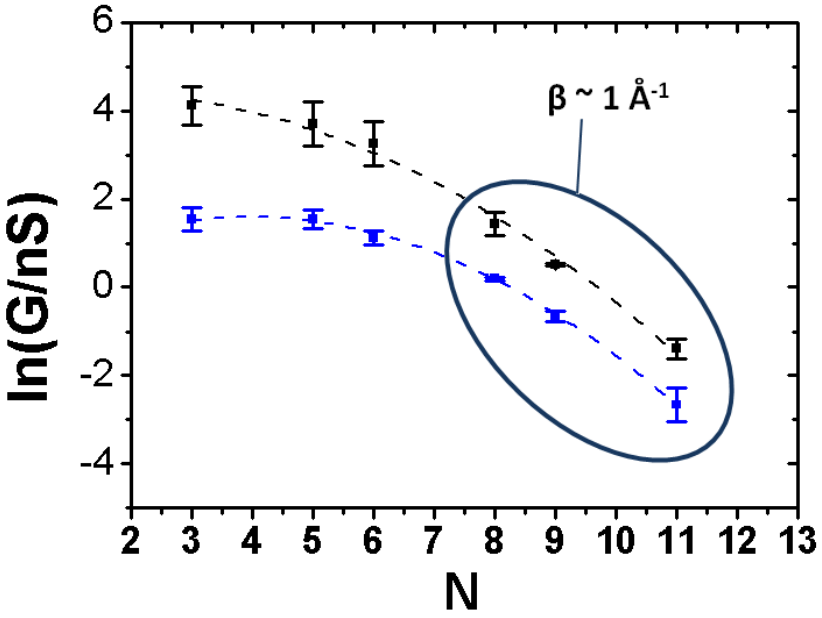

Figure 41: Logarithm of the low conductance group **A** (blue) and medium conductance group **B** (black) as a function of the number of CH_2 units in the polymethylene chain, for alkanedithiols in the ionic liquid BMIOTf; V_{BIAS} = +0.6 V; I_0 = 20 nA. When N > 8, the conductance decays exponentially as a function of length with a decay factor $\beta \approx 1$ Å^{-1}, as shown on the plot in the dark blue ellipse.

For molecules with a chain length greater than 8 CH_2 units, the conductance decays exponentially and a decay factor of $\beta \approx 1$ Å^{-1} is calculated. This value is consistent with the β values found in the literature for longer chain alkanedithiols.[3, 4, 6, 7]

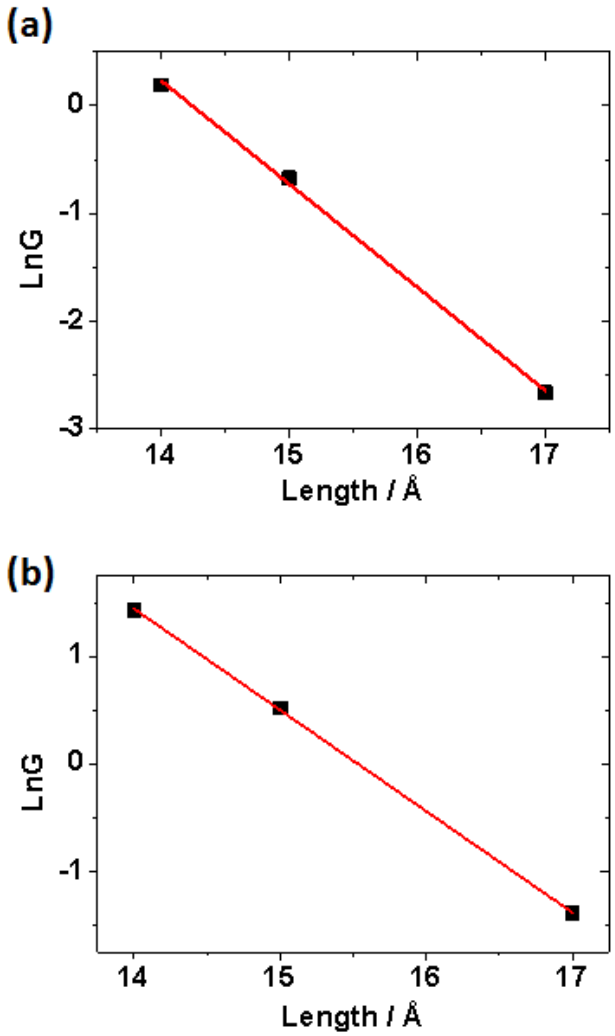

Figure 42: Plots of the logarithm of the conductance G versus the length of the alkanedithiol for both the low conductance group **A** (a) and the medium conductance group **B** (b). The slope of these plots gives the decay factor β which for both conductance groups is approximately 1 $Å^{-1}$.

These measurements drew inspiration from the measurements performed by Haiss *et al.* in 2009.[4] The data from these measurements in BMIOTf was compared to the data obtained by Haiss *et al*. in ambient conditions, in reference 4 in *Figure 43*.

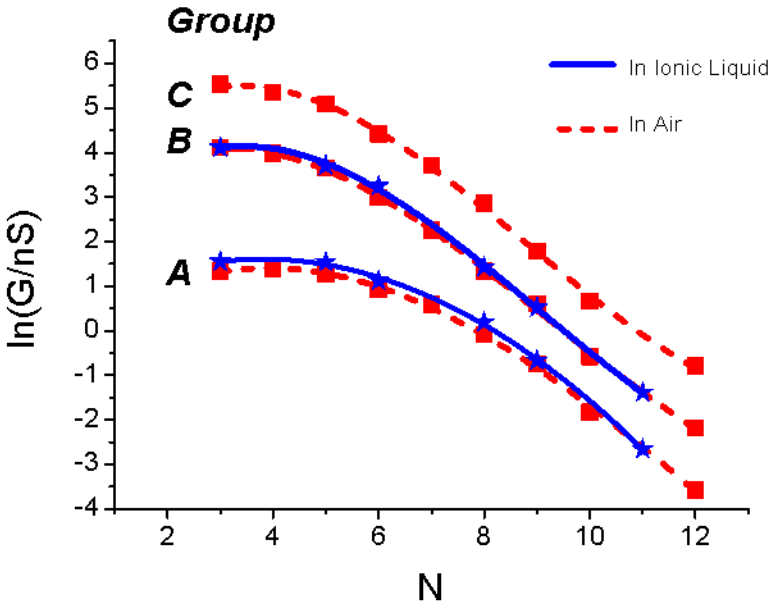

Figure 43: A comparison of the logarithm of the conductance versus the number of CH_2 units in the polymethylene chain of alkanedithiols measured in air (red) and in the RTIL BMIOTf (blue). The data for the measurements recorded in air were taken from reference 4.

As can be seen from *Figure 43*, the data recorded by Haiss *et al*. in ambient conditions[4] and the present measurements in the RTIL BMIOTf[l] for the low conductance group **A** and the medium conductance group **B** practically superimpose. The high conductance group **C** was observed in the measurements taken in ambient conditions by Haiss *et al*. but was however not observed in the present measurements in BMIOTf. The accepted theory explaining the different conductance groups involves the thiol-Au bond having different coordinations. The **C** group has been suggested to occur when the molecule is adsorbed at high coordination sites at either end.[25] It is proposed that the **C** form is either unobtainable, or occurs with relatively low probability in comparison to the lower conductance groups **A** and **B**. The chemistry of the Au(111) surface in RTILs is known to vary from the condition of the surface in ambient conditions. This may in some way hinder the adsorption of the alkanedithiol molecules at higher coordination sites, thus explaining the lack of a **C** conductance group in BMIOTf.

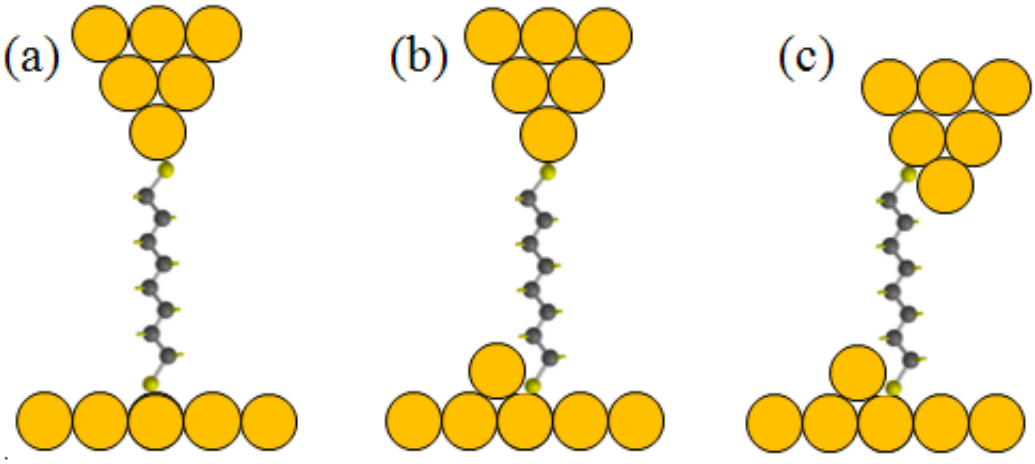

Figure 44: The three different conductance groups **A** (a), **B** (b) and **C** (c). The molecule exhibiting a group **A** conductance is adsorbed on a flat, terraced surface, or connected to a single gold adatom. For a group **B** conductance, one of the terminal groups is adsorbed at a step edge site whereas both the terminal groups are adsorbed at a step edge when the **C** group conductance is observed.

The bias voltage V_{BIAS} dependence of the **A** group was investigated for ODT and is shown in *Figure 45*.

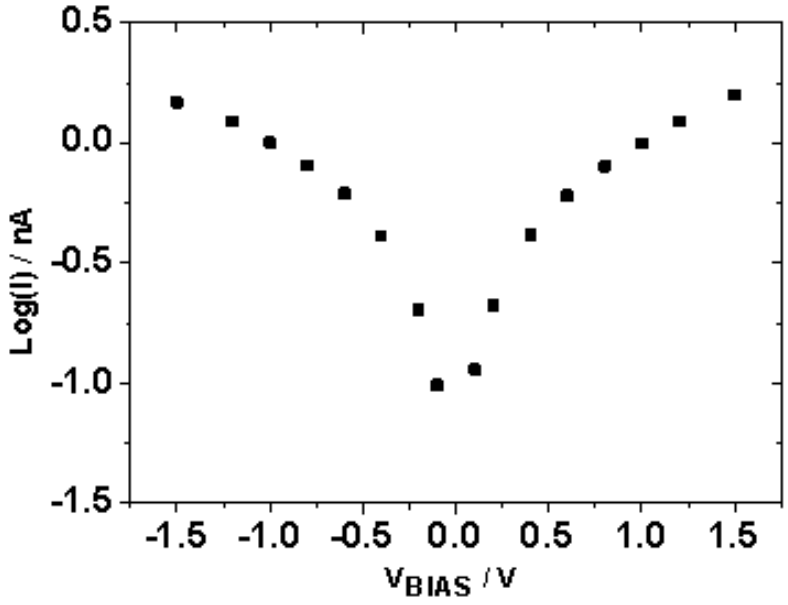

Figure 45: Logarithm of the current flowing through ODT as a function of the bias voltage, for the conductance group **A** measured in the RTIL BMIOTf.

Haiss *et al*. also investigated the bias voltage dependence for alkanedithiols in ambient conditions.[4] When the bias voltage dependence data for ODT collected by Haiss *et al*. for alkanedithiols in ambient conditions and the present data concerning alkanedithiols in the RTIL BMIOTf for the conductance group **A** were overlaid, they were found to be very similar although there are deviations at higher bias voltages. These deviations may occur due to the effect the ionic liquid would have on the Au electrodes at higher bias voltages. Lin *et al*. have described how the Au(111) surface undergoes a degree of restructuring due to the BMI^+ cation adsorbing on the surface.[27] This adsorption of the cationic species causes the metal-metal bonds in the substrate to weaken which causes defects in the electrode.[27] Between -0.9 V and -1.2 V, tiny pits of atomic height formed on the Au surface. When the potential is held between -1.2 V and -2.4 V for an extended period of time, a "worm-like" structure forms on the Au surface.[27] The nature of these measurements means that the bias potential is maintained for a considerable amount of time, which at higher bias potentials would possibly cause the Au electrodes to undergo similar surface restructuring to what Lin *et al*. observed.

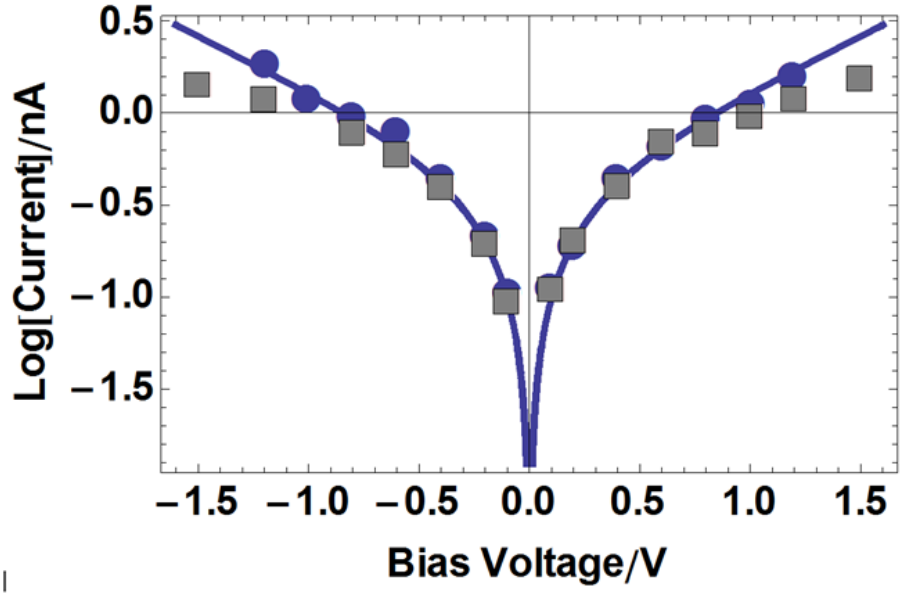

Figure 46: Logarithm of the current flowing through ODT as a function of the bias voltage measured using the *I*(*s*) method for the low conductance group **A**. The data collected by Haiss *et al*. in reference 4 are shown by the blue circles, and the data

collected in the RTIL BMIOTf are shown by the gray squares. The solid blue line is the Simmons model fit.

The Simmons model has been described in detail in an earlier section of this thesis. For ODT, the uncorrected barrier height and barrier width were determined to be ϕ = 2 eV and s = 1.4 nm respectively.[4] When these uncorrected values are used with *equations 1.9-1.11* in the introduction, to take into account the image charge, then the corrected barrier height and barrier width become ϕ_{eff} = 1.36 eV and Δs = 1.26 nm respectively. The value of α, which is a fitting constant, was calculated to be 0.52. Haiss *et al*.[4] suggest that α is related to the effective mass of an electron m_{eff} by the equation:

$$m_e \times \alpha^2 = m_{eff} \qquad \textit{Equation 2.2}$$

Where m_e is the mass of an electron. With α = 0.52, this is very close to the value which was predicted by Tomfohr and Sankey, who computed $m_{eff} = 0.28 m_e$.[4, 28]

For alkanedithiols in both ambient conditions[4] and in the RTIL BMIOTf[1], it can be seen in *Figure 43* that at shorter chain lengths, the conductance displays an "anomalous length dependence", that the conductance is length-independent. The relatively simple Simmons model does not adequately explain the ET through alkanedithiols of such short chain length and a much more robust model of ET is yet to be developed. Haiss *et al*. have suggested that the image potential may have an effect on m_{eff} and this can be modelled by making the m_{eff} an adjustable parameter in the Simmons model, which can then be used to fit both the length dependence and bias dependence.[4] This modification of the Simmons model however still does not fully explain the anomalous length dependence and the deviation in the bias dependence from the Simmons model with a short chain length.[4]

2.5 Conclusions

A room temperature ionic liquid has been used as a medium for recording the single molecule conductance. BMIOTf was used as the medium to measure the conductance of alkanedithiols of various chain lengths. Both conventional histograms and 2-D conductance tip-to-substrate distance histograms have been constructed. The data recorded for the alkanedithiols measured shows that the SMC

for the low conductance group **A** and the medium conductance group **B** are similar in both ambient conditions[4] and in BMIOTf. However, it is noted that no **C** group is observed in the RTIL and this may be due to the RTIL influencing the structure of the gold contacts, which are formed during *I*(*s*) scans. It appears that the formation of **C**- type contacts is suppressed. For both the **A** and **B** groups in BMIOTf, an anomalous length dependence is observed when N<5 and an exponential length dependence is evident when N>8 with a decay factor $\beta \approx 1$ Å^{-1}, as is also the case in ambient conditions. These measurements do indeed show that SMC measurements in an ionic liquid are viable. RTILs offer several advantages in the field of SME including high conductivity, low volatility and a wider potential window, which means that the single molecule conductance can be studied in molecules where the redox potential is outside of the range available to conventional aqueous electrolytes. Another considerable advantage of RTILs as a medium in SME compared to conventional electrolytes, is their wider thermal range; ionic liquids are stable at much more extreme temperatures than alternative electrolytes. This could be of assistance when studying ET through molecular bridges and quantifying thermal activation processes. Thermally-influenced ET has been discussed briefly earlier in this thesis and RTILs could be used to further characterise ET mechanisms such as thermionic emission and hopping. These attributes of RTILs make them an interesting medium to perform SMC measurements in and they are expected to be more widely deployed in the field in the future.

2.6 References

1. N. J. Kay, R. J. Nichols, S. J. Higgins, W. Haiss, G. Sedghi, W. Schwarzacher and B.-W. Mao, Journal of Physical Chemistry C, 2011, 115, 21402-21408.

2. J. C. Cuevas and E. Scheer, Molecular electronics : an introduction to theory and experiment, World Scientific, Singapore ; Hackensack, NJ, 2010.

3. B. Q. Xu and N. J. J. Tao, Science, 2003, 301, 1221-1223.

4. W. Haiss, S. Martin, L. E. Scullion, L. Bouffier, S. J. Higgins and R. J. Nichols, Physical Chemistry Chemical Physics, 2009, 11, 10831-10838.

5. W. Haiss, R. Nichols, H. van Zalinge, S. Higgins, D. Bethell and D. Schiffrin, Physical Chemistry Chemical Physics, 2004, 6, 4330-4337.

6. V. B. Engelkes, J. M. Beebe and C. D. Frisbie, Journal of the American Chemical Society, 2004, 126, 14287-14296.

7. M. Paulsson, C. Krag, T. Frederiksen and M. Brandbyge, Nano Letters, 2009, 9, 117-121.

8. X. D. Cui, A. Primak, X. Zarate, J. Tomfohr, O. F. Sankey, A. L. Moore, T. A. Moore, D. Gust, G. Harris and S. M. Lindsay, Science, 2001, 294, 571-574.

9. X. D. Cui, X. Zarate, J. Tomfohr, O. F. Sankey, A. Primak, A. L. Moore, T. A. Moore, D. Gust, G. Harris and S. M. Lindsay, Nanotechnology, 2002, 13, 5-14.

10. X. D. Cui, A. Primak, X. Zarate, J. Tomfohr, O. F. Sankey, A. L. Moore, T. A. Moore, D. Gust, L. A. Nagahara and S. M. Lindsay, Journal of Physical Chemistry B, 2002, 106, 8609-8614.

11. W. Haiss, H. van Zalinge, D. Bethell, J. Ulstrup, D. Schiffrin and R. Nichols, Faraday Discussions, 2006, 131, 253-264.

12. W. Haiss, T. Albrecht, H. van Zalinge, S. Higgins, D. Bethell, H. Hobenreich, D. Schiffrin, R. Nichols, A. Kuznetsov, J. Zhang, Q. Chi and J. Ulstrup, Journal of Physical Chemistry B, 2007, 111, 6703-6712.

13. X. L. Li, J. He, J. Hihath, B. Q. Xu, S. M. Lindsay and N. J. Tao, Journal of the American Chemical Society, 2006, 128, 2135-2141.

14. L. Aldous, D. S. Silvester, C. Villagran, W. R. Pitner, R. G. Compton, M. C. Lagunas and C. Hardacre, New Journal of Chemistry, 2006, 30, 1576-1583.

15. T. Albrecht, K. Moth-Poulsen, J. B. Christensen, J. Hjelm, T. Bjornholm and J. Ulstrup, Journal of the American Chemical Society, 2006, 128, 6574-6575.

16. Y. C. Fu, H. M. Zhang, Y. Z. Su, D. Y. Wu, Z. X. Xie and B. W. Mao, Zeitschrift Fur Physikalische Chemie-International Journal of Research in Physical Chemistry & Chemical Physics, 2007, 221, 1109-1121.

17. X. B. Ji, D. S. Silvester, L. Aldous, C. Hardacre and R. G. Compton, Journal of Physical Chemistry C, 2007, 111, 9562-9572.

18. L. G. Lin, J. W. Yan, Y. Wang, Y. C. Fu and B. W. Mao, Journal of Experimental Nanoscience, 2006, 1, 269-278.

19. Y. Z. Su, Y. C. Fu, J. W. Yan, Z. B. Chen and B. W. Mao, Angewandte Chemie-International Edition, 2009, 48, 5148-5151.

20. Y. M. Wei, X. S. Zhou, J. G. Wang, J. Tang, B. W. Mao and D. M. Kolb, Small, 2008, 4, 1355-1358.

21. F. Endres and S. Z. El Abedin, Physical Chemistry Chemical Physics, 2006, 8, 2101-2116.

22. G. Sedghi, K. Sawada, L. Esdaile, M. Hoffmann, H. Anderson, D. Bethell, W. Haiss, S. Higgins and R. Nichols, Journal of the American Chemical Sociery, 2008, 130, 8582-8583.

23. W. Haiss, R. J. Nichols, H. van Zalinge, S. J. Higgins, D. Bethell and D. J. Schiffrin, Physical Chemistry Chemical Physics, 2004, 6, 4330-4337.

24. C. Li, I. Pobelov, T. Wandlowski, A. Bagrets, A. Arnold and F. Evers, Journal of the American Chemical Society, 2008, 130, 318-326.

25. W. Haiss, S. Martin, E. Leary, H. van Zalinge, S. Higgins, L. Bouffier and R. Nichols, Journal of Physical Chemistry C, 2009, 113, 5823-5833.

26. N. A. Kautz and S. A. Kandel, Journal of the American Chemical Society, 2008, 130, 6908-6909.

27. L. G. Lin, Y. Wang, J. W. Yan, Y. Z. Yuan, J. Xiang and B. W. Mao, Electrochemistry Communications, 2003, 5, 995-999.

28. J. K. Tomfohr and O. F. Sankey, Physical Review B, 2002, 65, 245105.

Chapter 3

The Electrochemistry Of Pyrrolo-Tetrathiafulvalene

3 The Electrochemistry Of Pyrrolo-Tetrathiafulvalene

3.1 Introduction

Pyrrolo-tetrathiafulvalene (pyrrolo-TTF) is a redox-active molecular wire which exhibits two reversible redox reactions, one of which is in the potential range available in aqueous electrolytes.[1-4]

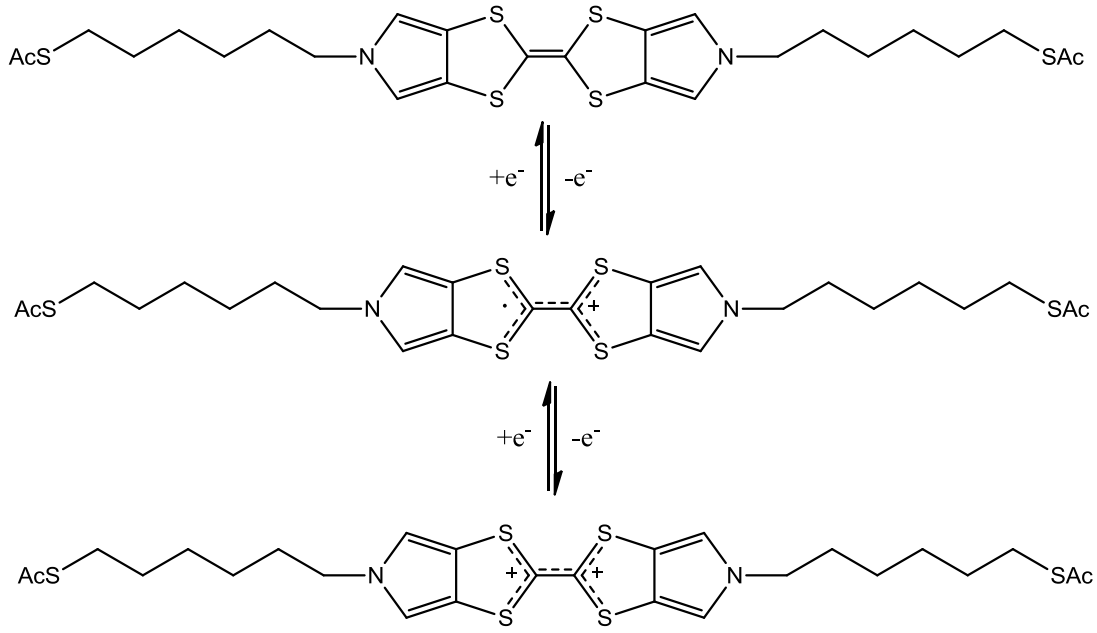

Figure 47: The two stable, fully-reversible redox reactions of pyrrolo-TTF. The first transition, from the neutral pyrrolo-TTF^{0} to the radical cation pyrrolo-$TTF^{\cdot+}$ is visible in aqueous electrolyte, whereas the second transition from the radical cation pyrrolo-$TTF^{\cdot+}$ to the dication pyrrolo-TTF^{2+} is not.

It is the stability of the three redox states which makes pyrrolo-TTF such an attractive system to study. The addition of the $(CH_2)_6SAc$ chains at either end of the pyrrolo-TTF moiety allows the molecule to be tethered between two electrodes. This chapter however concentrates on the electrochemistry of pyrrolo-TTF only.

Leary *et al.* performed cyclic voltammetry on pyrrolo-TTF in an aqueous electrolyte, which clearly showed the first redox transition from pyrrolo-TTF^{0} to pyrrolo-$TTF^{\cdot+}$.[2] The large increase in current at +0.8 V vs. SCE is due to surface oxidation and desorption of pyrrolo-TTF.[2]

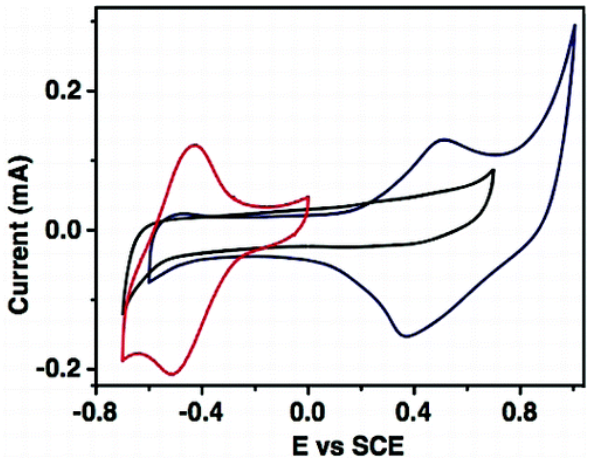

Figure 48: Cyclic voltammograms of pyrrolo-TTF (blue), viologen 6V6 (red) and 6Ph6 (black), where Ph is a phenylene group. The redox peaks are clearly visible for both 6V6 and pyrrolo-TTF. For the latter, the redox peak seen is indicative of the first redox transition from pyrrolo-TTF^{0} to pyrrolo-$TTF^{\cdot+}$.[2] Figure taken from reference 2.

The second redox transition from the radical cation to the dication does not occur in the potential range available to conventional aqueous electrolytes. Therefore, in order to observe the second redox reaction, a different electrolyte must be used with a wider or more positive potential range.

3.2 Aim

The second redox transition from pyrrolo-$TTF^{\cdot+}$ to pyrrolo-TTF^{2+} cannot be observed in the aqueous electrolyte used by Leary *et al*. The aim of this study is to first reproduce the voltammetry of pyrrolo-TTF obtained by Leary *et al*., and then to use an electrolyte with a wider potential window to observe the second redox reaction. This study acts as a preliminary investigation with the wider aim of performing conductance measurements on pyrrolo-TTF using electrochemical in-situ STM, specifically focussing on the second redox transition.

3.3 Experimental Methods

All experiments were performed on Ecochemie Autolab potentiostats, either the PGSTAT 20 or PGSTAT 30 model and the corresponding Autolab GPES software. A three-electrode set-up was utilised and unless otherwise specified, used a Au(111)

working electrode (WE), Pt mesh counter electrode (CE) and a saturated calomel (SCE) reference electrode (RE) in a glass cell. The glass cell was cleaned in a 1:1 mixture of H_2SO_4 and HNO_3 prior to use and rinsed several times in MilliQ® water. The CE and WE were flame annealed prior to use. All aqueous electrolytes were made using MilliQ® water. The electrolyte was bubbled with N_2 gas for approximately 20 minutes prior to use, to remove any O_2 present in the solution which may be reduced at the WE. A range of scan rates were used, which are stated in the results and discussion section. To convert the potential scale to Fc/Fc^+, ferrocene was added to the BMIOTf solutions after the cyclic voltammetry was recorded. This was then repeated at the same scan rates. $E_{1/2}$ was measured and this was set as zero on the potential scale.

3.4 Results And Discussion

3.4.1 Confirmation Of The Cyclic Voltammetry Of Leary *et al.*

Cyclic voltammetry was used to observe the first redox transition of pyrrolo-TTF^0 to pyrrolo-$TTF^{\cdot+}$. The experimental procedure used was identical to that of Leary *et al*.[2] A 10 mM Na_2HPO_4/NaH_2PO_4 buffer solution was used as the electrolyte, which had a pH of 6.9. The Au(111) WE was immersed in a 0.1 mM pyrrolo-TTF solution in dichloromethane (DCM), which had been distilled over CaH_2, for approximately 24 hours, to form a stable monolayer of the pyrrolo-TTF on the WE. This was then rinsed with the distilled DCM before being inserted into the electrochemical cell.

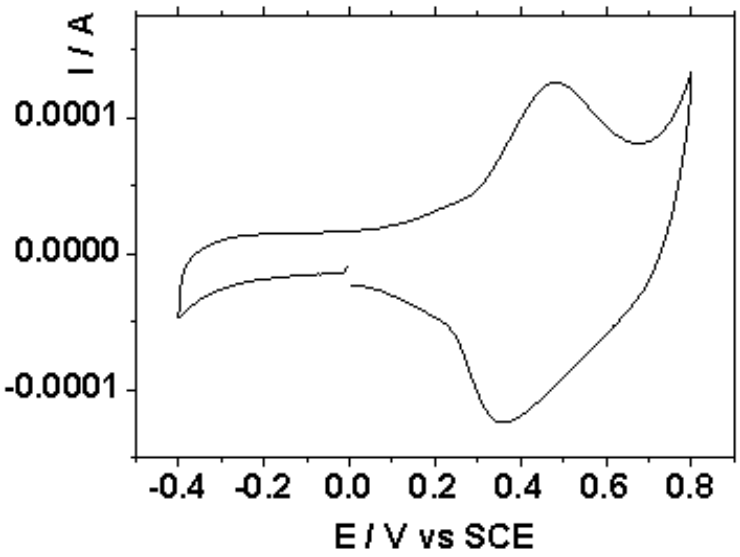

Figure 49: Cyclic voltammogram of a pyrrolo-TTF monolayer on Au(111), in a 10 mM Na_2HPO_4/NaH_2PO_4 electrolyte pH = 6.9 with a scan rate of 1 Vs^{-1}.

Over time, difficulties were encountered observing the redox peaks seen in the voltammogram in *Figure 49*. The peaks shifted to a less positive potential and became significantly less prominent. The oxidative desorption of the pyrrolo-TTF also shifted to a less positive potential, so a narrower potential range was available. To demonstrate the difficulty in obtaining reproducible and good quality cyclic voltammetry of adsorbed pyrrolo-TTF, this early data recorded in October 2008 is compared with voltammetry recorded in October 2009 using the same procedure. Many more trials have been completed, but these two show the range of responses that have been achieved for this system.

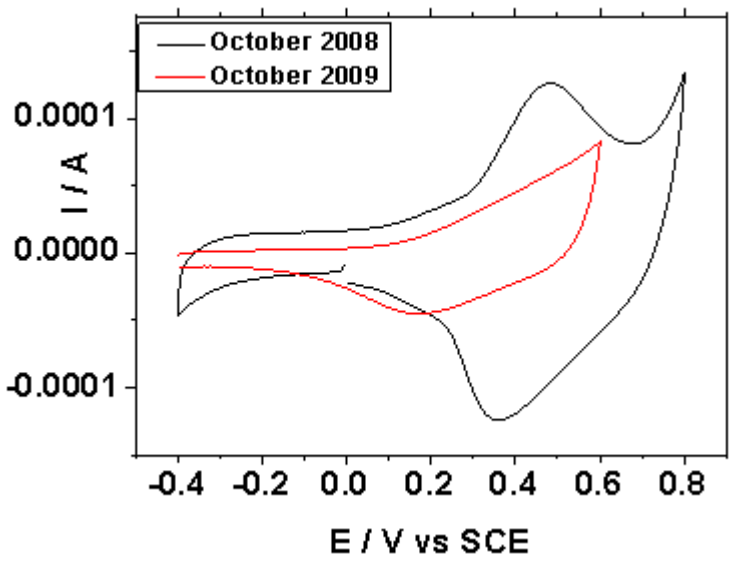

Figure 50: Cyclic voltammogram of a pyrrolo-TTF monolayer on Au(111) with a scan rate of 1 Vs^{-1}. The black voltammogram is also shown in *Figure 49* and was recorded in October 2008. The red scan was recorded in October 2009 using the same procedure. However, no redox peaks are present.

Several procedures have been attempted to obtain reproducible, good quality voltammetry of pyrrolo-TTF, with little success. These attempts include varying the electrolyte, the immersion solution and conditions, and using different electrodes and are shown in *Table 6*.

Table 6: Examples of some of the attempts to obtain good quality, reproducible voltammetry of pyrrolo-TTF. The voltammetry of some of these attempts can be found in the Appendix of this thesis.

Conditions	Date	Quality Of CV
Re-examination of Leary *et al*.	Oct-08	Good, clear, well-defined peaks
$HClO_4$ electrolyte	Oct-08 to Jan-09	Peaks observed but ill-defined
H_2SO_4 electrolyte	Jan-10	Peaks observed but ill-defined
Re-examination of Leary *et al*.	Oct-09 to Feb-10	Peaks observed but broad and ill-defined
72 hour immersion	Oct-09	No peaks observed
72 hours immersion light exposure	Nov-09	No peaks observed
60 minute immersion at 30°C	Oct-09	Peaks observed but ill-defined
90 minute immersion at 30°C	Oct-09	Peaks observed but ill-defined
120 minute immersion at 40°C	Oct-09	Peaks observed but ill-defined
24 hour immersion 1 mM concentration	Oct-09	No peaks observed
24 hour immersion 0.1 mM in THF	Feb-10	No peaks observed

One possible explanation as to why the voltammetry of pyrrolo-TTF is of so poor quality is that the molecule may have suffered some level of degredation over time. This was investigated using mass spectrometry and the resulting mass spectrum is shown in *Figure 51*.

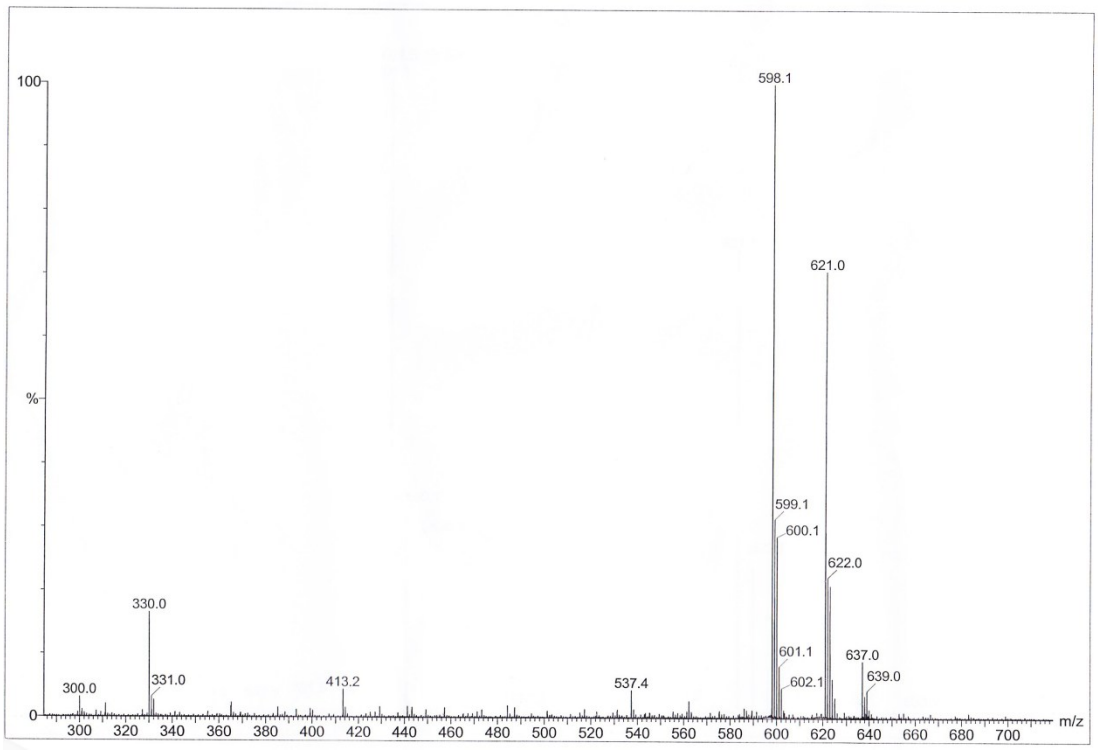

Figure 51: Mass spectrum of pyrrolo-TTF. The peaks at 598.1 and 599.1 show the molar mass of pyrrolo-TTF, confirming that the molecule has not degraded. Acknowledgements to Jean Ellis and Moya McCarron of the Mass Spectrometry Service in the Department Of Chemistry,University Of Liverpool.

As can be seen in the mass spectrum, the pyrrolo-TTF molecule is intact, as shown by the peaks at 598.1 and 599.1. It was then suggested that the quality of the voltammetry of pyrrolo-TTF was so poor as a stable monolayer was not present on the electrode surface. Polarisation modulation infrared reflection absorption spectroscopy (PM-IRRAS) is a spectroscopic technique which can be used to characterise a species on a surface. Its increased sensitivity means that it can be used to observe the IR vibrational spectrum of a molecular monolayer on a metal substrate. A commercial gold-on-glass (Arrandee®) slide was flame annealed and immersed in a 0.1 mM pyrrolo-TTF in THF solution for approximately 24 hours. PM-IRRAS was used to confirm that pyrrolo-TTF was forming a stable monolayer on the Au(111) substrate.

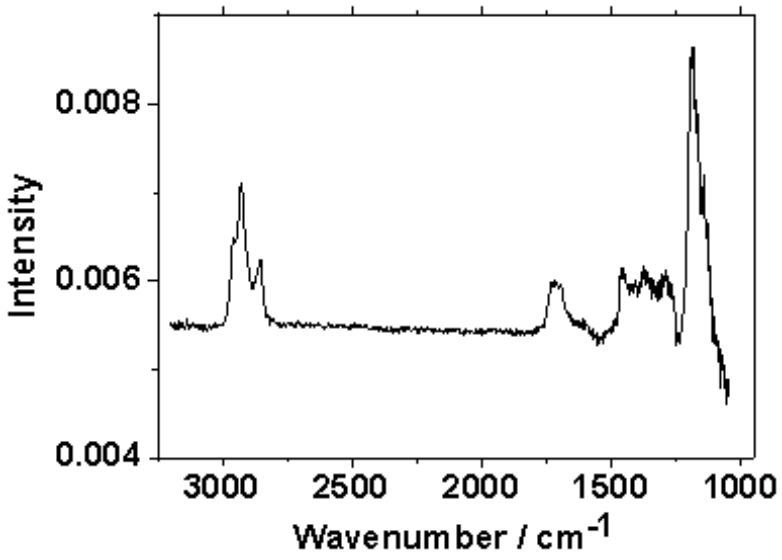

***Figure 52*: IR spectrum of a pyrrolo-TTF monolayer on a gold-on-glass slide recorded using PM-IRRAS. The substrate had been immersed for approximately 24 hours before the spectrum was obtained.**

Strong evidence of a pyrrolo-TTF monolayer on the surface is clear on the PM-IRRAS spectrum. Peaks at 2929 cm^{-1} and 2854 cm^{-1} correspond to the asymmetric and symmetric stretches respectively of CH_2. The broad peak at approximately 1722 cm^{-1} is the C=O stretch and the peaks between 1475 cm^{-1} and 1250 cm^{-1} correspond with the skeletal vibrations of the pyrrole rings. The large peak at 1187 cm^{-1} is the C-N stretch. This spectrum strongly suggests that pyrrolo-TTF does indeed form a stable monolayer on a gold substrate.

3.4.2 Pyrrolo-TTF In A Room Temperature Ionic Liquid

It was observed that the immersion solutions containing pyrrolo-TTF turned from a yellow colour to a green colour over time. This suggests that the pyrrolo-TTF undergoes a degree of protonation over time. This most likely hinders the redox reaction, which explains why no redox activity is clear in the more recent voltammograms but strong evidence shows that a monolayer is still formed on the gold substrate surface. Use of a basic electrolyte may possibly hinder the protonation of pyrrolo-TTF, but the surface oxidation of the electrode would be shifted in a negative direction, which would most likely obscure the redox peaks in the voltammetry.

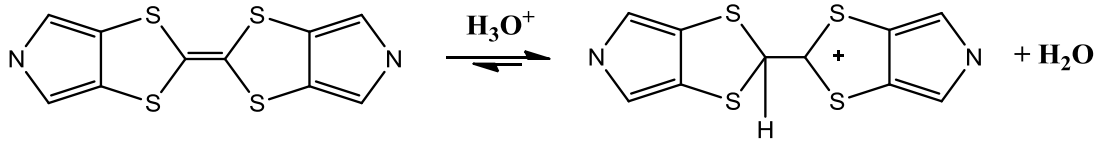

Figure 53: Reaction scheme showing the protonation of the pyrrolo-TTF moiety in the presence of water.[5, 6]

A way of preventing the protonation of pyrrolo-TTF would be using a non-aqueous solvent in the immersion solution. A room temperature ionic liquid would be the obvious choice as the solvent as they must be kept dry, which would of course prevent protonation. As described in an earlier section of this thesis, ionic liquids are also advantageous in electrochemistry due to their wide potential window, high conductivity and low volatility.[7-14] Pyrrolo-TTF undergoes two distinct redox transitions, shown in *Figure 47*, first from the neutral pyrrolo-TTF^0 to the radical cation pyrrolo-$TTF^{\cdot+}$ and then from the radical cation pyrrolo-$TTF^{\cdot+}$ to the dication pyrrolo-TTF^{2+}. Only the first transition is observable in aqueous electrolyte, shown by Leary *et al*.[2] and re-examined in this project in *Figure 49*. Using a RTIL as the electrolyte in cyclic voltammetry would lead to a wider potential window which may allow the second redox transition to be observed. The RTIL 1-butyl-3-methylimidazolium trifluoromethanesulfonate (BMIOTf) was used as the immersion solution solvent and also as the electrolyte. This RTIL was also used as a medium in SMC measurements described in Chapter 2 of this thesis.[14] BMIOTf was dried according to the method described in Chapter 2; it was heated to 110-120°C with dry N_2 flow for a minimum of 1 hour immediately prior to use and was treated with 3 Å molecular sieves. The airtight EC cell was assembled in a glove box containing an inert N_2 atmosphere. The WE was a Au(111) bead, the CE was Pt wire and a quasi-RE was used of Pt wire. This results in an unstable reference potential, so a reference of a known potential must be used. For these experiments, the ferrocene redox couple was used as the reference.

Solution voltammetry of pyrrolo-TTF was recorded and the BMIOTf electrolyte contained 1 mM pyrrolo-TTF. Once voltammograms were recorded at various scan rates, 1 mM ferrocene was added to the electrolyte and the experiment repeated. The potential scale was then calibrated to the ferrocene redox couple Fc/Fc^+.

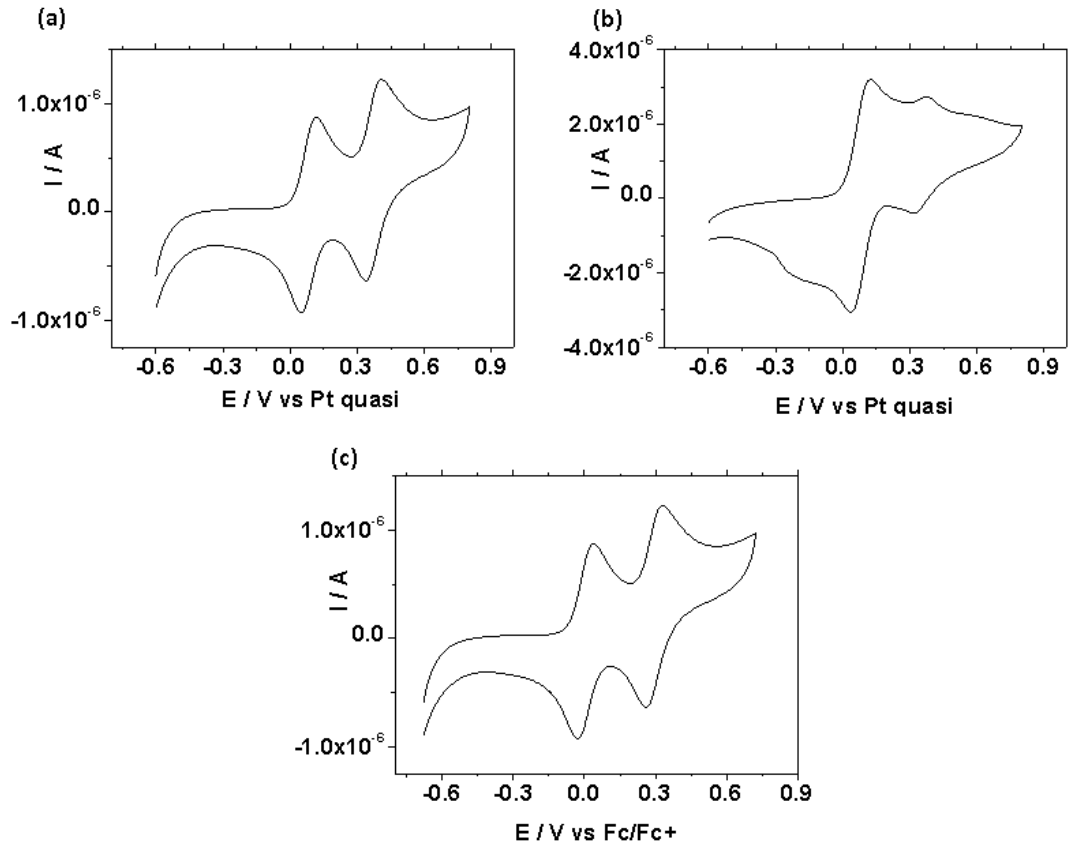

Figure 54: Cyclic voltammograms of (a) 1 mM pyrrolo-TTF in BMIOTf, (b) 1 mM ferrocene and pyrrolo-TTF in BMIOTf and (c) 1 mM pyrrolo-TTF in BMIOTf shown in (a) but the potential scale has been calibrated to the Fc/Fc^+ redox couple. The scan rate employed for these voltammograms is 50 mVs^{-1}.

As can be seen in *Figure 54*, two redox transitions are visible, which are reminiscent of the redox transitions observed for the parent monopyrrolo-TTF by Jeppesen and Becher, seen in *Figure 55*.[3] The voltammogram for compound A is shifted in the positive direction compared to the voltammogram for compound B due to the electron-withdrawing effect of the tosylate group.[3]

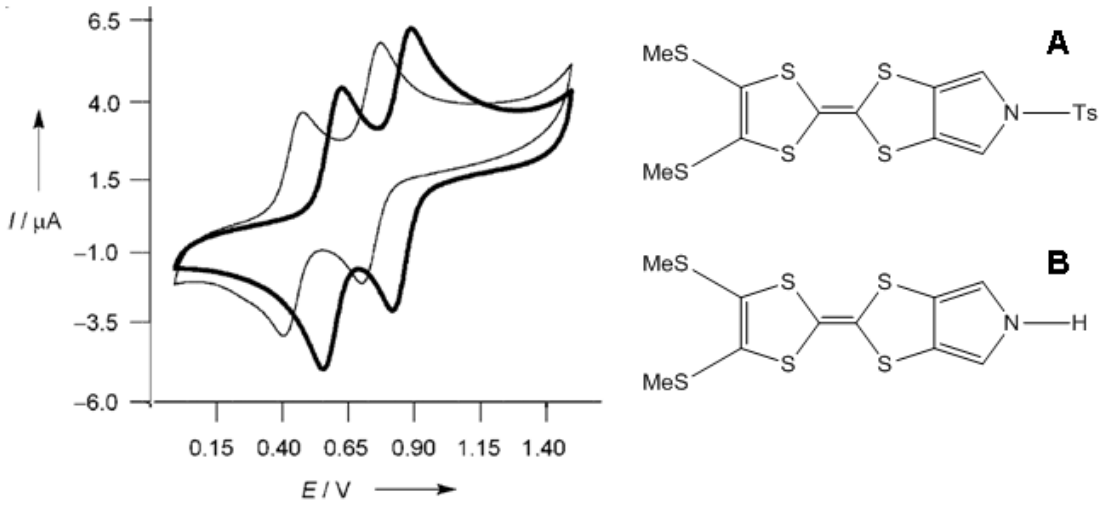

Figure 55: Cyclic voltammograms of the N-tosylated monopyrrolo-TTF A (bold trace) and monopyrrolo-TTF B (light trace) in acetonitrile. The working and counter electrodes were Pt and the potential scale was calibrated to the Ag/AgCl reference.[3] Figure adapted from reference 3.

Table 7: The difference between the anodic and cathodic peak potentials ΔE_p, and the redox potential $E_{1/2}$, given as the midpoint of the anodic and cathodic peak; given for a 1 mM pyrrolo-TTF in N_2 dried BMIOTf solution and with ferrocene added. The average ferrocene $E_{1/2}$ value is used to calibrate the potential scale.

Scan Rate	1st Redox Pyrrolo-TTF V vs Pt quasi		2nd Redox Pyrrolo-TTF V vs Pt quasi		Ferrocene V vs Pt quasi	
	ΔE_p/V	$E_{1/2}$/V	ΔE_p/V	$E_{1/2}$/V	ΔE_p/V	$E_{1/2}$/V
20 mVs^{-1}	0.059	0.081	0.056	0.374	0.077	0.078
50 mVs^{-1}	0.057	0.082	0.056	0.374	0.089	0.082
100 mVs^{-1}	0.071	0.083	0.066	0.373	0.087	0.083
200 mVs^{-1}	0.057	0.082	0.064	0.382	0.075	0.077
500 mVs^{-1}	0.061	0.084	0.06	0.39	0.087	0.077
1 Vs^{-1}	0.069	0.084	0.063	0.394	0.103	0.077
Average	0.062	0.082	0.061	0.381	0.086	0.0785

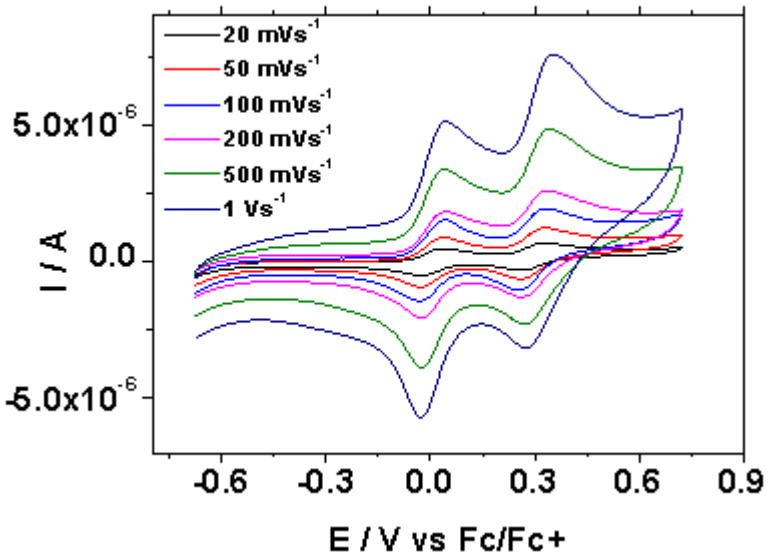

Figure 56: Cyclic voltammogram of a 1 mM solution of pyrrolo-TTF in N_2 BMIOTf at different scan rates.

The next stage was to perform voltammetry on a pyrrolo-TTF monolayer in the RTIL. The Au(111) WE was immersed in the 1 mM pyrrolo-TTF in BMIOTf solution for approximately 24 hours. This was rinsed with BMIOTf before being inserted into the EC cell, containing BMIOTF electrolyte. Similarly to the previous experiment, 1 mM of ferrocene was added to the BMIOTf electrolyte after the first set of measurements were taken, in order to calibrate the potential scale to the Fc/Fc^+ redox couple.

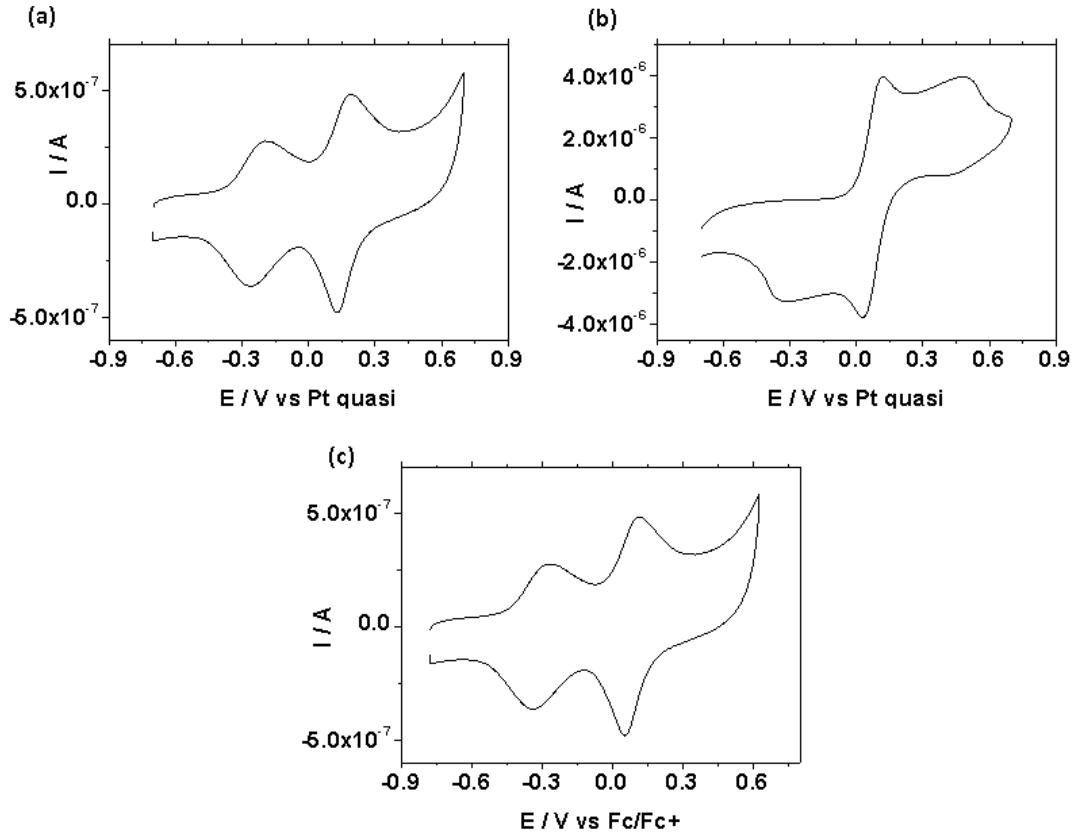

Figure 57: Cyclic voltammograms of (a) pyrrolo-TTF monolayer on Au(111) in BMIOTf, (b) 1 mM ferrocene in BMIOTf with the pyrrolo-TTF monolayer on Au(111) and (c) pyrrolo-TTF monolayer on Au(111) in BMIOTf shown in (a) but the potential scale has been calibrated to the Fc/Fc^{+} redox couple. The scan rate employed for these voltammograms is 50 mVs^{-1}.

The cyclic voltammetry in *Figure 57* shows the two redox transitions of a pyrrolo-TTF monolayer on a Au(111) substrate in a BMIOTf electrolyte.

Table 8: The difference between the anodic and cathodic peak potentials ΔE_p, and the redox potential $E_{1/2}$, given as the midpoint of the anodic and cathodic peak; given for a pyrrolo-TTF monolayer on Au(111) in N_2 dried BMIOTf solution and with ferrocene added. The average ferrocene $E_{1/2}$ value is used to calibrate the potential scale.

Scan Rate	1st Redox Pyrrolo-TTF V vs Pt quasi		2nd Redox Pyrrolo-TTF V vs Pt quasi		Ferrocene V vs Pt quasi	
	ΔE_p/V	$E_{1/2}$/V	ΔE_p/V	$E_{1/2}$/V	ΔE_p/V	$E_{1/2}$/V
20 mVs^{-1}	0.058	-0.245	0.049	0.16	0.09	0.077
50 mVs^{-1}	0.065	-0.235	0.056	0.16	0.086	0.074
100 mVs^{-1}	0.054	-0.24	0.059	0.159	0.08	0.077
200 mVs^{-1}	0.103	-0.208	0.06	0.152	0.096	0.076
500 mVs^{-1}	0.097	-0.194	0.063	0.148	0.118	0.075
1 Vs^{-1}	0.101	-0.196	0.072	0.148	0.134	0.078
Average	0.080	-0.220	0.060	0.154	0.101	0.0762

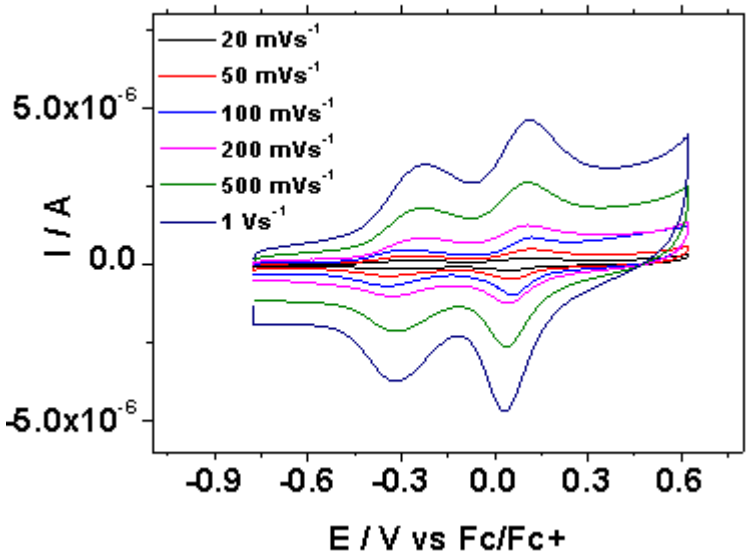

Figure 58: Cyclic voltammogram of a pyrrolo-TTF monolayer on Au(111) in N_2 BMIOTf at different scan rates.

BMIOTf is known to be a hydrophobic RTIL[15], so very low water content is more likely to be achieved than with hydrophilic RTILs. It is usual to vacuum dry the RTIL prior to use, in order to ensure that water is eliminated. To satisfy this, BMIOTf was vacuum-dried for approximately 18 hours at 120°C[16] and treated with

3 Å molecular sieves. A 1 mM solution of pyrrolo-TTF in BMIOTf solution was prepared and the voltammetry is shown in *Figure 59* below.

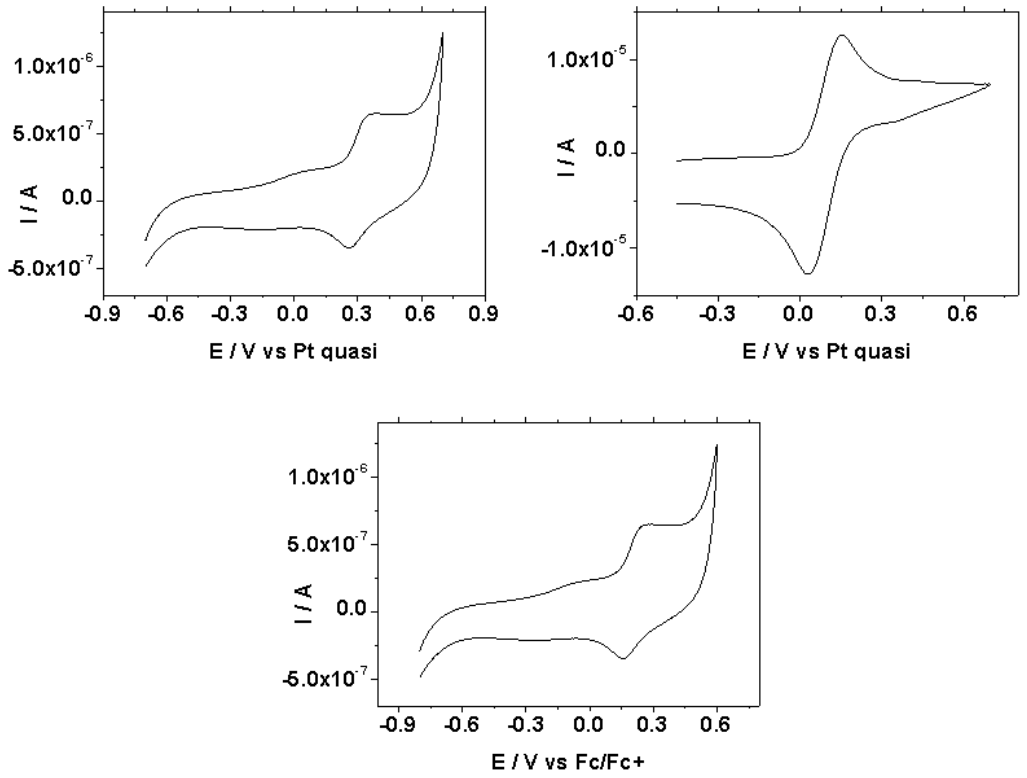

Figure 59: Cyclic voltammograms of (a) a 1 mM solution of pyrrolo-TTF in vacuum dried BMIOTf, (b) 10 mM ferrocene in BMIOTf with 1 mM pyrrolo-TTF and (c) 1 mM solution of pyrrolo-TTF in BMIOTf shown in (a) but the potential scale has been calibrated to the Fc/Fc^+ redox couple. The scan rate employed for these voltammograms is 50 mVs^{-1}.

The redox peaks for a 1 mM solution of pyrrolo-TTF in vacuum dried BMIOTf are not to the same high quality as for the N_2 dried BMIOTf. The peak for the 1st redox transition is barely visible and the 2nd redox peak is of poor quality compared to the voltammetry obtained in the N_2 dried BMIOTf.

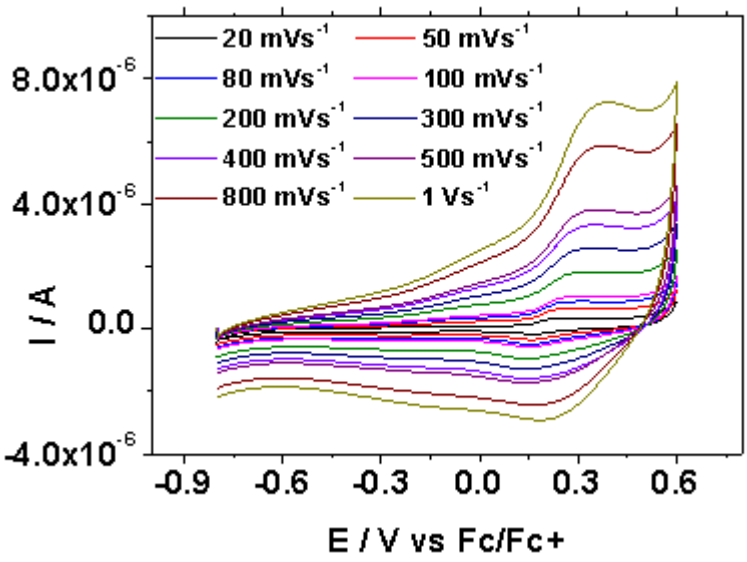

Figure 60: Cyclic voltammogram of a 1 mM solution of pyrrolo-TTF in vacuum dried BMIOTf at different scan rates.

It was decided to increase the concentration of the pyrrolo-TTF to 10 mM in order to improve the resolution of the redox peaks.

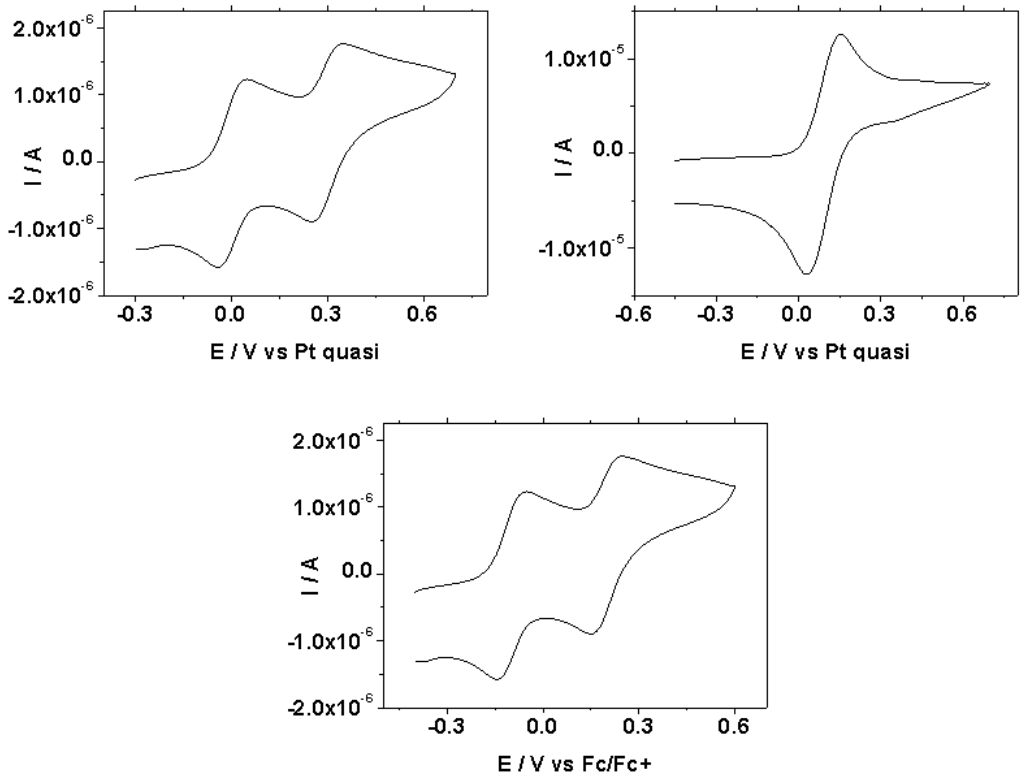

Figure 61: Cyclic voltammograms of (a) a 10 mM solution of pyrrolo-TTF in vacuum dried BMIOTf, (b) 10 mM ferrocene in BMIOTf with 1 mM pyrrolo-TTF

and (c) 10 mM solution of pyrrolo-TTF in BMIOTf shown in (a) but the potential scale has been calibrated to the Fc/Fc^+ redox couple. The scan rate employed for these voltammograms is 50 mVs^{-1}.

As can be seen in *Figure 61*, increasing the concentration of pyrrolo-TTF to 10 mM vastly improved the quality of the voltammetry obtained. The two redox peaks are clear and well defined.

Table 9: The difference between the anodic and cathodic peak potentials ΔE_p, and the redox potential $E_{1/2}$, given as the midpoint of the anodic and cathodic peak; given for a 10 mM pyrrolo-TTF in vacuum dried BMIOTf solution and with ferrocene added. The average ferrocene $E_{1/2}$ value is used to calibrate the potential scale.

Scan Rate	1st Redox Pyrrolo-TTF V vs Pt quasi		2nd Redox Pyrrolo-TTF V vs Pt quasi		Ferrocene V vs Pt quasi	
	ΔE_p/V	$E_{½}$/V	ΔE_p/V	$E_{½}$/V	ΔE_p/V	$E_{½}$/V
20 mVs^{-1}	0.001	0.037	0.092	0.308	0.099	0.095
50 mVs^{-1}	0.088	0.008	0.098	0.296	0.116	0.092
80 mVs^{-1}	0.088	0.008	0.093	0.294	0.131	0.096
100 mVs^{-1}	0.088	0.008	0.098	0.296	0.134	0.097
200 mVs^{-1}	0.092	0.01	0.107	0.301	0.16	0.101
300 mVs^{-1}	0.097	0.008	0.107	0.306	0.177	0.102
400 mVs^{-1}	0.092	0.01	0.093	0.318	0.205	0.103
500 mVs^{-1}	0.102	0.01	0.103	0.323	0.198	0.105
800 mVs^{-1}	0.107	0.013	0.112	0.332	0.225	0.112
1 Vs^{-1}	0.107	0.013	0.122	0.332	0.235	0.112
Average	0.086	0.012	0.103	0.31	0.168	0.101

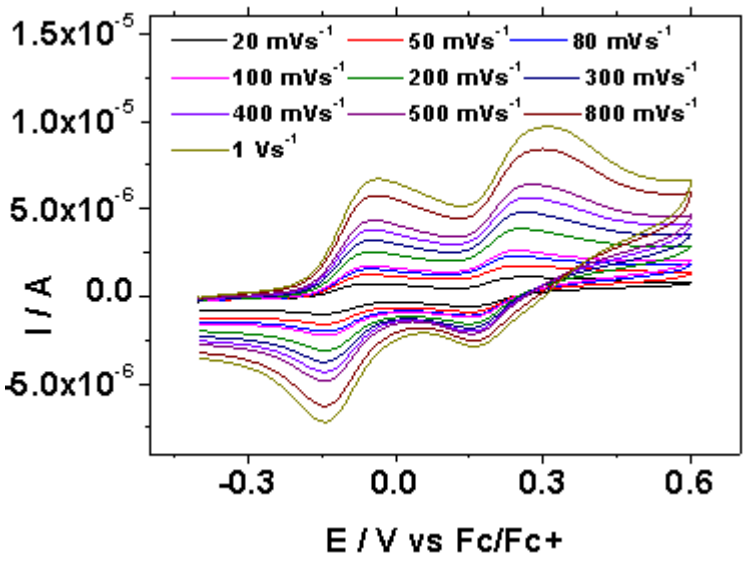

Figure 62: Cyclic voltammogram of a 10 mM solution of pyrrolo-TTF in vacuum dried BMIOTf at different scan rates.

A monolayer of pyrrolo-TTF on the gold sample was then assembled on a Au(111) electrode and the voltammetry of this was investigated in the vacuum dried BMIOTf, as seen in *Figure 63*.

The voltammetry of a pyrrolo-TTF monolayer in the vacuum dried BMIOTF does show both redox peaks. However, they are of much poorer quality than for the N_2 dried BMIOTf. The most likely explanation for this, is that the BMIOTf which was N_2 dried was of a different batch to the vacuum dried BMIOTf. The batch which was N_2 dried was yellow whereas the vacuum dried batch was more orange in colour.

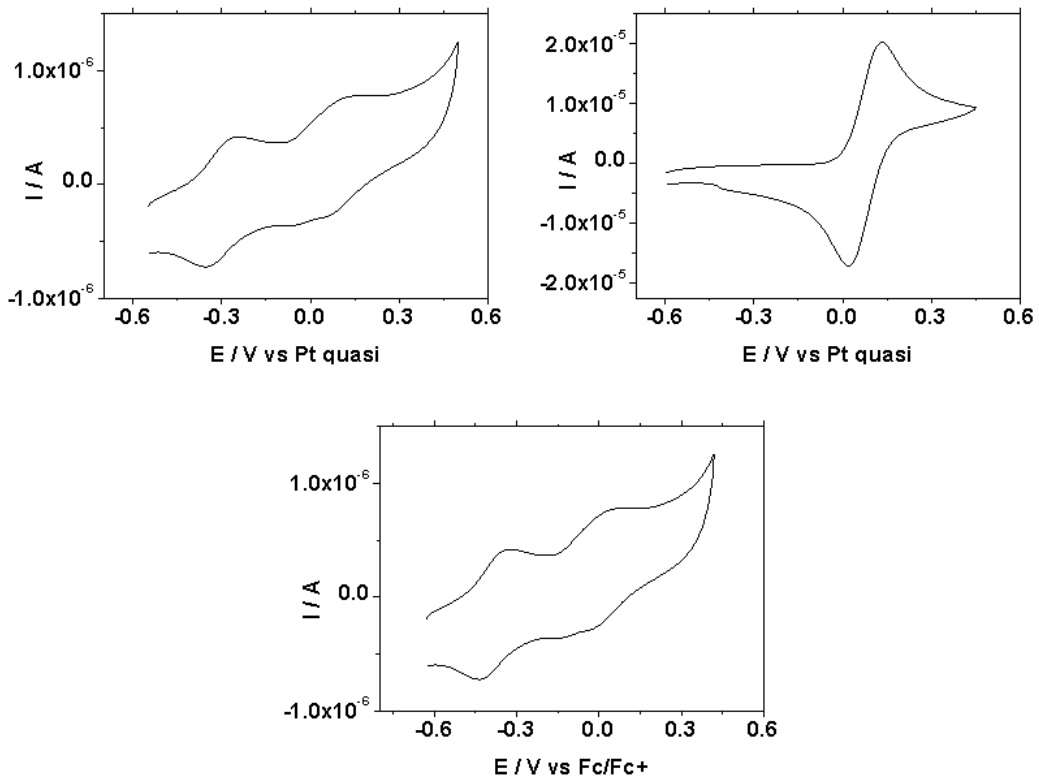

Figure 63: Cyclic voltammograms of (a) pyrrolo-TTF monolayer on Au(111) in vacuum dried BMIOTf, (b) 10 mM ferrocene in BMIOTf with the pyrrolo-TTF monolayer on Au(111) and (c) pyrrolo-TTF monolayer on Au(111) in BMIOTf shown in (a) but the potential scale has been calibrated to the Fc/Fc^{+} redox couple. The scan rate employed for these voltammograms is 50 mVs^{-1}.

This is probably due to a different quantity or ratio of impurities in the two different batches. Assuming the orange batch of BMIOTf was the more contaminated batch, this would be a probable reason for a more concentrated solution of pyrrolo-TTF showing more resolved peaks, and would also explain the poorer quality of voltammetry. This issue could be resolved by synthesising BMIOTf instead of purchasing it. However, due to time restraints, this was not an option in this project.

Table 10: The difference between the anodic and cathodic peak potentials ΔE_p, and the redox potential $E_{1/2}$, given as the midpoint of the anodic and cathodic peak; given for a pyrrolo-TTF monolayer on Au(111) in vacuum dried BMIOTf solution and with ferrocene added. The average ferrocene $E_{1/2}$ value is used to calibrate the potential scale.

Scan Rate	1st Redox Pyrrolo-TTF V vs Pt quasi		2nd Redox Pyrrolo-TTF V vs Pt quasi		Ferrocene V vs Pt quasi	
	ΔE_p/V	$E_{½}$/V	ΔE_p/V	$E_{½}$/V	ΔE_p/V	$E_{½}$/V
20 mVs^{-1}	0.075	-0.295	0.115	0.017	0.088	0.065
50 mVs^{-1}	0.134	-0.272	0.225	0.063	0.11	0.075
80 mVs^{-1}	0.156	-0.262	0.095	0.129	0.114	0.079
100 mVs^{-1}	0.318	-0.176	0.1	0.126	0.124	0.079
200 mVs^{-1}	0.164	-0.237	0.13	0.12	0.138	0.082
300 mVs^{-1}	0.174	-0.222	0.114	0.118	0.152	0.084
400 mVs^{-1}	0.174	-0.222	0.109	0.116	0.157	0.087
500 mVs^{-1}	0.159	-0.22	0.109	0.121	0.162	0.084
800 mVs^{-1}	0.159	-0.22	0.099	0.116	0.178	0.087
1 Vs^{-1}	0.149	-0.22	0.064	0.128	0.183	0.09
Average	0.151	-0.234	0.116	0.105	0.141	0.081

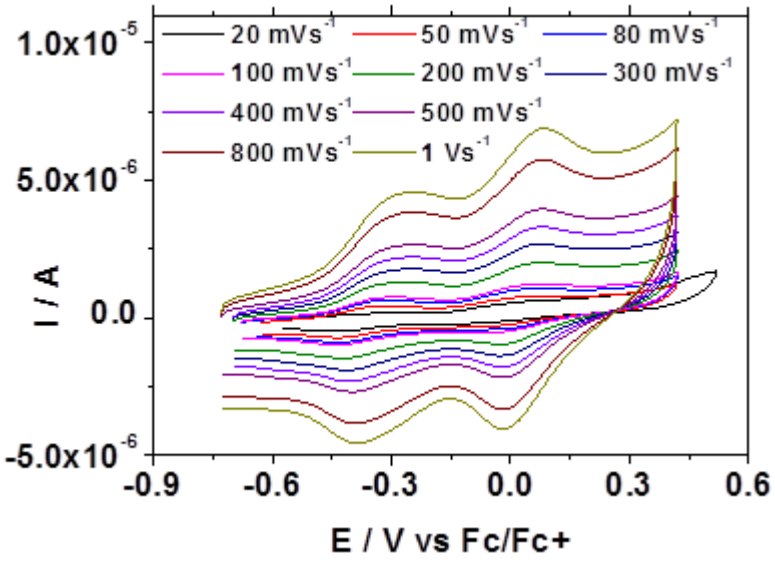

Figure 64: Cyclic voltammogram of a pyrrolo-TTF monolayer in vacuum dried BMIOTf at different scan rates.

3.5 Conclusions

The electrochemistry of the redox active molecular wire pyrrolo-TTF has been investigated using cyclic voltammetry. Attempts at repeating the data obtained by Leary *et al*.[2] met little success. It was first thought that the pyrrolo-TTF was not forming a stable monolayer on the Au(111) surface and several adsorption methods were attempted. A polarisation modulation infrared reflection absorption spectrum (PM-IRRAS) was obtained and this showed the presence of pyrrolo-TTF on the Au(111) surface. It has been found that pyrrolo-TTF is very sensitive to protonation in the presence of water over time. Therefore, pyrrolo-TTF should be handled in a dry environment. There was much difficulty reproducing the quality of voltammetry obtained by Leary *et al*.[2] indicating that the pyrrolo-TTF had been protonated due to prolonged exposure to water in the atmosphere. It was found that the redox behaviour of pyrrolo-TTF could be recovered by use of a RTIL as a solvent and as the electrolyte in cyclic voltammetry experiments. Using the RTIL BMIOTf as an electrolyte also allowed the observation of the second redox transition of pyrrolo-TTF, which is out of the potential window of conventional aqueous electrolytes.

Pyrrolo-TTF has shown promise in the field of SMC as it seems to behave according to the two-step Kuznetsov-Ulstrup (KU) ET model, at least for the first oxidation step.[17-29] The next chapter of this thesis explores this in more detail.

3.6 References

1. J. Becher, J. O. Jeppesen and K. Nielsen, Synthetic Metals, 2001, 133, 309-315.

2. E. Leary, S. Higgins, H. van Zalinge, W. Haiss, R. Nichols, S. Nygaard, J. Jeppesen and J. Ulstrup, Journal of the American Chemical Sociery, 2008, 130, 12204-12205.

3. J. O. Jeppesen and J. Becher, European Journal of Organic Chemistry, 2003, 3245-3266.

4. F. Giacalone, M. A. Herranz, L. Gruter, M. T. Gonzalez, M. Calame, C. Schonenberger, C. R. Arroyo, G. Rubio-Bollinger, M. Velez, N. Agrait and N. Martin, Chemical Communications, 2007, 4854-4856.

5. Y. Kobayashi, M. Yoshioka, K. Saigo, D. Hashizume and T. Ogura, Journal of the American Chemical Society, 2009, 131, 9995-10002.

6. A. J. Olaya, P. Ge, J. r. m. F. Gonthier, P. Pechy, C. m. Corminboeuf and H. H. Girault, Journal of the American Chemical Society, 2011, 133, 12115-12123.

7. L. Aldous, D. S. Silvester, C. Villagran, W. R. Pitner, R. G. Compton, M. C. Lagunas and C. Hardacre, New Journal of Chemistry, 2006, 30, 1576-1583.

8. T. Albrecht, K. Moth-Poulsen, J. B. Christensen, J. Hjelm, T. Bjornholm and J. Ulstrup, Journal of the American Chemical Society, 2006, 128, 6574-6575.

9. Y. C. Fu, H. M. Zhang, Y. Z. Su, D. Y. Wu, Z. X. Xie and B. W. Mao, Zeitschrift Fur Physikalische Chemie-International Journal of Research in Physical Chemistry & Chemical Physics, 2007, 221, 1109-1121.

10. X. B. Ji, D. S. Silvester, L. Aldous, C. Hardacre and R. G. Compton, Journal of Physical Chemistry C, 2007, 111, 9562-9572.

11. L. G. Lin, J. W. Yan, Y. Wang, Y. C. Fu and B. W. Mao, Journal of Experimental Nanoscience, 2006, 1, 269-278.

12. Y. Z. Su, Y. C. Fu, J. W. Yan, Z. B. Chen and B. W. Mao, Angewandte Chemie-International Edition, 2009, 48, 5148-5151.

13. Y. M. Wei, X. S. Zhou, J. G. Wang, J. Tang, B. W. Mao and D. M. Kolb, Small, 2008, 4, 1355-1358.

14. N. J. Kay, R. J. Nichols, S. J. Higgins, W. Haiss, G. Sedghi, W. Schwarzacher and B.-W. Mao, Journal of Physical Chemistry C, 2011, 115, 21402-21408.

15. F. Endres and S. Z. El Abedin, Physical Chemistry Chemical Physics, 2006, 8, 2101-2116.

16. S. Schaltin, P. Nockemann, B. Thijs, K. Binnemans and J. Fransaer, Electrochemical and Solid State Letters, 2007, 10, D104-D107.

17. A. M. Kuznetsov and J. Ulstrup, Russian Journal of Electrochemistry, 2006, 42, 760-766.

18. A. M. Kuznetsov and J. Ulstrup, Journal of Electroanalytical Chemistry, 2004, 564, 209-222.

19. J. D. Zhang, A. M. Kuznetsov, I. G. Medvedev, Q. J. Chi, T. Albrecht, P. S. Jensen and J. Ulstrup, Chemical Reviews, 2008, 108, 2737-2791.

20. A. G. Hansen, H. Wackerbarth, J. U. Nielsen, J. Zhang, A. M. Kuznetsov and J. Ulstrup, Russian Journal of Electrochemistry, 2003, 39, 108-117.

21. A. M. Kuznetsov and J. Ulstrup, Journal of Chemical Physics, 2002, 116, 2149-2165.

22. T. Albrecht, A. Guckian, A. M. Kuznetsov, J. G. Vos and J. Ulstrup, Journal of the American Chemical Society, 2006, 128, 17132-17138.

23. A. A. Kornyshev, A. M. Kuznetsov and J. Ulstrup, Proceedings of the National Academy of Sciences of the United States of America, 2006, 103, 6799-6804.

24. J. D. Zhang, A. M. Kuznetsov and J. Ulstrup, Journal of Electroanalytical Chemistry, 2003, 541, 133-146.

25. E. P. Friis, Y. I. Kharkats, A. M. Kuznetsov and J. Ulstrup, The Journal of Physical Chemistry A, 1998, 102, 7851-7859.

26. J. Zhang, Q. Chi, A. M. Kuznetsov, A. G. Hansen, H. Wackerbarth, H. E. M. Christensen, J. E. T. Andersen and J. Ulstrup, Journal of Physical Chemistry B, 2002, 106, 1131-1152.

27. A. M. Kuznetsov, I. G. Medvedev and J. Ulstrup, Journal of Chemical Physics, 2007, 127, 104708.

28. A. M. Kuznetsov and J. Ulstrup, Chemical Physics, 1991, 157, 25-33.

29. I. V. Pobelov, Z. H. Li and T. Wandlowski, Journal of the American Chemical Society, 2008, 130, 16045-16054.

Chapter 4

Conductance Measurements Of Pyrrolo-Tetrathiafulvalene In A Room Temperature Ionic Liquid

4 Conductance Measurements Of Pyrrolo-Tetrathiafulvalene In A Room Temperature Ionic Liquid

4.1 Introduction

Pyrrolo-tetrathiafulvalene (pyrrolo-TTF) shows considerable promise in the field of SME. It undergoes two stable, fully reversible redox transitions, the potential of which can be altered by the addition of various substituents.[1-4]

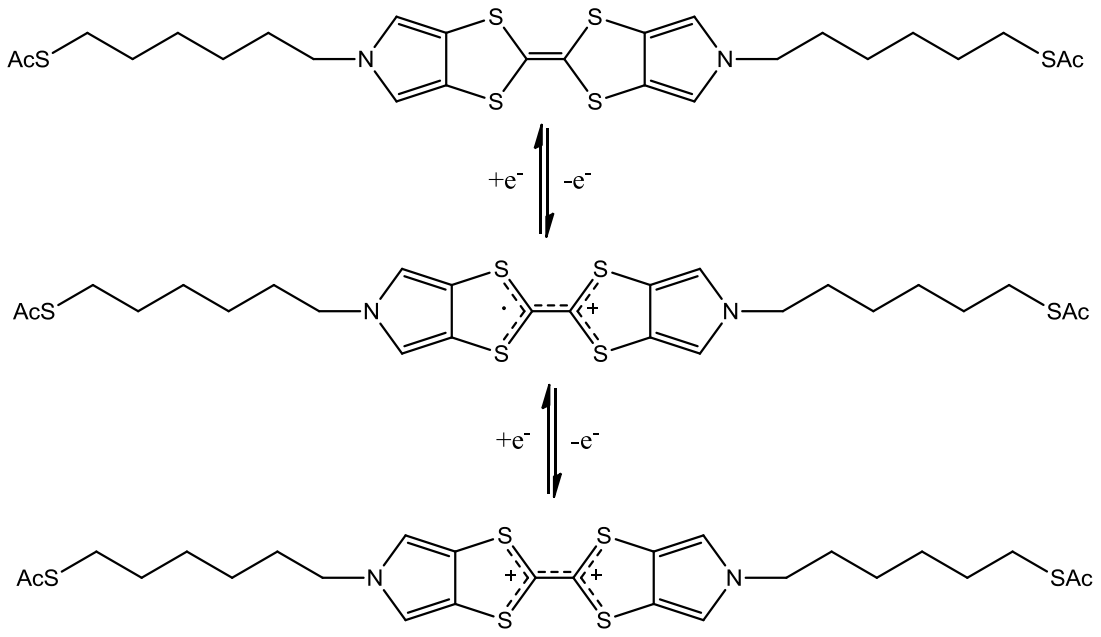

Figure 65: The two stable, fully-reversible redox reactions of pyrrolo-TTF. The first transition, from the neutral pyrrolo-TTF^{0} to the radical cation pyrrolo-$TTF^{\cdot+}$ is visible in aqueous electrolyte, whereas the second transition from the radical cation pyrrolo-$TTF^{\cdot+}$ to the dication pyrrolo-TTF^{2+} is not.

The first of these redox transitions, from the neutral pyrrolo-TTF^{0} to the radical cation pyrrolo-$TTF^{\cdot+}$ is within the potential range available to aqueous electrolytes and has been studied by Leary *et al*. using both cyclic voltammetry and electrochemical in-situ STM (ECSTM).[2] Pyrrolo-TTF was found to possess switching behaviour, exhibiting a sharp "off-on-off" transition around this redox potential. This can be seen clearly in *Figure 66*.

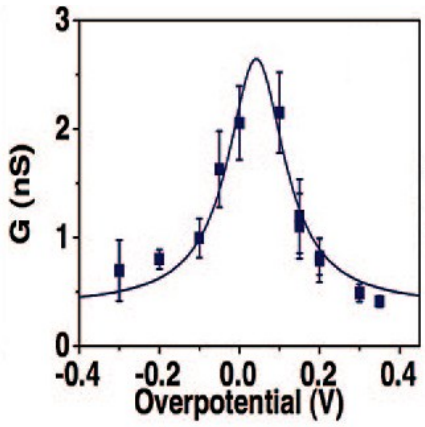

Figure 66: Single molecule conductance for pyrrolo-TTF. A sharp rise in the conductance was observed at the first redox transition. This corresponds to the "on" state of the molecule.[2] Figure adapted from reference 2.

The second redox transition from pyrrolo-$TTF^{\cdot+}$ to pyrrolo-TTF^{2+} is outside of the potential range accessible with aqueous electrolytes. Room temperature ionic liquids (RTILs) have been shown in the previous chapter to be a suitable electrolyte for observing this second redox transition. Both redox transitions can clearly been seen in cyclic voltammograms of pyrrolo-TTF in the RTIL 1-butyl-3-methylimidazolium trifluoromethanesulfonate (BMIOTf).

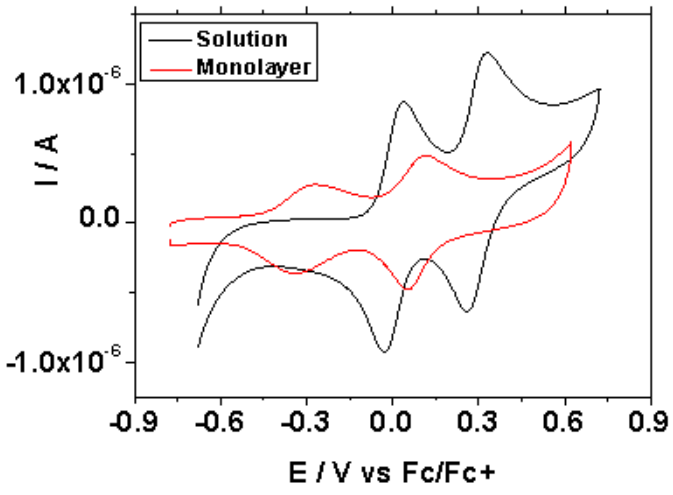

Figure 67: Cyclic voltammetry of pyrrolo-TTF in a solution of N_2 dried BMIOTf (black) and as a monolayer on Au(111) in an electrolyte of N_2 dried BMIOTf (red). Scan rate = 50 mVs^{-1}.

BMIOTf has been shown to be a suitable medium for SMC measurements in a previous chapter of this thesis.[5] The conductance of various alkanedithiols was measured using the STM based $I(s)$ technique and it was found that the presence of BMIOTf did not alter the ET properties of the alkanedithiols at a low bias potential. At higher bias potentials, the electron conducting properties of 1,8-octanedithiol deviated from the Simmons ET model.[5] It was suggested that a possible reason for this is that RTILs have been shown to cause a degree of restructuring on gold single crystal electrodes. Lin *et al*. demonstrated this surface etching using the RTIL 1-butyl-3-methylimidazolium tetrafluoroborate ($BMIBF_4$) on the Au(111) surface.[6] Between -0.9 and -1.2 V, tiny pits of atomic height begin to emerge on the substrate. When the potential of the substrate is maintained between -1.2 and -2.4 V for an extended period of time, "worm-like" structures appear on the Au(111) surface. They suggested that the cause of these defects on the substrate could be the BMI^+ cation interacting with the substrate.[6] Nevertheless, RTILs could provide a fresh insight into SME, particularly of redox-active molecular wires.

4.2 Aim

RTILs enjoy several advantages over conventional aqueous electrolytes, including a wider potential range, high conductivity without the need to add a supporting electrolyte, and low volatility.[5, 7-13] This makes them ideal as a medium for performing single molecule conductance measurements on redox-active molecular wires. This is particularly the case for pyrrolo-TTF, as the second redox transition from pyrrolo-$TTF^{\cdot+}$ to pyrrolo-TTF^{2+} is outside of the range of aqueous electrolytes, yet is observable in the RTIL BMIOTf. This particular RTIL has already been used in the single molecule conductance measurements of various alkanedithiols, with success.[5] BMIOTf is a hydrophobic RTIL so water content is not expected to be an issue.[14] The aim of this study is to measure the conductance of pyrrolo-TTF using ECSTM over a range of sample potentials (E_s) in an ionic liquid medium, to determine how the conductance changes according to the redox state of the molecule. The conductance over the first redox transition has been studied previously by Leary *et al*.[2] in an aqueous electrolyte. However, the conductance over the second redox transition is yet to be studied and it is hoped that a better understanding of the switching behaviour of pyrrolo-TTF can be gained by use of an ionic liquid medium.

The data obtained from these measurements will then be modelled to the Kuznetsov-Ulstrup model of 2-step ET, which is described in detail in the introduction to this thesis.

4.3 Experimental Methods

All of the experiments were performed using an Agilent 2500 or 5500 STM controller in conjunction with the Agilent Picoscan 5.3.3 software. Due to the sensitivity of the RTIL to air/water, an environmental chamber was fitted to the STM head, to maintain a dry, inert N_2 atmosphere. The environmental chamber also contained a small amount of silica dessicant. Au STM tips were prepared using 0.25 mm Au wire (99.99%, Goodfellows) which were electrochemically etched in a 1:1 solution of HCl and ethanol at approximately +7.0 V. The Au tips were then coated with a layer of Apiezon® wax, ensuring that only the very end of the tip was exposed. Commercial gold-on-glass substrates (Arrandee®) were flame annealed for approximately 5 minutes prior to use. Pyrrolo-TTF was provided by the group of Professor Jan Jeppesen of the University Of Odense, Denmark. The RTIL 1-butyl-3-methylimidazolium trifluoromethanesulfonate (BMIOTf) was purchased from Iolitec. This was dried at 120°C for approximately 18 hours prior to use and treated with 3 Å molecular sieves, unless otherwise specified.[15] Pyrrolo-TTF monolayers were formed on the gold-on-glass substrate by immersing the substrate in a 1 mM solution of pyrrolo-TTF in BMIOTf for approximately 5 minutes. This was then rinsed with BMIOTf, then ethanol and blown dry using N_2. In order to perform STM under electrochemical potential control, a Teflon cell was used in the STM setup and a Pt quasi reference and counter electrode system was employed. Once BMIOTf had been added to the STM cell, the environmental chamber was purged with dry N_2 for approximately 16 hours prior to measurements being taken.

The STM $I(s)$ technique was employed in these measurements with a setpoint current (I_0) of 20 nA and a sample bias voltage (V_{BIAS}) of +0.6 V. The tip was withdrawn by 4 nm relative to the setpoint current and the scan duration was 0.1 seconds. The resulting current-distance scans were plotted into a histogram, which was used to calculate the molecular conductance. The sample potential was varied between -0.6 V and +0.5 V with respect to the Pt quasi. The initial tip-to-sample distance s_0 was approximated using the method described in Chapter 2 of this thesis.

4.4 Results And Discussion

The *I*(*s*) technique was used to determine the single molecule conductance of pyrrolo-TTF at various sample potentials, in the RTIL BMIOTf. The *I*(*s*) measurements were performed in an environmental chamber purged with dry N_2 gas and *I*(*s*) scans were recorded by setting the current setpoint and bias voltage, and then rapidly retracting the Au tip at a rate of 41 nm s^{-1}. Approximately 5% of the *I*(*s*) scans contained a current plateau indicative of molecules bridging the gap between the Au tip and gold-on-glass substrate.

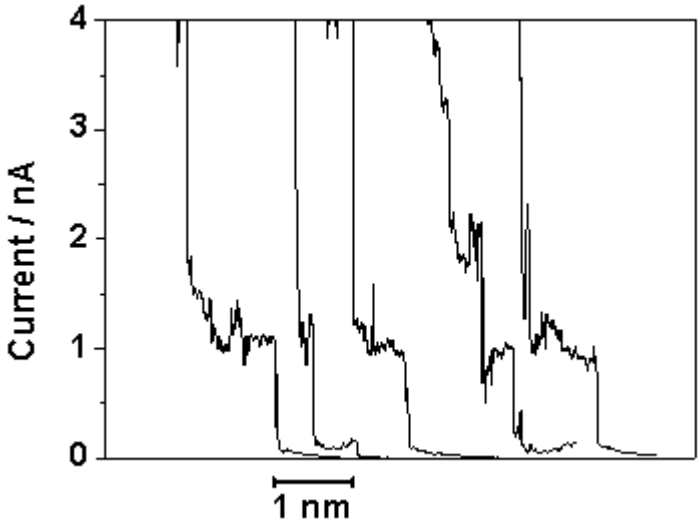

Figure 68: Examples of *I*(*s*) scans of pyrrolo-TTF in BMIOTf at a sample potential of +0.12 V.

Every *I*(*s*) scan which contained a plateau was used in the histogram analysis. The histograms for sample potentials of -0.5, -0.35, -0.25, -0.1, 0, 0.12, 0.2, and 0.4 V vs Pt quasi reference, contained at least 500 scans, and the histograms for sample potentials of -0.6, -0.55, -0.45, -0.3, -0.2, -0.05, 0.05, 0.1, 0.15, 0.25, 0.3, 0.45, and 0.5 V vs Pt quasi reference contained at least 100 scans. In each histogram, a clear peak is present and can be used to calculate the conductance of the molecule.

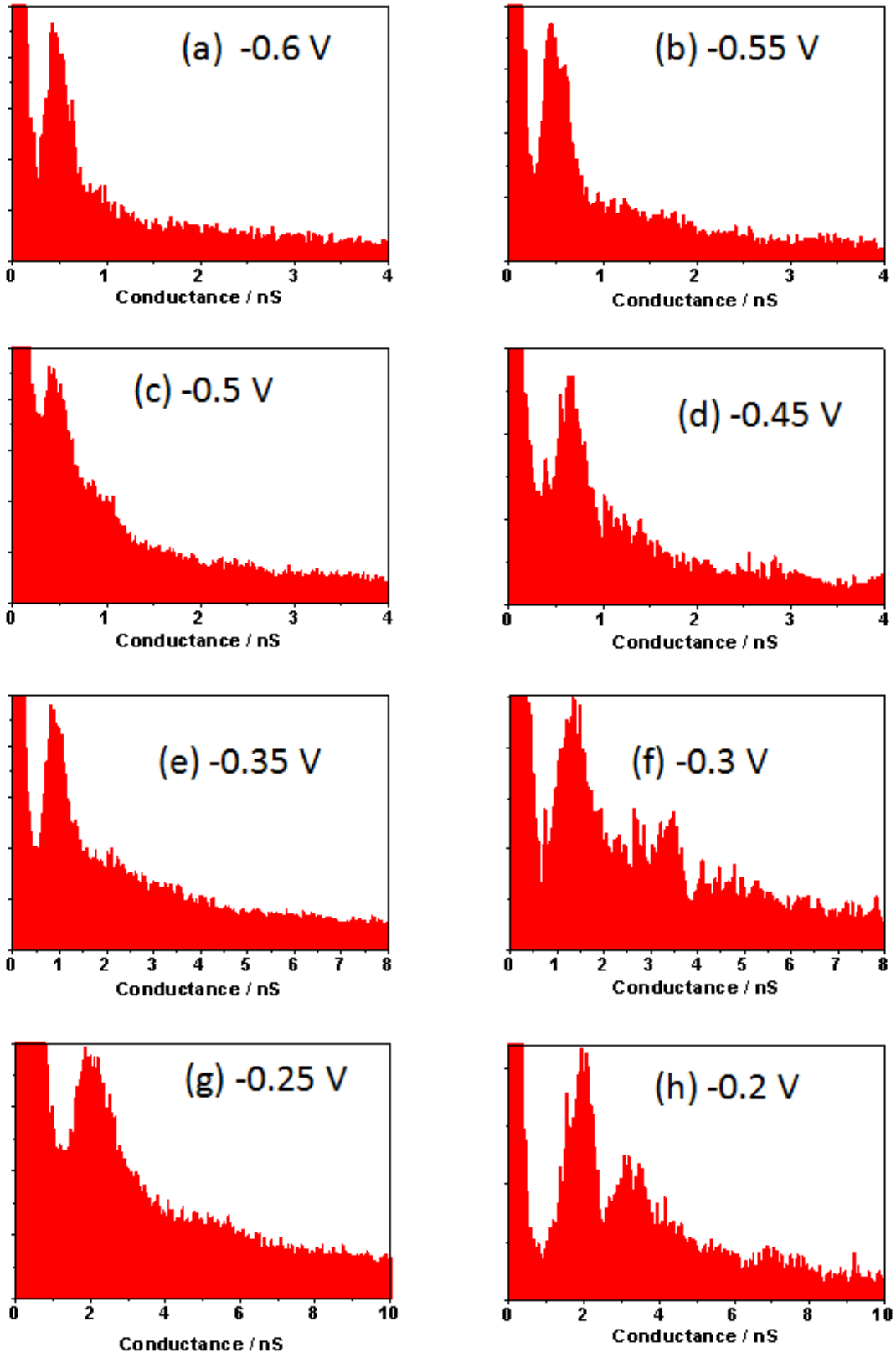

Figure 69: Conductance histograms of pyrrolo-TTF using sample potentials of (a) -0.6 V, (b) -0.55 V, (c) -0.5 V, (d) -0.45 V, (e) -0.35 V, (f) -0.3 V, (g) -0.25 V, and (h) -0.2 V obtained using the *I*(*s*) method; V_{BIAS} = +0.6 V ; I_0 = 20 nA ; 100, 102, 500,

101, 501, 100, 503, and 100 scans were analysed respectively. Sample potentials are with respect to the Pt quasi reference.

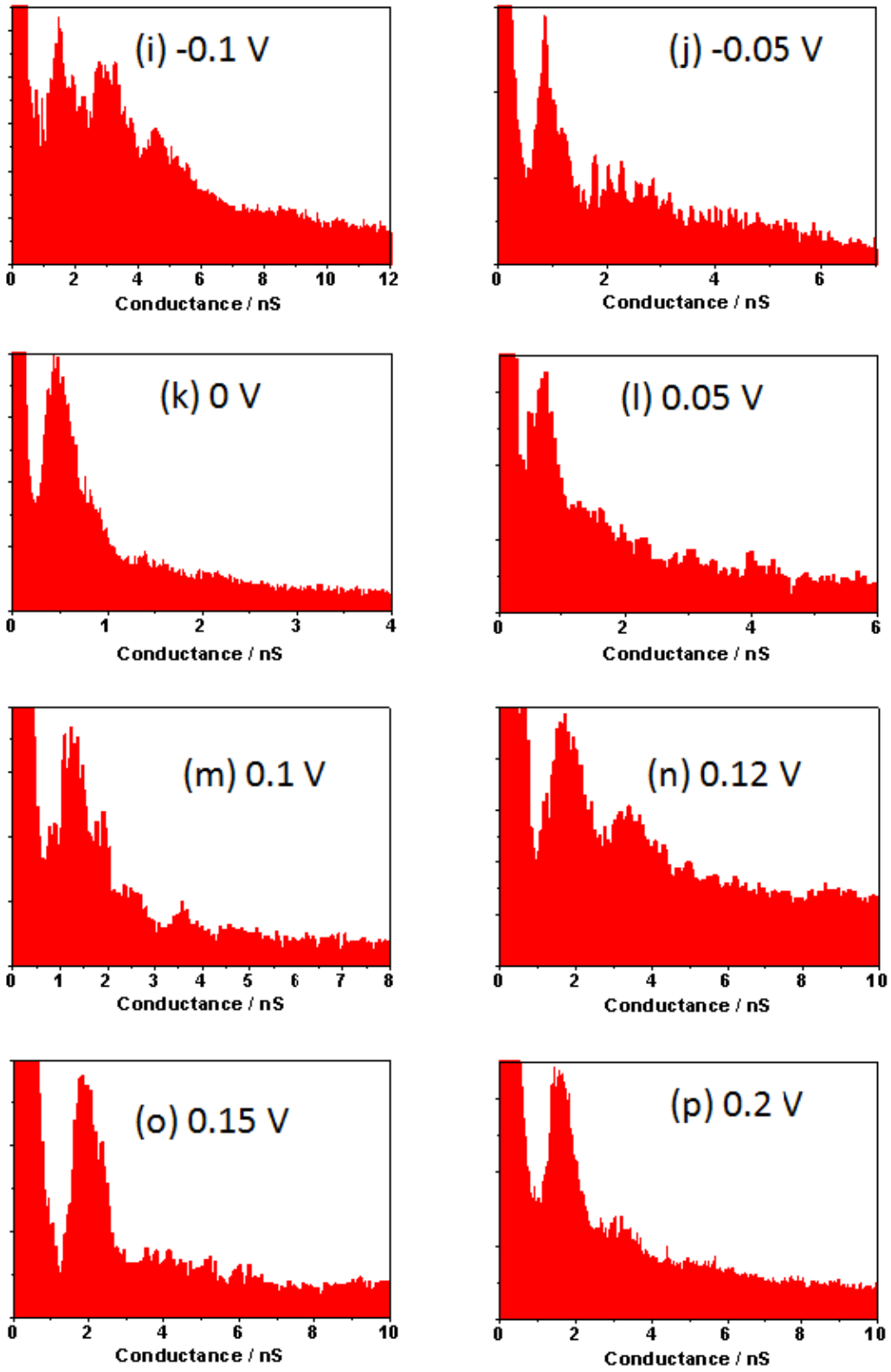

Figure 70: Conductance histograms of pyrrolo-TTF using sample potentials of (i) -0.1 V, (j) -0.05 V, (k) 0 V, (l) 0.05 V, (m) 0.1 V, (n) 0.12 V, (o) 0.15 V, and (p) 0.2

V obtained using the $I(s)$ method; V_{BIAS} = +0.6 V ; I_0 = 20 nA ; 500, 105, 500, 100, 100, 501, 110, and 510 scans were analysed respectively. Sample potentials are with respect to the Pt quasi reference.

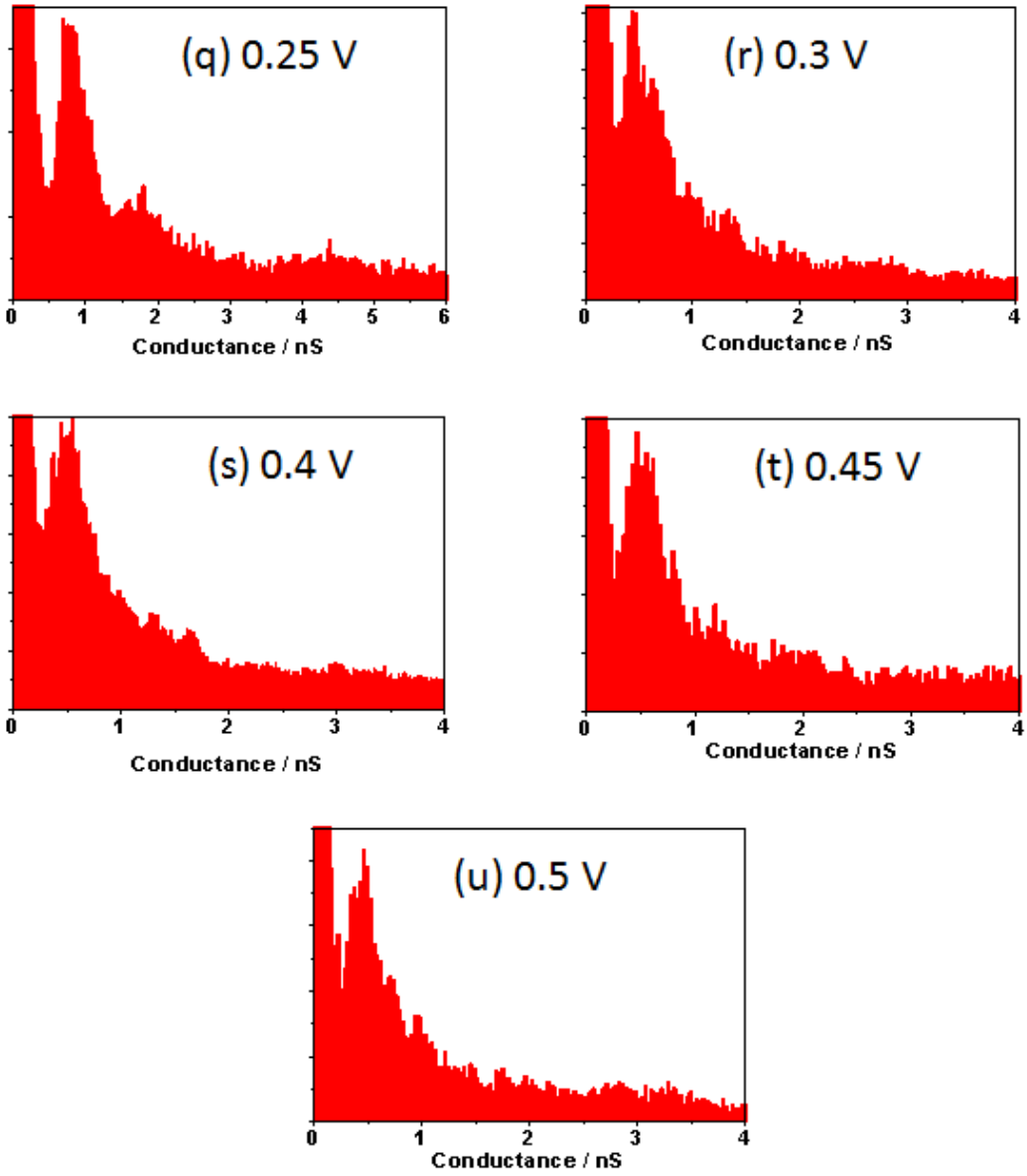

Figure 71: Conductance histograms of pyrrolo-TTF using sample potentials of (q) 0.25 V, (r) 0.3 V, (s) 0.4 V, (t) 0.45 V, and (u) 0.5 V, obtained using the $I(s)$ method; V_{BIAS} = +0.6 V ; I_0 = 20 nA ; 100, 100, 503, 100, and 100 scans were analysed respectively. Sample potentials are with respect to the Pt quasi reference.

The break-off distance of pyrrolo-TTF was estimated using the method described in Chapter 2, for each sample potential. This was then compared to the length of a single molecule of pyrrolo-TTF which was estimated using Spartan® as

approximately 3.2 nm. A number of the break-off distances estimated were slightly lower than expected. A possible explanation for this is that the structure of the tip at the nanoscale is not known and the pyrrolo-TTF may have adsorbed at a site other than the terminal atom, which would result in a lower break-off. Although the break-off distance provides a reasonable means of confirming the measurement of one single molecule, it is by no means absolute proof. The break-off distances estimated are given below in *Table 11*.

Table 11: The break-off distances estimated for pyrrolo-TTF at the sample potentials measured. The sample potentials given are with respect to the Pt quasi reference.

Sample Potential / V vs Pt	Break-off distance / nm
-0.6	2.3 ± 0.4
-0.55	2.2 ± 0.3
-0.5	1.9 ± 0.5
-0.45	2.1 ± 0.4
-0.35	2.2 ± 0.6
-0.3	2.9 ± 0.4
-0.25	2.2 ± 0.5
-0.2	1.6 ± 0.3
-0.1	2.5 ± 0.6
-0.05	1.9 ± 0.3
0	1.8 ± 0.4
0.05	2.5 ± 0.6
0.1	2.7 ± 0.4
0.12	3.4 ± 0.7
0.15	3.2 ± 0.5
0.2	2.4 ± 0.5
0.25	2.5 ± 0.4
0.3	3.8 ± 0.4
0.4	1.8 ± 0.6
0.45	2.6 ± 0.4
0.5	2.2 ± 0.4

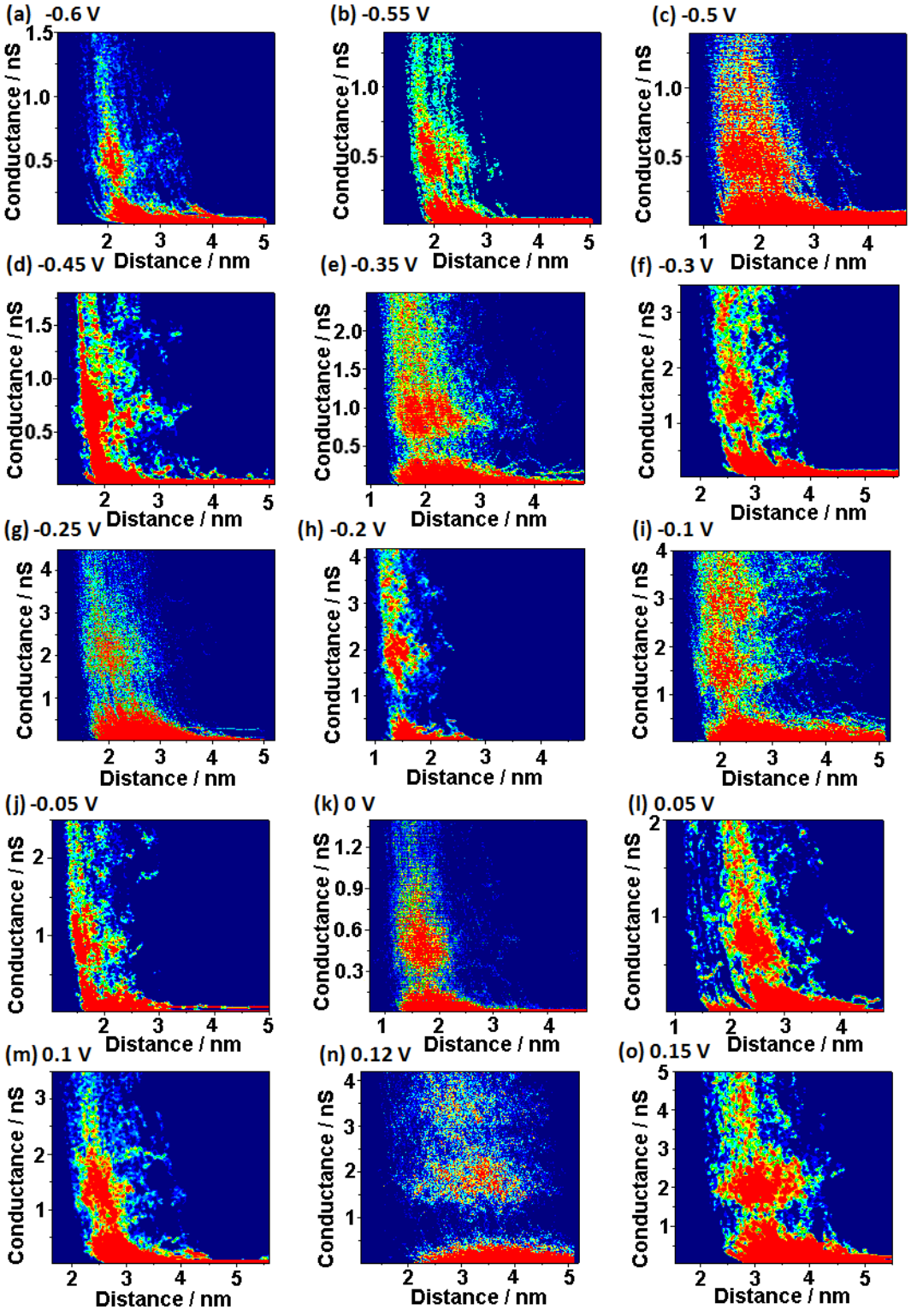

Figure 72: 2-D histogram representations of pyrrolo-TTF conductance data at sample potentials of (a) -0.6 V, (b) -0.55 V, (c) -0.5 V, (d) -0.45 V, (e) -0.35 V, (f) -0.3 V, (g) -0.25 V, (h) -0.2 V , (i) -0.1 V, (j) -0.05 V, (k) 0 V, (l) 0.05 V, (m) 0.1 V, (n) 0.12 V, and (o) 0.15 V vs the Pt quasi reference, obtained using the *I*(*s*) method.

The conductance of pyrrolo-TTF, and break-off decay regions are clearly visible on each plot.

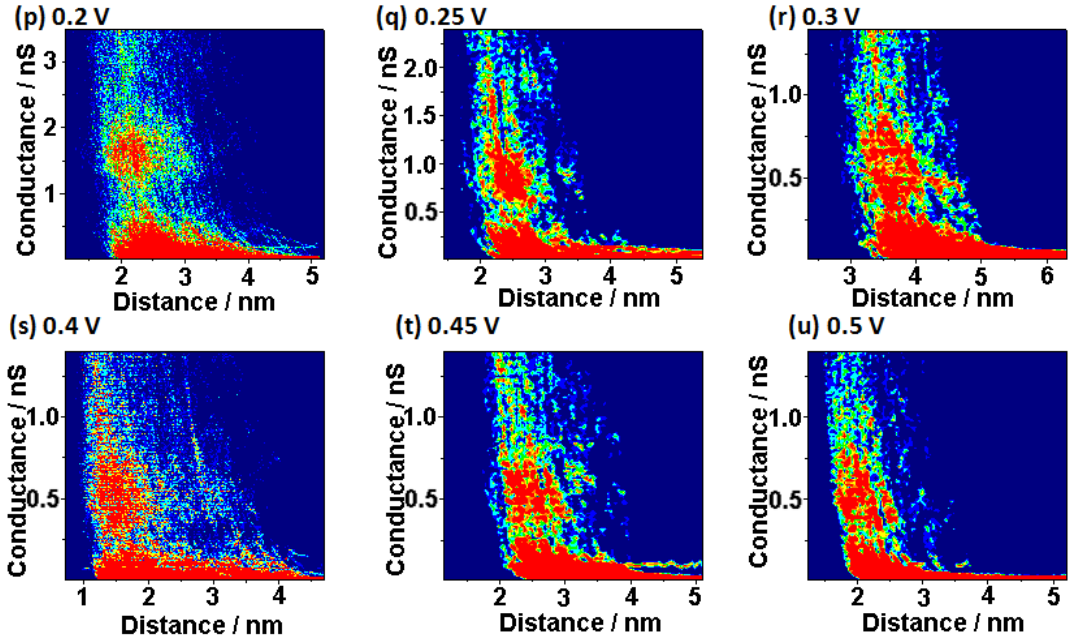

Figure 73: 2-D histogram representations of pyrrolo-TTF conductance data at sample potentials of (p) 0.2 V, (q) 0.25 V, (r) 0.3 V, (s) 0.4 V, (t) 0.45 V, and (u) 0.5 V vs the Pt quasi reference, obtained using the *I*(*s*) method. The conductance of pyrrolo-TTF, and break-off decay regions are clearly visible on each plot.

All of the data obtained concerning the conductance of pyrrolo-TTF is plotted in *Figure 74* and shows the conductance of pyrrolo-TTF versus the electrochemical sample potential. The potential scale is with respect to the Fc/Fc^{+} redox couple, as described in Chapter 3 of this thesis. For both redox transitions, a peak in the conductance was observed around the redox potential, from ~0.5 nS to ~2 nS.

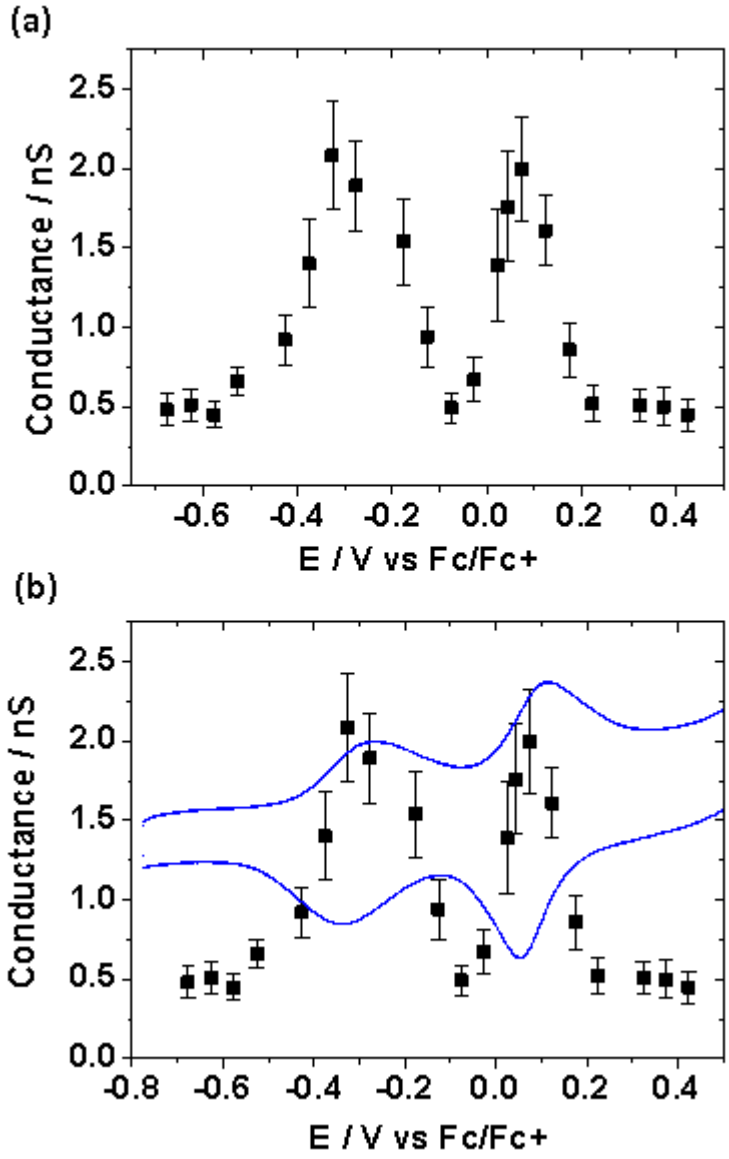

Figure 74: (a) Plot of conductance of pyrrolo-TTF against the sample potential and (b) the plot in (a) overlaid with a cyclic voltammogram (blue line) of a pyrrolo-TTF monolayer. The point of maximum conductance corresponds with the redox potential of each redox transition of pyrrolo-TTF. The voltammogram shown here was recorded in N_2 dried BMIOTf. A detailed explanation for this can be found in the previous chapter.

The conductance data shown above was then modelled using the Kuznetsov-Ulstrup (KU) model of 2-step ET. This model of ET is described in detail in the introduction of this thesis. The KU model with partial vibrational relaxation results in a peak in the current flowing through the molecular bridge.[16-20] In the case of pyrrolo-TTF, the

first step of the charge transfer occurs when the HOMO is close to the Fermi level of the acceptor Au electrode, and involves the hole tunnelling to the HOMO of the molecular bridge. The oxidised and vibrationally excited pyrrolo-TTF group relaxes towards the Fermi level of the donor Au electrode. However, before this relaxation is complete, the second charge transfer occurs and the hole tunnels to the donor Au electrode. The now fully occupied orbital then relaxes back to its original energy, where it can receive another hole and the process repeats itself. Hole tunnelling occurs as opposed to electron tunnelling, because pyrrolo-TTF is being oxidised as the sample potential made more positive. The KU model has two forms which can be used to model the ET in pyrrolo-TTF. The first numerical form is shown in *Equation 4.1*.

$$I_e = 1820 \cdot V_{BIAS}\left\{exp\left[\frac{9.73}{\lambda_{reorg}}\left(\lambda_{reorg} + \xi\eta + \gamma V_{BIAS}\right)^2\right] + exp\left[\frac{9.73}{\lambda_{reorg}}\left(\lambda_{reorg} + V_{BIAS} - \xi\eta - \gamma V_{BIAS}\right)^2\right]\right\}^{-1} \qquad \textit{Equation 4.1}$$

Where I_e is the enhanced current, V_{BIAS} is the bias potential, λ_{reorg} is the total reorganisation energy, η is the overpotential applied to the substrate, and ξ and γ are modelling parameters relating to the proportion of electrochemical potential and the bias potential respectively, that affect the redox moiety.[17] This equation can be simplified further to give:[17]

$$I_e = \frac{910 \cdot V_{BIAS}.exp\left[-9.73\left(\lambda_{reorg} + V_{BIAS}\right)\right]}{\cosh[19.4(\xi\eta + (\gamma - 0.5)V_{BIAS})]} \qquad \textit{Equation 4.2}$$

Equation 2 makes the assumption that η and V_{BIAS} are lower than λ_{reorg}. Both forms of the equation were used to model the ET properties of pyrrolo-TTF and shall be referred to from this point as the "long KU" and "simplified KU" models respectively. The best fit achieved using both the long and simplified KU for both redox transitions is shown in *Table 12*.

Table 12: Values of λ_{reorg}, γ, and ξ used in the modelling of both redox transitions of pyrrolo-TTF using the long KU and simplified KU model of ET.

	Long KU		Simplified KU	
	1st Redox	2nd Redox	1st Redox	2nd Redox
λ_{reorg} / eV	1.165	1.18	1.245	1.255
γ	0.5	0.5	0.5	0.5
ξ	0.8	1	0.7	1

The long and simplified KU model is visualised in *Figure 75*. For both redox transitions of pyrrolo-TTF, the fittings of both variations of KU model match the conductance data well.

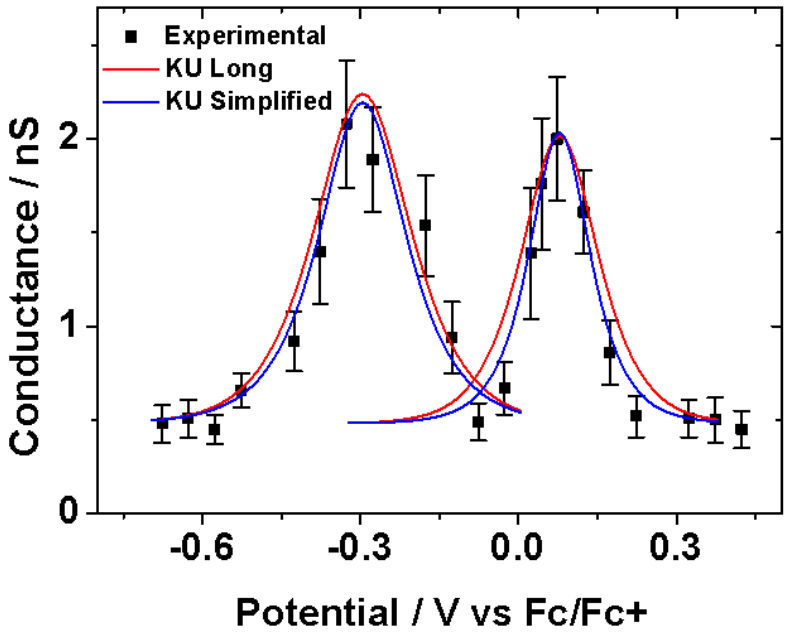

Figure 75: Conductance-sample potential relationship of pyrrolo-TTF in the RTIL BMIOTf. The red lines show the long KU model (*Equation 4.1*), and the blue lines show the simplified KU model (*Equation 4.2*). For both redox transitions, both KU model variations fit the experimental data well.

The values of λ_{reorg}, γ, and ξ are altered in the KU model to achieve the best fit. γ, which is the proportion of the bias potential which affects the central redox moiety must be between 0 and 1, with an optimum value of 0.5 for a symmetrical molecule such as pyrrolo-TTF. As can be seen clearly in *Table 12*, a γ value of 0.5 indeed gave

the best fitting for pyrrolo-TTF for both redox transitions and for both the long and simplified KU model. Changing the γ value shifts the peak of enhanced current along the x-axis, with a γ smaller than 0.5 resulting in the peak maximum having a negative overpotential (η), and a γ larger than 0.5 resulting in the peak maximum moving in a positive direction. The proportion of the electrochemical potential ξ can also have values ranging between 0 and 1. However, the "ideal" ξ value is 1. Changing ξ alters the width of the peak, with a higher ξ approaching 1 having a narrower peak and lower ξ values resulting in a wider peak. These fitting parameters are independent from one another, changing one does not affect another. In this instance, both types of KU model fit the experimental data for the 2nd redox transition best, with the optimum ξ value of 1. For the 1st redox transition however, the best fit used ξ values of 0.8 and 0.7 for the long and simplified KU models respectively. Changing the reorganisation energy λ_{reorg} changes the height of the peak for enhanced current; a lower λ_{reorg} results in a larger enhanced current and vice versa. Using the long KU, λ_{reorg} was estimated to be 1.165 eV and 1.18 eV for the 1st and 2nd redox transitions, respectively, and using the simplified KU, λ_{reorg} values of 1.245 eV and 1.255 eV were estimated for the 1st and 2nd redox transitions respectively. It can be noted that the λ_{reorg} values for both redox transitions are very similar using each KU model variation. As described in the introduction to this thesis, λ_{reorg} consists of two parts, λ_{intra} and λ_{solv} which describe the inner-sphere and outer-sphere interactions respectively. λ_{intra} of pyrrolo-TTF has not been calculated. However, other various TTF derivatives have been investigated and have been found to have a λ_{intra} between 200 meV and 600 meV.[21-24] It is a reasonable assumption that λ_{intra} of pyrrolo-TTF would be similar to other TTFs. For non-polar and low-polarity solvents, λ_{solv} is negligible as the solvent coordination does not change significantly as the redox state of the molecule changes.[22] However, when the solvent is a RTIL, λ_{solv} is a large and considerable proportion of λ_{reorg}.[25-27] This is because, unlike a moderately polar solvent such as water, a RTIL consists solely of ions. As the redox state of pyrrolo-TTF changes, the ions must rearrange themselves around the pyrrolo-TTF. This requires a larger amount of energy than for a water molecule to simply rotate, hence why λ_{solv} is much more significant.[25-27] λ_{solv} would be incredibly difficult if indeed even possible to calculate to any degree of accuracy within the nanogap. The pyrrolo-TTF molecule in this scenario is being tethered between two Au electrodes with a bias voltage applied between them, which results in the calculations being

extremely complex. However, the Marcus theory, which is described in more detail in the introduction, enables λ_{solv} to be estimated with relative ease.

$$\lambda_{solv} = \left(\frac{e^2}{4\pi\varepsilon_0}\right)\left(\frac{1}{2(R_A)} + \frac{1}{2(R_B)} - \frac{1}{r}\right)\left(\frac{1}{n^2} - \frac{1}{\varepsilon_r}\right) \qquad \textit{Equation 4.3}$$

Where ε_0 is the relative permittivity of free space, R_A and R_B are the ionic radii, r is the distance between the centre of the ions, which is taken to be $R_A + R_B$. n is the refractive index of the solvent[28] and ε_r is the relative permittivity of the solvent[29], which in this instance is BMIOTf.[30, 31] As this equation can only approximately represent pyrrolo-TTF in the nanogap, R_A and R_B are assumed to be equal and set at half the distance between the N atoms in the redox active moiety. This produces a λ_{solv} value of approximately 0.56 eV. This very approximate value of λ_{solv} when added to a very approximate value of between 0.2 eV and 0.6 eV for λ_{intra} results in a λ_{reorg} value very similar to that observed for pyrrolo-TTF in a BMIOTf solvent using the KU model. Further confirmation of this can be seen when the data of Leary *et al.*[2] is modelled using the KU model.

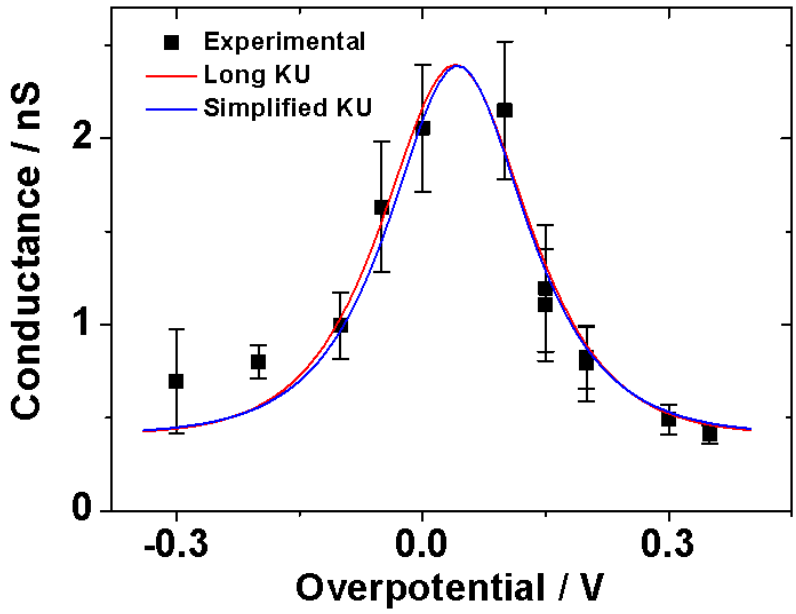

Figure 76: Conductance-overpotential relationship of pyrrolo-TTF in an aqueous buffer electrolyte at pH 6.8, recorded by Leary *et al.*[2] The red line shows the long KU model (*Equation 4.1*), and the blue line shows the simplified KU model (*Equation 4.2*). The λ_{reorg} of pyrrolo-TTF in an aqueous buffer was estimated as 0.405 eV using the long KU model and 0.43 eV using the simplified KU model.

Both the long and simplified KU models were used to model the ET through pyrrolo-TTF during the 1st redox transition in an aqueous buffer electrolyte, which was recorded by Leary *et al*.[2]

Table 13: Values of λ_{reorg}, γ, and ξ used in the modelling of pyrrolo-TTF in aqueous electrolyte recorded by Leary *et al*.[2] using the long KU and simplified KU model of ET.

	Pyrrolo-TTF in aqueous electrolyte	
	Long KU	Short KU
λ_{reorg} / eV	0.405	0.43
γ	0.4	0.35
ξ	0.5	0.7

Table 13 shows the λ_{reorg}, γ, and ξ values which were used in the KU modelling of the data obtained by Leary *et al*.[2] The values of λ_{reorg} are much lower for pyrrolo-TTF in the aqueous electrolyte than in BMIOTf. This is expected as the aqueous buffer electrolyte expends much less energy reorganising around the pyrrolo-TTF molecule as the redox state changes.

4.5 Conclusions

The single molecule conductance of the redox active molecular wire pyrrolo-TTF has been measured using electrochemical potential control in the RTIL BMIOTf. A range of sample potentials was investigated and the conductance of pyrrolo-TTF was measured over the two redox transitions it undergoes. Both conventional and 2-D conductance tip-to-substrate histograms have been constructed. Taking advantage of the wider potential window available to BMIOTf over conventional aqueous electrolytes, both redox transitions of pyrrolo-TTF were observed using both cyclic voltammetry and STM *I*(*s*) measurements. In aqueous electrolytes, only the first redox transition, from pyrrolo-TTF^0 to pyrrolo-$TTF^{\cdot+}$ is observed.[2] For both redox transitions, an increase was observed in the conductance from ~0.5 nS to ~2 nS, around the redox potential. The conductance data obtained for pyrrolo-TTF in BMIOTf was then modelled to the KU model of 2-step ET, which provided a good fit to the data. λ_{reorg} was estimated to be ~1.2 eV for both redox transitions in

BMIOTf, compared to ~0.4 eV for the first redox transition in an aqueous electrolyte, recorded by Leary *et al*.[2] This is due to the large contribution of λ_{solv} in BMIOTf. This work shows some of the advantages of using a RTIL as a medium in SMC measurements, particularly the wider potential window. It is expected that RTILs will be more widely deployed in the future in the field of SME. One possible avenue of research includes using RTILs with porphyrins, which have interesting redox properties which the use of RTILs may be able to exploit.[32, 33]

4.6 References

1. J. O. Jeppesen and J. Becher, European Journal of Organic Chemistry, 2003, 3245-3266.

2. E. Leary, S. Higgins, H. van Zalinge, W. Haiss, R. Nichols, S. Nygaard, J. Jeppesen and J. Ulstrup, Journal of the American Chemical Society, 2008, 130, 12204-12205.

3. J. Becher, J. O. Jeppesen and K. Nielsen, Synthetic Metals, 2001, 133, 309-315.

4. F. Giacalone, M. A. Herranz, L. Gruter, M. T. Gonzalez, M. Calame, C. Schonenberger, C. R. Arroyo, G. Rubio-Bollinger, M. Velez, N. Agrait and N. Martin, Chemical Communications, 2007, 4854-4856.

5. N. J. Kay, R. J. Nichols, S. J. Higgins, W. Haiss, G. Sedghi, W. Schwarzacher and B.-W. Mao, Journal of Physical Chemistry C, 2011, 115, 21402-21408.

6. L. G. Lin, Y. Wang, J. W. Yan, Y. Z. Yuan, J. Xiang and B. W. Mao, Electrochemistry Communications, 2003, 5, 995-999.

7. T. Albrecht, K. Moth-Poulsen, J. B. Christensen, J. Hjelm, T. Bjornholm and J. Ulstrup, Journal of the American Chemical Society, 2006, 128, 6574-6575.

8. Y. C. Fu, H. M. Zhang, Y. Z. Su, D. Y. Wu, Z. X. Xie and B. W. Mao, Zeitschrift Fur Physikalische Chemie-International Journal of Research in Physical Chemistry & Chemical Physics, 2007, 221, 1109-1121.

9. X. B. Ji, D. S. Silvester, L. Aldous, C. Hardacre and R. G. Compton, Journal of Physical Chemistry C, 2007, 111, 9562-9572.

10. L. G. Lin, J. W. Yan, Y. Wang, Y. C. Fu and B. W. Mao, Journal of Experimental Nanoscience, 2006, 1, 269-278.

11. L. Aldous, D. S. Silvester, C. Villagran, W. R. Pitner, R. G. Compton, M. C. Lagunas and C. Hardacre, New Journal of Chemistry, 2006, 30, 1576-1583.

12. Y. Z. Su, Y. C. Fu, J. W. Yan, Z. B. Chen and B. W. Mao, Angewandte Chemie-International Edition, 2009, 48, 5148-5151.

13. Y. M. Wei, X. S. Zhou, J. G. Wang, J. Tang, B. W. Mao and D. M. Kolb, Small, 2008, 4, 1355-1358.

14. F. Endres and S. Z. El Abedin, Physical Chemistry Chemical Physics, 2006, 8, 2101-2116.

15. S. Schaltin, P. Nockemann, B. Thijs, K. Binnemans and J. Fransaer, Electrochemical and Solid State Letters, 2007, 10, D104-D107.

16. J. D. Zhang, A. M. Kuznetsov, I. G. Medvedev, Q. J. Chi, T. Albrecht, P. S. Jensen and J. Ulstrup, Chemical Reviews, 2008, 108, 2737-2791.

17. I. V. Pobelov, Z. H. Li and T. Wandlowski, Journal of the American Chemical Society, 2008, 130, 16045-16054.

18. A. M. Kuznetsov and J. Ulstrup, Russian Journal of Electrochemistry, 2006, 42, 760-766.

19. A. M. Kuznetsov and J. Ulstrup, Journal of Electroanalytical Chemistry, 2004, 564, 209-222.

20. A. M. Kuznetsov and J. Ulstrup, Journal of Chemical Physics, 2002, 116, 2149-2165.

21. J. Casado, M. Z. Zgierski, M. C. R. Delgado, J. T. L. Navarrete, M. Mas-Torrent and C. Rovira, Journal of Physical Chemistry C, 2007, 111, 10110-10118.

22. H.-x. Li, R.-h. Zheng and Q. Shi, Physical Chemistry Chemical Physics, 2011, 13, 5642-5650.

23. S. T. Bromley, M. Mas-Torrent, P. Hadley and C. Rovira, Journal of the American Chemical Society, 2004, 126, 6544-6545.

24. M. Mas-Torrent, P. Hadley, S. T. Bromley, X. Ribas, J. Tarres, M. Mas, E. Molins, J. Veciana and C. Rovira, Journal of the American Chemical Society, 2004, 126, 8546-8553.

25. Y. Shim, J. S. Duan, M. Y. Choi and H. J. Kim, Journal of Chemical Physics, 2003, 119, 6411-6414.

26. Y. Shim, M. Y. Choi and H. J. Kim, Journal of Chemical Physics, 2005, 122, 044510.

27. E. J. Maginn, Journal of Physics-Condensed Matter, 2009, 21, 373101.

28. M. Shamsipur, A. A. M. Beigi, M. Teymouri, S. M. Pourmortazavi and M. Irandoust, Journal of Molecular Liquids, 2010, 157, 43-50.

29. M.-M. Huang, Y. Jiang, P. Sasisanker, G. W. Driver and H. Weingartner, Journal of Chemical and Engineering Data, 2011, 56, 1494-1499.

30. R. A. Marcus, Angewandte Chemie-International Edition in English, 1993, 32, 1111-1121.

31. M. Liang, A. Kaintz, G. A. Baker and M. Maroncelli, Journal of Physical Chemistry. B, 2012, 116, 1370-1384.

32. G. Sedghi, K. Sawada, L. Esdaile, M. Hoffmann, H. Anderson, D. Bethell, W. Haiss, S. Higgins and R. Nichols, Journal of the American Chemical Society, 2008, 130, 8582-8583.

33. G. Sedghi, V. M. Garcia-Suarez, L. J. Esdaile, H. L. Anderson, C. J. Lambert, S. Martin, D. Bethell, S. J. Higgins, M. Elliott, N. Bennett, J. E. Macdonald and R. J. Nichols, Nature Nanotechnology, 2011, 6, 517-523.

Chapter 5

Conclusions

5 Conclusions

The main focus of the research presented in this thesis was to investigate the viability of room temperature ionic liquids (RTILs) as a medium in single molecule electronics (SME). RTILs have considerable advantages over the more widely used media of aqueous or organic solvents, which make them an interesting choice as a medium in single molecule conductance measurements. Scanning tunnelling microscopy (STM) methods used were the current-distance STM *I*(*s*) technique, whereby the STM tip is retracted from the surface and the tunnelling current is measured as a function of distance, and the STM break junction (BJ) technique, where the tip is crashed into the surface, and then retracted and the current measured as with the *I*(*s*) measurements. Cyclic voltammetry was used to observe the electrochemical properties of redox-active systems, and polarisation modulation infrared reflection absorption spectroscopy (PM-IRRAS) was used to characterise a monolayer on the substrate surface.

The viability of RTILs as a suitable medium in SME measurements was shown by measuring the conductance of a variety of alkanedithiols of differing chain length in an ionic liquid medium, specifically 1-butyl-3-methylimidazolium trifluoromethanesulfonate (BMIOTf). The *I*(*s*) method and the BJ method were used to observe the low and medium **A** and **B** conductance groups respectively. An anomalous length dependence was observed at lower chain length, with the alkanedithiols exhibiting an exponential length dependence at chain lengths N>8. The high **C** conductance group was not observed in the RTIL medium. This was attributed to the BMIOTf affecting the surface of the Au electrodes, lowering the probability of the thiol forming a high coordination bond to the Au surface, indicative of the **C** group. The bias voltage dependence of 1,8-octanedithiol (ODT) was then measured and this was used to model the charge transport through the alkanedithiol to the Simmons model of electron transport. It was found that ODT does provide a good fit to the Simmons model, albeit with a slight deviation at high bias potentials. This was attributed to surface etching at the gold electrodes at high negative potentials. This surface etching may have an impact on the electron transfer through the molecule at such potentials, causing the deviation. It must be noted

however, that one of the advantages of RTILs is that they allow such high bias potentials to be employed, due to their wide potential window.

Once it had been made clear that the RTIL BMIOTf is a viable medium in SME, its advantages were exploited by using it as a medium to measure the conductance of the redox active molecular wire pyrrolo-tetrathiafulvalene (pyrrolo-TTF). Pyrrolo-TTF undergoes two reversible redox transitions, from pyrrolo-TTF^{0} to pyrrolo-$TTF^{\cdot+}$, and pyrrolo-$TTF^{\cdot+}$ to pyrrolo-TTF^{2+}. Only one of these redox transitions is within the potential range available to aqueous electrolytes. However, pyrrolo-TTF is a very sensitive system and undergoes a degree of protonation in the presence of water, which hinders the redox reactions. This makes the cyclic voltammetry unpredictable. Before it was clear that this was the cause of the poor voltammetry, it was thought that pyrrolo-TTF was not forming stable monolayers on the gold electrode surface. Many different procedures were attempted with little success. PM-IRRAS and mass spectrometry were used to show that the pyrrolo-TTF had not degraded and that it was indeed forming a stable monolayer on the gold surface. The protonation of pyrrolo-TTF can be avoided by using a very dry immersion solution and electrolyte. The RTIL BMIOTf was ideal as it is hydrophobic and can be vacuum dried at high temperatures to ensure a very low water content. Using BMIOTf in the immersion solution and as the electrolyte, yielded very good quality voltammetry with very clear and well-defined redox peaks. BMIOTf was then used as the electrolyte in STM $I(s)$ measurements of pyrrolo-TTF under electrochemical potential control. The conductance of pyrrolo-TTF was observed over both its redox transitions for the first time, due to the wider potential window enjoyed by BMIOTf. This is the first time such measurements have been attempted, to the best of our knowledge. When the conductance was plotted against the sample potential, the conductance showed a significant increase at the potential of the redox transitions. This conductance data was then modelled to the Kuznetsov-Ulstrup (KU) model of 2-step electron transfer with partial vibrational relaxation, which provided a good fit to the data. The previous research on pyrrolo-TTF in an aqueous electrolyte conducted by Edmund Leary in 2008 was also modelled to the KU model. It was noted that the reorganisation energy λ_{reorg} was much higher in the ionic liquid medium than in the aqueous medium. This can be explained by the Marcus Theory and outer-sphere interactions.

The outcome of the work conducted in this thesis shows that RTILs are an interesting medium in SME and it is anticipated that their use in the field will increase substantially in the near future. They offer an especially interesting avenue in the research of redox active molecular wires, particularly porphyrins and organometallic complexes which show fascinating redox behaviour, which may not be observable in conventional electrolytes.

Chapter 6

Appendix

6 Appendix

6.1 Cyclic Voltammetry of Pyrrolo-TTF

The cyclic voltammetry described in *Table 6* in chapter 3 of this thesis are shown below.

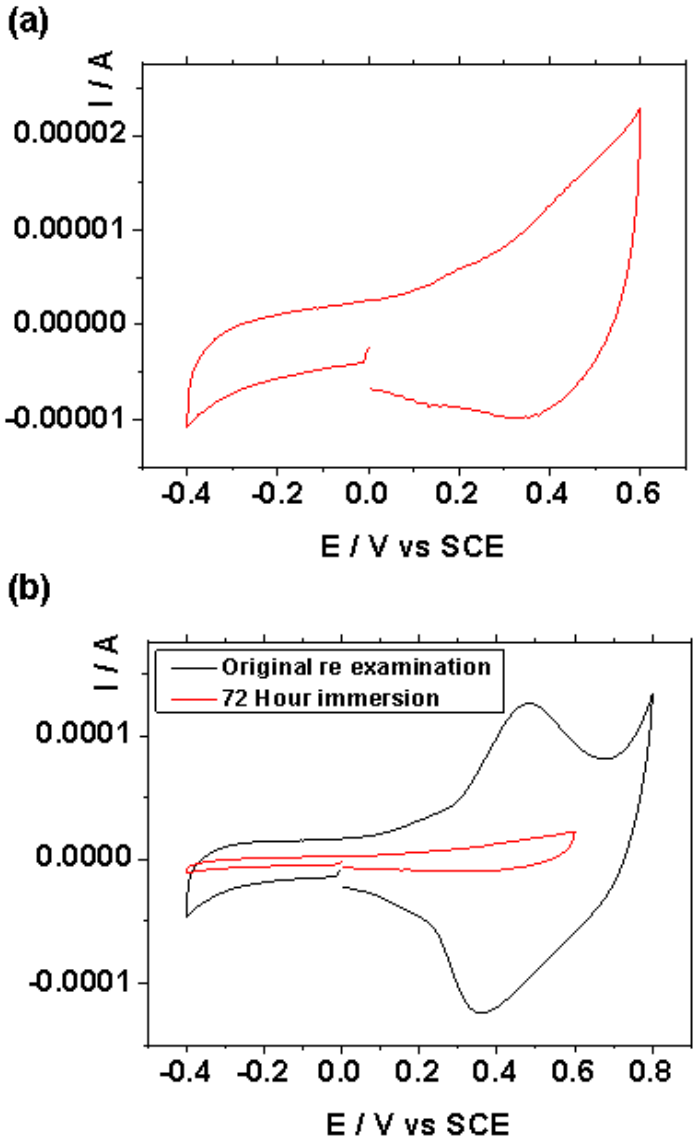

Figure A-1: *(a)* Cyclic voltammogram of pyrrolo-TTF re-examined using the procedure by Leary *et al.*[1] after approximately one year, with an immersion time of approximately 72 hours. *(b)* The second re-examination (red) shows no evidence of a redox reaction taking place, in comparison to the first re-examination (black) where the redox peaks are clearly visible.

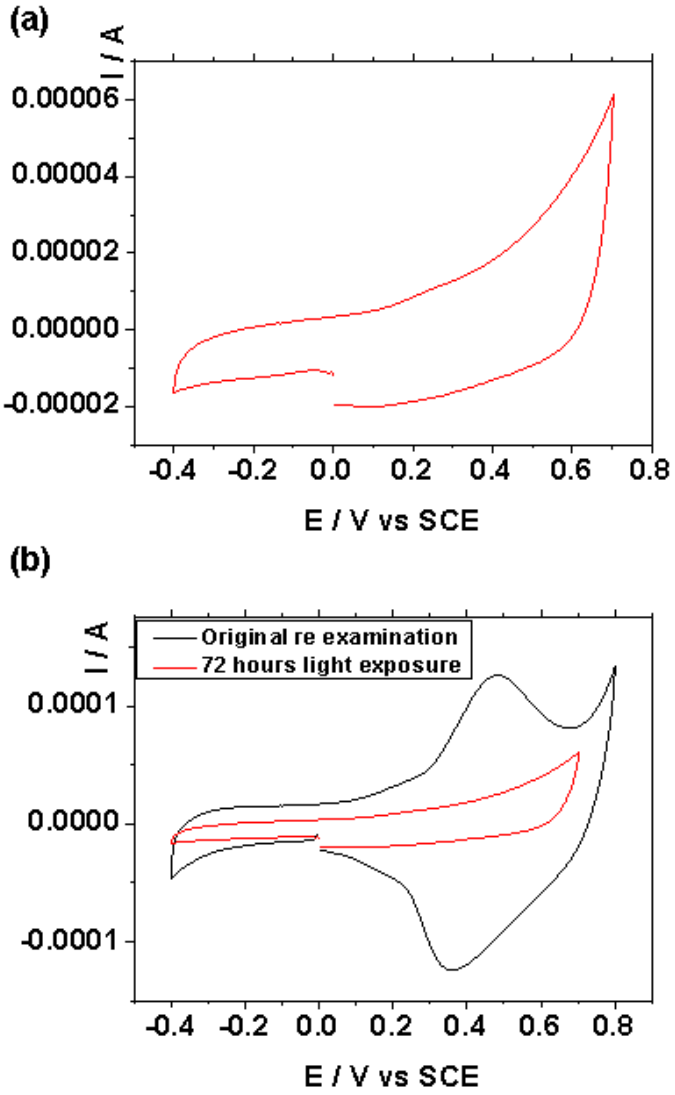

Figure A-2: *(a)* Cyclic voltammogram of pyrrolo-TTF re-examined using the procedure by Leary *et al*.[1] after approximately one year with an immersion time of approximately 72 hours and exposed to light. *(b)* The second re-examination (red) shows no evidence of a redox reaction taking place, in comparison to the first re-examination (black) where the redox peaks are clearly visible.

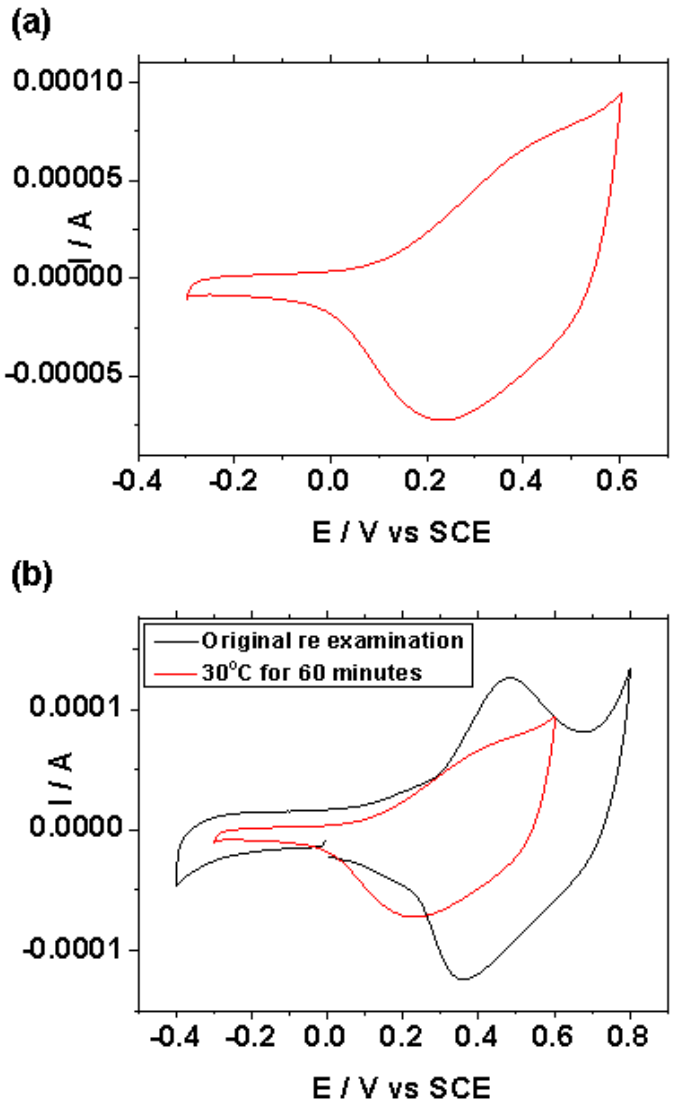

Figure A-3: *(a)* Cyclic voltammogram of pyrrolo-TTF re-examined using the procedure by Leary *et al*.[1] after approximately one year with the immersion solution heat to 30°C and the WE immersed for approximately 60 minutes. *(b)* The second re-examination (red) shows little evidence of a redox reaction taking place, in comparison to the first re-examination (black) where the redox peaks are clearly visible.

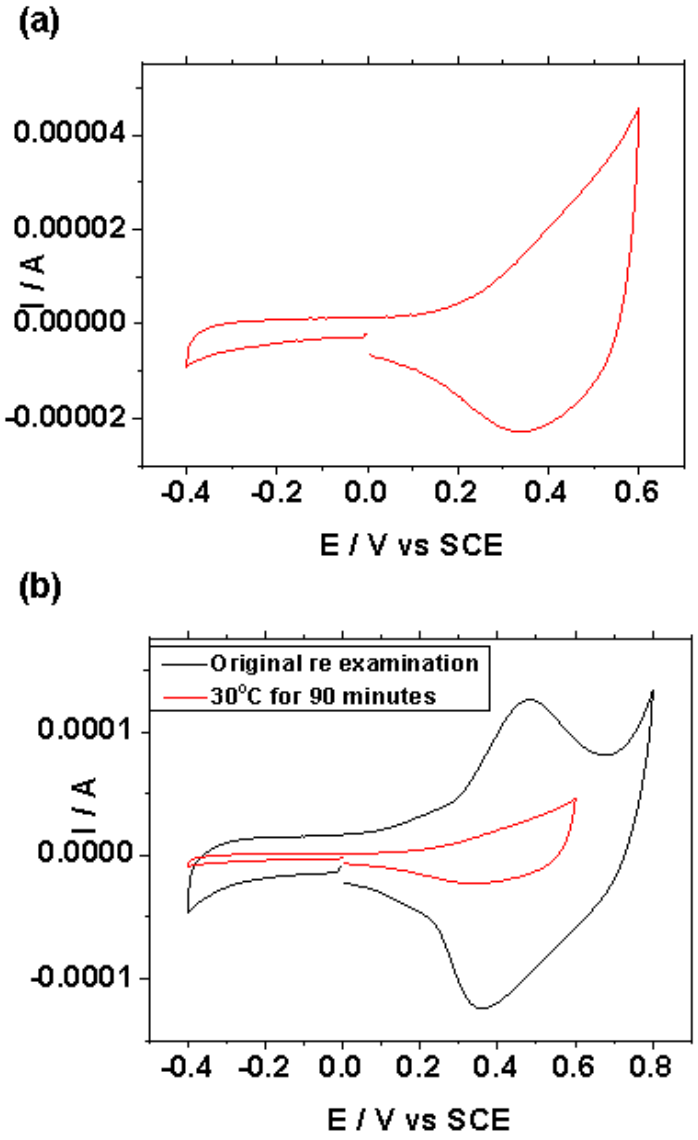

Figure A-4: *(a)* Cyclic voltammogram of pyrrolo-TTF re-examined using the procedure by Leary *et al.*[1] after approximately one year with the immersion solution heat to 30°C and the WE immersed for approximately 90 minutes. *(b)* The second re-examination (red) shows little evidence of a redox reaction taking place, in comparison to the re-examination (black) where the redox peaks are clearly visible.

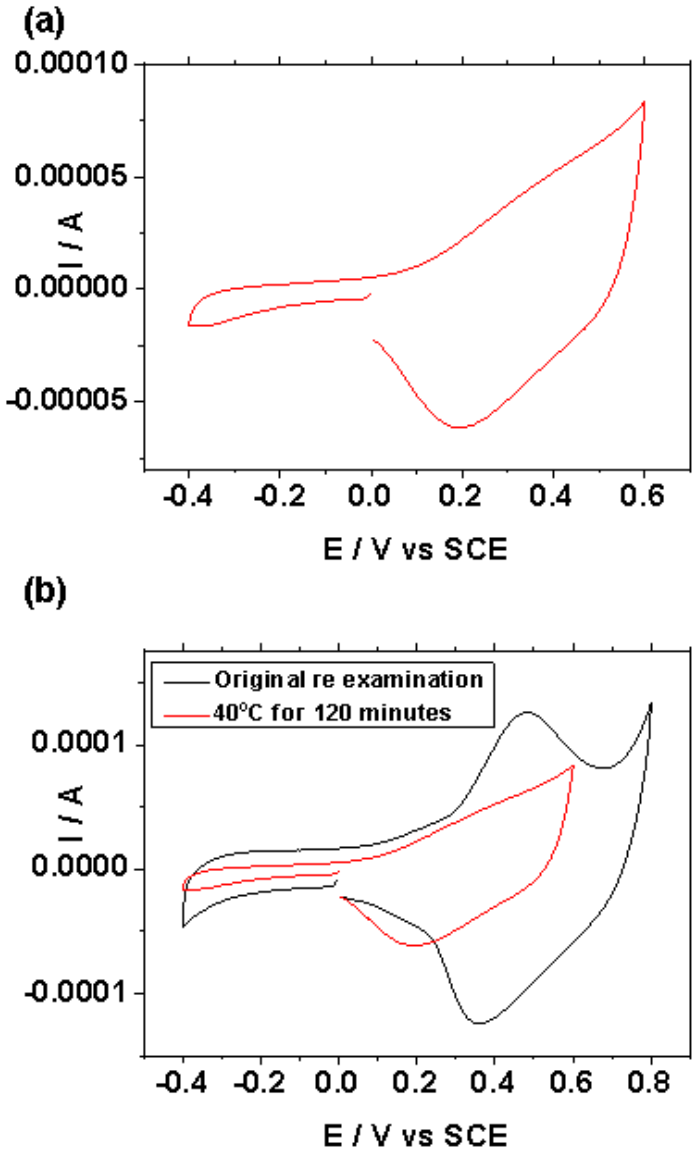

Figure A-5: *(a)* Cyclic voltammogram of pyrrolo-TTF re-examined using the procedure by Leary *et al*.[1] after approximately one year with the immersion solution heat to 40°C and the WE immersed for approximately 120 minutes. *(b)* The second re-examination (red) shows little evidence of a redox reaction taking place, in comparison to the first re-examination (black) where the redox peaks are clearly visible.

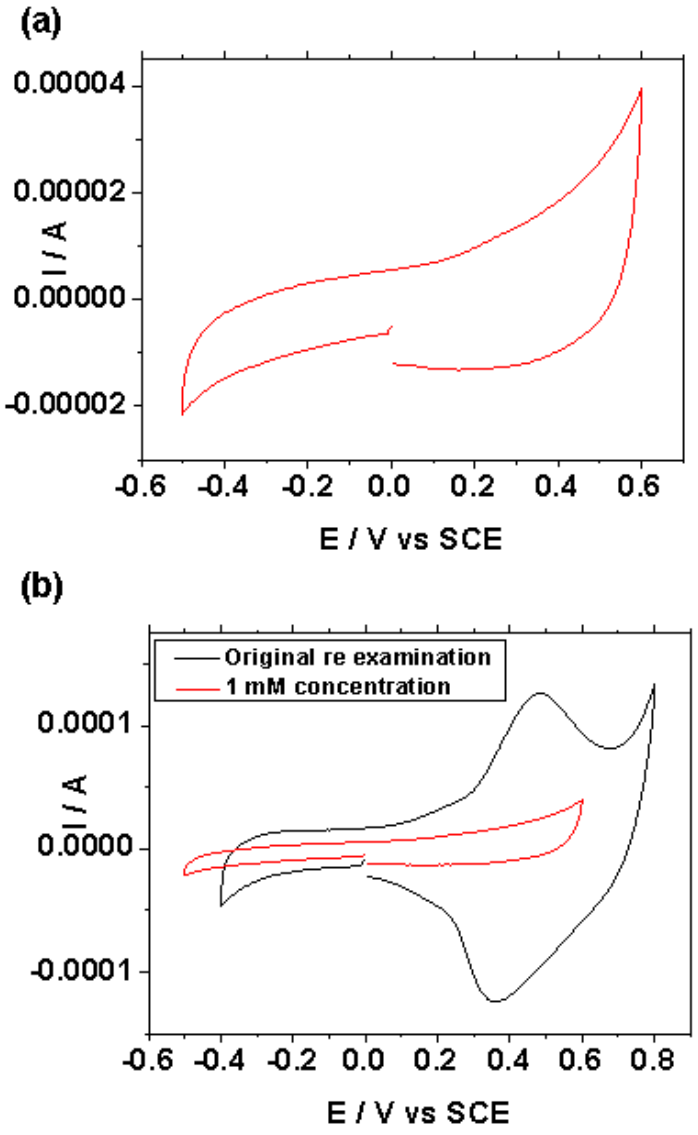

Figure A-6: *(a)* Cyclic voltammogram of pyrrolo-TTF re-examined using the procedure by Leary *et al.*[1] after approximately one year. The concentration of the immersion solution had been increased to 1 mM and the immersion time was approximately 24 hours. *(b)* The second re-examination (red) shows no evidence of a redox reaction taking place, in comparison to the first re-examination (black) where the redox peaks are clearly visible.

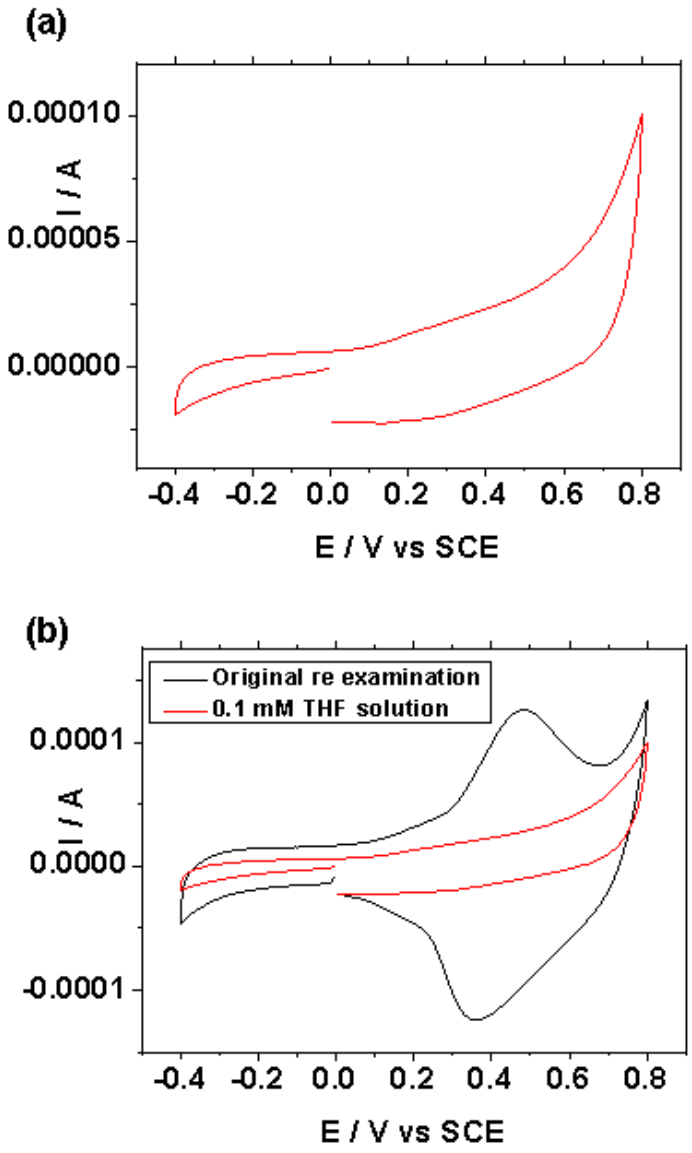

Figure A-7: *(a)* Cyclic voltammogram of pyrrolo-TTF re-examined using the procedure by Leary *et al.*[1] after approximately one year. THF was used as the solvent in place of DCM with a pyrrolo-TTF concentration of 0.1 mM. The Au(111) WE was immersed for approximately 24 hours. *(b)* The second re-examination (red) shows no evidence of a redox reaction taking place, in comparison to the first re-examination (black) where the redox peaks are clearly visible.

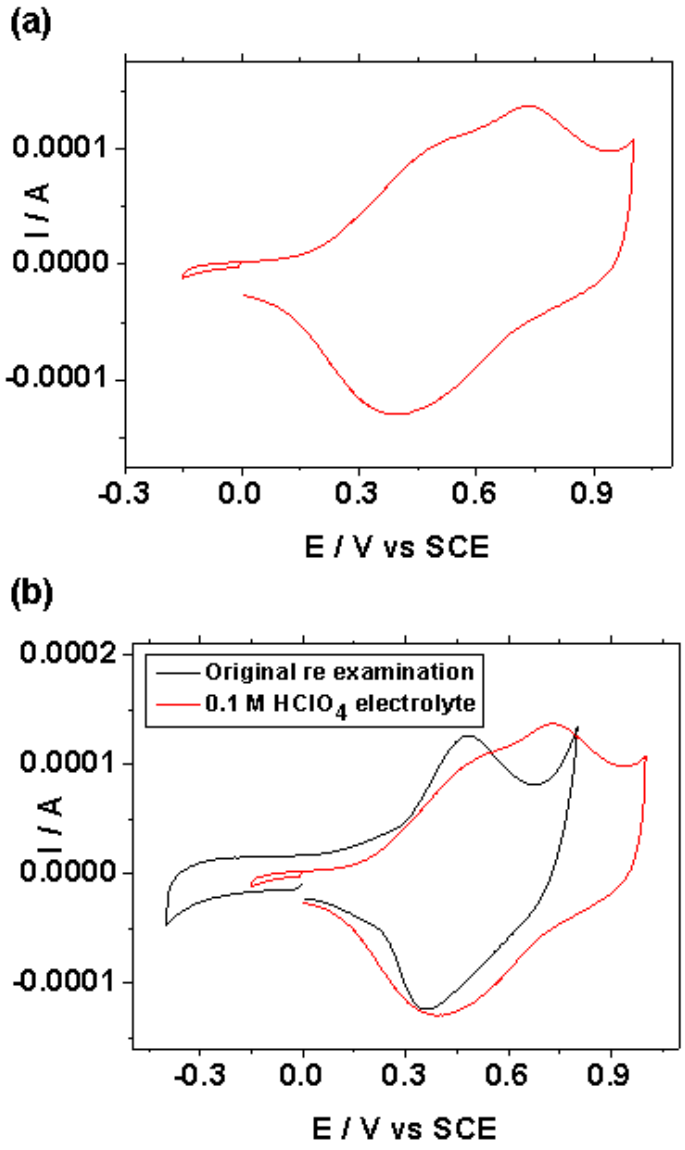

Figure A-8: *(a)* Cyclic voltammogram of pyrrolo-TTF using 0.1 M $HClO_4$ as the electrolyte. The Au(111) WE was immersed for approximately 1 hour. *(b)* The second re-examination (red) shows both of the redox reactions taking place, with two peaks visible, albeit ill-defined, in comparison to the first re-examination (black) where the redox peaks are clearly visible and well-defined.

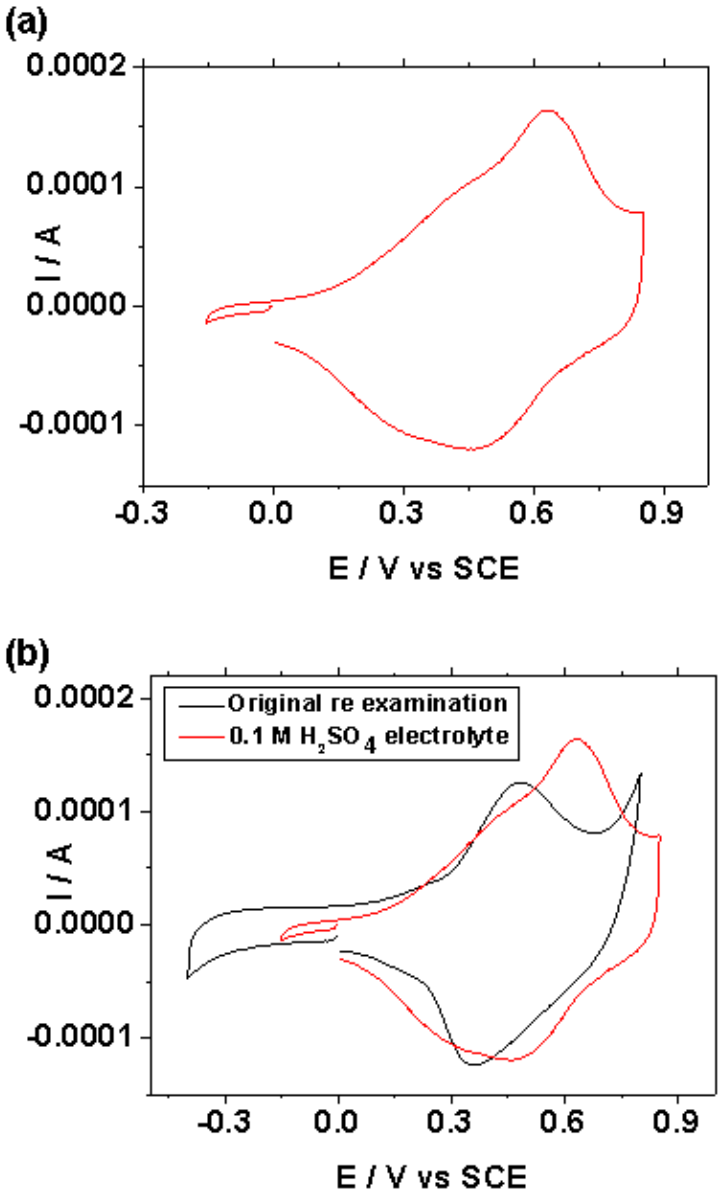

Figure A-9: Cyclic voltammogram of pyrrolo-TTF using 0.1 M H_2SO_4 as the electrolyte. The Au(111) WE was immersed for approximately 1 hour. *(b)* The second re-examination (red) shows both of the redox reactions taking place, with two peaks visible, albeit ill-defined, in comparison to the first re-examination (black) where the redox peaks are clearly visible and well-defined.

6.2 Polarisation Modulation Infrared Reflection Adsorption Spectroscopy

Polarisation Modulation Infrared Reflection Adsorption Spectroscopy (PM-IRRAS) is a surface characterisation technique, which is useful for the characterisation of a monolayer or thin film on a metal surface. A schematic of the PM-IRRAS set-up is shown in *Figure A-10* below.

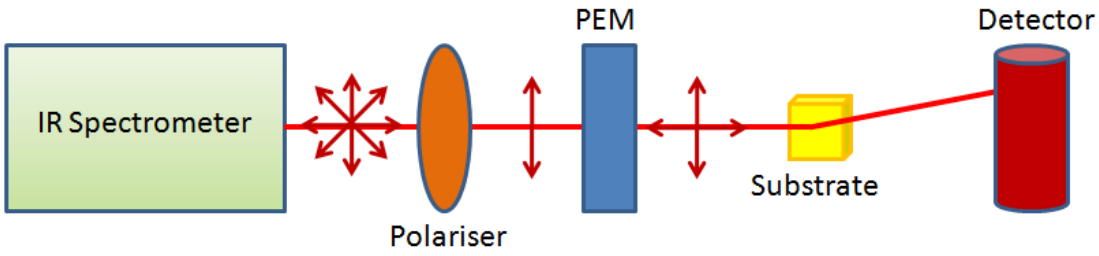

***Figure A-10*:** Schematic of the PM-IRRAS set-up. The IR beam leaves the spectrometer and is converted to s- and p-polarised light by the polariser. The PEM results in a retardation of λ/2, meaning the s- and p-polarised light are out of phase by half a wavelength. The IR beam is then reflected off the substrate into the detector.

The IR beam first passes through a polariser, which converts the unpolarised IR beam into s- and p-polarised radiation (perpendicular and parallel respectively). This polarised IR beam then passes through a photoelastic modulator (PEM). The theory behind the PEM is based on the photoelastic effect. When a light beam passes through certain types of material which have two distinct refractive indices, it splits into two beams (birefringence), which are travelling at slightly different speeds. The PEM used in the experiments is a Hinds Instruments PEM-90. This system uses a rectangular fused silica bar as the modulator, which is made to vibrate at a resonant frequency of approximately 50 kHz. This vibration is maintained by a piezoelectric transducer, which is connected to the fused silica bar. It is this vibration which induces the birefringence of the IR beam. When the modulator is relaxed, there is no change to the IR beam. However, when the modulator is stretched, the vertical component of the light beam travels slightly faster through the modulator, resulting in a retardation of the horizontal component. The opposite occurs when the modulator is compressed; the vertical component of the IR beam is then retarded as it travels at a slightly slower speed than the horizontal component through the modulator. In the PM-IRRAS set-up used, the PEM is set at a retardation of λ/2. This means that the s- and p-polarised light are out of phase by half a wavelength. This is visible in *Figure A-11* shown below.

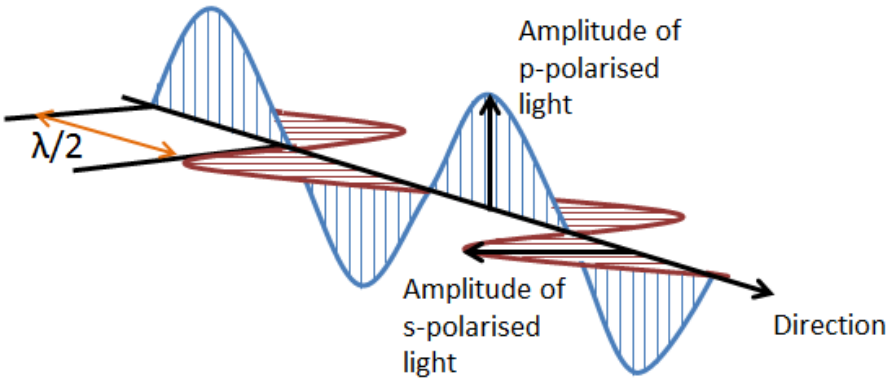

Figure A-11: Half-wave retardation of an IR beam.

The modulated IR beam is then reflected off the sample substrate at an incident angle of approximately 80°. Since the s-polarised light undergoes a phase shift of approximately 180° upon reflection from the substrate surface, it has a net amplitude of zero. On the other hand, the phase shift of p-polarised light when it is reflected off the substrate surface depends strongly on the angle of incidence, hence the incident angle being around 80°.[2] This is demonstrated in *Figure A-12* below. The p-polarised light can interact with the monolayer adsorbed onto the substrate providing that the molecule in question has a dipole moment which is perpendicular to the substrate surface as per the IR surface selection rule.

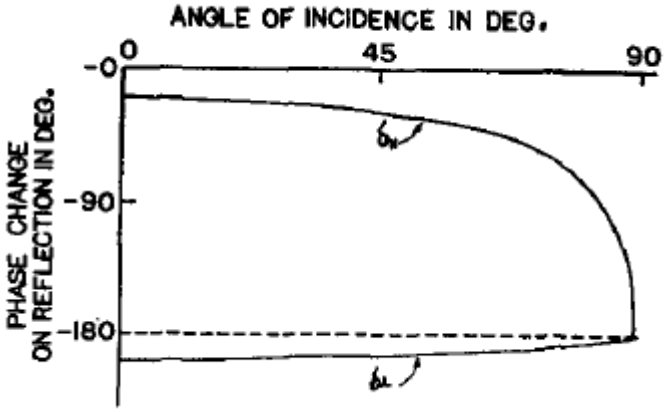

Figure A-12: How the angle of incidence varies the phase shift of the s-polarised and p-polarised light.[2] Figure taken from reference 2.

After the IR beam passes into the detector, the resulting signal is pass through a pre-amplifier and then split into a sum and difference signal by either a high pass or low pass filter. A low pass filter allows a signal with a lower frequency to pass through, which in this case is the sum (DC) signal. A high pass filter, being the opposite of the low pass filter allows a signal with higher frequency to pass through, which in this instance is the difference (AC) signal. In the case of PM-IRRAS, the high pass filter is set to 50 kHz. The signal from the high pass filter is then sent to the lock-in amplifier (LIA).

The light that reaches the detector is subject to a large amount of background noise. A LIA is required to retrieve the IR signal of interest. The LIA used in this set-up is a Stanford Research Systems SR830 DSP LIA. The signal of interest is recovered by a technique known as phase-sensitive detection, which as the name suggests, singles out a signal with a specific phase and reference frequency. The bulk of the signal received from the spectrometer is from the IR beam interacting with the atmosphere. Since both s and p-polarised light interact with the atmosphere, this signal is very large. It is only the portion of the IR beam which interacts with the substrate surface which is useful and this is very small. Since only the p-polarised light interacts with the surface, this small signal is going to have an oscillation equal to the frequency of the PEM, which is 50 kHz as discussed previously. The LIA locks onto this small signal, which it recognises due to its distinctive frequency. This reference signal is used to recognise the sample signal during the measurements meaning the sample signal from the substrate is amplified while the bulk noise signal is discarded. Both the signals from the low pass filter and high pass filter are then sent to a multiplexer (MUX) which combines the signals before they reach the analog-to-digital converter (ADC), which allows the signal to be analysed.

Within the resulting interferogram, the odd points refer to the difference signal, while the even points refer to the sum signal. This multiplexed interferogram then undergoes a Fourier Transform (FT) which results in a sum single-beam spectrum and a difference single beam spectrum. These spectra are then ratioed, which results in the differential reflectance spectrum ($\Delta R/R$).[3] In order to obtain a PM-IRRAS spectrum, differential reflectance spectra of both bare substrate (raw) and a substrate containing the self-assembled monolayer (SAM) in question (sample), are required.

The software used to analyse the spectra (OPUS) can then use the raw and sample ΔR/R spectra to create a baseline-corrected PM-IRRAS spectrum.

6.3 Gold-On-Glass Substrate

The Au(111) gold-on-glass substrates used for the STM measurements throughout this thesis are purchased from Arrandee®. This has been imaged and is shown in *Figure A-13*.

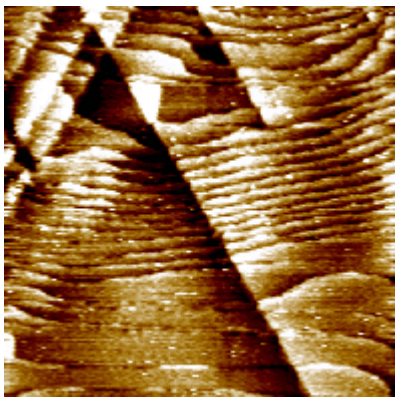

Figure A-13: STM image of gold-on-glass substrate with a Au(111) surface structure. Image is 200 by 200 nm and has a height range of 4 Å.

6.4 References

1. E. Leary, S. Higgins, H. van Zalinge, W. Haiss, R. Nichols, S. Nygaard, J. Jeppesen and J. Ulstrup, Journal of the American Chemical Society, 2008, 130, 12204-12205.

2. R. G. Greenler, Journal of Chemical Physics, 1966, 44, 310-315.

3. B. L. Frey, R. M. Corn and S. C. Weibel, in Handbook of Vibrational Spectroscopy, eds. J. Chalmers and P. Griffiths, John Wiley & Sons Ltd., 2002, vol. 2.

6.5 Publications

N. J. Kay, R. J. Nichols, S. J. Higgins, W. Haiss, G. Sedghi, W. Schwarzacher and B.-W. Mao, Journal of Physical Chemistry C, 2011, 115, 21402-21408.

L. M. Ballesteros, S. Martin, G. Pera, P. A. Schauer, **N. J. Kay**, M. Carmen Lopez, P. J. Low, R. J. Nichols and P. Cea, Langmuir, 2011, 27, 3600-3610.

THE JOURNAL OF PHYSICAL CHEMISTRY C

ARTICLE

pubs.acs.org/JPCC

Ionic Liquids As a Medium for STM-Based Single Molecule Conductance Determination: An Exploration Employing Alkanedithiols

Nicola J. Kay,[†] Richard J. Nichols,*[,†] Simon J. Higgins,[†] Wolfgang Haiss,[†] Gita Sedghi,[†] Walther Schwarzacher,[‡] and Bing-Wei Mao[§]

[†]The Chemistry Department, University of Liverpool, Liverpool L69 7ZD, United Kingdom

[‡]HH Wills Physics Laboratory, University of Bristol, Bristol, BS8 1TL, United Kingdom

[§]State Key Laboratory of Physical Chemistry of Solid Surfaces and College of Chemistry and Chemical Engineering, Xiamen University, Xiamen 361005, Fujian, P. R. China

ABSTRACT: A scanning tunnelling microscope (STM) has been used to measure the single-molecule conductance of a homologous series of α,ω-alkanedithiols in the room-temperature ionic liquid (RTIL) 1-butyl-3-methylimidazolium trifluoromethanesulfonate (BMIOTf). The alkanedithiol system is chosen because it is a well-known model system for single-molecule conductance evaluation, hence allowing us to evaluate ionic liquids as a medium for such determinations. The STM-based measurements have been made in the RTIL under environmentally controlled conditions with the exclusion of water and oxygen. Conductance values measured in the RTIL for the low (**A**) and medium (**B**) conductance groups compare very well with those previously made in different environments including air and organic solvents. Anomalous length dependence of the conductance has been observed for the shorter alkanedithiols in RTILs, and this is compared with similar previous observations for measurements in air. These measurements made on the model alkanedithiol system show that single molecule conductance can be reliably determined in ionic liquids. Indeed, given the physical attributes of ionic liquids, they are an attractive medium for such measurements.

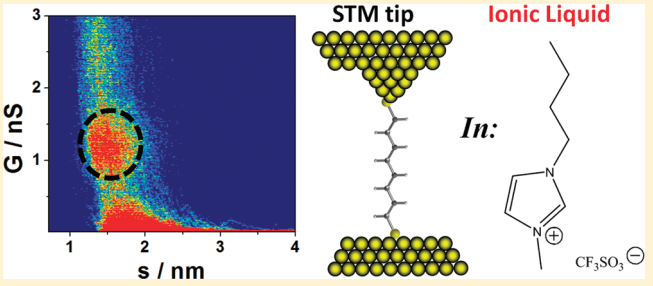

INTRODUCTION

A primary concern of the contemporary scientific field of molecular electronics is the electrical properties of small and defined assemblies of molecules within electrical junctions. Major progress has been achieved in this field over the past decade, and it is now possible to measure relatively routinely the electrical properties of molecules down to the single molecule level. This has been accomplished using experimental methods that are aimed at entrapping the molecules between a pair of electrical contacts. A number of methods have been employed to achieve this feat, including STM,[1−3] conducting AFM,[4] and mechanical break junctions.[5−9] Gold nanoparticles[10] and carbon nanotubes[11] have also been used for the electrical "wiring" of single molecules. There are several STM methods for measuring single-molecule conductance. In 2003, Xu et al.[1] developed an STM method in which molecular junctions were repeatedly formed. Metal | molecule | metal junctions were created by first establishing a metal−metal junction between a gold STM tip and a substrate and then retracting the STM tip beyond the point at which the metallic contact between tip and substrate cleaved. Molecular bridges formed within these "break-junctions" and contacts to the gold leads were provided by chemical anchoring moieties at each end of the molecular target. Thiol and pyridyl end groups were used initially[1] as chemical contacting groups, and they have been deployed in many following studies.[12−14] Statistical analysis of the junction conductance is used to reveal the single-molecule conductance. The term "in-situ break junction method" (in situ BJ method) has been coined to describe such measurements.[1] In 2003, Haiss et al. showed that molecular junctions can be formed and electrically analyzed in the absence of metal-to-metal contact between the STM tip and substrate, providing a complementary method (the current−distance or $I(s)$ method) for determining single-molecule conductance.[3] In 2004, they showed that single-molecule conductance can be determined by monitoring the stochastic formation of molecular junctions in the time domain using the current−time ($I(t)$) method.[2] These techniques, namely, the in situ BJ method, the $I(s)$ technique, and the $I(t)$ technique, have now become well-established methods for determining single-molecule conductance.

The STM and break junction techniques have been adapted for the measurement of single-molecule conductance under a range of different environments.[1] The first in situ BJ measurements were

Received: July 1, 2011
Revised: September 20, 2011
Published: September 25, 2011

performed under organic liquids containing the target molecules. Mesitylene purified by distillation was used in these first studies and has been a popular medium ever since.[1] Haiss et al. were the first to show that single-molecule conductance could be measured in an aqueous electrochemical environment.[3] This enabled single-molecule conductance changes to be followed as a function of electrochemical potential, bringing the advantages of a defined electrochemical surface science approach to single-molecule electronics.[3,15,16] A number of other environments have also been deployed for single-molecule conductance measurements using an STM, including other organic solvents (e.g., dodecane, fluorocarbons),[17] air, UHV,[18] and dry gas atmospheres such as argon.[19] The range of possible environments has provided the ability to examine how the medium (solvent and temperature) influences the conductance of single-molecule bridges.

Room-temperature ionic liquids (RTILs) are a type of molten salt with a melting point close to room temperature and high boiling points compared with common organic solvents. They are composed of organic cations and inorganic or organic anions, and they afford a very different electrolytic environment to conventional aqueous and nonaqueous electrolytes because they provide a very high volumetric density of anions and cations with no solvent. RTILs have been widely used in electrochemistry, where they have been shown to have attractive attributes. Such attributes include a wide electrochemical window, extremely low vapor pressure, wide thermal range, and dielectric and solubility properties which can be beneficial for a range of applications. They have also been used recently in defined electrochemical surface science studies, where attention has been paid to the purification of the RTILs and single-crystal substrates have been used to provide defined electrode surface structures.[20−24] Impressive, high-resolution STM imaging has been achieved in RTILs, including the imaging of surface reconstructions of Au(111)[22] and Au(100)[20] substrates as well as molecular imaging of adsorbed ionic liquid anions and cations.[20] Molecules introduced into RTIL solutions have also been imaged adsorbed on single-crystal gold electrodes, including, for example, self-assembled monolayers of the inorganic molecule $SbCl_3$.[25] These studies clearly show that RTILs are attractive media for defined electrochemical surface science studies. Scanning tunnelling spectroscopy (STS) has also been performed within an ionic liquid by Albrecht et al.[26] In such measurements, the STM tip is held at a constant height above the substrate surface and either the electrochemical potential of the substrate is swept or the tip−substrate bias voltage is swept. Such measurements have been performed for Os(II)/Os(III) containing monolayers adsorbed on Au(111) in the ionic liquid and tunnelling current enhancements have been observed around the Os(II)/Os(III) equilibrium potential.[26] However, ionic liquids have not yet been used in studies of single-molecule conductance where molecular targets are contacted chemically at both of their ends to metal leads.

The aim of the present study is to show that single-molecule conductance can be determined using an STM in a room-temperature ionic liquid. This will be demonstrated with α,ω-alkanedithiols as molecular targets. The alkanedithiols represent the most widely studied system in single-molecule electronics, and this will enable us to compare the conductance of metal | alkanedithiol | metal junctions formed in ionic liquids with values obtained in other media. Alkanedithiols are a model system for which it is well-established that charge transport through the polymethylene ($-(CH_2)_n-$) backbone occurs by tunnelling. Specific chemical interactions between the ionic liquid and polymethylene backbone are not expected, and because of the large separation between the HOMO/LUMO structure of the polymethylene chain and the Fermi levels of the gold leads, tunnelling is expected to remain as the charge-transfer mechanism on changing to the ionic liquid medium. These attributes make the alkanedithiol system a good choice for the first studies of single-molecule conductance in RTILs.

EXPERIMENTAL METHODS

All experiments were performed with an Agilent Picoplus 2500 STM system in conjunction with the PicoScan 5.3.3 software. A glass environmental chamber was connected to the STM and filled with oxygen-free nitrogen and a small amount of silica desiccant. Au STM tips were prepared by electrochemical etching of 0.25 mm gold wire (99.99%) in a 1:1 solution of HCl and ethanol at a voltage of approximately +7.0 V. The tips were then coated with a layer of apiezon wax, leaving only the very end of the tip exposed. The α,ω-alkanedithiols were used as received; 1,3 propanedithiol (1,3 PrDT) and 1,8 octanedithiol (1,8 ODT) from Alfa Aesar and 1,5 pentanedithiol (1,5 PDT), 1,6 hexanedithiol (1,6 HDT), 1,9 nonanedithiol (1,9 NDT), and 1,11 undecanedithiol (1,11 UDT) from Sigma Aldrich. Commercial gold-on-glass substrates with a chromium adhesive layer were used. These substrates were flame-annealed immediately prior to use, and the alkanedithiol molecules were then adsorbed by immersion of the substrates in 5×10^{-5} M methanolic solutions for 2 min. The substrate was then rinsed in ethanol and blown dry using nitrogen. The resulting SAMs are stable for several days. The RTIL 1-butyl-3-methylimidazolium trifluoromethanesulfonate (BMIOTf) was purchased from Iolitec and was heated to 110−120 °C with dry nitrogen flow prior to use for at least 1 h to remove any water present. The ionic liquids were handled in a glovebox environment and treated with molecular sieves to help toward removing remaining trace water. The STM environmental chamber, which contained desiccant, was purged with oxygen-free nitrogen for ∼16 h prior to measurements being taken.

Conductance measurements were performed using the $I(s)$ and BJ methods. The $I(s)$ measurements were made by performing scans from 0 to +4 nm (measured relative to the set-point) with a scan duration of 0.0946 s. For $I(s)$ measurements, a bias voltage, U_{bias}, of +0.6 V and set-point current, I_0, of 20 nA were used throughout. The resulting current−distance scans were plotted into a histogram to determine the molecular conductance. For the bias voltage dependence measurements, U_{bias} values of ±0.1, ±0.2, ±0.4, ±0.6, ±0.8, ±1.0, ±1.2, and ±1.5 V, and histograms were used to determine conductance. The BJ measurements were made by performing scans from −4 to +4 nm with a scan duration of 1 s.

The initial tip-to-sample distance (s_0) was estimated by selecting a number of exponential decay scans from each set of experiments that show no evidence of molecular bridging. For each exponential scan, ln(I) versus distance (s) was plotted, and the slope was obtained. This was then used with eq 1 to estimate the initial tip−sample separation.

$$s_0 = \frac{\ln\left(G_0.\frac{U_0}{I_0}\right)}{\mathrm{d}\ln(I)/\mathrm{d}s} \quad (1)$$

G_0 is the metal-to-metal point contact conductance (77.4 μS). The s_0 value is then added to the distance retracted (Δs) to obtain

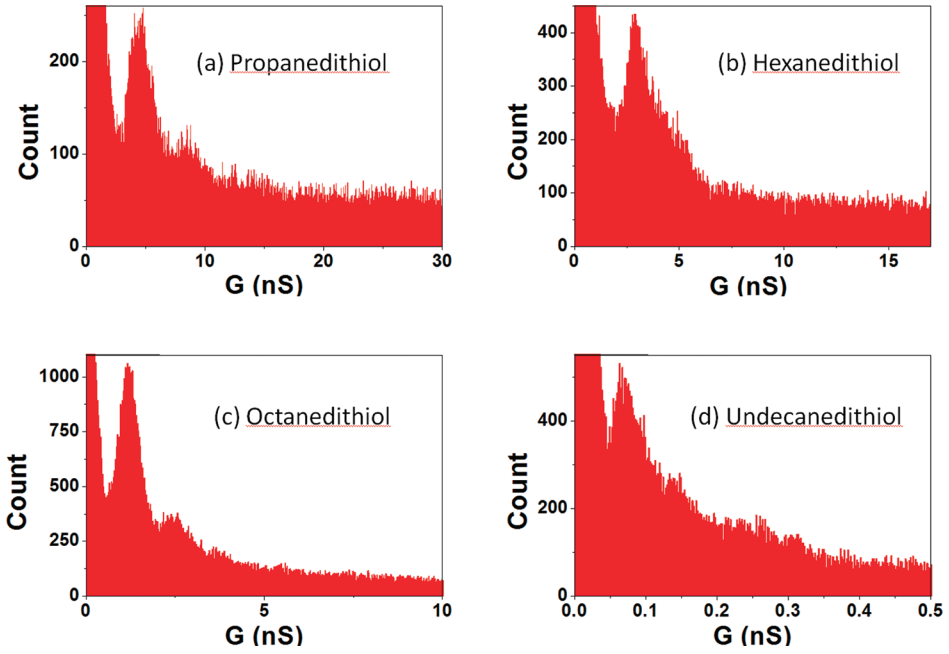

Figure 1. Conductance histograms of (a) PrDT, (b) HDT, (c) ODT, and (d) UDT on Au(111) obtained using the $I(s)$ method; U_{bias} = +0.6 V; I_0 = 20 nA; 500, 500, 538, and 503 scans were analyzed, respectively.

the tip-to-sample distance s, which in turn is used to estimate the break-off distance of the molecular bridge.

RESULTS AND DISCUSSION

The $I(s)$ technique has been used to determine the single-molecule conductance of 1,3 PrDT, 1,5 PDT, 1,6 HDT, 1,8 ODT, 1,9 NDT, and 1,11 UDT in ionic liquid. As described in the Experimental Section, BMIOTf was used as the ionic liquid, and care was taken to avoid air contact and to perform all $I(s)$ measurements under the environmental control of a dry N_2 atmosphere. $I(s)$ curves were recorded by selecting the set-point conditions of the STM (set-point current, I_0, and bias voltage U_{bias}) and then rapidly retracting the STM tip from the surface at 42.3 nm s^{-1}. About 5% of the resulting $I(s)$ curves resulted in current plateaus that are characteristic of molecules spanning the gap between the gold surface and STM tip. All $I(s)$ curves showing characteristics of molecular junction formation were used in the histogram analysis. Figure 1 shows conductance histograms for 1,3 PrDT, 1,6 HDT, 1,8 ODT, and 1,11 UDT. Each histogram is composed of at least 500 $I(s)$ scans that showed evidence of molecular bridge formation. In all of these histograms, a clear histogram peak is seen, the conductance value of which decreases markedly with molecular length.

Several differing conductance groups have been observed previously for Au | alkanedithiol | Au junctions and have been referred to as low, medium, and high (or **A**, **B**, and **C** conductance groups).[17,18,27−29] These differing conductance groups have been attributed to different ways in which the sulfur headgroup contacts with the gold leads,[12,17,27,29] although alterative explanations have been offered.[18,28] In the model proposed by Haiss et al., the **A** group is attributed to the sulfur atoms binding single Au atoms (e.g. on flat areas of the surface), whereas the **B** and **C** groups have been attributed to sulfur coordinating with multiple gold atoms at the contact.[29] It has been previously shown that using the $I(s)$ technique at relatively low set-point currents and with a high-sensitivity STM current preamplifier favors the observation of the low conductance (**A**) group,[12,29] whereas higher conductance groups can be additionally observed at high set-point current values or when using the in situ break junction technique. By choosing appropriate set-point current conditions in the $I(s)$ technique, or by using the in situ BJ technique, it is possible to focus selectively on either the **A** group or high current groups.[12,29] To collect the data in Figure 1, we used the $I(s)$ technique under relatively low set-point current conditions. These conditions can be viewed as a low-pass filter of the data in that they lead to the favored observation of the **A** group. We therefore assign all histogram peaks in Figure 1 to the **A** (low) conductance group.

To observe high conductance groups, we have used the in situ BJ technique developed by Xu and Tao.[1] Because this involves initially driving the STM tip into the gold substrate, the currents at the start of the tip retraction are much higher and less defined than in the $I(s)$ technique. As we record our in situ BJ data with much higher set-point currents, observation of relatively high conductance currents are favored. The resulting histograms for 1,3 PrDT, 1,6 HDT, 1,8 ODT, and 1,11 UDT are shown in Figure 2. In each case, a defined conductance peak is seen, which is of much greater conductance than the respective values observed in Figure 1. The conductance values obtained from Figure 2 are not an integer multiple of the respective **A** group values in Figure 1, so they cannot simply be attributed to multiple molecules in the junction. Instead, they are assigned to the higher conductance **B** group. Interestingly, no clear **C** (high conductance) group is observed at higher conductance, as has been observed for measurements in organic solvents such as mesitylene or under ambient conditions in air.[12,17,18,28,29] This observation is discussed later.

Although the conductance histograms enable ready identification of molecular conductance values, the distance data of the $I(s)$ or in situ BJ scans is lost. A 2-D histogram representation retains the distance data. An example of a 2-D histogram for

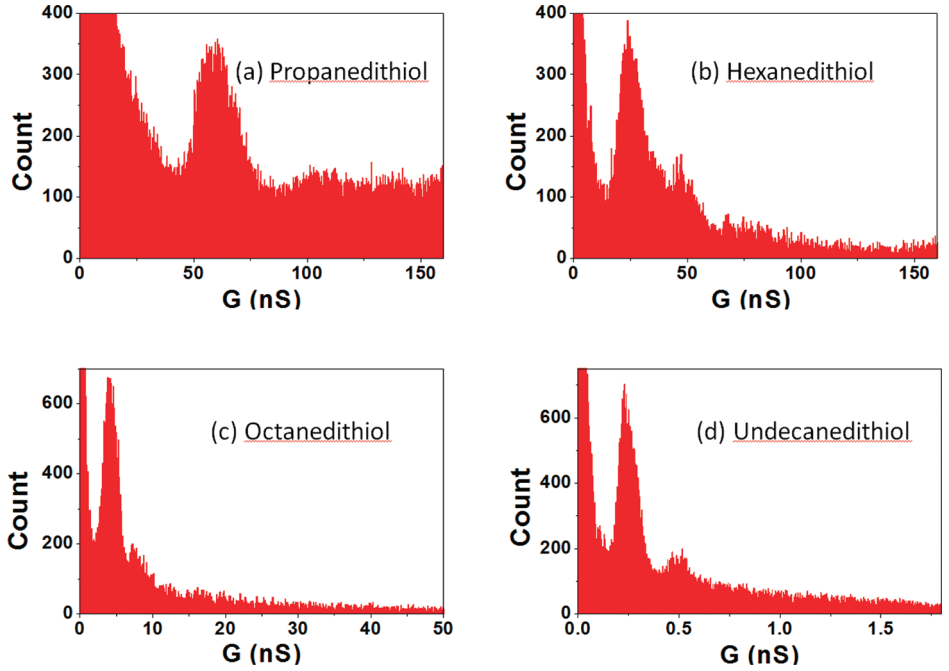

Figure 2. Conductance histograms of (a) PrDT, (b) HDT, (c) ODT, and (d) UDT on Au(111) obtained using the BJ method; U_{bias} = +0.6 V; I_0 = 20 nA; 501, 507, 504, and 505 scans were analyzed, respectively.

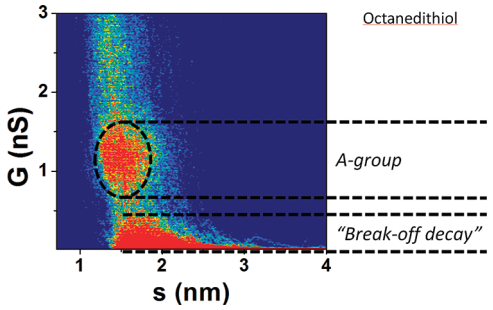

Figure 3. 2-D histogram of ODT showing the conductance and tip-displacement of ODT using the $I(s)$ method including 538 scans. The low conductance group **A** is clearly visible and a defined "break-off tail" is observed at low conductance values, as marked.

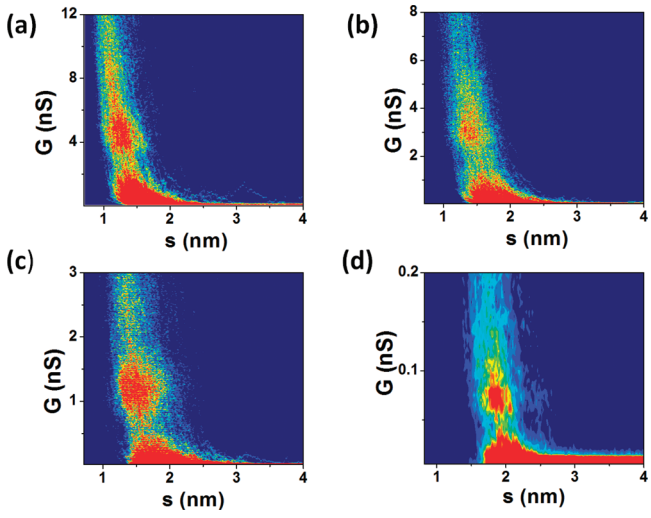

Figure 4. 2-D histograms of (a) PrDT, (b) HDT, (c) ODT, and (d) UDT on Au(111) obtained using the $I(s)$ method previously described. The low conductance group **A** and break-off region is visible on all histograms. The streaking seen on the 2-D histogram of UDT arises as a larger bin size was required because of the very low conductance of this system.

octanedithiol is shown in Figure 3. Conductance is shown on the y axis, and tip-to-substrate separation is shown on the x axis. The color scaling represents the density of points having a high conductance, ranging from low (darker blue) to high (red). To construct this 2-D plot, we employed a bin size of 0.012 nS for the conductance data and a bin size of 0.015 nm for the distance data. In this plot, the distance is the actual tip-to-sample separation, rather than just the distance retracted from the set-point distance at the start of the $I(s)$ retraction scan. The tip-to-sample distance (s) is obtained by adding the distance retracted (Δs) to an estimated value for the initial tip-to-sample distance (s_0). This procedure is explained in the Experimental Section. The **A** group can be clearly picked out in the 2-D histogram, and it is marked with the dashed ellipse. Another high point-density (red) region is observed at low current (conductance) values, and this corresponds to the break-off regions of the $I(s)$ curves, which lead to a current decay as the molecular bridge is broken. Analogous 2-D plots are shown for 1,3 PrDT, 1,6 HDT, and 1,11 UDT alongside the 1,8 ODT data in Figure 4. In each case, the **A** conductance group can be clearly identified, and it can be associated with a distance range, which increases in the order 1,3 PrDT, 1,6 HDT, 1,8 ODT, and 1,11 UDT, as expected from the lengths of the molecules. Noise and streaking is more apparent on the 2-D histograms for 1,11 UDT because these measurements are for the lowest conductance values.

2-D histograms are also constructed for 1,3 PrDT, 1,6 HDT, 1,8 ODT, and 1,11 UDT using the in situ BJ technique, and these are shown in Figure 5. In each case, the **B** conductance group can

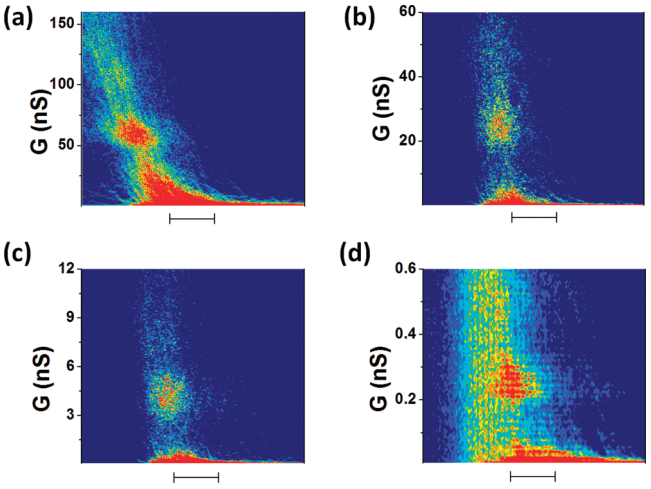

Figure 5. 2-D histograms of (a) PrDT, (b) HDT, (c) ODT, and (d) UDT on Au(111) obtained using the in situ BJ method. The medium conductance group **B** is visible on all histograms. *X* axis scale bar = 1 nm.

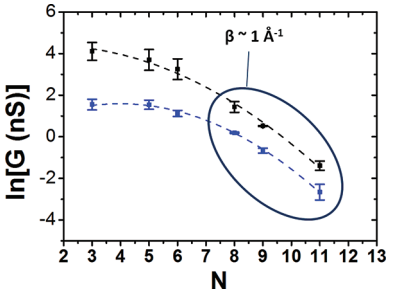

Figure 6. Logarithm of the low conductance group **A** (blue) and medium conductance group **B** (black) measured for alkanedithiols in ionic liquid between Au contacts as a function of the number of CH_2 groups (N) at U_{bias} = +0.6 V. When $N > 8$ the conductance decays exponentially as a function of length with a decay factor $\beta \approx 1$ Å^{-1}.

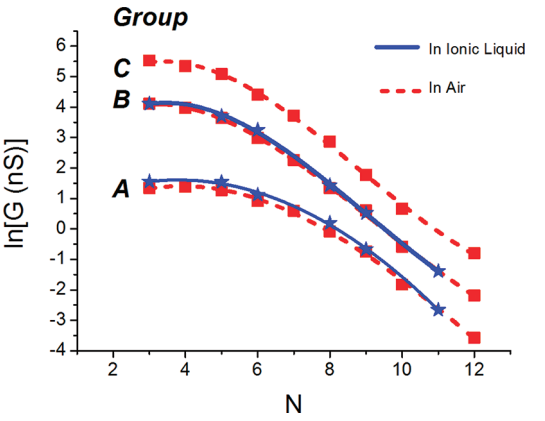

Figure 7. Comparison of the logarithm of the conductance group values as a function of the number of CH_2 groups of alkanedithiols under ambient air conditions (red) and under ionic liquid (blue). The ambient air data used for comparison have been taken from ref 30.

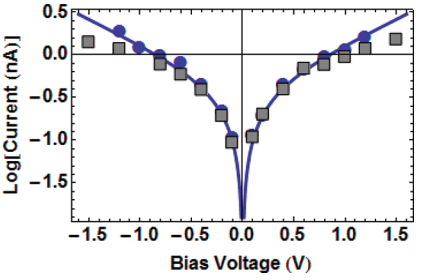

Figure 8. Current through ODT as a function of U_{bias} measured by the $I(s)$ method for the conductance group **A** in air[30] (blue circles) and in ionic liquid (gray squares). The fit line is to the Simmons equation; the height and width of the uncorrected barrier are 2 eV and 1.4 nm, respectively. With image charge correction, these values become 1.36 eV and 1.26 nm, respectively. α was calculated to be 0.52. The ambient air data used for comparison have been taken from ref 30.

be identified. Here a distance scale bar is shown rather than an absolute tip-to-sample separation because there is greater uncertainty in this value due to the initial metallic contact between tip and sample and the subsequent breaking of the metallic contact. Nevertheless, the **B** conductance group and its spatial extension can be readily identified from these 2-D histograms.

The collected single-molecule conductance data for the six alkanedithiols investigated and the **A** and **B** group values observed in each case are shown in Figure 6, which plots the logarithm of the conductance against number of carbons in the polymethylene chain (N). For the longer molecules (N = 8 and upward), the conductance decays exponentially with molecular length, with a exponential decay factor (β) of ~1 Å^{-1}. This value is consistent with other measurements in the literature, and the conductance values also lie close to those reported in ref 30 for measurements under ambient conditions. Figure 7 compares the present data for the single-molecule conductance of alkanedithiol in ionic liquids with data recorded under ambient air conditions taken from ref 30. This Figure shows that the data for the **A** and **B** groups in ionic liquid and air practically superimpose. The **C** group, which was observed in the air measurements, has, however, not been observed for the ionic liquid measurements. Because the appearance of differing conductance groups has been related to different molecule−substrate coordination possibilities, it is suggested that the **C** form is unobtainable or occurs with relatively low probability in the ionic liquids. The high conductance **C** group has been previously associated to adsorption of the thiol end group at more highly coordinated sites such as step edges or alongside gold adatoms.[12,29] It would then appear that **C** group sites are less favorable for the measurements in ionic liquid environments, even with in situ formed break junctions. Because the surface chemistry of the Au(111) surface in RTILs will be very different from that in aqueous or organic liquid environments, notably because of the adsorption of the concentrated ionic solvent species of the RTIL in the former case, it is not surprising that different contact configurations are achieved in both cases.

In addition to the length dependence of the single-molecule conductance, we have also studied the bias voltage dependence of the **A** conductance group of 1,8 octanedithiol, and this is shown in Figure 8. The data recorded in ionic liquid lie close to that in ambient air apart from deviations at the higher bias voltages. These deviations may arise because of the effect of the ionic liquid on the Au electrodes at the higher bias voltages. It has been found that at more extreme potentials the surface of the Au electrodes undergoes a degree of restructuring due to adsorption of the cationic species BMI^+.[20] Lin et al. found that pits on the

order of ~1 nm were formed when a potential between −0.9 and −2.0 V with respect to SCE was applied.[31] This surface etching may have an effect on the electron transport through any adsorbed molecular bridges and may contribute to the deviation from the Simmons model. The fit line is to the Simmons model with image charge-corrected values of 1.36 eV and 1.26 nm for the corrected barrier height and width, respectively. The fitting parameter α is related to the effective mass (m_{eff}) of the tunnelling hole/electron, where $m_e\alpha^2 = m_{eff}$, and the solid fit line corresponds to $\alpha = 0.52$. This value of α corresponds to an effective hole mass of ($0.28m_e$, where m_e is the rest mass) and, as previously noted,[30] this is very close to theoretical predictions for hole tunnelling through octanedithiol.[32]

The length dependence of the single-molecule conductance data recorded in ionic liquid, which is shown in Figure 7, also exhibits the same curvature as the data from the ambient air experiments. In both cases, for short molecules, the decay of conductance becomes less pronounced as the molecular length decreases, and it reaches a length-independent conductance for the shortest molecular bridges ($N < 5$). This has been previously referred to as an "anomalous length dependence" because simple barrier tunnelling models predict an almost constant exponential decay factor (β) as a function of the number of CH_2 groups (N).[30] No definitive theory has been put forward to explain this anomalous behavior, but it has been suggested that this may arise from the influence of image potential on the effective mass of the tunnelling electron (hole).[30] It was found that by making this effective mass an adjustable parameter in the Simmons model for barrier tunnelling both the experimentally determined length dependence and voltage dependence for Au | alkanedithiol | Au junction conductance could be fitted.[30] It seems likely that the effective mass of the tunnelling hole may well be influenced by image charge effects and the length of the molecule, but more sophisticated theoretical models than the Simmons equation (even when corrected for static image charge effects) are still needed to describe these anomalous length effects more satisfactorily.

CONCLUSIONS

In summary, we demonstrate that ionic liquids can be used as media for recording single molecule conductance. This is demonstrated for a series of α,ω-alkanedithiols in BMIOTf (ionic liquid), and conventional conductance histograms and 2-D conductance-junction length histograms are presented. Data recorded for a series of alkanedithiols show that single-molecule conductance values for the low (**A**) and medium (**B**) conductance groups are very similar for ionic liquid and air measurements, respectively. In both cases, an anomalous length dependence is observed, with the longer bridges exhibiting exponential decay factors (β) of ~1 $Å^{-1}$, whereas for short bridges ($N < 5$), the molecular conductance reaches a length-independent conductance. These measurements made on the model α,ω-alkanedithiol system show that single-molecule conductance can be reliably determined in ionic liquids. Ionic liquids offer several attractive features for single-molecule conductance determination. First, they have a wide electrochemical window, which offers us the possibility to study single molecule conductance for a much wider range of electrochemically active molecular targets than have been addressed to date. Second, they offer a wider thermal range than organic liquids and aqueous solutions, which have been the media most commonly used in single-molecule studies. Exploring a wide thermal range is of great assistance when analyzing charge-transport mechanisms through molecular bridges and in quantifying thermal activation processes. We believe that these attributes will lead to their wider deployment in molecular electronics, and we are currently investigating the single molecular conductance of electrochemically active molecular bridges in such media.

AUTHOR INFORMATION

Corresponding Author

*E-mail: nichols@liv.ac.uk. Phone: +44 151 794 3533. Fax: +44 151 794 3588.

ACKNOWLEDGMENT

This work was supported by EPSRC under grants EP/H001980/1 and EP/H002227/1.

REFERENCES

(1) Xu, B. Q.; Tao, N. J. J. *Science* **2003**, *301*, 1221.
(2) Haiss, W.; Nichols, R. J.; Higgins, S. J.; Bethell, D.; Hobenreich, H.; Schiffrin, D. J. *Faraday Discuss.* **2004**, *125*, 179.
(3) Haiss, W.; van Zalinge, H.; Higgins, S. J.; Bethell, D.; Hobenreich, H.; Schiffrin, D. J.; Nichols, R. J. *J. Am. Chem. Soc.* **2003**, *125*, 15294.
(4) Cui, X. D.; Primak, A.; Zarate, X.; Tomfohr, J.; Sankey, O. F.; Moore, A. L.; Moore, T. A.; Gust, D.; Harris, G.; Lindsay, S. M. *Science* **2001**, *294*, 571.
(5) Reed, M. A.; Zhou, C.; Muller, C. J.; Burgin, T. P.; Tour, J. M. *Science* **1997**, *278*, 252.
(6) Kergueris, C.; Bourgoin, J. P.; Palacin, S.; Esteve, D.; Urbina, C.; Magoga, M.; Joachim, C. *Phys. Rev. B.* **1999**, *59*, 12505.
(7) Weber, H. B.; Reichert, J.; Weigend, F.; Ochs, R.; Beckmann, D.; Mayor, M.; Ahlrichs, R.; von Lohneysen, H. *Chem. Phys.* **2002**, *281*, 113.
(8) Smit, R. H. M.; Noat, Y.; Untiedt, C.; Lang, N. D.; van Hemert, M. C.; van Ruitenbeek, J. M. *Nature* **2002**, *419*, 906.
(9) Huber, R.; Gonzalez, M. T.; Wu, S.; Langer, M.; Grunder, S.; Horhoiu, V.; Mayor, M.; Bryce, M. R.; Wang, C. S.; Jitchati, R.; Schonenberger, C.; Calame, M. *J. Am. Chem. Soc.* **2008**, *130*, 1080.
(10) Dadosh, T.; Gordin, Y.; Krahne, R.; Khivrich, I.; Mahalu, D.; Frydman, V.; Sperling, J.; Yacoby, A.; Bar-Joseph, I. *Nature* **2005**, *436*, 677.
(11) Guo, X. F.; Gorodetsky, A. A.; Hone, J.; Barton, J. K.; Nuckolls, C. *Nat. Nanotechnol.* **2008**, *3*, 163.
(12) Nichols, R. J.; Haiss, W.; Higgins, S. J.; Leary, E.; Martin, S.; Bethell, D. *Phys. Chem. Chem. Phys.* **2010**, *12*, 2801.
(13) Tao, N. J. *Nat. Nanotechnol.* **2006**, *1*, 173.
(14) Quek, S. Y.; Kamenetska, M.; Steigerwald, M. L.; Choi, H. J.; Louie, S. G.; Hybertsen, M. S.; Neaton, J. B.; Venkataraman, L. *Nat. Nanotechnol.* **2009**, *4*, 230.
(15) Leary, E.; Higgins, S. J.; van Zalinge, H.; Haiss, W.; Nichols, R. J.; Nygaard, S.; Jeppesen, J. O.; Ulstrup, J. *J. Am. Chem. Soc.* **2008**, *130*, 12204.
(16) Pobelovt, I. V.; Li, Z. H.; Wandlowski, T. *J. Am. Chem. Soc.* **2008**, *130*, 16045.
(17) Li, X. L.; He, J.; Hihath, J.; Xu, B. Q.; Lindsay, S. M.; Tao, N. J. *J. Am. Chem. Soc.* **2006**, *128*, 2135.
(18) Fujihira, M.; Suzuki, M.; Fujii, S.; Nishikawa, A. *Phys. Chem. Chem. Phys.* **2006**, *8*, 3876.
(19) Leary, E.; Hobenreich, H.; Higgins, S. J.; van Zalinge, H.; Haiss, W.; Nichols, R. J.; Finch, C. M.; Grace, I.; Lambert, C. J.; McGrath, R.; Smerdon, J. *Phys. Rev. Lett.* **2009**, *102*, 086801.
(20) Su, Y. Z.; Fu, Y. C.; Yan, J. W.; Chen, Z. B.; Mao, B. W. *Angew. Chem., Int. Ed.* **2009**, *48*, 5148.
(21) Su, Y. Z.; Fu, Y. C.; Wei, Y. M.; Yan, J. W.; Mao, B. W. *ChemPhysChem* **2010**, *11*, 2764.
(22) Atkin, R.; Borisenko, N.; Druschler, M.; El Abedin, S. Z.; Endres, F.; Hayes, R.; Huber, B.; Roling, B. *Phys. Chem. Chem. Phys.* **2011**, *13*, 6849.

(23) Pajkossy, T.; Kolb, D. M. *Electrochem. Commun.* **2011**, *13*, 284.
(24) Gnahm, M.; Pajkossy, T.; Kolb, D. M. *Electrochim. Acta* **2010**, *55*, 6212.
(25) Fu, Y. C.; Su, Y. Z.; Wu, D. Y.; Yan, J. W.; Xie, Z. X.; Mao, B. W. *J. Am. Chem. Soc.* **2009**, *131*, 14728.
(26) Albrecht, T.; Moth-Poulsen, K.; Christensen, J. B.; Hjelm, J.; Bjornholm, T.; Ulstrup, J. *J. Am. Chem. Soc.* **2006**, *128*, 6574.
(27) Haiss, W.; Nichols, R. J.; van Zalinge, H.; Higgins, S. J.; Bethell, D.; Schiffrin, D. J. *Phys. Chem. Chem. Phys.* **2004**, *6*, 4330.
(28) Li, C.; Pobelov, I.; Wandlowski, T.; Bagrets, A.; Arnold, A.; Evers, F. *J. Am. Chem. Soc.* **2008**, *130*, 318.
(29) Haiss, W.; Martin, S.; Leary, E.; van Zalinge, H.; Higgins, S. J.; Bouffier, L.; Nichols, R. J. *J. Phys. Chem. C* **2009**, *113*, 5823.
(30) Haiss, W.; Martin, S.; Scullion, L. E.; Bouffier, L.; Higgins, S. J.; Nichols, R. J. *Phys. Chem. Chem. Phys.* **2009**, *11*, 10831.
(31) Lin, L. G.; Wang, Y.; Yan, J. W.; Yuan, Y. Z.; Xiang, J.; Mao, B. W. *Electrochem. Commun.* **2003**, *5*, 995.
(32) Tomfohr, J. K.; Sankey, O. F. *Phys. Rev. B* **2002**, *65*, 245105.

Langmuir

ARTICLE

pubs.acs.org/Langmuir

Directionally Oriented LB Films of an OPE Derivative: Assembly, Characterization, and Electrical Properties

Luz M. Ballesteros,[†,‡] Santiago Martín,[†,‡] Gorka Pera,[†,‡] Phil A. Schauer,[§] Nicola J. Kay,[∥] María Carmen López,[†,‡] Paul J. Low,[§] Richard J. Nichols,[∥] and Pilar Cea[†,‡,*]

[†]Departamento de Química Física, Facultad de Ciencias, Universidad de Zaragoza, 50009 Spain

[‡]Instituto de Nanociencia de Aragón (INA), edificio I+D+I, C/Mariano Esquilor s/n Campus Rio Ebro, 50018 Zaragoza, Spain

[§]Department of Chemistry, University of Durham, Durham DH1 3LE, United Kingdom

[∥]Department of Chemistry, University of Liverpool, Crown Street, Liverpool, L69 7ZD United Kingdom

ABSTRACT: Langmuir films have been fabricated from 4-[4′-(4″-thioacetyl-phenyleneethynylene)-phenyleneethynylene]-aniline (NOPES) after cleavage of the thioacetyl protecting group. Characterization by surface pressure vs area per molecule isotherms and Brewster angle microscopy reveal the formation of a high quality monolayer at the air−water interface. One layer Langmuir−Blodgett (LB) films were readily fabricated by the transfer of the NOPES Langmuir film onto solid substrates. X-ray photoelectron spectroscopy (XPS), surface polarization-modulated infrared reflection−absorption spectroscopy (PM-IRRAS), and quartz crystal microbalance (QCM) experiments conclusively demonstrate the formation of one layer LB films in which the functional group associated with binding to the substrate can be tailored by the film transfer conditions. Using LB methods this molecule could be transferred to gold samples with either the amine or thiol group attached to the gold surface. The amine group is directly attached to the gold substrate (Au-NH_2-OPE-SH) when the substrate is initially immersed in the subphase and withdrawn during the transfer process; in contrast, monomolecular films in which the thiolate group is attached to the gold substrate (Au-S-OPE-NH_2) are obtained when the substrate is initially out of the subphase and immersed during the transfer process. The morphology of these films was analyzed by atomic force microscopy (AFM), showing the formation of homogeneous layers. Film homogeneity was confirmed by cyclic voltammetry, which revealed a large passivation of gold electrodes covered by NOPES monolayers. Electrical properties for both polar orientated junctions have been investigated by scanning tunnelling microscopy (STM), with both orientations featuring a nonrectifying behavior.

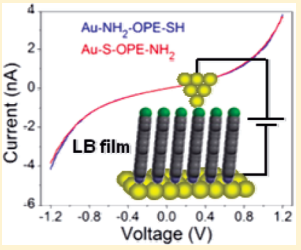

INTRODUCTION

Metal−molecule−metal junctions are convenient models that can be used to explore the structural and electronic factors affecting electrical transport through molecules. In these junctions individual molecules or molecular assemblies are contacted by two metal electrodes, and a growing number of experimental techniques are now being utilized to fabricate and measure charge transport through such junctions. These techniques include break and contact junctions formed in which one contact is based on the tip of either a scanning tunnelling microscope (STM)[1−6] or a conducting atomic force microscope (c-AFM).[7−10]

Molecular conductance values obtained from metal−molecule−metal junctions depend not only on the inherent molecular features of the junction, but also on other important parameters such as the metal−molecule contact; small variations in the nature or characteristics of the metal−molecule contact can often have a pronounced effect on charge transport in the junction.[11,12] Consequently, the exploration of different organic−metal contacts is a matter of current interest in order to determine the role that the interface plays in measurements of the conductance of single molecules or assembles of molecules.[13−15] The gold−sulfur contact has been widely used for connecting molecules to metal surfaces, but other combinations are also known.[3,16−21] In this context, the amino group is also a convenient functionality for coupling the molecules to metal surfaces in molecular junctions.[16,22−25]

To date the major focus on conductance studies of molecular assemblies has been centered on "symmetric" molecules, where the respective chemical contacting groups at either end of the molecule that bind to the electrode surfaces are identical. However, systems where the contacting groups at either end of the molecule are different are also of potential interest for a number of reasons, such as facilitating efficient contact to different electrode materials or directed orientation of molecules between pairs of nonsimilar electrodes.[26−30] One of the best-known and most widely employed techniques to fabricate well-ordered monolayers on metal surfaces is the self-assembly (SA) method since it permits the fabrication of thin films with high internal order and homogeneous arrangements. Certain limitations are nevertheless inherent to this fabrication method, such as the requirement for specific sites of interaction with the substrate and restrictions on the nature of both the surface material and chemical contacting group. In addition, there is an inherent ambiguity in determining the surface-bound group when utilizing

Received: November 28, 2010
Revised: January 24, 2011
Published: March 03, 2011

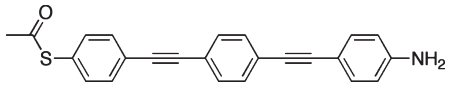

Figure 1. 4-[4′-(4″-Thioacetyl-phenyleneethynylene)-phenyleneethynylene]-aniline (thioacetyl protected NOPES).

molecular wires which have different terminal groups at each ends, when both of which are capable of binding to the substrate (we refer to such molecules with different terminal chemical groups at each end as "antisymmetric" molecular wires).

Prompted by this picture of the current landscape, we have sought to employ alternative self-assembly methodologies for the preparation of oriented molecular films from an "antisymmetric" oligomeric phenylene ethynylene oligomer (OPE) derivative, namely 4-[4′-(4″-thioacetyl-phenyleneethynylene)-phenyleneethynylene]-aniline (Figure 1, NOPES). OPE derivatives exhibit a wide range of interesting physicochemical properties[31−35] and have been shown to act as molecular wires[36−41] and other components for molecular electronics.[42−44] The majority of these OPE derivatives have been introduced into metal-molecule-metal based device structures in the form of self-assembled monolayers. The Langmuir−Blodgett (LB) technique is an alternative method that permits the formation of well-ordered molecular films on surfaces. From a device point of view, the LB method is especially interesting due to the capacity of the technique to form not only chemisorbed films but also physisorbed films, which significantly broadens the range of molecular systems and surfaces that can be employed in a junction.[45] In this regard NOPES allows for a comparative study of junctions in which either the thiol functional group that is revealed after removal of the acetyl protecting group or amine is initially bound to the substrate. In this paper we will demonstrate that the LB technique provides a method for selectively anchoring the NOPES molecule to the substrate through either nitrogen or sulfur based functional groups, depending on the movement direction of the substrate during the film transfer step, affording a stable and controlled monomolecular architecture. In addition, this OPE derivative does not feature a poorly conductive terminal alkyl-chain tail, which has been included in many OPE derivatives previously assembled into highly ordered molecular films by the LB technique.[14,46−49] The direct connections between the conjugated skeleton of the molecule through functional groups with the gold substrate and the gold tip of the STM are expected to improve the conductance through these molecular assemblies.

EXPERIMENTAL SECTION

General Synthetic Conditions. All reactions were carried out under an atmosphere of nitrogen using standard Schlenk techniques. Nonaqueous solvents were purified and dried using an Innovative Technology SPS-400, or in the case of NEt_3 by distillation from $CaSO_4$, and degassed before use. No special precautions were taken to exclude air or moisture during workup. The compounds 1-ethynyl-4-((4′-aminophenyl)ethynylene)benzene,[50] 1-iodo-4-thioacetylbenzene,[51] $[PdCl_2(PPh_3)_2]$,[52] and $[Pd(P^tBu_3)_2]$[53] were prepared by the literature methods. Other reagents were purchased and used as received. NMR spectra were recorded on a Varian VNMRS-700 spectrometer from $CDCl_3$ solutions and referenced against residual solvent resonances ($CDCl_3$, δ_H 7.26 ppm/δ_C 77.16 ppm). IR spectra were recorded on a Nicolet-6700 spectrometer utilizing samples prepared as a Nujol mull suspended between NaCl plates. Electrospray ionization mass spectra were recorded on an Acquity LCT Premier XE (Waters UK Ltd.) TOF mass spectrometer.

Synthesis of 4-[4′-(4″-Methylthioacetate-Phenylethynyl)-Phenylethynyl]-Aniline (Thioacetyl Protected NOPES).

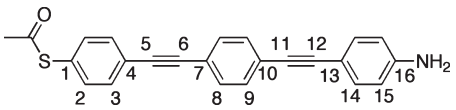

A Schlenk flask was charged with 1-iodo-4-thioacetylbenzene (258 mg, 0.928 mmol), 1-ethynyl-4-((4′-aminophenylene)ethynylene) benzene (200 mg, 0.922 mmol), $[PdCl_2(PPh_3)_2]$ (61 mg, 0.086 mmol) and CuI (15 mg, 0.079 mmol) and triethylamine (20 mL) to give a suspension. The mixture was stirred at ambient temperature for 20 h, and the resulting precipitate collected, washed with hexane, and subsequently purified through silica gel chromatography by elution with 1:1 dichloromethane:hexane. Recrystallization of the main fraction from tetrahydrofuran/methanol afforded the title compound as a yellow powder (130 mg, 0.36 mmol, 39%). A similar reaction using 5 mol % $[Pd(P^tBu_3)_2]$/CuI as catalyst afforded the protected form of NOPES in ca. 60% isolated yield. IR/cm^{-1}: 3468 (w), 3372 (m), 2206 (m), 2173 (w), 1687 (s), 1620 (m), 1607 (m), 1596 (m), 1585 (m), 1519 (s). ^1H NMR: δ (ppm) 7.550 (d, 2H, $^3J_{HH}$ = 8.37 Hz, H3), 7.474 (m, 4H, H9 and H8), 7.400 (d, 2H, $^3J_{HH}$ = 8.37 Hz, H2), 7.342 (d, 2H, $^3J_{HH}$ = 8.56 Hz, H14), 6.642 (d, 2H, $^3J_{HH}$ = 8.56 Hz, H15), 3.843 (br.s, 2H, NH_2), 2.437 (s, 3H, Ac). $^{13}C\{^1H\}$ NMR: δ (ppm) 193.57 (CO), 147.02 (C13), 134.37 (C2), 133.20 (C14), 132.30 (C3), 131.70 (C9/C8), 131.41 (C9/C8), 128.31 (C1), 124.57 (C4), 124.33 (C10/C7), 122.09 (C10/C7), 114.89 (C15), 112.46 (C16), 92.53 (C12), 91.11 (C11/C6), 90.27 (C5), 87.31 (C11/C6), 30.44 (Me). ES^+-MS: m/z 368.3 $[M+H]^+$. HR-ES^+-MS calcd. for $C_{24}H_{18}N_1O_1S_1$ ($[M+H]^+$): m/z 368.1109; found: 368.1123.

Film Fabrication and Characterization. The films were prepared on a Nima Teflon trough with dimensions 720 × 100 mm^2, which was housed in a constant temperature (20 ± 1 °C) clean room. A Wilhelmy paper plate pressure sensor was used to measure the surface pressure (π) of the monolayers. The subphase was an aqueous (Millipore Milli-Q, resistivity 18.2 MΩ cm) solution of HCl (pH 3.0) in which the amine groups are expected to be protonated, leading to a more expanded isotherm due to the repulsive Coulombic forces between the positively charged amine groups, which should reduce the formation of 3D aggregates at the air−water interface. Three μL of concentrated NH_4OH were added to 5 mL of a 10^{-5} M solution of the protected NOPES derivative in 4:1 chloroform:ethanol (both HPLC grade, 99.9%, Sigma-Aldrich). This mixture was incubated at room temperature for 15 min to deprotect the thioacetyl group and generate the free NOPES molecule in solution. To construct the Langmuir films the deprotected NOPES solution was spread by a syringe held very close to the surface, allowing the surface pressure to return to a value close to zero between each addition. After waiting about fifteen minutes to allow the solvent to evaporate, slow compression of the film began at a speed of 0.025 nm^2/(molecule min). The use of ethanol in the spreading solvent serves to limit the formation of hydrogen-bonded amine aggregates. Under these experimental conditions the isotherms were highly reproducible. The direct visualization of the monolayer formation at the air/water interface was studied using a commercial mini-Brewster angle microscope (mini-BAM) from Nanofilm Technologie GmbH, Göttingen, Germany.

The monolayers at the air−water interface were transferred onto solid supports at a constant surface pressure by the vertical dipping method (dipping speed was 6 mm/min) onto cleaved mica, gold, or quartz substrates. Deposition of the monolayer onto quartz substrates during the downstroke process required a pretreatment of the substrates

with the aim of obtaining a good deposition ratio (the substrates were immersed for 24 h in hexamethyldisilazane, 99.9% Sigma-Aldrich). All the substrates were initially dried under N_2 flow for 1 h, followed by drying for at least 24 h in a desiccator before being subjected to the different characterization techniques. Quartz crystal microbalance (QCM) measurements were carried out using a Stanford Research Systems instrument and with AT-cut, α-quartz crystals with a resonant frequency of 5 MHz and circular gold electrodes patterned on both sides. UV−visible (UV−vis) spectra of the LB films were acquired on a Varian Cary 50 spectrophotometer and recorded using a normal incident angle with respect to the film plane.

X-ray photoelectron spectroscopy (XPS) spectra were acquired on a Kratos AXIS ultra DLD spectrometer with a monochromatic Al Kα X-ray source (1486.6 eV) using a pass energy of 20 eV. The photoelectron takeoff angle was 90° with respect to the sample plane. To provide a precise energy calibration, the XPS binding energies were referenced to the C1s peak at 284.6 eV. The thickness of LB films on gold substrates was estimated using the attenuation of the Au 4f signal from the substrate according to $I_{\text{LB film}} = I_{\text{substrate}} \exp(-d/\lambda \sin \theta)$, where d is the film thickness, $I_{\text{LB film}}$ and $I_{\text{substrate}}$ are the average of the intensities of the Au $4f_{5/2}$ and Au $4f_{7/2}$ peaks attenuated by the LB film and from bare gold, respectively, θ is the photoelectron takeoff angle, and λ is the effective attenuation length of the photoelectron (4.2 ± 0.1 nm).[54] Surface polarization-modulated infrared reflection−absorption spectroscopy (PM-IRRAS) was performed using a Bruker PMA37 coupled with a Bruker IFS 66v/s Fourier transform infrared spectrometer. A Hinds Instruments PEM-90 Photoelastic Modulator and a Stanford Research Systems Model SR830 DSP lock-in amplifier were also employed. The software used was Bruker Opus 5.5. The spectra are an average of 500 scans and the resolution was 2 cm^{-1}. Atomic force microscopy (AFM) experiments were performed by means of a multimode extended microscope with Nanoscope IIIA electronics from Digital Instruments, using tapping mode. The data were collected with a silicon cantilever provided by Nanoworld, with a force constant of 42 mN/m and operating at a resonant frequency of 285 kHz. The images were collected with a scan rate of 1 Hz, an amplitude set point lower than 1 V, and in ambient air conditions.

Cyclic voltammetry (CV) experiments were carried out in an electrochemical cell containing three electrodes. The working electrode was made of a gold substrate modified by the deposited LB film, the counter electrode was a platinum sheet, and the reference electrode was Ag|AgCl|saturated KCl.

An Agilent STM running Picoscan 4.19 software was used for the characterization of the electrical properties of the LB films. In these measurements the tip potential is referred to as U_t. STM tips were freshly prepared for each experiment by etching of a 0.25 mm Au wire (99.99%) in a mixture of HCl (50%) and ethanol (50%) at +2.4 V. Gold films employed as substrates were purchased from Arrandee, Schroeer, Germany. These were flame-annealed at approximately 800−1000 °C with a Bunsen burner immediately prior to use. This procedure is known to result in atomically flat Au(111) terraces.[55]

RESULTS AND DISCUSSION

Fabrication of Langmuir and Langmuir−Blodgett Films. Figure 2 illustrates a reproducible surface pressure−area per molecule (π−A) isotherm of a NOPES Langmuir film fabricated onto an aqueous HCl subphase. The π−A isotherm is characterized by a zero surface pressure in the 1.8−0.65 nm^2/molecule range, featuring a lift-off at ca. 0.65 nm^2/molecule followed by a monotonous increase of the surface pressure upon compression. Brewster angle microscopy (BAM) investigations were made during the compression of the Langmuir film and gave further insight to the characteristics of the monolayer (inset of Figure 2). It is important to note that in spite of the tendency for molecules

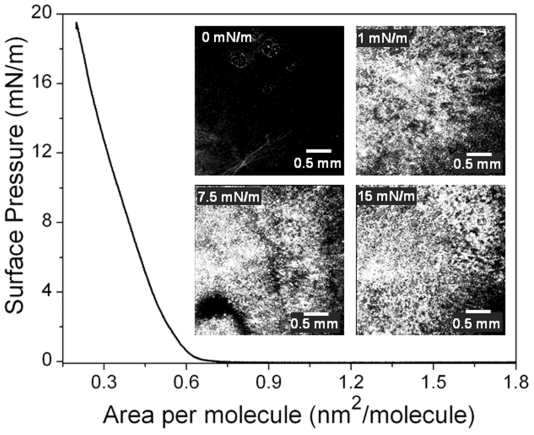

Figure 2. Surface pressure versus area per molecule isotherm of NOPES on a HCl aqueous subphase (pH 3.0) at 20 °C, and, inset, BAM images of NOPES at the air−liquid interface at the indicated surface pressures. The field of view along the x axes for the BAM images is 1650 μm.

containing polyaromatic moieties to aggregate because of strong π−π lateral interactions, no three-dimensional aggregates were observed in BAM images under the experimental conditions used to fabricate these films. A rapid increase in the brightness of the monolayer after the lift-off is indicative of an increase in the tilt angle of the molecules with respect to the water surface. At higher surface pressures (e.g., 15 mN/m) BAM images show that the monolayer almost totally covers the water surface.

Langmuir monolayers were transferred onto solid substrates (cleaved mica, gold, and quartz) by the vertical dipping method at 15 mN/m since this is the optimum surface pressure for transference according to AFM data (vide infra). Specifically, two deposition modes were explored (Scheme 1):

(1) When the substrates were initially inside the water subphase and they were withdrawn, a monolayer was deposited onto the substrates with a transfer ratio of 1. This deposition rate was also assessed using a quartz crystal microbalance (QCM). Thus, the frequency change (Δf) for a QCM quartz resonator before and after the deposition process was determined. Taking into account the Sauerbrey equation[56]

$$\Delta f = -\frac{2f_0^2 \Delta m}{A \rho_q^{1/2} \mu_q^{1/2}} \qquad (1)$$

where f_0 is the fundamental resonant frequency of 5 Hz, Δm is the mass change (g), A is the electrode area, ρ_q is the density of the quartz (2.65 g/cm^3), and μ_q is the shear modulus (2.95×10^{11} dyn/cm^2). Using the Sauerbrey equation the surface coverage (Γ) is determined as 6.7×10^{-10} mol/cm^2. This value is in excellent agreement with that estimated for the saturated surface coverage, 6.7×10^{-10} mol/cm^2, determined from the molecular area of NOPES at the air−water interface at a surface pressure of 15 mN/m. X-ray photoelectron spectroscopy (XPS) was used to provide some insight into the organization of NOPES molecules onto a gold substrate deposited under these experimental conditions. An XPS spectrum of the S2p region for a powdered sample of acetyl-protected NOPES (Figure 3, top), together with the spectrum of a one layer LB film of the deprotected sample deposited

Scheme 1. Organization of the NOPES Molecules in the LB Films Formed When the Substrate Is: (a) Initially Immersed in the Subphase and (b) Outside the Subphase before Starting the Transfer Process

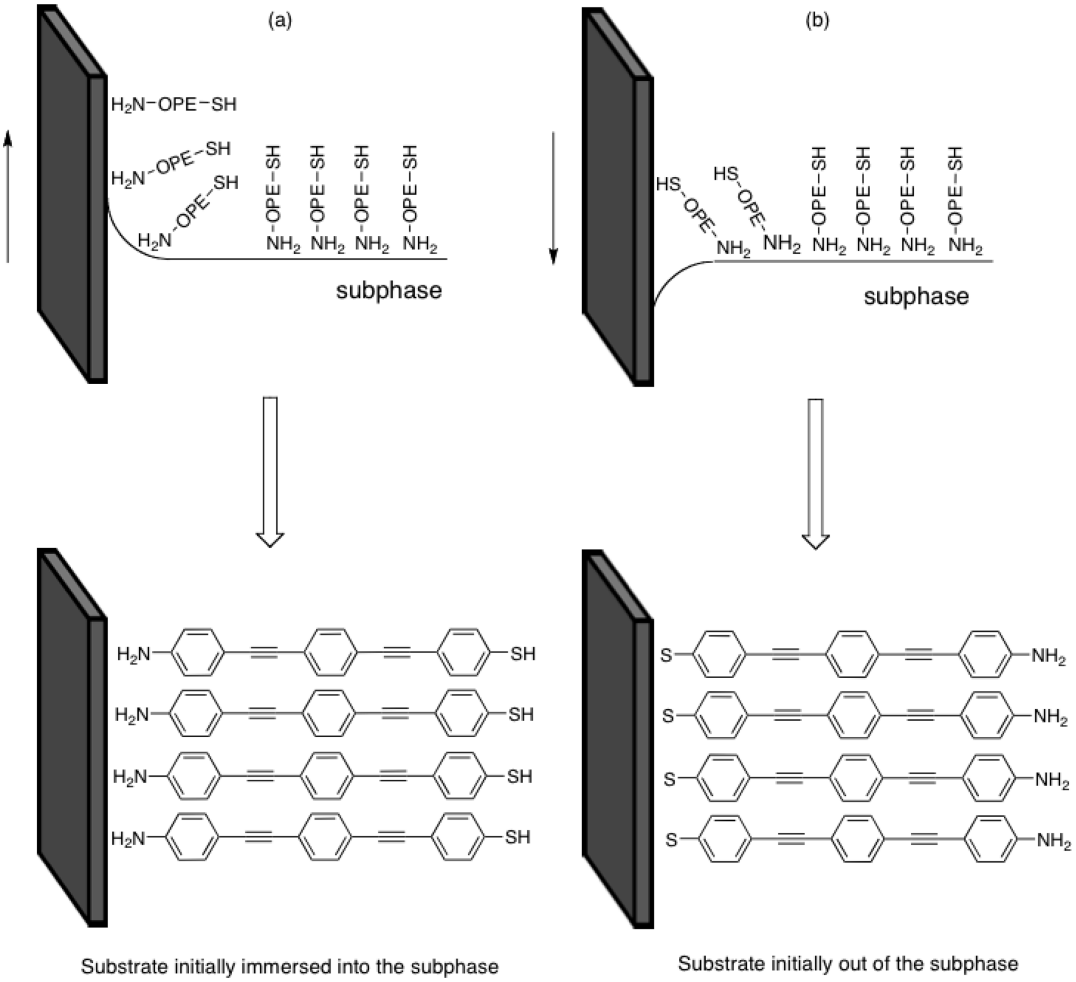

onto a substrate initially immersed in the subphase (Figure 3, middle), are shown in Figure 3. The XPS spectrum of the LB film (Figure 3, middle) features a doublet at 164.52 and 163.20 eV. The binding energies for this doublet are associated with thiol species not bound to the Au surface,[57,58] in agreement with the doublet at 164.78 and 163.38 eV observed for a solid sample of the acetyl-protected NOPES powder (Figure 3, top), both of which correspond to an organic sulfur-containing group. The doublet at 162 eV ($sp_{3/2}$), which is characteristic of a thiolate-gold bond,[57,59] is clearly not present in the spectrum of this film. Therefore, these results seem to indicate that when the substrate is initially immersed in the subphase, the NOPES molecules are attached to the gold substrate by the amine group (Scheme 1). More evidence supporting this conclusion will be provided later on. Henceforward, we will refer to these films as Au-NH_2-OPE-SH for brevity.

(2) Substrates initially out of the subphase were immersed into the water subphase when the monolayer had reached a surface pressure of 15 mN/m (Scheme 1). The deposition process took place during the downstroke of the substrate with a transfer ratio of ca. 1. Under these conditions, the QCM experiments revealed a surface coverage of 6.5×10^{-10} mol cm^{-2}, again in very good agreement with the surface density at the air−water interface. Figure 3, bottom shows the XPS spectrum of a one layer film transferred during the downstroke of the substrate. This spectrum features a doublet at 161.70 and 160.50 eV characteristic of a thiolate−gold bond.[57,59] The doublet at 164.78 and 163.38 eV, associated with organic sulfur species that do not interact with the Au surface[57,58] is not observed. These results suggest that the molecules are chemisorbed onto the gold substrate through connection to the thiol group, resulting in a thiolate−gold bond. These films are designated as Au-S-OPE-NH_2. Finally, it should be noted that the spectra obtained just after mounting the sample in the XPS and after long irradiation time showed not differences in the position of the peaks revealing that no degradation of the samples took place.

Conclusive information regarding the orientation of the LB films was obtained through surface polarization-modulated infrared reflection−absorption spectroscopy (PM-IRRAS). Representative spectra of the two types of LB films and a self-assembled (SA, prepared by immersion of a gold substrate into a NOPES $CHCl_3$ solution for 24 h) film are shown in Figure 4. The

dx.doi.org/10.1021/la104734j |*Langmuir* 2011, 27, 3600–3610

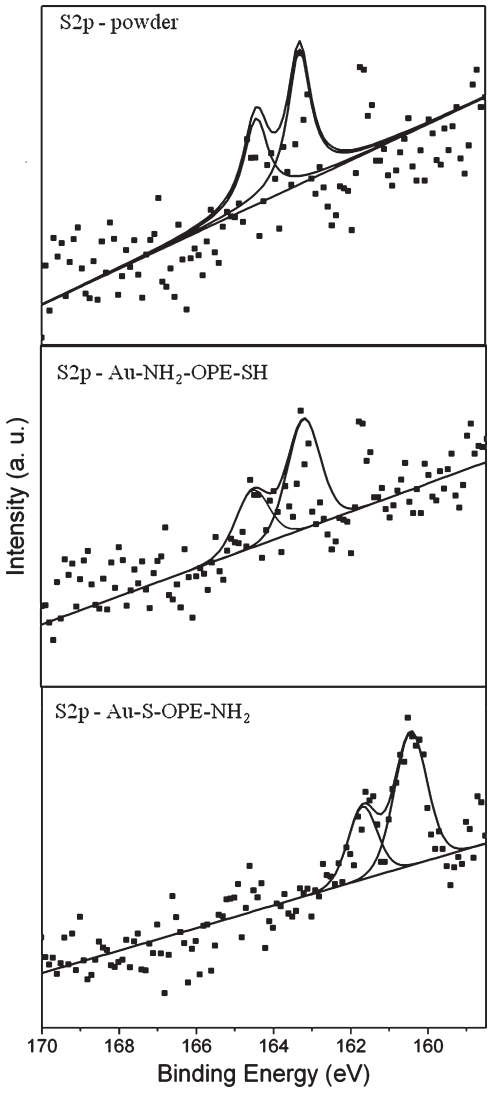

Figure 3. XPS spectra of the S2p region for the powder (top), and for a one-layer LB film deposited at 15 mN/m onto a gold electrode with the substrate initially immersed into the subphase (middle) and out of the subphase (bottom).

magnitude of the PM-IRRAS signal is very sensitive to the position of the sample and hence data cannot be reliably compared from one sample to the other. Data is therefore reported here in arbitrary units. The band at 1524 cm^{-1} is attributable to an IR-active benzene ring stretching mode and its position remains unchanged in the three types of films. The peak centered at 1679 cm^{-1} in the self-assembled film as well as in the Au-S-OPE-NH_2 film is assigned to the -NH_2 scissoring mode. This peak is shifted to 1650 cm^{-1} in the Au-NH_2-OPE-SH, with the shift in frequency attributable to the chemisorption of the amine group onto the gold surface.

The XPS and PM-IRRAS experiments confirmed the presence of directionally oriented films from the two different LB deposition sequences. However, the question of whether these films exhibit a preferential orientation of the sample, or are truly homogeneous films of anisotropically aligned NOPES molecules may still be open. To further address the homogeneity of the molecular order, a quantitative study based on the different chemical reactivity of the -NH_2 and -SH terminal groups with a

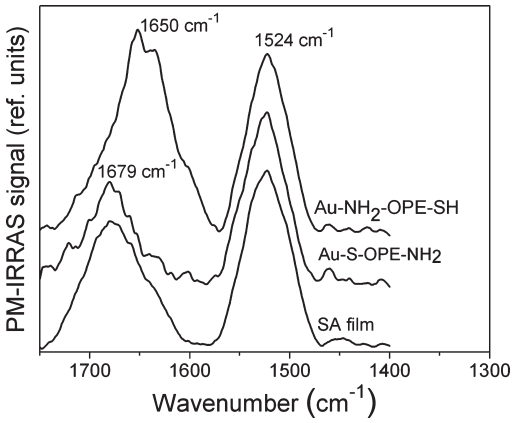

Figure 4. PM-IRRAS spectra of a self-assembled (SA) monolayer and a one-layer LB film deposited at 15 mN/m onto a gold electrode with the substrate initially immersed into the subphase and out of the subphase.

fatty acid was undertaken (Scheme 2). The frequency change (Δf) for a QCM quartz resonator before and after the exposure of an Au-S-OPE-NH_2 film to a behenic acid solution (10^{-2} M in $CHCl_3$, 30 min) indicates that a monolayer of behenic acid was deposited on the NOPES film with a surface coverage of 6.3×10^{-10} mol/cm^2, corresponding to 97% of the terminal groups reacting with the carboxylic acid. In contrast, no frequency change (Δf) for the QCM quartz resonator was observed before and after the exposure of an Au-NH_2-OPE-SH film to a behenic acid. These results are indicative of a complete orientation of the NOPES molecules in the films according to the deposition mode.

Atomic force microscopy (AFM) was used to provide topographic images of the LB films, and thus, to check the homogeneity and quality of the films transferred onto mica substrates. Representative images and section analysis profile for the two types of films (mica-S-OPE-NH_2 and mica-NH_2-OPE-SH) are shown in Figure 5. It is important to note here that XPS spectra of these films deposited onto mica showed a doublet at 167.8 and 169.1 eV (mica-S-OPE-NH_2) and at 163.2 and 164.3 eV (mica-NH_2-OPE-SH), which again are consistent with the transfer of directionally oriented Langmuir films on to the mica substrate (Scheme 1). Both types of films are of high quality, with a low root-mean-square (rms) roughness (0.089 nm for mica-NH_2-OPE-SH films and 0.045 nm for mica-S-OPE-NH_2 films). AFM images of films transferred at lower and higher surface pressures were also obtained with the purpose of optimizing the transfer conditions. The results indicated that films transferred at lower surface pressures featured some pinhole defects (especially in mica-NH_2-OPE-SH films) whereas films transferred at higher surface pressures (e.g., 18 mN/m) showed evidence of local disorder and collapse.

An indirect evaluation of defect densities in thin solid films[60] may be conveniently obtained by cyclic voltammetry using surface modified electrodes and following electron transfer reactions between a redox couple in an electrolyte solution and the underlying electrode. Figure 6 shows the cyclic voltammograms obtained from aqueous solutions containing 1 mM $K_3[Fe(CN)_6]$ and 0.1 M KCl, using a bare gold substrate and two series of gold working electrodes, each modified series being composed of films of one orientation of NOPES monomolecular LB films deposited at several different transfer surface pressures. The electrochemical response of the bare gold electrode exhibits a clear voltammetric wave for ferricyanide.

dx.doi.org/10.1021/la104734j |*Langmuir* 2011, 27, 3600–3610

Scheme 2. Chemistry Used to Verify the Formation of Directionally Oriented Films

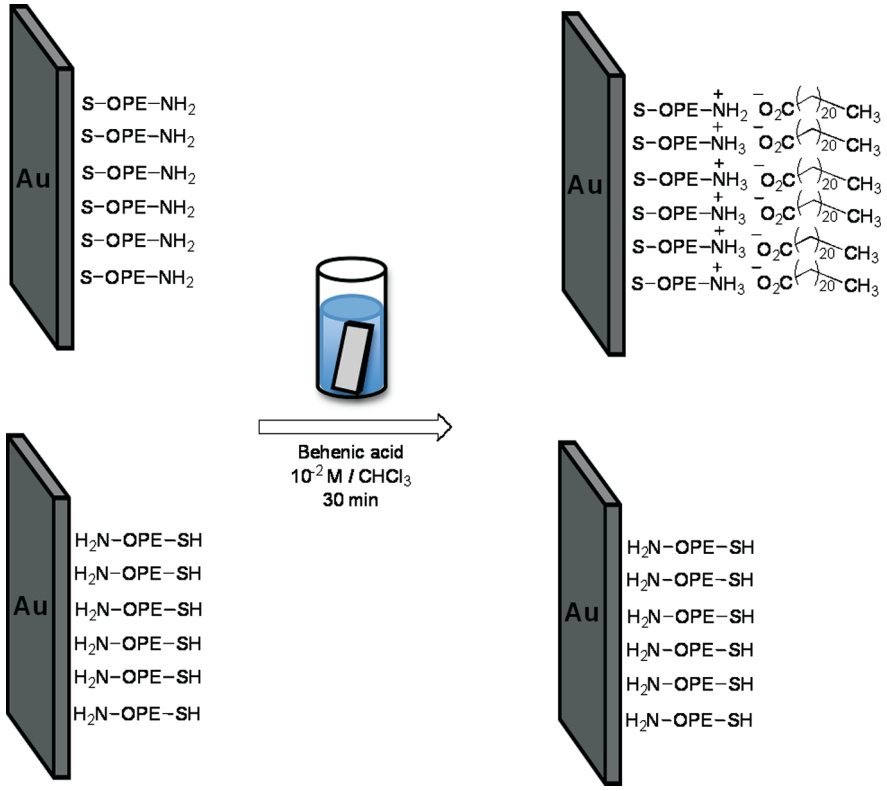

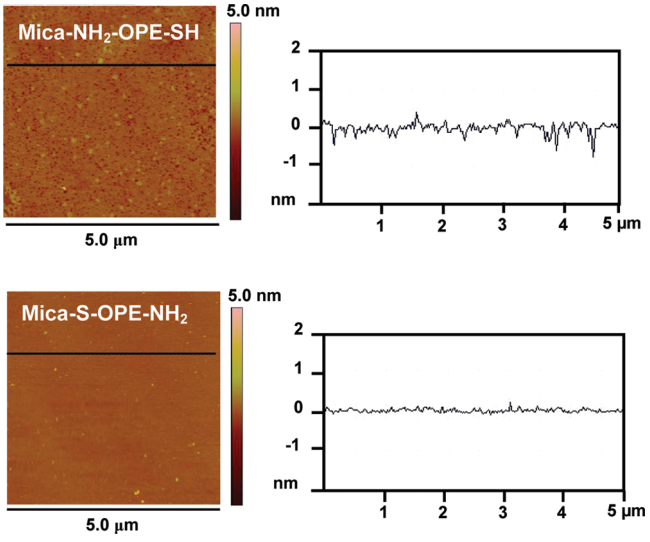

Figure 5. AFM images (left) and section analysis profile (right) of a one-layer LB film transferred at 15 mN/m onto freshly cleaved mica, with the substrate initially immersed into the subphase (top) and with the substrate initially out of the subphase (bottom).

In contrast, the electrode is largely passivated for the system covered by one monolayer (either Au-S-OPE-NH_2 or Au-NH_2-OPE-SH) transferred at 15 mN/m, indicating a low density of holes in the monolayer. The lower passivation effect for films deposited at low surface pressures indicate that 15 mN/m is an optimum surface pressure of transference. Higher surface pressures of transference did not improve the passivation effect.

The optical properties of the transferred films offer additional insight into the molecular arrangement and degree of order within the film. Langmuir films of NOPES were transferred onto quartz substrates at 15 mN/m either during the upstroke or downstroke of the substrate and the UV−vis absorption spectra were recorded (Figure 7). For the purpose of comparison, the UV−vis spectrum of acetyl-protected NOPES in chloroform solution is also plotted. The spectra of the LB films show a main band centered at 314 nm (quartz-NH_2-OPE-SH) and 320 nm (quartz-S-OPE-NH_2), while the solution spectrum exhibits a band centered at 350 nm, corresponding to a $\pi-\pi^*$ transition of the conjugated molecular backbone and at an energy comparable to that of the parent molecule 1,4-bis(phenylethynylene-benzene).[34] The blue shift of 36 and 30 nm of the spectra of the films with respect to that of the solution spectrum is attributable to the formation of two-dimensional H-aggregates. These aggregates are commonly found in LB films in which the chromophore has the main dipole transition moment arranged more or less along the backbone, such as *trans*-stilbenes,[61,62] *trans*-azobenzenes,[63] hemicyanine derivatives,[64] tolan,[65] and OPE derivatives.[47]

Electrical Characteristics of the LB Films. To determine the electrical characteristics of the LB films deposited as described before, $I-V$ curves were recorded using a scanning tunnelling microscope (STM) and averaged from 350 scans. To ensure reproducibility and reliability of the results, $I-V$ curves were obtained at different locations on the substrate and using different samples. Before determining $I-V$ curves, the thickness of the monolayer as well as the tip−substrate distance (s) must be evaluated so that the vertical placement of the tip with respect to the monolayer is known. Depending on the set-point conditions the STM tip can be above the monolayer, just touching the

dx.doi.org/10.1021/la104734j |*Langmuir* 2011, 27, 3600–3610

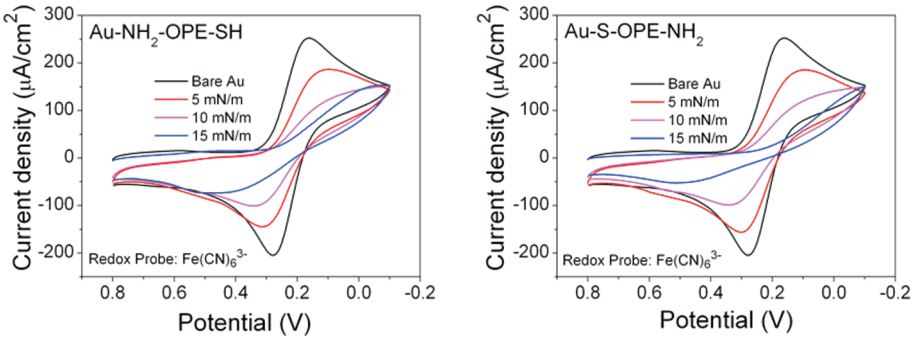

Figure 6. Cyclic voltammograms (CVs) of a bare gold and monomolecular LB film of NOPES deposited onto gold electrodes at the indicated transfer surface pressures: (a) with the substrate initially immersed in the subphase (Au-NH_2-OPE-SH); and (b) out of the subphase (Au-NH_2-OPE-SH). The gold working electrode was immersed in an aqueous solution of 1 mM $K_3[Fe(CN)_6]$ and 0.1 M KCl and CVs were recorded at 0.05 V/s with the scan direction being from positive to negative potentials. An Ag|AgCl|saturated KCl reference electrode was employed and the counter electrode was a Pt sheet.

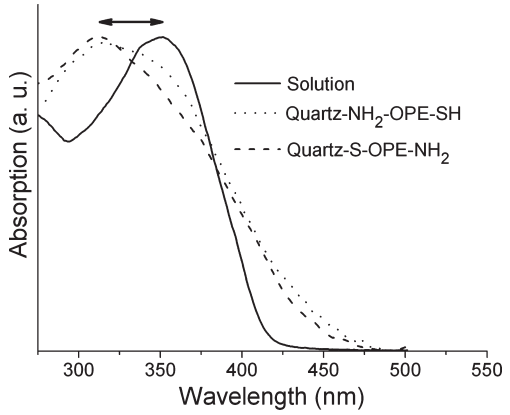

Figure 7. UV−vis spectra of the acetyl-protected NOPES dissolved in chloroform (solid line) and UV−vis spectra of a one-layer film of NOPES transferred at 15 mN/m onto a quartz substrate during the withdrawal of the substrate from the water subphase (dotted line: quartz-NH_2-OPE-SH) and during the immersion of the substrate into the water subphase (dashed line: quartz-S-OPE- NH_2).

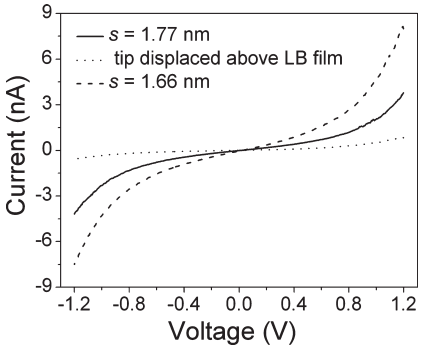

Figure 8. $I-V$ curves of a one-layer LB film of NOPES transferred onto Au(111) at 15 mN/m using several set-point parameters: 0.75 nA (s = 1.77 nm) (solid line); 1.5 nA (s = 1.66 nm) (dashed line); and 0.1 nA (tip displaced above the LB film) (dotted line). U_t = 0.6 V.

monolayer or embedded within the monolayer. If the STM tip is not in contact with the monolayer, the tunnelling current measured represents tunnelling through both the monolayer and the gap which exists between the top of the monolayer and the tip. Calibration of the tip−substrate distance is required in order to determine the vertical displacement of the tip. In particular, we need to determine the set-point conditions where the tip is located directly on-top of the LB film. In order to evaluate this distance at which contact between the tip and top of the film occurs, a quantification of the current decay ($d \ln(I)/ds$) within the LB film is required. For conditions where the tip is embedded within the film, current-distance scans which display a monotonic exponential decrease of the tunneling current were recorded at regular intervals during the measurements. These monotonic exponential decay curves were then plotted as $\ln(I)$ versus s. Averaging the slope of the corresponding $d \ln(I)/ds$ curves yields $d \ln(I)/ds$ values typically on the order of 6.22 ± 1.04 nm^{-1}, which is in good agreement with values reported for other highly conjugated compounds incorporated in monomolecular films.[66] This $d \ln(I)/ds$ value for within the LB film, together with the assumption that the conductance at the point where metal−tip contact occurs is the conductance quantum G_0 ($G_0 = 2e^2/h$ = 77.4 μS), provide the basis for an absolute calibration of the gap separation at a given current according to the following equation:

$$s = \frac{\ln(G_0 U_t / I_0)}{d \ln(I)/ds} \quad (2)$$

where I_0 and U_t are the set-point parameters of the STM (I_0 = "set-point-current" and U_t = "tip bias").

Using this calibration method, and the thicknesses of these LB films, 1.77 ± 0.05 and 1.71 ± 0.05 nm for Au-NH_2-OPE-SH and Au−S−OPE-NH_2 LB films, respectively (calculated using the attenuation of the Au 4f signal from the substrate as explained in the experimental section), the $I-V$ curves can be measured with the tip directly in contact with the monolayer. Set-point conditions can also be selected where either the tip is within the film or displaced above the top of the film. In the former case the measured $d \ln(I)/ds$ values together with eq 2 can be used to estimate the distance of the tip within the film, while in the latter case it cannot since $d \ln(I)/ds$ above the film will differ from that within.

Figure 8 shows $I-V$ curves obtained for a one layer LB film transferred onto Au(111), at 15 mN/m with the substrate initially immersed in the subphase (Au-NH_2-OPE-SH) using several set-point parameters (U_t = 0.6 V and I_0 = 1.5, 0.75, and 0.1 nA). According to eq 2 the set-point parameters of 0.6 V and 1.5 nA place the tip within the film at s = 1.66 nm. At set-point

dx.doi.org/10.1021/la104734j |*Langmuir* 2011, 27, 3600–3610

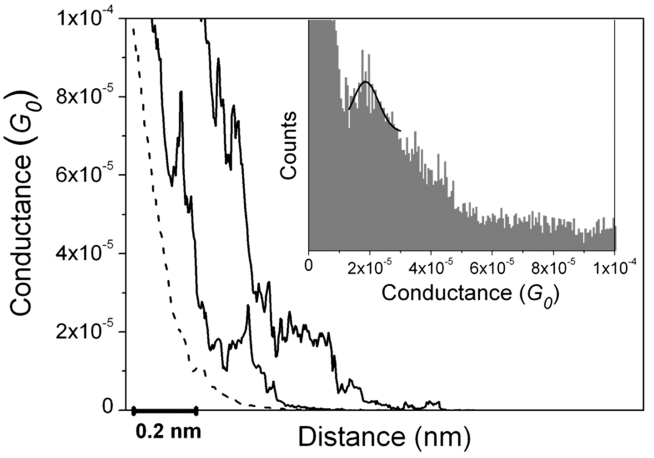

Figure 9. Representative conductance-distance curves (solid lines) using the $I(s)$ method at low set-point current (5 nA) for a one layer film. The curves are shifted horizontally for clarity and the dashed line shows an exponential decay curve in the absence of molecular wire formation. The inset shows a conductance histogram built by adding together all the points of 150 conductance traces that showed a discernible plateau. Conductance data are presented in units of the conductance quantum $G_0 = 2e^2/h = 77.4\ \mu$S. $U_{tip} = 0.6$ V. The solid line is a constrained Gaussian fit to the peak.

parameters of 0.6 V and 0.75 nA $s = 1.77$ nm. Since the thickness of a one-layer LB film is 1.77 ± 0.05 nm, at these set-point values the tip is positioned directly on the monolayer. Meanwhile, decreasing the set-point current to 0.1 nA (for $U_t = 0.6$ V) causes the tip to move away from the top of the monolayer.

The profile of all the $I-V$ curves is nearly symmetrical and each exhibits an approximately sigmoidal profile over the full voltage region. Nevertheless, the $I-V$ curves become linear in the low voltage region (from −0.5 to +0.5 V), the ohmic region, where the conductance value for the $I-V$ curve at 0.75 nA is $1.37 \times 10^{-5}\ G_0$, which is in good agreement with the conductance value ($(1.84 \pm 0.42) \times 10^{-5}\ G_0$) obtained by the $I(s)$ technique with a low current amplifier for a one-layer LB film, Figure 9.

The $I(s)$ STM method developed by Haiss et al.[2,67] has been widely used to determine the conductance of single molecules[3,68,69] and molecules assembled into monolayers.[24,25,70] In the present case, the junctions were formed by placing the gold STM tip at a given distance determined by the set-point parameters ($U_t = 0.6$ V and $I_0 = 5$ nA). We found that these parameters were sufficient to penetrate the monolayer ($s = 1.47$ nm, according to eq 2). When the proper distance was achieved, the feedback was disabled, and the STM tip was retracted while keeping a constant $x-y$ position. One (or more) chemical Au−S or Au−NH_2 linkages between the STM tip and monolayer are thereby established, and the current as a function of distance was recorded until this linkage(s) breaks. This procedure results in a current plateau followed by a step in the $I(s)$ retraction curve (Figure 9), which may be attributed to conduction through a molecular bridge simultaneously bound to the tip and the substrate.[1,2] Current−distance [$I(s)$] curves were analyzed statistically in the form of histogram plots to determine the molecule conductance. These histograms (inset of Figure 9) were built by adding all the current (or conductance) points from ca. 150 current versus distance curves showing a discernible

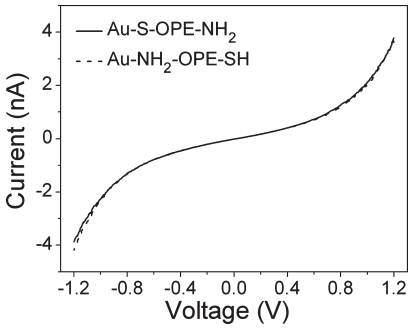

Figure 10. $I-V$ curves of a one layer LB film of NOPES transferred onto Au(111) at 15 mN/m for the indicated films. $U_t = 0.6$ V, $I_0 = 0.75$ nA ($s = 1.69$ nm) and 0.75 nA ($s = 1.77$ nm) for Au-NH_2-OPE-SH and Au-S-OPE-NH_2, respectively.

plateau. It should be noted here that this method of measurement is obviously destructive for the monolayer structure, since the initial distance between the tip and the substrate is less than the LB film thickness; that is, the tip penetrates into monolayer. As a consequence the molecule (or molecules) initially trapped within the junction must presumably tilt toward the horizontal in order to compensate for the vertical approach of the tip. Then, during measurement, the molecule is "lifted" until the molecule bridge-(s) breaks.

The nearly symmetrical profiles of the $I-V$ curves (Figure 8), despite the asymmetry of the molecule, indicate that NOPES does not behave like a molecular diode with strong rectifying behavior. In other words, the molecule is essentially acting as a nonrectifying molecular bridge. Similar nonrectifying behavior has been previously reported for other "antisymmetric" π-conjugated compounds.[14,71−74]

We have shown that films can be assembled with either the thiol of amine group of NOPES in contact with the gold substrate. This clearly gives a directionality to the film and we now examine if the headgroup which is in contact with the gold substrate can have any influence on the electrical response of the films. With this in mind, Au-S-OPE-NH_2 monolayers have also been studied with STM and compared with Au-NH_2-OPE-SH films. $I-V$ curves for Au-S-OPE-NH_2 LB films were determined using the same protocol explained above for Au-NH_2-OPE-SH LB films. The following set point parameters were used: $U_t = 0.6$ V and $I_0 = 0.75$ nA ($d\ln(I)/ds = 6.58 \pm 1.98$), resulting in a tip−substrate distance of 1.69 nm. This value corresponds to the thickness of the film determined by the XPS measurements (1.71 ± 0.05 nm), and the resulting $I-V$ curve (Figure 10) is practically identical to the one obtained for Au-NH_2-OPE-SH monolayers. This result conveys new possibilities for the assembly of well-defined sandwich-type structures, as either of the functional groups may be utilized to bind to the substrate (while the remaining functional group allows for further chemical modification at the film), without affecting the conductance profile of the molecule.

The sigmoidal $I-V$ curves and absence of any spectroscopic peaks in these $I-V$ curves points toward a nonresonant tunnelling mechanism of transport through these metal-molecule-metal junctions. The Simmons model[75] is one of the simplest tunnelling barrier models which has been widely used for describing transport through metal |SAM|metal junctions,[76,77] and single molecules.[78,79] The Simmons model is used here to fit the experimental $I-V$ data for an Au-NH_2-

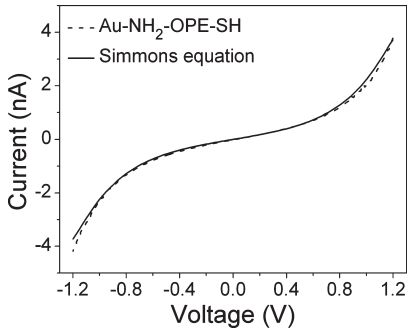

Figure 11. $I-V$ curve of a one layer LB film of NOPES transferred onto Au(111) at 15 mN/m (dashed line) and fitting according to the Simmons equation, Φ = 0.83 eV, α = 0.56 (solid line). U_t = 0.6 V, I_0 = 0.75 nA (s = 1.77 nm).

OPE-S-Au(tip) junction (Figure 11). In this model, the current I is defined as

$$I = \frac{Ae}{4\pi^2\hbar s^2}\left\{\left(\Phi - \frac{eV}{2}\right)\exp\left[-\frac{2(2m)^{1/2}}{\hbar}\alpha\left(\Phi - \frac{eV}{2}\right)^{1/2}s\right] - \left(\Phi + \frac{eV}{2}\right)\exp\left[-\frac{2(2m)^{1/2}}{\hbar}\alpha\left(\Phi + \frac{eV}{2}\right)^{1/2}s\right]\right\} \quad (3)$$

where V is the applied potential, A is the cross-sectional area of the molecular junction between substrate and tip (taken as the area occupied per molecule which is 0.254 nm^2 from QCM experiments), s is the width of the tunnelling barrier (assumed to be the through-bond distance between the functional groups in OPE calculated with a molecular modeling program as 2.03 nm), Φ is the effective barrier height of the tunnelling junction (relative to the Fermi level of the Au), α is related to the effective mass of the tunnelling electron, and m and e represent the mass and the charge of an electron. Φ and α are the parameters which are then used to best fit the $I-V$ data in Figure 11. Good agreement between the data and the model obtained for Φ = 0.83 eV and α = 0.56. Despite the molecular asymmetry of NOPES, this effective barrier height is only slightly larger than that obtained by Liu et al.[39] for a symmetric OPE with thiol functional groups at both ends (Φ = 0.77 eV); and much lower than that found in saturated systems.[68,80−82] It is worth emphasizing that eq 3, which is based on a very simple model of nonresonant tunnelling, gives a reasonable description of our experimental $I-V$ data, and it is therefore reasonable to assume that the mechanism of transport through these metal-molecule-metal junctions is nonresonant tunnelling.

CONCLUSIONS

4-[4′-(4″-Thioacetyl-phenyleneethynylene)-phenyleneethynylene]-aniline has been synthesized, subsequently deprotected to afford the free thiol derivative NOPES, which has been assembled into well-packed monomolecular films by means of the Langmuir−Blodgett method. Langmuir films of NOPES were prepared at the air−water interface and characterized by surface pressure vs area per molecule isotherms and Brewster angle microscopy, which revealed that this molecule can form true monomolecular films at the air−water interface. LB films were transferred onto solid substrates which were either initially immersed in the water subphase or out of the water subphase. In both cases a transfer ratio close to unity was obtained. XPS, PM-IRRAS, and QCM experiments demonstrated that NOPES was linked through the amino group to the gold substrate (Au-NH$_2$−OPE-SH) when the deposition took place during the upstroke of the solid support, whereas the molecule was bonded to the gold substrate through the thiol group when the transfer occurred during the immersion of the gold substrate (Au−S−OPE-NH$_2$). Atomic force microscopy images together with cyclic voltammetry experiments revealed the formation of highly homogeneous films free of three-dimensional defects at an optimized transfer surface pressure of 15 mN/m. The presence of a reactive, "free", terminal functional group at the LB monolayer additionally raises the prospect of chemically anchoring a second layer, of a different compound, to the monolayer, thereby offering a new route to the construction of well-defined sandwich-type structures. Electrical characteristics of the LB films on gold substrates were determined, via $I-V$ curves, by positioning a gold STM tip in contact with the monolayer (as determined from calibration of the tip-to-substrate distance and knowing the thickness of the LB film determined from XPS measurements). $I-V$ curves were symmetric, despite antisymmetric contacts of the molecule with respect to the tip and the substrate. These $I-V$ curves and good Simmons model fit indicate that charge flow through the NOPES metal-molecule-metal junction is via a nonresonant tunnelling mechanism.

AUTHOR INFORMATION

Corresponding Author
*E-mail: pilarcea@unizar.es.

ACKNOWLEDGMENT

The authors are grateful for financial assistance from Ministerio de Educación y Ciencia (MEC) from Spain and fondos FEDER in the framework of Project CTQ2009-13024. P.J.L holds an EPSRC Leadership Fellowship. R.J.N acknowledges support from EPSRC under Grant EP/C00678X/1 (Mechanisms of Single Molecule Conductance). L.M.B acknowledges her grant from Banco Santander, and S.M acknowledges his Juan de la Cierva position from Ministerio de Ciencia e Innovación (Spain). G.P is grateful for his FPU grant from MEC. We are also grateful to Dr. Jordi Díaz from the University of Barcelona and Dr. Guillermo Antorrena from Instituto de Nanociencia de Aragón for their assistance with the AFM and XPS measurements, respectively.

REFERENCES

(1) Xu, B. Q.; Tao, N. J. *Science* **2003**, *301*, 1221.
(2) Haiss, W.; van Zalinge, H.; Higgings, S. J.; Bethell, D.; Höbenreich, H.; Schiffrin, D. J.; Nichols, R. J. *J. Am. Chem. Soc.* **2003**, *125*, 15294.
(3) Wang, C. S.; Batsanov, A. S.; Bryce, M. R.; Martin, S.; Nichols, R. J.; Higgings, S. J.; Garcia-Suarez, V. M.; Lambert, C. J. *J. Am. Chem. Soc.* **2009**, *131*, 15647.
(4) Quek, S. Y.; Kamenetska, M.; Stigerwald, M. L.; Choi, H. J.; Louie, S. G.; Hybertsen, M. S.; Neaton, J. B.; Venkataraman, L. *Nat. Nanotechnol.* **2009**, *4*, 230.
(5) Lafferentz, L.; Ample, F.; Yu, H.; Hecht, S.; Joachim, C.; Grill, L. *Science* **2009**, *323*, 1193.
(6) Yazdani, A.; Eigler, D. M.; Lang, N. D. *Science* **1996**, *272*, 1921.
(7) Zhou, J. F.; Chen, F.; Xu, B. *J. Am. Chem. Soc.* **2009**, *131* (30), 10439.

(8) Cui, X. D.; Primak, A.; Zarate, X.; Tornfohr, J.; Sankey, O. F.; Moore, A. L.; Moore, A. T.; Gust, D.; Harris, G.; Lindsay, S. M. *Science* **2001**, *294*, 571.
(9) Wang, G.; Kim, T.-W.; Jo, G.; Lee, T. *J. Am. Chem. Soc.* **2009**, *131* (16), 5980.
(10) Ramachandran, G. K.; Hopson, T. J.; Rawlett, A. M.; Nagahara, L. A.; Primak, A.; Lindsay, S. M. *Science* **2003**, *300*, 1413.
(11) Beebe, J. M.; Engeelkes, V. B.; Miller, L. L.; Frisbie, C. D. *J. Am. Chem. Soc.* **2002**, *124*, 11268.
(12) Engelkes, V. B.; Beebe, J. M.; Frisbie, C. D. *J. Am. Chem. Soc.* **2004**, *126*, 14287.
(13) Lewis, P. A.; Inman, C. E.; Maya, F.; Tour, J. M.; Hutchison, J. E.; Weiss, P. S. *J. Am. Chem. Soc.* **2005**, *127*, 17421.
(14) Villares, A.; Lydon, D. P.; Low, P. J.; Robinson, B. J.; Ashwell, G. J.; Royo, F. M.; Cea, P. *Chem. Mater.* **2008**, *20* (1), 258.
(15) Villares, A.; Pera, G.; Martin, S.; Nichols, R. J.; Lydon, D. P.; Applegarth, L.; Beeby, A.; Low, P. J.; Cea, P. *Chem. Mater.* **2010**, *22* (6), 2041.
(16) Venkataraman, L.; Park, Y. S.; Whaley, A. C.; Nuckolls, C.; Hybertsen, M. S.; Steigerwald, M. L. *Nano Lett.* **2007**, *7* (2), 502.
(17) Chen, F.; Li, X.; Hihath, J.; Huang, Z.; Tao, N. J. J. *J. Am. Chem. Soc.* **2006**, *128* (49), 15874.
(18) Martin, S.; Haiss, W.; Higgins, S.; Cea, P.; Lopez, M. C.; Nichols, R. J. *J. Phys. Chem. C* **2008**, *112* (10), 3941.
(19) Kim, B.; Beebe, J. M.; Jun, Y.; Zhu, X. Y.; Frisbie, C. D. *J. Am. Chem. Soc.* **2006**, *128*, 4970.
(20) Kiguchi, M.; Miura, S.; Hara, K.; Sawamura, M.; Murakoshi, K. *Appl. Phys. Lett.* **2006**, *89*, 213104.
(21) Yasuda, S.; Yoshida, S.; Sasaki, J.; Okutsu, Y.; Nakamura, T.; Taninaka, A.; Takeuchi, O.; Shigekawa, H. *J. Am. Chem. Soc.* **2006**, *128*, 7746.
(22) Venkataraman, L.; Klare, J. E.; Tam, I. W.; Nuckolls, C.; Hybertsen, M. S.; Steigerwald, M. N. *Nano Lett.* **2006**, *6*, 458.
(23) Venkataraman, L.; Klare, J. E.; Nuckolls, C.; Hybertsen, M. S.; Steigerwald, M. L. *Nature* **2006**, *442*, 904.
(24) Sek, S.; Misicka, A.; Swiatek, K.; Maicka, E. *J. Phys. Chem. B* **2006**, *110*, 19671.
(25) Sek, S. *J. Phys. Chem. C* **2007**, *111*, 12860.
(26) Ashwell, G. J.; Gandolfo, D. S. *J. Mater. Chem.* **2001**, *11*, 246.
(27) Baldwin, J. W.; Amaresh, R. R.; Peterson, I. R.; Shumate, W. J.; Cava, M. P.; Amiri, M. A.; Hamilton, R.; Ashwell, G. J.; Metzger, R. M. *J. Phys. Chem. B* **2002**, *106*, 12158.
(28) Martin, A. S.; Sambles, J. R.; Ashwell, G. J. *Thin Solid Films* **1992**, *210*, 313.
(29) Kushmerick, J. G.; Holt, D. B.; Yang, J. C.; Naciri, J.; Moore, M. H.; Shashidhar, R. *Phys. Rev. Lett.* **2002**, *89*, 086802.
(30) Kushmerick, J. G.; Whitaker, C. M.; Pollack, S. K.; Schull, T. L.; Shashidhar, R. *Nanotechnology* **2004**, *15*, S489.
(31) Wong, M. S.; Nicoud, J. F. *Tetrahedron Lett.* **1994**, *35*, 6113.
(32) Bunz, U. H. F. *Chem. Rev.* **2000**, *100*, 1605.
(33) Franken, P. A.; Hill, L. E.; Peters, C. W.; Weinrich, G. *Phys. Rev. Lett.* **1961**, *7*, 118.
(34) Beeby, A.; Findlay, K.; Low, P. J.; Marder, T. B. *J. Am. Chem. Soc.* **2002**, *124* (28), 8280.
(35) Breen, C. A.; Tischler, J. R.; Bulovic, V.; Swager, T. M. *Adv. Mater.* **2005**, *17*, 1981.
(36) Donhauser, Z. J.; Mantooth, B. A.; Kelly, K. F.; Bumm, L. A.; Monnell, J. D.; Stapleton, J. J.; Price, D. W., Jr; Rawlett, A. M.; Allara, D. L.; Tour, J. M.; Weiss, P. S. *Science* **2001**, *292*, 2303.
(37) Huber, R.; Gonzalez, M. T.; Wu, S.; Langer, M.; Grunder, S.; Horhoiu, V.; Mayor, M.; Bryce, M. R.; Wang, C. S.; Jitchati, R.; Schonenberger, C.; Calame, M. *J. Am. Chem. Soc.* **2008**, *130* (3), 1080.
(38) Xiao, X. Y.; Nagahara, L. A.; Rawlett, A. M.; Tao, N. J. J. *J. Am. Chem. Soc.* **2005**, *127*, 9235.
(39) Liu, K.; Wang, X.; Wang, F. *ACS Nano* **2008**, *2*, 2315.
(40) Wu, S.; Gonzalez, M. T.; Huber, R.; Grunder, S.; Mayor, M.; Schonenberger, C.; Calame, M. *Nat. Nanotechnol.* **2008**, *3* (9), 569.
(41) Haiss, W.; Wang, C. S.; Grace, I.; Batsanov, A. S.; Schiffrin, D. J.; Higgins, S. J.; Bryce, M. R.; Lambert, C. J.; Nichols, R. J. *Nat. Mater.* **2006**, *5* (12), 995.
(42) Chen, J.; Reed, M. A.; Rawlett, A. M.; Tour, J. M. *Science* **1999**, *286*, 1550.
(43) Gergel, N. H.; Majumdar, N.; Martin, Z. *J. Vac. Sci. Technol.* **2006**, *24*, 1243.
(44) Tour, J. M. *Acc. Chem. Res.* **2000**, *33*, 791.
(45) Gyepi-Garbrah, S. H.; Silerova, R. *Phys. Chem. Chem. Phys.* **2002**, *4*, 3436.
(46) Tang, Z. X.; Hicks, R. K.; Magyar, R. J.; Tretiak, S.; Gao, Y.; Wang, H. L. *Langmuir* **2006**, *22*, 8813.
(47) Villares, A.; Lydon, D. P.; Porrès, L.; Beeby, A.; Low, P. J.; Cea, P.; Royo, F. M. *J. Phys. Chem. B* **2007**, *111*, 7201.
(48) Villares, A.; Martin, S.; Giner, I.; Diaz, J.; Lydon, D. P.; Low, P. J.; Cea, P. *Soft Matter* **2008**, *4* (7), 1508.
(49) Villares, A.; Lydon, D. P.; Robinson, B. J.; Ashwell, G.; Royo, F. M.; Low, P. J.; Cea, P. *Surf. Sci.* **2008**, *602* (24), 3683.
(50) Lavastre, O.; Cabioch, S.; Dixneuf, P. H.; Vohlidal, J. *Tetrahedron* **1997**, *53*, 7595.
(51) Hortholary, C.; Coudret, C. *J. Org. Chem.* **2003**, *68*, 2167.
(52) Clark, H. C.; Dixon, K. R. *J. Am. Chem. Soc.* **1969**, *91*, 596.
(53) Paul, F.; Patt, J.; Hartwig, J. F. *Organometallics* **1995**, *14*, 3030.
(54) Bain, C. D.; Whitesides, G. M. *J. Phys. Chem.* **1989**, *93*, 1670.
(55) Haiss, W.; Lackey, D.; Sass, J. K.; Besocke, K. H. *J. Chem. Phys.* **1991**, *95*, 2193.
(56) Sauerbrey, G. *Z. Physik* **1959**, *155*, 206ff.
(57) Liu, K.; Li, G.; Wang, X.; Wang, F. *J. Phys. Chem. C* **2008**, *112*, 4342.
(58) Liang, T.-T.; Naitoh, Y.; Horikawa, M.; Ishida, T.; Mizutani, W. *J. Am. Chem. Soc.* **2006**, *128*, 13720.
(59) Kankate, L.; Turchanin, A.; Gölzhäuser, A. *Langmuir* **2009**, *25* (18), 10435.
(60) Porter, M. D.; Bright, T. B.; Allara, D. L.; Chidsey, C. E. D. *J. Am. Chem. Soc.* **1987**, *109*, 3559.
(61) Kaji, H.; Shimoyama, Y. *Jpn. J. Appl. Phys.* **2001**, *40*, 1396.
(62) Martín, S.; Cea, P.; Pera, G.; Haro, M.; López, M. C. *J. Colloid Interface Sci.* **2007**, *308*, 239.
(63) Pedrosa, J. M.; Martín-Romero, M. T.; Camacho, L. *J. Phys. Chem. B* **2002**, *106*, 2583.
(64) Heesemann, J. *J. Am. Chem. Soc.* **1980**, *102*, 2167.
(65) Pera, G.; Villares, A.; López, M. C.; Cea, P.; Lydon, D. P.; Low, P. J. *Chem. Mater.* **2007**, *19* (4), 857.
(66) Holmlin, R. E.; Haag, R.; Chabinyc, M. L.; Ismagilov, R. F.; Cohen, A. E.; Terfort, A.; Rampi, M. A.; Whitesides, G. M. *J. Am. Chem. Soc.* **2001**, *123*, 5075.
(67) Haiss, W.; Nichols, R. J.; van Zalinge, H.; Higgins, S. J.; Bethel, D.; Schiffrin, D. J. *Phys. Chem. Chem. Phys.* **2004**, *6*, 4330.
(68) Haiss, W.; Martin, S.; Leary, E.; van Zalinge, H.; Higgins, S. J.; Bouffier, L.; Nichols, R. J. *J. Phys. Chem. C* **2009**, *113*, 5823.
(69) Sedghi, G.; Sawada, K.; Esdaile, L. J.; Hoffmann, M.; Anderson, H. L.; Bethell, D.; Haiss, W.; Higgins, S. J.; Nichols, R. J. *J. Am. Chem. Soc.* **2008**, *130*, 8582.
(70) Sek, S.; Swiatek, K.; Misicka, A. *J. Phys. Chem. B* **2005**, *109*, 23121.
(71) Ashwell, G. J.; Urasinska, B.; Tyrrell, W. D. *Phys. Chem. Chem. Phys.* **2006**, *8*, 3314.
(72) Reichert, J.; Ochs, R.; Beckmann, D.; Weber, H. B.; Mayor, M.; von Lohneysen, H. *Phys. Rev. Lett.* **2002**, *88*, 176804.
(73) Ashwell, G. J.; Wierzchowiec, P.; Phillips, L. J.; Collins, C. J.; Gigon, J.; Robinson, B. J.; Finch, C. M.; Grace, I. R.; Lambert, C. J.; Buckle, P. D.; Ford, K.; Wood, B. J.; Gentle, I. R. *J. Phys. Chem. Chem. Phys.* **2008**, *10*, 1859.
(74) Ashwell, G. J.; Stokes, R. J. *J. Mater. Chem.* **2004**, *14*, 1228.
(75) Simmons, J. G. *J. Appl. Phys.* **1963**, *281*, 1793.
(76) Akkerman, H. B.; Naber, R. C. G.; Jongbloed, B.; van Hal, P. A.; Blom, P. W. M.; de Leeuw, D. M.; de Boer, B. *Proc. Natl. Acad. Sci. U.S.A.* **2007**, *104* (27), 11161.

(77) Wang, W. Y.; Lee, T.; Reed, M. A. *Phys. Rev.* **2003**, *68*, 035416.
(78) Haiss, W.; Martin, S.; Scullion, L. E.; Bouffier, L.; Higgings, S. J.; Nichols, R. J. *Phys. Chem. Chem. Phys.* **2009**, *11* (46), 10831.
(79) Li, X. L.; He, J.; Hihath, J.; Xu, B. Q.; Lindsay, S. M.; Tao, N. J. J. *J. Am. Chem. Soc.* **2006**, *128*, 2135.
(80) Wold, D. J.; Frisbie, C. D. *J. Am. Chem. Soc.* **2001**, *123* (23), 5549.
(81) Chu, C.; Na, J.-S.; Parsons, G. N. *J. Am. Chem. Soc.* **2007**, *129*, 2287.
(82) Beebe, J. M.; Kim, B.; Frisbie, C. D.; Kushmerick, J. G. *ACS Nano* **2008**, *2*, 827.

■ NOTE ADDED IN PROOF

While this paper was being edited, we became aware of a related paper describing competitive thiol/amine binding to gold surfaces. Ashwell, G. J.; Williams, A.T.; Barnes, S.A.; Chappell, S. L.; Phillips, L.J., Robinson, B.J.; Urasinska-Wojcik, B.; Wierzchowiec, P.; Gentle, I.R.; Wood, B.J. *J. Phys. Chem C* **2011**, in press.